



**HAL**  
open science

# Sum frequency generation study of CO adsorbed on palladium single crystal and nanoparticles: adsorption and catalytic oxidation as a function of size

Jijin Wang

► **To cite this version:**

Jijin Wang. Sum frequency generation study of CO adsorbed on palladium single crystal and nanoparticles: adsorption and catalytic oxidation as a function of size. Other [cond-mat.other]. Université Paris Sud - Paris XI, 2013. English. NNT : 2013PA112343 . tel-00933675

**HAL Id: tel-00933675**

**<https://theses.hal.science/tel-00933675>**

Submitted on 20 Jan 2014

**HAL** is a multi-disciplinary open access archive for the deposit and dissemination of scientific research documents, whether they are published or not. The documents may come from teaching and research institutions in France or abroad, or from public or private research centers.

L'archive ouverte pluridisciplinaire **HAL**, est destinée au dépôt et à la diffusion de documents scientifiques de niveau recherche, publiés ou non, émanant des établissements d'enseignement et de recherche français ou étrangers, des laboratoires publics ou privés.

UNIVERSITE PARIS-SUD

ÉCOLE DOCTORALE : EDOM  
LABORATOIRE : ISMO

DISCIPLINE : PHYSIQUE-CHIMIE

**THÈSE DE DOCTORAT**

**soutenue le 05/12/2013**

**par**

**Jijin Wang**

**Titre de la these**

**Sum frequency generation study of CO adsorbed on palladium  
single crystal and nanoparticles :  
adsorption and catalytic oxidation as a function of size**

M. Bernard Bourguignon  
M. Rémi Lazzari  
Mme. Marie-Claire Saint-Lager  
M. Abderrahmane Tadjeddine  
M. Georges Sitja  
Mme. Carine Michel

Directeur de thèse  
Rapporteur  
Rapporteur  
Président du jury  
Examineur  
Examineur



## Acknowledgement

We are travellers in this world. The most beautiful traveller is who in his own way, never stops his own pace. During my journey in France, I can go forward only with your help.

I would like to express my great gratitude to my supervisor Bernard Bourguignon, who gave me this chance as a Ph.D. student in France, for his kindness, patience, suggestions and assistance during my work. I would like to thank my colleagues Aimeric Ouvrard, who helped me much in the details of experiments, data analysis and thesis correction, Henri Dubost for the article composition and theoretical work, Wanquan and Serge Carrez for the theoretical discussion and thesis corrections. I would like also thank the Dr. Guo Ziang, Dr. Emilie Bulard and Dr. Ahmed Ghalgaoui for their experimental instructions and life help.

I would like to thank the secretary Mme Basset (EDOM) for her assistance in the inscription and the daily life.

I would also like to thank China Scholarship Council and the staffs in education department of embassy, Wang Xiaotao, Qiang Yaping and Zhao Jingmei, for supporting my study and life aboard.

I would like to give my kindest gratitude to our friends, thanks to you, the life is always wonderful.

Thanks to Meng Limin, Xiang Yang, Xie Ning, Li Chengjun, Jia Juanjuan, Lu Lili, Li Lu, Xiao Ji and Jiang Peng for your help and every happy time with you.

Thanks to Li Xiaoyu, Wang Ruijiao and Zhao Tian for your help in the beginning of my life in France.

Thanks to Gao Jing, Sha Zhu, Chen Peng, Huang Jin, Ju Jinchuan, Lin Nan, Song Jinyan, Qian Jin, Lu Yunyu, Zhang Linlin, Luo Xianwen, Tang Qingshan, Ji Botao, Liu Jiagui, Lv Zhihan, Wang Yujue, Xu Chenghai, Li Dikai, Shu Tan, Luo Zhengjie, Zhang Lu, Zhong Jiaqiang, Momo, Qu Long, Zhao Lisha, Fan Xiaoliang, Xia Yun, Wang Xuefeng, Liu Bo and Li Weiwei.

I would like to thank Shi Dunfu, Shi Keliang Mao Xuegang and Bai Zhongtian for the kind reception in other country.

I would like to thank the couple Lieutaud Catherine and Jacques for the best French diners and chats every month.

Thanks much Pierre Soullisse and Li Sha for their help on the habitation in Montrouge, Georges Audi for the interesting experience in the chorus.

Thanks very much for my dear family members, you are my strongest support.

At last, the deepest love to my mother and my father in heaven, this thesis is dedicated for you.

Wang Jijin  
Orsay, France  
13 Oct. 2013

# Contents

<b>Introduction</b>	9
<b>1. Sum frequency generation (SFG) applied to adsorbed molecules</b>	13
<b>1.1 Introduction</b>	14
<b>1.2 Nonlinear optics on surface</b>	15
1.2.1 Generation of 2 <sup>nd</sup> order nonlinear optics on surface	15
1.2.2 Theory of SFG on surface	17
1.2.3 Several applications of femtoseconde SFG model	22
<b>1.3 Experimental setup of SFG</b>	25
1.3.1 Femtosecond laser system	25
1.3.2 Experimental setup of SFG spectroscopy	29
<b>1.4 Data treatment</b>	33
<b>1.5 Conclusion</b>	37
<b>References</b>	38
<b>2. Elaboration of nanoparticle based catalysts in Ultra-High Vacuum (UHV)</b>	39
<b>2.1 Introduction</b>	40
<b>2.2 The UHV system</b>	40
2.2.1 Role of the different UHV chambers	41
2.2.2 Evaporation chamber (EVAP)	43
2.2.3 Pumping of the UHV chambers and security systems	45
2.2.4 Sample characterization by LEED and Auger	45
2.2.5 Modifications of the UHV system	47
<b>2.3 Preparation of Pd nanoparticle on MgO/Ag(100) and Pd(100) single crystal samples</b>	48
2.3.1 Principles of growth	48
2.3.2 Structure of Pd nanoparticles/MgO/Ag(100)	51
2.3.3 Sample cleaning and characterization	53
2.3.4 Growth of MgO films on Ag(100)	54

2.3.5 Growth of Pd nanoparticles on MgO films on Ag(100)	57
<b>2.4 Conclusion</b>	59
<b>References</b>	60
<b>3. CO adsorption on Pd(100) single crystal by SFG</b>	61
<b>3.1. Introduction</b>	62
<b>3.2 CO adsorption on single Pd single crystals: State of the art</b>	63
3.2.1 Vibration modes of CO adsorbed on Pd surfaces	63
3.2.2 Adsorption sites and adsorption phases of CO on Pd(111) and Pd(100) surfaces	64
<b>3.3 Experimental procedure to expose the Pd surface to CO</b>	67
<b>3.4 SFG and LEED studies of CO adsorption as a function of CO coverage</b>	68
<b>3.5 SFG results in the time domain</b>	77
<b>3.6 Simulation of dipolar coupling</b>	79
<b>3.7 Discussion</b>	85
<b>3.8 Conclusion</b>	86
<b>References</b>	87
<b>4. Study of CO adsorption on Pd nanoparticles</b>	91
<b>4.1. Introduction</b>	92
<b>4.2. CO adsorption on Pd NP/MgO/Ag(100)</b>	92
<b>4.3. SFG experiments of CO adsorbed on Pd NP: Size effect of NP</b>	93
<b>4.4 Calculations of single CO adsorption on Pd NPs</b>	99
<b>4.5. Effect of CO adsorption on non-resonant contribution</b>	101
<b>4.6. SFG spectra of CO adsorption on Pd nanoparticles at high CO pressure</b>	103
<b>4.7. Conclusion</b>	104
<b>Reference</b>	105
<b>5. The study of catalytic CO oxidation on Pd(100) and Pd nanoparticles</b>	107
<b>5.1 Introduction</b>	108
5.1.1 O adsorption on Pd crystal and NP	110
5.1.2. CO oxidation pathway on Pd crystal surface	111

5.1.3 CO oxidation on nanoparticles	112
<b>5.2 SFG experimental results of CO catalytic oxidation on Pd crystal and nanoparticles</b>	113
5.2.1 Non resonant SFG on Pd NP / MgO / Ag interacted with O <sub>2</sub>	113
5.2.2 Self-poisoning by CO on Pd surface	115
5.2.3 Catalytic CO oxidation on Pd(100) crystal surface at 300 K and low pressure	118
5.2.4 Size effect of CO oxidation on Pd NPs	123
5.2.5 CO + O co-adsorption on Pd NPs with a high CO pressure at 300 K	130
<b>5.3 Pump-probe study of O<sub>2</sub>+CO co-adsorption on Pd NP</b>	131
5.3.1 Introduction	131
5.3.2 Pump-probe study of O <sub>2</sub> +CO co-adsorption on Pd NP	133
<b>5.4 Conclusion</b>	135
<b>Reference</b>	137
<b>6. Simulation and experiment SFG spectra on ODT with a visible pulse formed by a pulse shaper and a Fabry-Perot</b>	141
<b>6.1 Introduction</b>	142
<b>6.2 Theory of SFG with a delayed visible pulse</b>	144
<b>6.3 Model of calculation</b>	146
6.3.1 Octadecanethiol (ODT)	147
6.3.2 Calculation of first-order polarization	148
6.3.3 Visible pulse formed by a Fabry-Perot etalon	149
6.3.4 Calculation of SFG with a delayed visible pulse in time domain	152
6.3.5 Effect of delay between IR and visible pulse in frequency domain: spectral phase	154
<b>6.4 Experiment set-up</b>	160
<b>6.5 Results and discussion</b>	161
6.5.1 SFG spectra of ODT	161
6.5.2 Experimental spectra	162
6.5.2.1 Spectra obtained with the FP etalon	162
6.5.2.2 Spectra obtained with the 4f pulse shaper	166
6.5.3. Spectro-temporal fit	167
6.5.3.1 Spectra obtained with the FP etalon	167

6.5.3.2 Spectra obtained with the 4f pulse shaper	169
6.5.4 Accuracy of purely spectral deconvolution into Lorentzian bands	169
6.5.4.1 FP etalon	169
6.5.4.2 4f pulse shaper	171
<b>6.6 Conclusion</b>	172
<b>Reference</b>	174
<b>Conclusion</b>	177
<b>Abbreviation</b>	180

# Introduction

Model catalysts made of metallic nanoparticles (NP) grown on ultrathin oxide layers on metallic single crystals [1] allow to study catalysis in conditions similar to the 3D industrial ones in very details using surface science techniques in ultra high vacuum (UHV) conditions. The efficiency of catalytic activity depends on the surface area, the surface structure and morphology of the NPs as well as on the oxide support. Transport of reactants and products which also plays a role is the only aspect of reactivity that cannot be studied by these model catalysts. Transition metals (Ru, Rh, Pd, Os, Re, Ir, Pt, Ni...) are the most commonly used metals for their high catalytic activity and specificity which is related to the presence of an incomplete d band. The interaction of carbon monoxide (CO) with metal is of great interest from the experimental and theoretical points of view because it has served as a model to understand the non-dissociative molecular chemisorption and reactions with O<sub>2</sub> or NO on metals. CO oxidation and NO reduction have also several industrial applications such as conversion of automobile exhaust and pollution suppression.

Vibrational spectroscopies are sensitive techniques for understanding the properties of molecules. The CO-metal interaction can be characterized by the CO internal stretch frequency, which can be easily measured thanks to the high dynamic dipole moment of C-O vibration. The frequency of CO as a function of coverage and NP size is an indicator of CO bonding and environment (including adsorption sites). It evolves as a function of CO coverage because of dipolar interactions and CO-metal bond strength weakening with increasing coverage. In addition it depends on the oxide support and on the co-adsorption of reactants (O in this work) that can strongly interact with the NP metal and change the behaviour of CO on the metal. In this work, Pd NP size effect on the coupling between the NPs and CO molecules is studied, CO molecules being both a reactant and a local probe of the NPs.

Sum Frequency Generation (SFG) is a non linear optical spectroscopy that was first applied to surfaces and interfaces by Y.R. Shen's group in the 1980's [2]. It involves a nonlinear optical process in which an IR pulse induces a coherent first-order polarization which is up-converted by a visible pulse into a second-order polarization at the sum frequency, allowing to observe the vibrational spectrum in the visible range. SFG is a powerful tool in surface science because it helps to overcome two main issues associated with classical vibrational spectroscopies: sensitivity and surface selectivity. The sensitivity comes from the process being coherent and highly directional. The surface selectivity comes from a symmetry

property of second-order susceptibility  $\chi^{(2)}$  processes, which are forbidden in a centrosymmetric medium within the electric dipole approximation. The symmetry being broken at surfaces, SFG signals are exclusively produced at surfaces of centrosymmetric media. This simplifies considerably experiments with respect to linear IR absorption techniques where surface signals are mixed with much larger bulk signals. BroadBand SFG (BBSFG) has been introduced at the end of the 90's by van der Ham et al. [3]. A spectrally broad IR femtosecond pulse and a narrow visible picosecond pulse allow to generate an SFG spectrum in the spectral region covered by the IR pulse with good spectral resolution without scanning the IR frequency: in BB SFG, the resolution is related to the bandwidth of the visible laser. In addition to providing spectroscopy without scanning the laser, BBSFG opens the possibility to probe dynamics at the femtosecond time scale. Finally a major interest of SFG and optical techniques for catalytic studies is the fact that it can be used at high pressure where most surface science techniques cannot be used. This allows to bridge the "pressure gap" and the "material gap" that may arise due to the difference of the state of NPs between UHV and high pressure. Besides SFG, "environmental" transmission electron microscopy (TEM) has been devised in the recent years to allow the observation by TEM of very thin samples at high pressure ( $\approx 10$ -100 mbar). Environmental TEM has established that NPs may change shape at high pressure, depending on the gases that interact with them (rounding NPs under oxygen, faceting under hydrogen). This has increased the interest for probing catalysis at high pressure. Due to the limited availability of SFG systems, there are still only a few systems that were studied by SFG, by the group of H. J. Freund: the co-adsorption of CO and H<sub>2</sub> on Pd(111) [4], and the decomposition and oxidation of methanol on Pd [5-6].

This thesis is composed of 6 chapters. In Chapter 1, we introduce the basic theory of nonlinear optics and SFG. The experimental setup of our SFG system and our method of data analysis are detailed. In Chapter 2, we present the UHV system and how we elaborate samples, including cleaning, characterization and growth of supported nanoparticles (Pd NPs / MgO / Ag(100)). In Chapter 3, we focus on the CO adsorption on Pd(100) using a combined SFG spectroscopy and LEED study. The evolution of CO SFG spectra adsorbed on Pd(100) as a function of coverage, involving dipolar coupling, CO adsorption in regular and compressed structures, and vibrational relaxation are discussed. In Chapter 4, the effect of size of Pd NPs on CO adsorption is studied by SFG and compared to preliminary DFT calculations done at ENS Lyon. In Chapter 5 we study CO oxidation by SFG for various sizes of Pd NPs as well as on Pd(100) single crystal up to several mbar and 390 K. Pump-probe SFG experiments of O<sub>2</sub>+CO co-adsorption are also presented.

In Chapter 6, we report experiments and numerical simulations of BBSFG spectra done on Octa-Decane-Thiol (ODT) Self Assembled Monolayer (SAM) / Au polycrystal. The goal is to examine the accuracy of relative intensities when several bands are present in the SFG spectrum. Because of the coherent nature of SFG, temporal and spectral aspects are mixed. The standard purely spectral deconvolution is compared to the “full” spectro-temporal analysis, and two methods of shaping the visible pulse to reduce its bandwidth are compared (4f pulse shaper or Fabry-Perot etalon).

## References:

- [1] G. Ertl, H. Knoezinger and J. Weitkamp, *Handbook of Heterogeneous Catalysis*, (VCH, Weinheim, 1997).
- [2] Y. R. Shen. *The Principles of Nonlinear Optics*, Chap. 2 and 25, J. Wiley, New York (1984).
- [3] E.W.M. van der Ham, Q.H.F. Vreken, E.R.Eliel, *Opt. Lett.* 21, 1448 (1996)
- [4] M. Morkel, G. Rupprechter and H. J. Freund, *J. Chem. Phys.* 119, 10853 (2003).
- [5] M. Morkel *et al.*, *J. Phys. Chem. B* 108, 12955 (2004).
- [6] M. Bäumer *et al.*, *Phys. Chem. Chem. Phys.* 9, 3541 (2007).



# Chapter 1

## Sum frequency generation (SFG) applied to adsorbed molecules

<b>1.1 Introduction</b>	14
<b>1.2 Nonlinear optics on surface</b>	15
1.2.1 Generation of 2 <sup>nd</sup> order nonlinear optics on surface	15
1.2.2 Theory of SFG on surface	17
1.2.3 Several applications of femtoseconde SFG model	22
<b>1.3 Experimental setup of SFG</b>	25
1.3.1 Femtosecond laser system	25
1.3.2 Experimental setup of SFG spectroscopy	29
<b>1.4 Data treatment</b>	33
<b>1.5 Conclusion</b>	37
<b>References</b>	38

## 1.1 Introduction

Vibrational spectroscopy is very important to understand the properties of molecules. In the field of surface/interface science, optical methods are very attractive because they can be applied in conditions where the surface is only accessible by light (buried interfaces, high pressure conditions). With the appearing and development of laser techniques since 1960, surface spectroscopic studies have been greatly developed. The major advantages of lasers for spectroscopic investigations are the high monochromaticity and coherence, directivity, and the possibility of ultrafast studies that provide us better means to characterize fundamental properties of materials. Thanks to the laser techniques, even order nonlinear optical spectroscopies exhibit high surface-specificity and detection sensitivity [1] and open wide possibilities that are not available in classical linear spectroscopy. The second-order nonlinear processes are second harmonic generation (SHG), sum frequency generation (SFG), and difference frequency generation (DFG). SHG and DFG can be considered as special cases of SFG [2].

The SFG technique involves a process in which two input laser beams at frequencies  $\omega'$  (IR in practice) and  $\omega''$  ('visible' in practice) interact in a medium to generate a third beam at the sum frequency  $\omega = \omega' + \omega''$ . SFG has been applied to surface/interfaces firstly by Y.R. Shen's group in the 1980's using high-intensity narrow-spectrum (picosecond) incident IR and visible sources. The BroadBand SFG (BBSFG), with a broad – spectrum incident IR pulse has been introduced at the end of the 90's by van der Ham et al. [3] and Richter et al. [4]. BBSFG is nowadays largely employed in the field of nonlinear vibrational spectroscopy of surfaces and interfaces [5]. This technique uses an infrared beam in resonance with a vibrational broad band and a 'visible' beam (habitually in the visible or the near-IR but historically always called 'visible'). The visible beam is normally non-resonant. SFG helps to overcome two main difficulties associated with classical vibrational interface spectroscopies: sensitivity and selectivity. The sensitivity comes from the process being coherent and highly directional. The surface selectivity comes from a symmetry propriety of the second-order susceptibility tensor  $\chi^{(2)}$ :  $\chi^{(2)}$  vanishes in a centro-symmetric medium within the electric dipole approximation. However the symmetry is broken at surface/interface, so the SFG signals are exclusively produced at surfaces or interfaces. This property of SFG suppresses therefore the contribution from the bulk [6], which is by far dominant in linear optical spectroscopy.

SFG has been applied successfully to different interfacial systems, including many systems which cannot be probed by other methods, for example liquid interfaces, solid/solid,

liquid/liquid interfaces, surface catalysis near atmospheric pressure, and has allowed the study of ultrafast surface dynamics. [7,8]

## 1.2 Nonlinear optics on surfaces

### 1.2.1 Generation of 2<sup>nd</sup> order nonlinear optics on surface

In the linear optical phenomena, for example reflexion or refraction, the frequency of incident photons is conserved. By contrast nonlinear phenomena include the generation of new frequencies (harmonic, sum, difference). In linear optics, the electrical polarization depends linearly on the electric field:

$$\vec{P} = \varepsilon_0 \chi \vec{E} \quad (1.1)$$

where  $\varepsilon_0$  is the permittivity of vacuum and  $\chi$  the susceptibility tensor (simple number in isotropic media, matrix in non-isotropic media). In the case of an intense light wave, it is necessary to introduce the dependence of the susceptibility tensor on the electrical field  $\vec{E}$ :

$$\chi = \chi^{(1)} + \chi^{(2)} \vec{E} + \chi^{(3)} \vec{E}\vec{E} + \chi^{(4)} \vec{E}\vec{E}\vec{E} + \dots + \chi^{(n+1)} \vec{E}^n \quad (1.2)$$

where  $\chi^{(n)}$  is a tensor of (n+1) rank with  $3^{n+1}$  components. In the case of the second order,  $\vec{\chi}^{(2)}$  is composed by  $3 \times 9 = 27$  terms. The induced polarization is written as:

$$\vec{P} = \varepsilon_0 [\chi^{(1)} + \chi^{(2)} \vec{E} + \chi^{(3)} \vec{E}\vec{E} + \chi^{(4)} \vec{E}\vec{E}\vec{E} + \dots + \chi^{(n+1)} \vec{E}^n] \vec{E} \quad (1.3)$$

- linear contribution:  $\vec{P}_L = \varepsilon_0 \chi^{(1)} \vec{E}$

- nonlinear contribution :  $\vec{P}_{NL} = \varepsilon_0 [\chi^{(2)} \vec{E}\vec{E} + \chi^{(3)} \vec{E}\vec{E}\vec{E} + \chi^{(4)} \vec{E}\vec{E}\vec{E}\vec{E} + \dots + \chi^{(n+1)} \vec{E}^{n+1}]$ ,

- second order nonlinear contribution:

$$\vec{P}_{NL}^{(2)} = \varepsilon_0 \chi^{(2)} \vec{E}\vec{E} \quad (1.4)$$

The electrical field may be composed of two overlapping plane waves with monochromatic frequencies  $\omega_1$  and  $\omega_2$ :

$$\vec{E} = A_1 e^{i(\omega_1 t - \vec{K}_1 \cdot \vec{r})} \hat{e}_1 + A_2 e^{i(\omega_2 t - \vec{K}_2 \cdot \vec{r})} \hat{e}_2 + c.c \quad (1.5)$$

with  $\hat{e}$  being the unitary vector which indicates the direction of field polarization,  $\vec{K}_i$  the wave vectors,  $A_i$  the complex amplitudes, c.c the complex conjugates.

$$\vec{P}_L = \varepsilon_0 \chi^{(1)} (A_1 e^{i(\omega_1 t - \vec{K}_1 \cdot \vec{r})} \hat{e}_1 + A_2 e^{i(\omega_2 t - \vec{K}_2 \cdot \vec{r})} \hat{e}_2) + c.c \quad (1.6)$$

It radiates an electrical field which oscillates with the same frequencies as the incident fields. To calculate the second order nonlinear polarization, we simplify the case where the fields oscillate along the x axis:

$$\vec{E} = A_1 e^{i(\omega_1 t - \vec{K}_1 \cdot \vec{r})} \hat{e}_x + A_2 e^{i(\omega_2 t - \vec{K}_2 \cdot \vec{r})} \hat{e}_x + c.c \quad (1.7)$$

The component (i=x,y,z) of the nonlinear polarization of the second order is given by:

$$P_{NLi}^{(2)} = \varepsilon_0 \sum_{j,k} \chi_{ijk}^{(2)} E_j E_k \quad (1.8a)$$

we obtain , in the simple case considered :

$$P_{NLi}^{(2)} = \varepsilon_0 \chi_{ixx}^{(2)} E_x E_x \quad (1.8b)$$

with :

$$E_x^2 = 2|A_1|^2 + 2|A_2|^2 + [A_1^2 e^{2i(\omega_1 t - \vec{K}_1 \cdot \vec{r})} + A_2^2 e^{2i(\omega_2 t - \vec{K}_2 \cdot \vec{r})} + 2A_1 A_2^* e^{i((\omega_1 - \omega_2)t - (\vec{K}_1 - \vec{K}_2) \cdot \vec{r})} + 2A_1 A_2 e^{i((\omega_1 + \omega_2)t - (\vec{K}_1 + \vec{K}_2) \cdot \vec{r})} + c.c] \quad (1.9)$$

The component i of the second order nonlinear polarization is written as :

$$P_{NLi}^{(2)} = \varepsilon_0 \chi_{ixx}^{(2)} [2|A_1|^2 + 2|A_2|^2 + [A_1^2 e^{2i(\omega_1 t - \vec{K}_1 \cdot \vec{r})} + A_2^2 e^{2i(\omega_2 t - \vec{K}_2 \cdot \vec{r})} + 2A_1 A_2^* e^{i((\omega_1 - \omega_2)t - (\vec{K}_1 - \vec{K}_2) \cdot \vec{r})} + 2A_1 A_2 e^{i((\omega_1 + \omega_2)t - (\vec{K}_1 + \vec{K}_2) \cdot \vec{r})} + c.c]] \quad (1.10)$$

So we can observe photons coming out with different frequencies: we have two terms at double frequencies ( $2\omega_1$  and  $2\omega_2$ , that correspond to second harmonic generation, SHG), one term at the sum frequency  $\omega_1 + \omega_2$ , (sum frequency generation, SFG) and one term at the difference frequency  $\omega_1 - \omega_2$ , (difference frequency generation, DFG). The energy level diagrams of these 3 processes are shown in **Fig. 1.1**. One may wonder why not using SHG (single input beam) rather than SFG (two input beams at different frequencies): SFG was developed for vibrational spectroscopy because output photons are in the visible region and easily detected by a photomultiplier or CCD [9]. SHG induced by IR beams falls in a spectral region where detectors are not competitive with photomultipliers or CCD cameras.

The direction of propagation of each beam is given by the spatial part of the phase term in **Eq. 1.10**. SHG and SFG propagate in the plane of incidence of the input beams in well defined directions:  $\vec{K}_{iSHG} = 2\vec{K}_i$ , for SFG,  $\vec{K}_{iSFG} = \vec{K}_1 + \vec{K}_2$ .

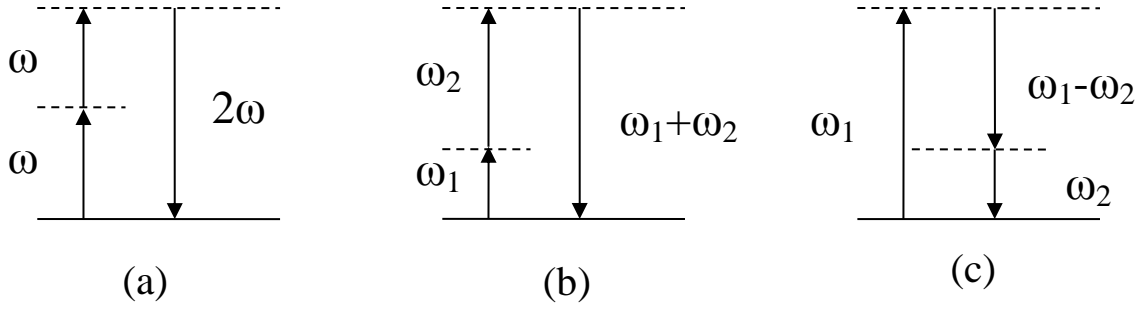


**Fig. 1.1.** Sketch presentation of the three second order nonlinear optical processes, (a) SHG, (b) SFG and (c) DFG.

As already mentioned in the introduction, the surface selectivity of 2<sup>nd</sup> order nonlinear processes is a symmetry property of second-order susceptibility tensors,  $\chi^{(2)}$ , which is null in a centro-symmetric environment. To explain this, we apply the inversion operation, which changes vectors into their opposites. **Eq. 1.4** gives:

$$-\vec{P}_{NL}^{(2)} = \varepsilon_0 \chi^{(2)} (-\vec{E})(-\vec{E}) = \vec{P}_{NL}^{(2)} \quad (1.11)$$

Which implies that  $\vec{P}_{NL}^{(2)} = 0$  and therefore  $\chi^{(2)} = 0$ . The media with inversion symmetry do not generate bulk SFG, but the inversion symmetry is broken at their interfaces and can produce significant SFG. In this case, the SFG signal can only come from the surface/interface region. In the case of non centro-symmetric media, a bulk signal is generated and can be used as a reference signal, for example with GaAs or ZnSe samples.

## 1.2.2 Theory of Sum frequency generation (SFG) on surfaces

SFG polarization have been explicated by Benderskii and co-workers [14, 15]. Here the theoretical expressions of SFG polarization are deduced again to well interpret and understand this theory. Owing to the fact that the sample response to the nonresonant interaction with the visible pulse is instantaneous, SFG can be described as a two-step process. The IR pulse induces a first-order polarization which is converted into a second-order polarization by the visible pulse (**Fig. 1.1**). The interaction of the sample with the IR pulse may involve a ‘resonant’ (R) response coming from the molecular vibrational transitions and a ‘nonresonant’ (NR) response coming from substrate electronic transitions, which interferes with the vibrational resonances.

The first-order IR polarization is the sum of resonant and nonresonant contributions:

$$P_{IR}^{(1)}(t) = \varepsilon_0 (\chi_R^{(1)} + \chi_{NR}^{(1)}) \vec{E} = P_R^{(1)} + P_{NR}^{(1)} \quad (1.12)$$

We assume that the energy levels  $E_1$  and  $E_0$  involved in the vibrational transition with a band center frequency  $\omega_{10} = (E_1 - E_0)/\hbar$  constitutes a two-level system (notably neglecting population transfer to higher vibrational levels).

The resonant polarization  $P_R^{(1)}$  is proportional to the off-diagonal elements of the density matrix [16, 17]. In the case of a single vibrational mode

$$P_R^{(1)}(t) = N \text{tr}[\hat{\rho} \hat{\mu}] = N \text{tr} \begin{bmatrix} \rho_{00} & \rho_{01} \mu_{00} & \mu_{01} \\ \rho_{10} & \rho_{11} \mu_{10} & \mu_{11} \end{bmatrix} = N(\rho_{10} \mu_{01} + \rho_{01} \mu_{10}) \quad (1.13)$$

where  $\hat{\rho}$  and  $\hat{\mu}$  are the density and dipole moment operators and  $N$  the molecular density.  $\rho_{10}(t)$  is determined by the following set of differential equations based on Schrödinger's equation:

$$\frac{\partial \rho_{10}}{\partial t} = -\left(i\omega_{10} + \frac{1}{T_2}\right) \rho_{10} + \frac{i}{\hbar} V_{10}(\rho_{11} - \rho_{00}) \quad (1.14a)$$

$$\frac{\partial \rho_{11}}{\partial t} = \frac{1}{i\hbar} (V_{10} \rho_{01} - \rho_{10} V_{01}) - \frac{1}{T_1} \rho_{11} \quad (1.14b)$$

with  $\rho_{00} + \rho_{11} = 1$  and  $\rho_{10} = \rho_{01}^*$

In the dipolar approximation the molecule-IR laser interaction is described by

$$V_{10} = V_{01}^* = \langle 1 | -\mu E_{IR}(t) | 0 \rangle = -\mu_{10} E_{IR}(t) \quad (1.14c)$$

where  $E_{IR}(t) = \mathbf{E}_{IR}(t) e^{-i\omega_{IR}t}$  is the electric field of the IR pulse.

Here  $\mu_{10} = \langle 1 | \mu | 0 \rangle$  is the transition dipole matrix element associated with the  $0 \rightarrow 1$  vibrational transition,  $T_1$  is the population relaxation time of the  $v = 1$  level.  $T_2$  is the dephasing time of the coherence between the two states  $v = 1$  and  $v = 0$ . The two processes are related by the equation:

$$\frac{2}{T_2} = \frac{1}{T_1} + \frac{2}{T_2^*} \quad (1.15)$$

where  $T_2^*$  is the pure dephasing time.

The solutions of these equations are obtained by perturbation expansion of the density matrix. To the first order the resonant polarization may be written as:

$$P_R^{(1)}(t) = -iH(t) B_R \Gamma e^{-(i\omega_{10} + \Gamma)t} \otimes E_{IR}(t) \quad (1.16)$$

where  $H(t)$  is the Heaviside step function ( $H(t) e^{-i\Gamma t}$  is the mathematical form of the response of the two level system : sudden excitation and exponential decay),  $B_R$  the amplitude of the resonant response,  $\Gamma (=1/T_2)$  the damping constant and  $\otimes$  denotes convolution.

$P_R^{(1)}(t)$  decays with the time constant  $T_2$  which is typically in the ps range for chemisorbed molecules. In contrast the electronic dephasing time of the metal is of the order of a few fs [18] so that the time evolution of  $P_{NR}^{(1)}(t)$  mirrors the femtosecond IR pulse

$$P_{NR}^{(1)}(t) = A_{NR} e^{i\varphi_{NR}} \delta(t) \otimes E_{IR}(t) \quad (1.17)$$

where  $A_{NR}$  is the amplitude of the non-resonant (NR) background and  $\varphi_{NR}$  the phase difference between R and NR signals.

Therefore the total first order infrared polarization may be written as:

$$P_{IR}^{(1)}(t) = S(t) \otimes E_{IR}(t) = \int_{-\infty}^{+\infty} S(t') E_{IR}(t-t') dt' \quad (1.18)$$

where  $S(t)$  is the linear response function given by the following expression [16, 19]:

$$S(t) = S_{NR}(t) + S_R(t) = A_{NR} e^{i\varphi_{NR}} \delta(t) - iH(t) B_R \Gamma e^{-(i\omega_0 + \Gamma)t} \quad (1.19)$$

The interaction with the visible pulse creates a second order polarization  $P_{SFG}^{(2)}(t)$  given by:

$$P_{SFG}^{(2)}(t, \tau) = [P_{NR}^{(2)}(t, \tau) + P_R^{(2)}(t, \tau)] \propto [(M_{NR} S_{NR}(t) + M_R S_R(t)) \otimes E_{IR}(t)] E_{vis}^{str}(t, \tau) \quad (1.20)$$

where  $E_{vis}^{str}(t, \tau) = E_{vis}^{str}(t, \tau) e^{-i\omega(t-\tau)}$  is the electric field of the delayed visible pulse generated by a stretcher, and  $M_{NR}$  and  $M_R$  are the second-order matrix elements of the electric dipole moment involved in the SFG process [17, 20]. The reference to a ‘‘stretched’’ visible beam comes from the fact that experimentally we start with femtosecond visible and IR pulses. Since the spectral resolution in BB SFG is equal to the visible beam bandwidth as will be explained below, the latter must be reduced to a few  $\text{cm}^{-1}$ , or equivalently the visible beam must be stretched to a few ps to achieve spectral resolution.

From **Eq. 1.16** and **1.20** we get the following expression for the second order resonant polarization

$$P_R^{(2)}(t, \tau) \propto B_R M_R \Gamma \int_{-\infty}^{+\infty} H(t') e^{-(i\omega_0 + \Gamma)t'} E_{IR}(t-t') e^{-i\omega(t-t')} dt' E_{vis}^{str}(t, \tau) e^{-i\omega(t-\tau)} \quad (1.21)$$

Under the assumption that the IR pulse duration is very short compared to the dephasing time  $T_2$  the time envelope of the IR pulse may be approximated as:

$$E_{IR}(t-t') = E_{IR}^0 \delta(t-t') \quad (1.22)$$

Such an approximation is not strictly valid in practice. However the finite IR pulse duration results only in a slower rise of  $P_{IR}^{(1)}(t)$  which translates into a slight distortion in the red wing of the band profile [21].

**Eq. 1.21** then becomes:

$$P_R^{(2)}(t, \tau) \propto B_R M_R \Gamma H(t) E_{IR}^0 e^{-i(\omega_{10} + \omega'')t} e^{-\Gamma t} e^{i\omega''\tau} E_{vis}^{str}(t, \tau) \quad (1.23)$$

As already pointed out by Ishibashi and Onishi [20] the time envelope of  $P_R^{(2)}(t, \tau)$  and its spectra depend on the time delay between IR and visible pulses.

In the case of several vibrational modes and in the presence of a nonresonant response the total SFG polarization can be written as:

$$P_{SFG}^{(2)}(t, \tau) = \left[ \left( \chi_{NR} e^{i\varphi_{NR}} \delta(t) - iH(t) \sum_i B_i e^{-[i(\omega_{10})_i + \Gamma_i]t} \right) \otimes E_{IR}(t) \right] E_{vis}^{str}(t, \tau) \quad (1.24)$$

where  $\chi_{NR} = A_{NR} M_{NR}$  and  $B_i = B_{Ri} M_{Ri} \Gamma_i$

In the frequency domain the spectral component of the resonant contribution to the second order polarization at the sum frequency  $\omega = \omega' + \omega''$  is given by the Fourier transform of **Eq. 1.24**:

$$\tilde{P}_{SFG}^{(2)}(\omega = \omega' + \omega'', \tau) \propto \left[ \left( \chi_{NR} e^{i\varphi_{NR}} + \sum_i A_i e^{i\varphi_i} \right) \tilde{E}_{IR}(\omega) \right] \otimes \tilde{E}_{vis}^{str}(\omega, \tau) \quad (1.25)$$

where  $\omega'$  and  $\omega''$  are still the IR and visible frequencies,  $A_i$  and  $\varphi_i$  are the amplitude and phase of the  $i^{\text{th}}$  resonant vibrational mode, respectively given by:

$$A_i(\omega') = \frac{B_i}{[(\omega' - (\omega_{10})_i)^2 + \Gamma_i^2]^{1/2}} \quad (1.26)$$

and

$$\varphi_i(\omega') = \varphi_{Ri} + \tan^{-1} \left( \frac{\Gamma_i}{(\omega_{10})_i - \omega'} \right) \quad (1.27)$$

where  $\varphi_{Ri}$  is an additional phase which may be different for each vibrational band. The  $\tan^{-1}$  term is responsible for a phase shift of  $\pi$  across the vibrational band.

If we neglect the physics which is beyond the convolution between the IR polarization and the visible pulse (assuming in fact that the visible beam is infinitely long), and in the case where the phase difference between resonant and nonresonant contributions is independent of the vibrational mode ( $\varphi_{Ri} = 0$  and  $\varphi_{NR} - \varphi_{Ri} = \varphi$ ), then the SFG intensity takes the familiar form:

$$I_{SFG}(\omega) \propto \left| \tilde{P}_{SFG}^{(2)}(\omega, \tau) \right|^2 \propto IR(\omega') \cdot \left| \chi_{NR} \cdot e^{i\varphi} + \sum_i \frac{B_i}{\omega' - (\omega_{10})_i + i\Gamma_i} \right| \quad (1.28)$$

where  $IR(\omega')$  is the spectral profile of the IR laser and  $B_i$ ,  $(\omega_{10})_i$  and  $\Gamma_i$  are respectively the Lorentzian amplitude, frequency and half-width of the  $i^{\text{th}}$  vibrational mode,  $\chi_{NR}$  being the nonresonant second-order susceptibility tensor of the surface. In the literature most experimental spectra are fitted with **Eq. 1.28** to obtain the values of the fitting parameters and

their uncertainty. Besides the fact that it neglects the spectro-temporal properties of the visible beam, a limitation of this fitting method is the possible multiple set of fitting parameters that can be obtained for the same spectrum due to the high number of parameters [22]. This will be discussed in details in **Chapter 6**.

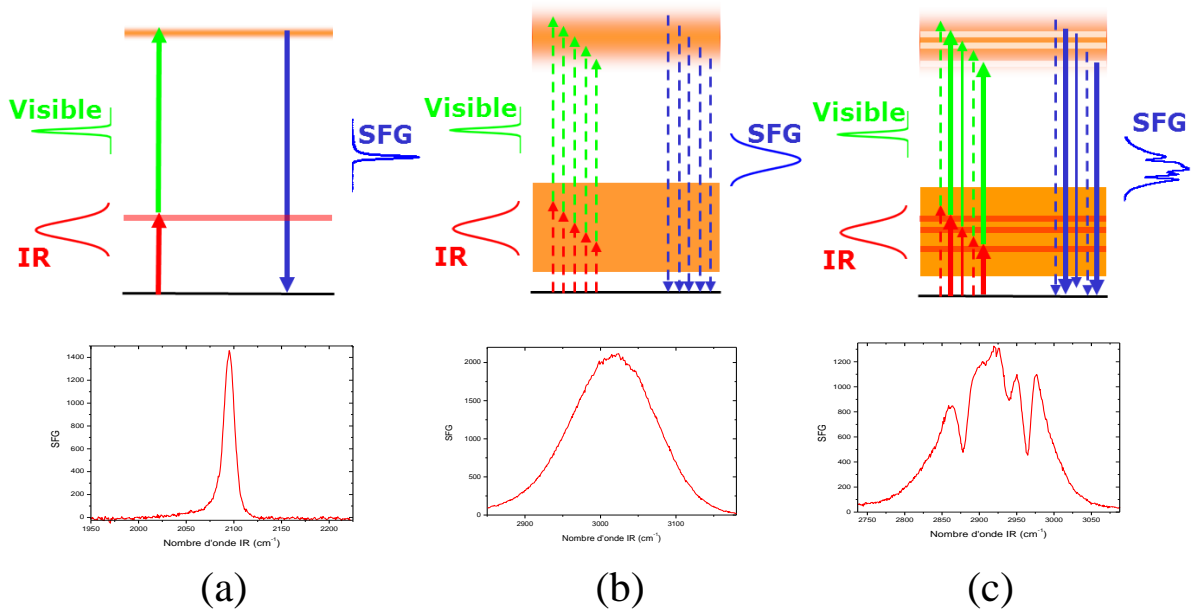


**Fig. 1.2.** Different types of SFG *fs(IR)*-*ps(vis)* spectra: resonant and nonresonant SFG processes. (a) resonant SFG only; (b) nonresonant SFG only; (c) interfering resonant and nonresonant SFG [23]. Examples of spectra come from our laboratory : (a) CO / Pt(111), (b) GaAs, (c) self assembled monolayer of octa-decanethiol / Au(111)

The resolution of SFG spectra is given by the width of the emitted band, which is equal to the width of the upper virtual state (**Fig. 1.2a**), which in turn is the convolution of the visible laser bandwidth with the natural width of the excited vibrational state : the width of the IR laser is not important. The spectral range of SFG depends on the IR laser bandwidth while the spectral resolution depends on the visible pulse bandwidth. BB SFG avoids to scan the IR laser frequency. The visible laser bandwidth must be smaller than the bandwidth of the vibrational bands. In **Fig. 1.2b**, only a “nonresonant” transition is present. It results from a broad electronic transition of the substrate which is almost spectrally flat at the scale of the IR laser bandwidth. The SFG spectrum directly reflects that of the IR laser. This allows us to obtain the spectral shape of the IR laser beam. In our experiment this spectral form can be generated either by a GaAs sample (in reflection, strong signal), or by a ZnSe sample (by transmission, even stronger

signal). The spectrally large infrared pulse excites any vibrational level in resonance: in **Fig. 1.2c**, the SFG spectrum includes several resonant responses and a NR background.

### 1.2.3 Several applications of femtoseconde SFG model

For the need of our experiments, we have done four different kinds of SFG experiment:

(1). IR (~120 fs) + visible (~4 ps) at fixed delay : measurement of the BBSFG spectra.

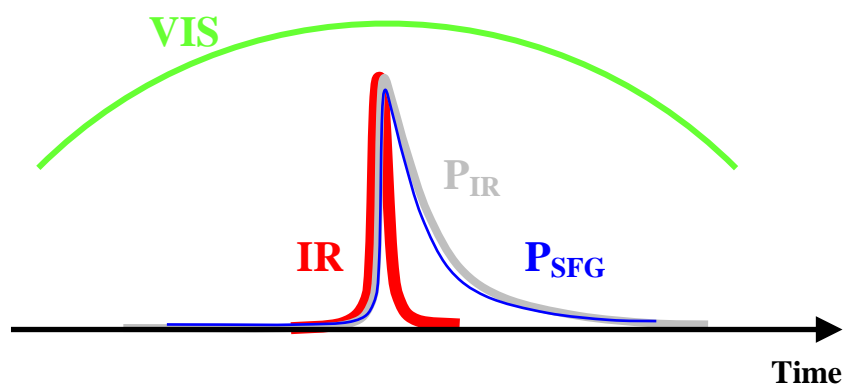


**Fig. 1.3.** fs IR - ps vis with one vibrational band for spectroscopy. The IR induces a polarization  $P$  which declines with the relaxation time  $T_2$ . The visible pulse is temporally large (shaped by a pulse shaper) and superimposed to the polarization to generate the SFG spectrum.

This SFG process shown in **Fig. 1.3** is a SFG measurement with spectral resolution. It involves a fs (IR) pulse with a broad spectral range and a ps (visible) pulse (a few  $\text{cm}^{-1}$ ) allowing for a good resolution. The picosecond visible pulse is obtained by passing a femtosecond pulse through a 4f pulse shaper (discussed in the experimental setup). In this case any temporal information is absent.

Introduction of temporal resolution is interesting and important because it gives us the chance to study the molecular dynamics and the reaction mechanisms, for example the vibrational polarization which will be discussed in **Chapter 3**, and the dynamics of chemical and physical processes at the time scale of  $10^{-13}$  s (**Chapter 5**).

(2). IR ( $\sim 120$  fs) + visible ( $\sim 120$  fs) with varied delay : measurement of  $T_2$  relaxation time (temporal resolution  $\sim 100$  fs).

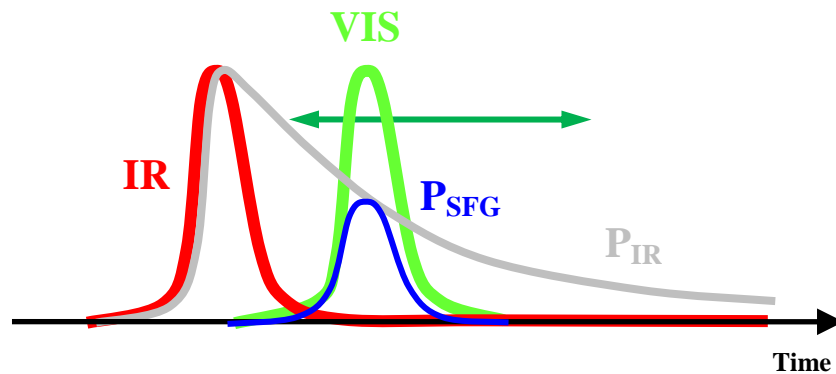


*Fig. 1.4. fs (IR) - fs (vis) temporal sketch of SFG with one vibrational band to measure  $T_2$ . The IR induces a polarization  $P$  which declines with a relaxation time  $T_2$ , the IR-vis delay is scanned as polarization decays.*

In the SFG fs IR - fs vis process shown in **Fig. 1.4**, the spectral resolution is lost but this method allows to measure the  $T_2$  of the vibrational state at femtosecond scale. The IR polarization is scanned by the short visible pulse (100 fs) to obtain the SFG polarization with a good temporal resolution.

(3) IR ( $\sim 120$  fs) + visible ( $\sim 4$  ps) at fixed delay + pump (at varied pump delay): pump-probe experiment.

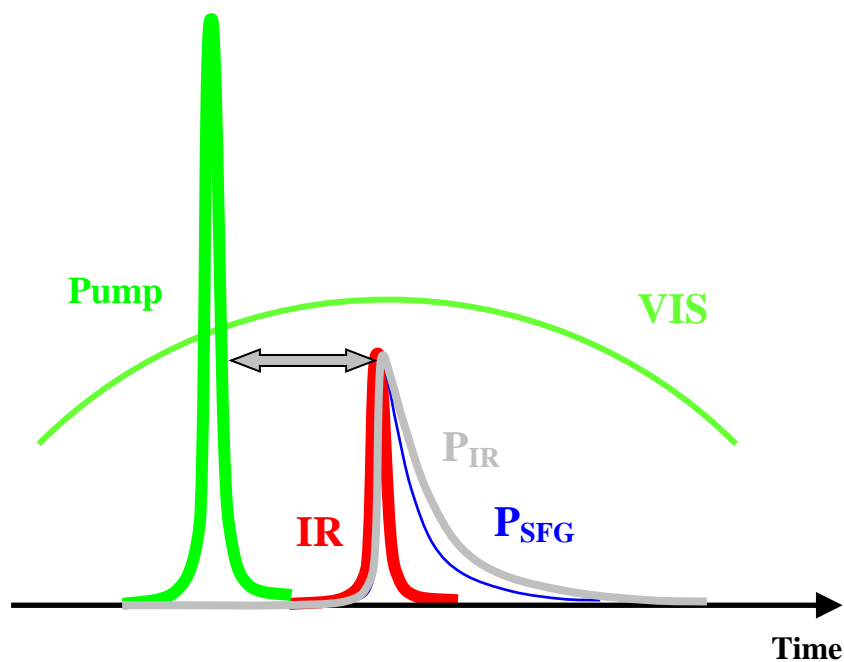


*Fig. 1.5. fs pump - fs IR - ps vis probe to measure the surface dynamics induced by the pump pulse. The IR ps - vis ps SFG spectrum is recorded as a function of the delay between the fs pump and the fs IR probe.*

The pump produces an intense electron excitation in the substrate. Multiple excited electrons excite the molecules and can induce reactions (including desorption). The molecular vibrations of the molecules that remain intact are spectators of the electronic excitation and of the evolution of the substrate. The probe therefore allows us to measure the surface and molecular dynamics induced by the pump. The temporal resolution is limited by the pulse duration.

(4) IR (~120 fs) + delayed visible shaped by a Fabry-Perot (FP) etalon (~500 fs) for spectroscopic measurements as a function of the IR - visible delay.

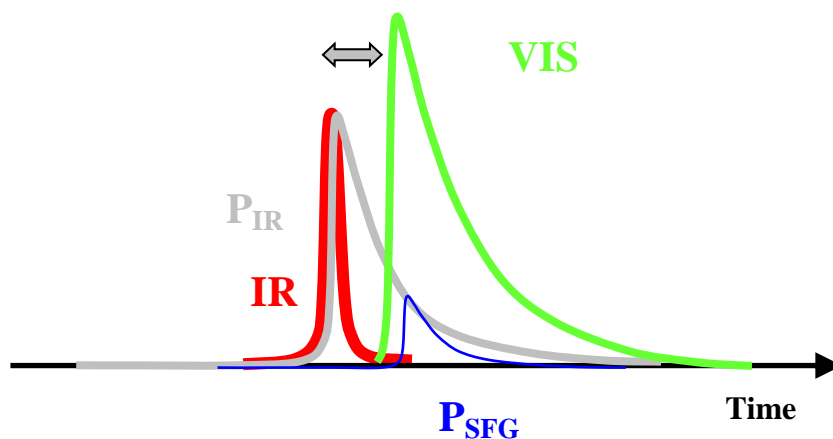


*Fig. 1.6. SFG spectroscopy with one vibrational band when the visible pulse is shaped by transmission through a Fabry-Perot etalon: fs IR - ps asymmetric vis. The IR induces a polarization  $P$  which declines with the relaxation time  $T_2$ , the visible pulse delay is scanned. In the case where a temporally short, non resonant (NR) component is present, this allows to remove the NR contribution from the spectrum.*

The visible pulse shaped by a FP is an asymmetric pulse, which has a temporal rising time of 100 fs at the wavefront and a duration of about 500 fs, allowing us to obtain a good time resolution by scanning the IR-visible delay while keeping high spectral resolution: the first application is to remove the fast response from NR contributions. But it generates a problem as shown in **Chapter 6**: the spectra are delay dependant. However, by measuring a series of SFG spectra with different delays between the IR and visible pulses, the parameters of the vibrational modes can be obtained more precisely.

## 1.3 Experimental setup of SFG

BBSFG spectroscopy has been used by different groups [10, 11]. Our femtosecond laser system setup and the Optical Parametric Amplifier (OPA) will be presented here.

### 1.3.1 Femtosecond laser system

The whole laser system (femtosecond laser system and three Optical Parametric Amplifiers (OPAs) is presented on **Fig. 1.7**.

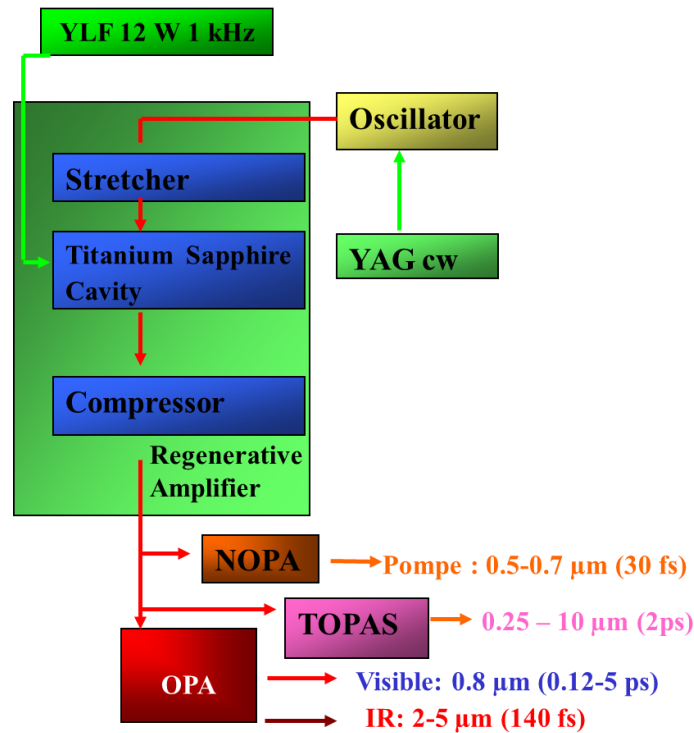


*Fig. 1.7. Femtosecond laser system. It is composed of a Ti:sapphire crystal oscillator followed by a regenerative amplifier which can pump three different OPA in the visible and IR with pulse durations from several tens of fs to several ps.*

The femtosecond laser system is based on a Ti:sapphire oscillator (Coherent MIRA). The sapphire crystal doped with titanium ions has two bands of absorption centred at 488 and 560 nm, and a large emission spectrum centred around 790 nm. The Ti:Sa oscillator, pumped by a continuous Nd:YVO<sub>4</sub> laser (Coherent VERDI), delivers tunable impulsions between 760 and 820 nm (15 nm spectral width) with 80 fs duration and 11 nJ pulse energy at a 76 MHz repetition rate leading to an average power of 600 mW.

These impulsions are amplified by a regenerative amplifier (RGA, Thales Laser ALPHA 1000) consisting of three steps: a stretcher, an amplifier cavity containing a Ti:sapphire crystal pumped by a Nd: YLF (Thales Laser) laser and a compressor. The stretcher increases the duration of the femtosecond pulses coming from the MIRA to obtain pulses with a duration a thousand times longer than the initial ones. The aim of this stretcher is to decrease the peak power of the laser that would otherwise damage the Ti:sapphire crystal in the regenerative cavity. Stretching is obtained by multiple passes on a grating, where dispersion is cumulated and angular separation is cancelled. The stretched pulses are amplified in the optical cavity without damage to the crystal. The compressor allows to recover the initial pulse duration by using a grating identical to w of the stretcher, in a different geometric configuration. We finally

obtain output pulses with 120 fs duration at 800 nm at a repetition rate of 1 KHz, with a mean power of 800 mW and a horizontally polarized beam. The laser parameters of our Ti:sapphire laser and regenerative amplifier are presented in **Table 1.1**.

The pulses coming from the regenerative amplifier can pump one of the three different optical parametric amplifiers: an OPA (3-9  $\mu\text{m}$ , 135 fs), a NOPA (500 -700  $\mu\text{m}$ , 30 fs) and a TOPAS (0.25-10 $\mu\text{m}$ , 2 ps). The results of this thesis are obtained with the OPA.

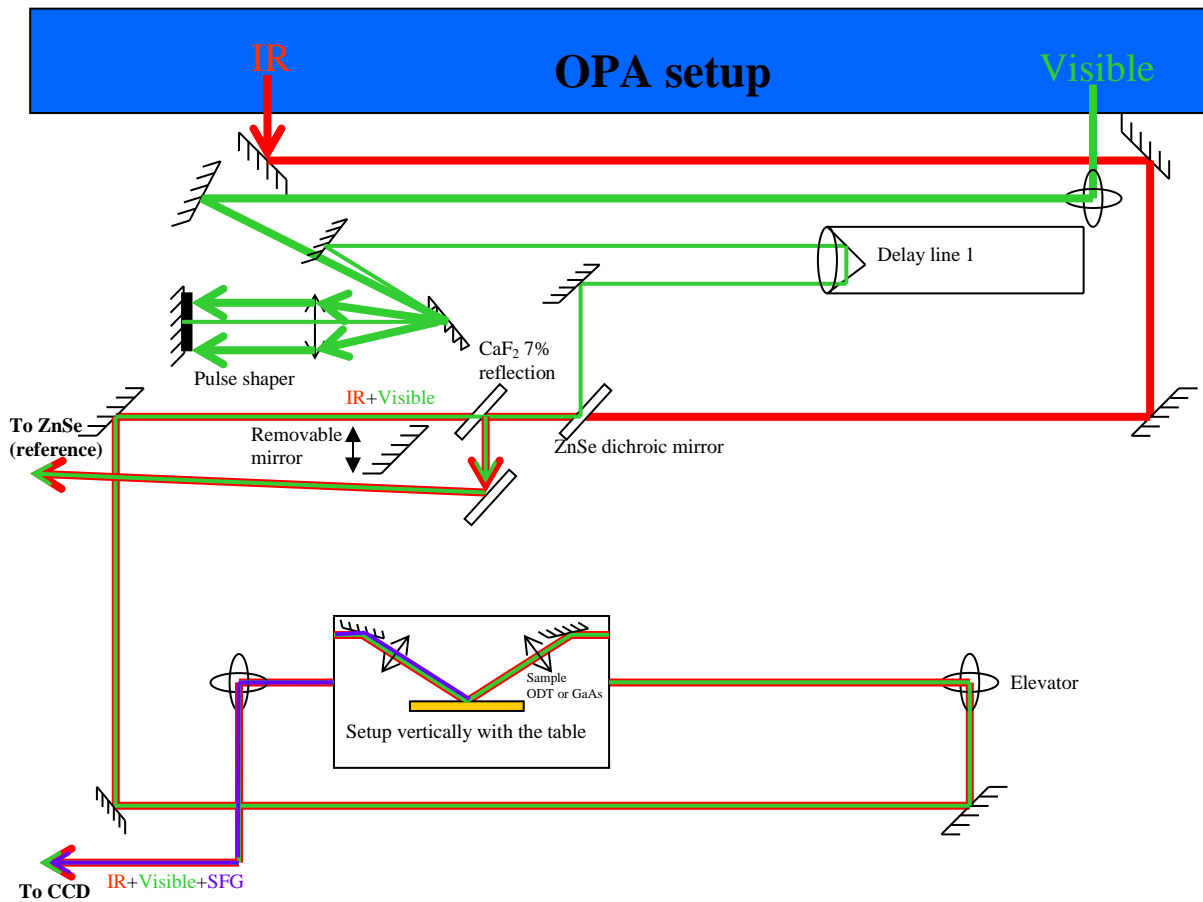
***Table 1.1.** Comparison of the laser pulse parameters exiting the Ti: Sapphire oscillator and the regenerative amplifier.*

	Ti: Sapphire oscillator	Regenerative amplifier
Average power in continuous	600 mW	800 mW
Repetition rate	76 MHz	1 kHz
Energy per pulse	11 nJ	0.8 mJ
Center wavelength	760-820 nm	806 nm
Spectral width	15 nm	10.5 nm
Duration	80 fs	120 fs

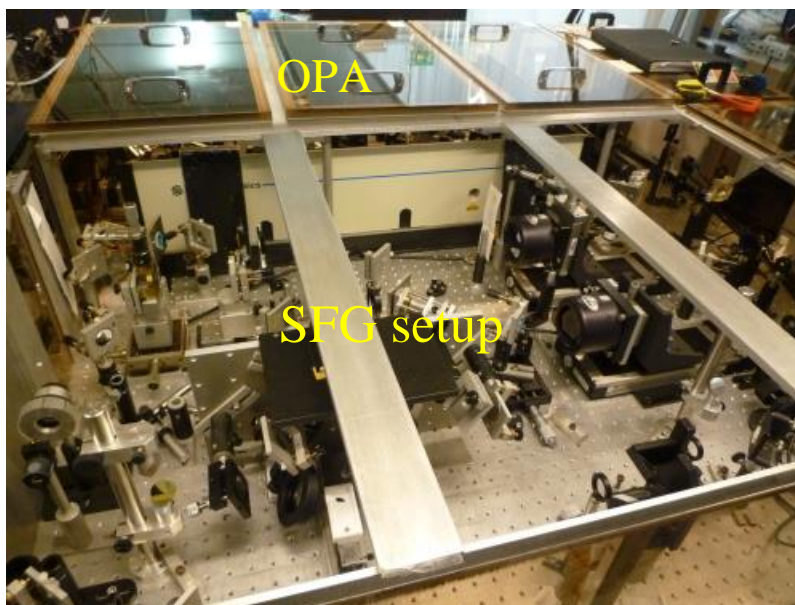
The Optic Parameter Amplifier (OPA) is pumped by the laser beam at 800 nm and generates two beams : the ‘signal’ one, horizontally polarized with a tuneable wavelength between 1.1 and 1.6  $\mu\text{m}$ , and the complementary one, the ‘idler’, vertically polarized with a wavelength between 1.6 and 2.9  $\mu\text{m}$ . Their frequencies follow the relation of conservation of energy and the phase matching condition between the pump beam, the signal beam and the idler beam in type 2, BBO crystal, according to the equation  $\omega_{\text{pump}} = \omega_{\text{signal}} + \omega_{\text{idler}}$ . A tunable IR beam between 3 and 10  $\mu\text{m}$ , horizontally polarized, is generated by the frequency difference process between signal and idler beams in an AgGaS<sub>2</sub> crystal according to  $\omega_{\text{IR}} = \omega_{\text{signal}} - \omega_{\text{idler}}$ . The remaining femtosecond beams at 800 nm, vertically polarized, are used as follow: one is used as the femtosecond pump for the pump-probe experiments; the other one is used as the ‘visible’, which, combined with IR, generates our SFG signal. The **Fig. 1.8** summarizes all of this through a sketch draw and the picture of our OPA.



### 1.3.2 Experimental setup of SFG spectroscopy



(a)



(b)

**Fig. 1.9.** (a) Sketches and (b) picture of the SFG setup, with a sample holder in air supporting a GaAs (reference) or an ODT sample on gold film.

The **Fig. 1.9** represents the optical SFG setup after the OPA. The IR and visible laser beams must be superimposed spatially and temporally. Spatial overlap is obtained in collinear propagation after recombination of the visible and IR beams through a ZnSe dichroic mirror which is transparent for infrared and fully reflective at 800 nm for 45° incidence. This configuration of co-propagation beams simplifies the optical adjustments because the SFG beam is then also collinear to the visible beam: this allow to make the whole alignment up to the detection using the visible light (IR is not visible because of its wavelength, SFG is not visible because of its very small intensity). Temporal overlap is obtained by means of a delay line of resolution 0.1  $\mu\text{m}$  (0.66 fs). Before the delay line and the recombination, the visible beam into a pulse shaper in order to be reshaped spectro-temporally. The sketch of the pulse shaper is shown on **Fig. 1.10**.

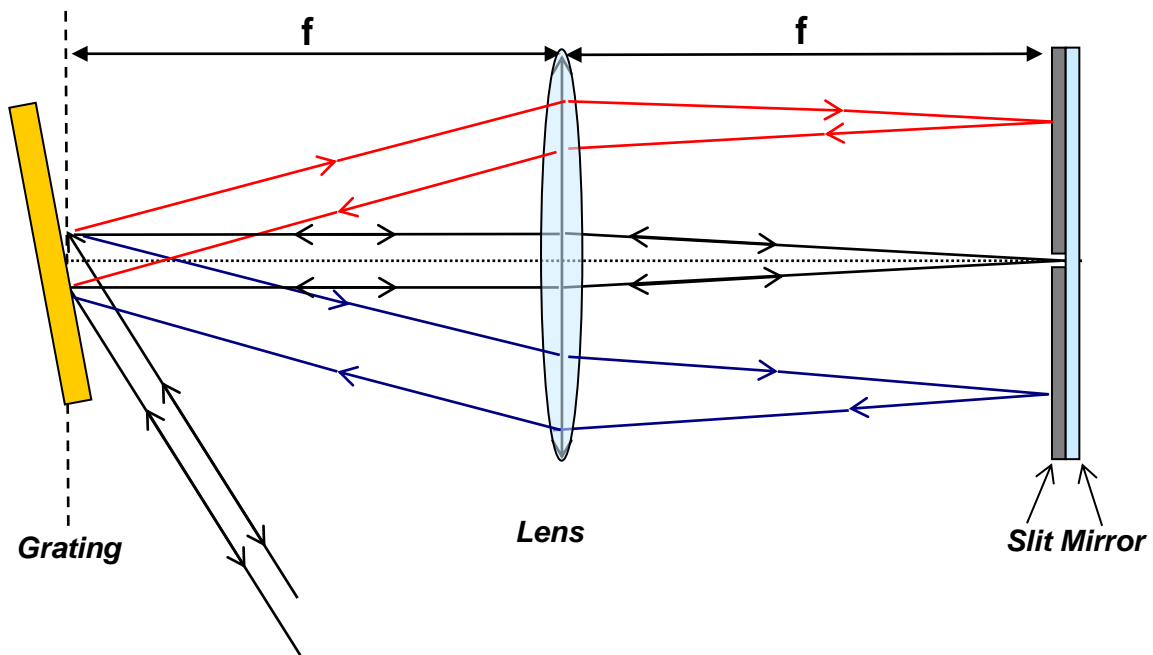


*Fig. 1.10. Sketch of the folded 4f pulse shaper used in our experiments.*

The input laser beam is reflected by a grating located at the focus point of the central lens. The grating disperses the frequencies which then go through the central lens. It follows that the spectrum is dispersed and focused in the focal plane where an adjustable slit located in the Fourier-plane selects in the input laser beam spectrum a small portion of adjustable width  $\Delta\omega_{\text{vis}} < 10 \text{ cm}^{-1}$  which is therefore nearly rectangular. This small portion of the input laser beam is reflected by a mirror located against the slit and passes again the lens and grating. A small angle on the mirror in the vertical plane allows to extract the shaped beam. In this pulse shaper,

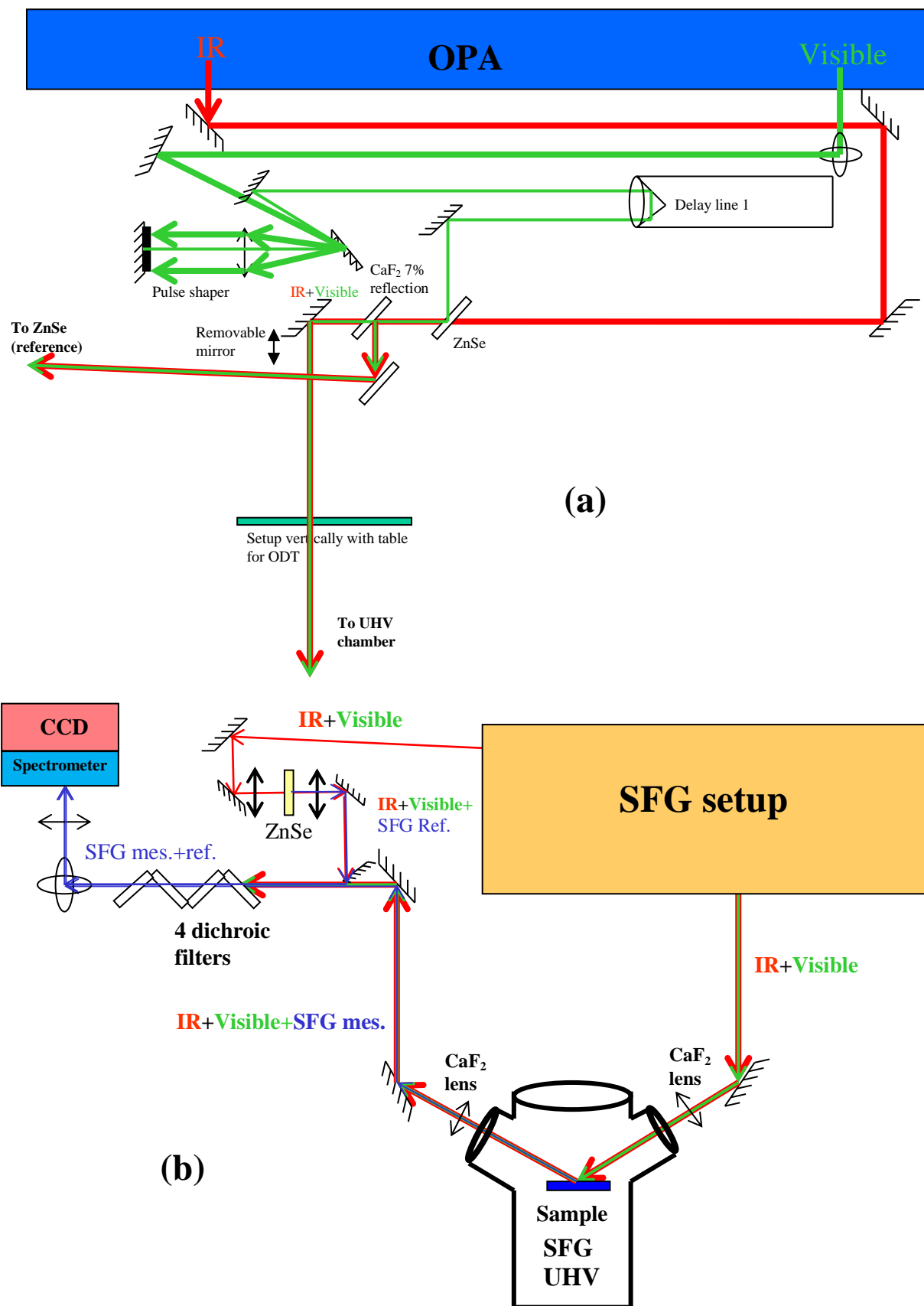


*Fig. 1.11. Sketches of (a) the SFG setup and (b) the optical setup for SFG on the sample in the UHV chamber and on the ZnSe reference.*

the optical path of the laser beam is  $4f$  ( $f$  being the lens focal length), independent of wavelength (the shaper introduces no chirp if it is perfectly aligned), so this kind of pulse shaper is called “ $4f$  pulse shaper” (**Fig. 1.10**). More complex spectral and/or temporal shapes can be obtained by replacing the slit by an array of liquid crystals: each spectral component can then be adjusted in phase and intensity.

With our pulse shaper we reduce the spectral width of the visible pulse to a few  $\text{cm}^{-1}$  to obtain the required spectral resolution for vibrational spectroscopy of chemisorbed molecules. In counterpart, the pulse duration now extends to about 1 to 4 ps. The two beams are “p” polarized on the sample (electric field in the incident plane): this is by far the best polarization on metals, where s-polarized radiation is nearly cancelled at the surface upon reflection. The superimposed IR and visible beams then pass through a  $\text{CaF}_2$  plate (7% reflected for the reference) and then arrive at the sample in air for the SFG measurement (ODT samples or GaAs reference) or alternatively they are reflected by a removable mirror to samples located in the Ultra-High Vacuum (UHV) chamber through a  $\text{CaF}_2$  lens and window. The sketches for the UHV SFG experiments is shown in **Fig. 1.11**.

The SFG experiments carried out in the UHV chamber involve the CO adsorption on the Pd(100) single crystals, or the Pd nanoparticles grown on an ultra-thin MgO layer epitaxially grown on Ag(100), the CO catalytic oxidation reactions and pump-probe experiments, as discussed in chapters 3-5. As shown in **Fig. 1.11**, the collinear incident IR and visible beams are focussed on the sample by a  $\text{CaF}_2$  lens. After the reflection on the sample and the generation of SFG, the SFG signal is easy to follow because it is still collinear with the IR and visible beam. However, collinear propagation has the drawback that spatial discrimination of the SFG beam against the much more intense visible beams is not possible. We reject the visible light with a series of four dichroic mirrors. Each reflects the visible light with an efficiency of  $10^4$ , which is sufficient to eliminate the visible light. The SFG beam finally enters a spectrometer equipped with a very low noise, very high photon yield CCD, as shown in **Fig. 1.11**.

It is important to normalize the detected SFG signal intensity by a reference in order to compensate the measured spectra for laser intensity fluctuations. A small part of IR+visible beams are reflected (about 7%) on a  $\text{CaF}_2$  plate and sent through a ZnSe plate to generate a reference SFG. The reference setup system in **Fig. 1.11**. ZnSe is a non-centrosymmetric crystal which generates “bulk SFG” very efficiently, allowing to get a good SFG reference intensity by using only 7% of input energy. However, the alignment and intensity of the beams through

ZnSe must be made very carefully. It is very easy to obtain distorted spectra (that is, which do not reflect accurately the IR beam spectrum).

The two SFG signals, measurement and reference, are injected simultaneously but separately into the entrance slit of the spectrometer on two different regions of interest (ROI) of the CCD as shown in **Fig. 1.12**. Therefore the measured and the reference SFG signals are acquired simultaneously.



*Fig. 1.12. Display of the two SFG signals on the detector: sample and reference at two ROI of the CCD.*

In **Fig. 1.12**, the horizontal axis displays the wavelength of the SFG spectra and the vertical axis corresponds to the SFG signal positions on the CCD camera. The upper and apparently thinner signal is the spectrum from the sample, the lower and larger signal is from the ZnSe reference. The dark vertical lines on the spectra originate from atmospheric water absorption lines, the IR frequency being centered at  $2000\text{ cm}^{-1}$ .

## 1.4 Data treatment

The data are processed using a Labview program designed by a member of our group (Aimeric OUVRARD). It imports a series of sample and reference data, eliminates the background from reference spectra taken without the IR laser beam, eliminates if necessary the absorption lines of water, smooth the spectra, compiles the data and exports them in several windows interfaces (**Fig. 1.13**).

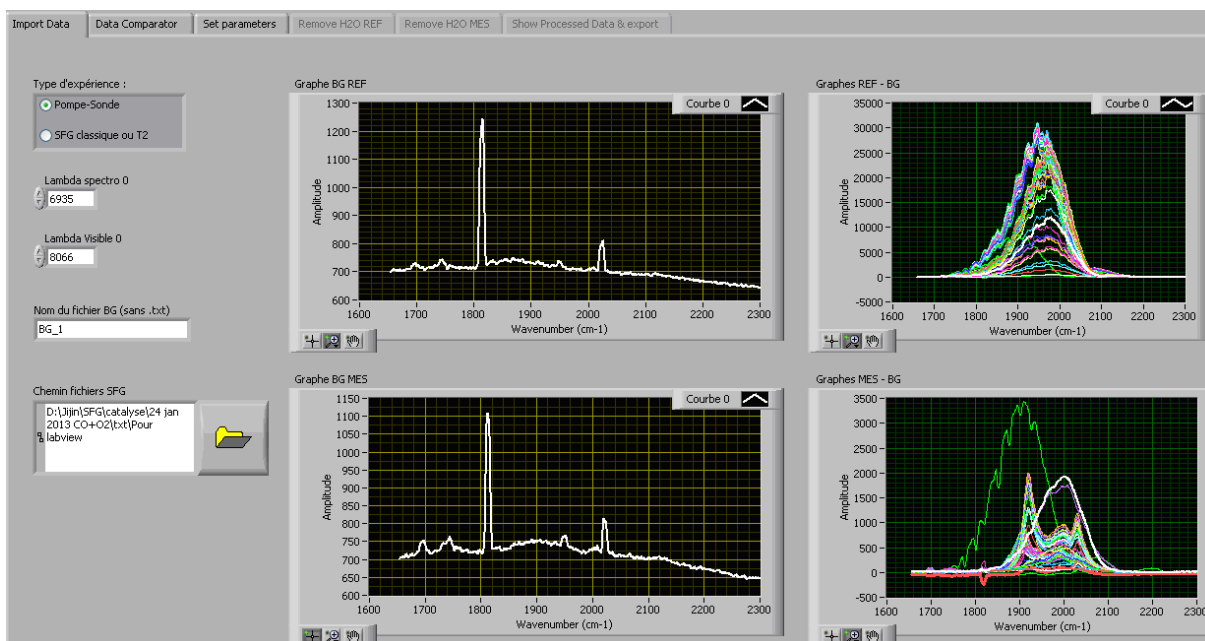


Fig. 1.13. The Labview interface windows for the processing of data of SFG experiments.

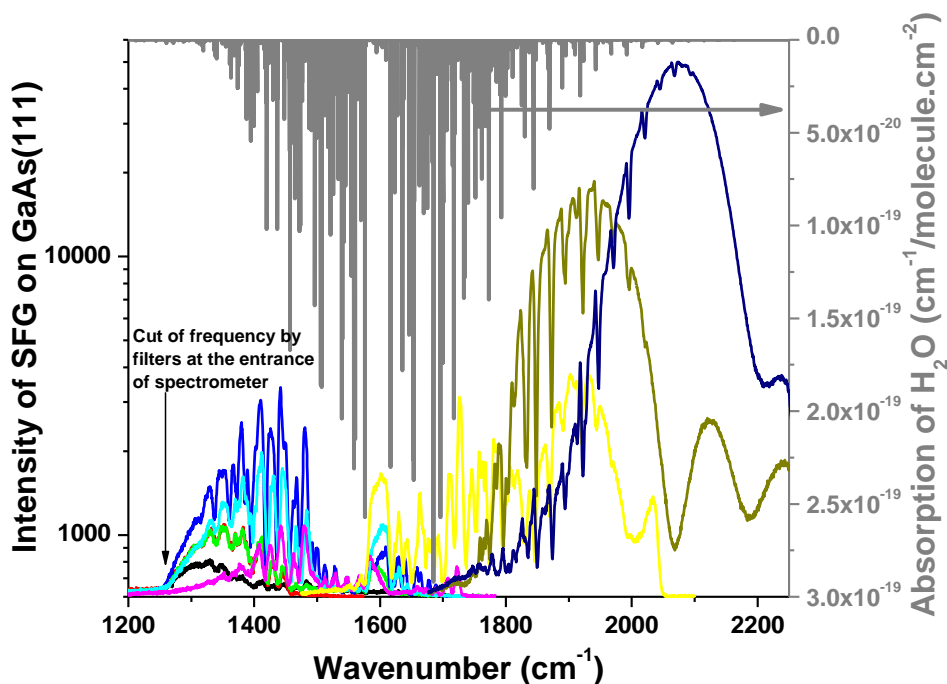
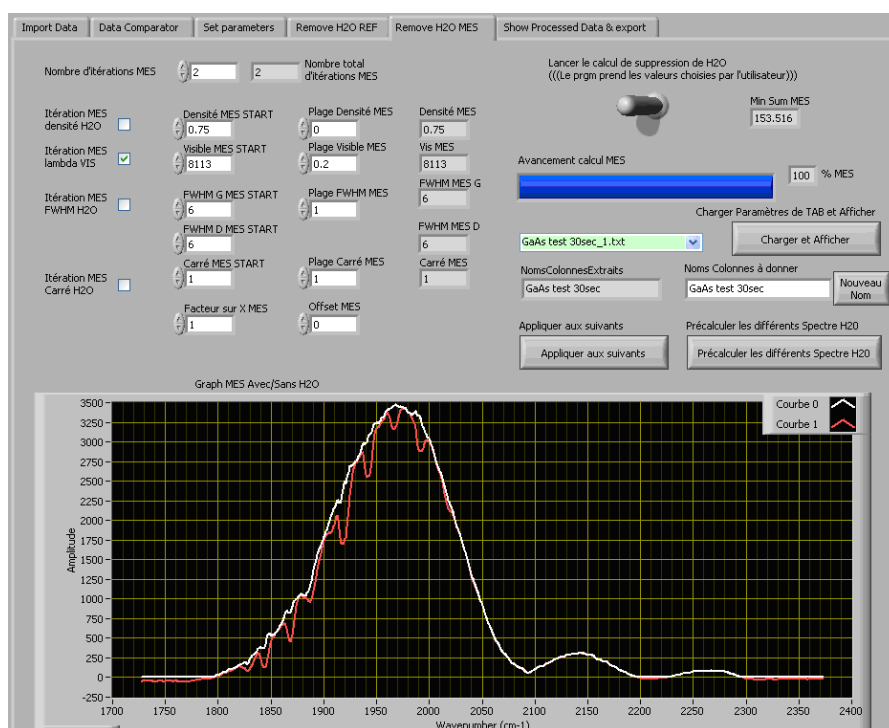


Fig. 1.14. SFG spectra on GaAs(111) for various wavelengths of the IR laser from 1200 to 2230  $\text{cm}^{-1}$ , showing the problem raised by atmospheric water. The spectrum of water absorption (bending mode) is displayed (gray line) on the top.

The Fig. 1.14 represents a series of SFG spectra from a GaAs(111) sample from 1250  $\text{cm}^{-1}$  to 2000  $\text{cm}^{-1}$ . The non-resonant SFG of GaAs reproduces in principle the Gaussian profile of

the IR spectrum. In the case of the figure, the profile is obviously not Gaussian (see e.g. the green-brown spectrum) revealing an inadequate angle of the OPA BBO crystal. More important, a strong absorption by water vapour is present and perturbs strongly the SFG spectra. It must be removed by purging the SFG setup with dry air. Removing the absorption dips in the data treatment is possible in the spectral regions where it is weak enough, that is only in the wings of the H<sub>2</sub>O band (**Fig. 1.15**). The absorption dips have the advantage to allow accurate frequency calibration.



**Fig. 1.15.** Elimination of absorption dips of water in the SFG spectra in the frequency range 1800 to 2000  $\text{cm}^{-1}$  by the program. The red curve is the original SFG spectrum with the atmospheric absorption dips of water in IR, the white curve is the spectrum after the elimination procedure.

After the above data treatment, the spectra are normalized by the reference in order to compensate for laser fluctuations during the acquisition of the spectra. There are two ways of normalization. The simplest one is by the area of the reference spectrum to compensate for intensity fluctuations (**Fig. 1.16a**). A more complex one is by the spectrum of the reference (**Fig. 1.16b**), in order to compensate for spectral fluctuations of the laser. This turns out to be complicated, because in practice the spectra measured on a sample that provides only a NR spectrum, and on the reference, never overlap exactly. In the particular case of a series of

spectra on the sample where the first spectrum has only a NR contribution, one can determine the ratio  $IR^0 / ref^0$  of the two spectra, and normalize spectrum #i by  $IR^i$  equal to:

$$IR^i = ref^i \frac{IR^0}{ref^0} \quad (1.29)$$

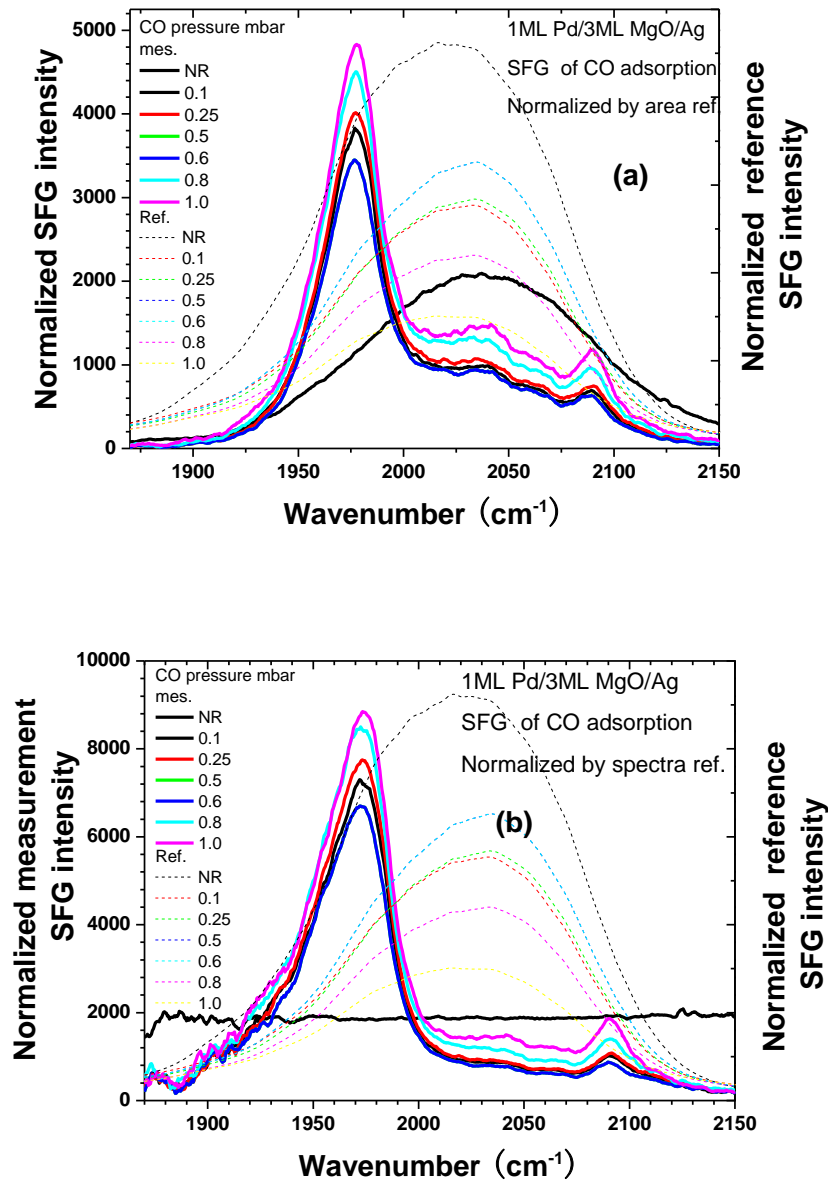


**Fig. 1.16.** SFG spectra of CO adsorbed on Pd nanoparticles supported on a MgO film and Ag(100) crystal. (a) The spectra are normalized by the overall intensity (area) of the ZnSe reference, (b) the spectra are normalized by the spectra of reference.

This works sometimes. The spectra of **Fig. 1.16b** are divided by the laser spectrum as derived from the reference spectra. The black line of the first (purely NR) spectrum is flat. Note

that **Eqs. 1.25** and **1.28** show that the mere division of spectra by the IR spectrum is not strictly correct. After normalization, the spectra are compiled into a file for exporting. All the processing program is completed step by step in within  $\approx 1$  hour, with efficiency and reliability.

## 1.5 Conclusion

In this chapter, the basis of linear and nonlinear optics are recalled briefly: the linear optics comes from the first order polarization of the media by the light, and the nonlinear optics comes from the second and higher orders of the polarization. The second order nonlinear effects include the SFG, SHG and DFG processes. In this work we concentrate on SFG. SFG has interesting properties (sensitivity, ultrafast response) and its surface selectivity allows to get the signal arising only from surface or interface regions on centrosymmetric media. Our SFG spectra are generated by an IR pulse and a visible pulse overlapping on the sample, that generate so called “Non-Resonant” response from electronic states of the substrate, and a “resonant” response from molecular vibrations resonant with the IR.

The femtosecond laser system and our SFG setup are presented. The IR beam, generated in the wavelength range of 2-9  $\mu\text{m}$  by an OPA, and a spectrally shaped visible beam (around 800 nm) produce the SFG signals on various surfaces: on the sample of ODT or GaAs in air, or on complex samples elaborated in UHV. The SFG reference produced in a ZnSe plate allows us to normalize the sample signal. The processing of data of spectra such as import, removing of water, normalization and export can be effectively done by a Labview program.

## References:

- [1] Y.R. Shen. *The Principles of Nonlinear Optics*, Chap. 2 and 25, J. Wiley, New York (1984).
- [2] R.W. Field, *Nonlinear Spectroscopy for Molecular Structure Determination*, Chapter 10, (1998)
- [3] E.W.M. van der Ham, Q.H.F. Vreken, E.R. Eliel, *Opt. Lett.* 21, 1448. (1996)
- [4] L.J. Richter, T.P. Petralli-Mallow, J.C. Stephenson, *Opt. Lett.* 23, 1594. (1998)
- [5] H. Arnolds, M. Bonn, *Surf. Sci. Rep.* 65, 45 (2010)
- [6] T. Stehlin, M. Feller. P. Guyot-Sionnest and Y. R. Shen. *Optics Lett.* 13. 389 (1988)
- [7] K. B. Eisenthal, *Chem. Rev.* 96, 1343, (1996)
- [8] D. Verreault, V. Kurz, C. Howell, P. Koelsch *Rev Sci Instrum.* 81, 063111.(2010)
- [9] P. Guyot-Sionnest, W. Chen and Y.R. Shen. *Phys. Rev. B* 33, 8254 (1986); P. Guyot-Sionnest and Y. R. Shen. *Phys. Rev. B* 35, 4420 (1987); *Phys. Rev. B*, 38, 7985 (1989) and references therein
- [10] H. Arnolds, M. Bonn. *Surf. Sci. Rep.* 65, 4566 (2010)
- [11] L. J. Richter, T. P. Petralli-Mallow, J.C. Stephenson. *Opt. Lett.* 23 1594 (1998)
- [12] T. Maeda, T.A. Ishibashi. *Applied Spectroscopy* 61, 459 (2007)
- [13] A. B. Sugiharto, C.M. Johnson, H.B. De Aguiar, L. Alloatti, S. Roke. *App. Phys. B.* 91, 315 (2008)
- [14] I.V. Stiopkin, H.D. Jayathilake, C. Veeraman, A.V. Benderskii, *J. Chem. Phys.*, 132, 234503, (2010)
- [15] A.N. Bordenyuk, H. Jayathilake, A.V. Benderskii, *J. Phys. Chem. B*, 109, 15941 (2005)
- [16] A.L. Harris, L. Rothberg, *J. Chem. Phys.*, 94, 2449, (1991)
- [17] R.W. Boyd, *Nonlinear Optics*, Academic Press, San Diego, CA, (1992)
- [18] N.E. Karatzas, A.T. Georges, *J. Opt. Soc. Am. B*, 26, 2218, (2009)
- [19] C. Weeraman, S.A. Mitchell, R. Lausten, L.J. Johnston, A. Stolow, *Opt. Express*, 18, 11483. (2010)
- [20] T. Ishibashi, H. Onishi, *Chem. Phys. Lett.*, 346, 413, (2001)
- [21] F. Fournier, W. Zheng, S. Carrez, H. Dubost, B. Bourguignon, *J. Chem. Phys.* 121, 4839. (2004)
- [22] B. Busson and A. Tadjeddine, *J. Phys. Chem. C*, 113, 21895, (2009)
- [23] F. Fournier, PhD thesis, University Paris-Sud (2003).

## Chapter 2

### Elaboration of nanoparticle based model catalysts in Ultra-High Vacuum (UHV)

<b>2.1 Introduction</b>	40
<b>2.2 The UHV system</b>	40
2.2.1 Role of the different UHV chambers	41
2.2.2 Evaporation chamber (EVAP)	43
2.2.3 Pumping of the UHV chambers and security systems	45
2.2.4 Sample characterization by LEED and Auger	45
2.2.5 Modifications of the UHV system	47
<b>2.3 Preparation of Pd nanoparticle on MgO/Ag(100) and Pd(100) single crystal samples</b>	48
2.3.1 Principles of growth	48
2.3.2 Structure of Pd nanoparticles/MgO/Ag(100)	51
2.3.3 Sample cleaning and characterization	53
2.3.4 Growth of MgO films on Ag(100)	54
2.3.5 Growth of Pd nanoparticles on MgO films on Ag(100)	57
<b>2.4 Conclusion</b>	59
<b>References</b>	60

## 2.1 Introduction

Supported catalytic nanoparticles (NPs) [1] are fabricated in UHV conditions ( $\approx 10^{-10}$  mbar) for well controlling the environment and states of NP growth. UHV is also necessary for many surface analytical techniques, in particular those based on electron beams [2-8]. In our UHV system, Auger electron spectroscopy (AES) [2] and low energy electron diffraction (LEED) [3] allow to characterize the surface elemental composition and the surface structure, respectively. Molecular beam epitaxy (MBE) [6] is a UHV technology for growing ultra-thin films and nanoparticles with a good crystalline quality and chemical purity. In this work, Pd(100) and Pd nanoparticles supported by a MgO thin oxide film epitaxially grown on a Ag(100) single crystal can be prepared and analyzed before they are exposed to molecular adsorption and catalytic oxidation. In this chapter our UHV system and the elaboration of samples are presented. This includes cleaning of single crystals (Ag(100) and Pd(100)), sample characterization by LEED and Auger, preparation and characterization of supported nanoparticle samples (Pd NPs / MgO / Ag(100)).

## 2.2 The UHV system

Our UHV system consists of 7 chambers with different functions, the pumps and sample characterization, valves and transfer rods. The base UHV pressure is below  $10^{-10}$  mbar. During my thesis, I have also worked on the modification of UHV samples. In this section we will introduce the composition, functions of and some modifications of this UHV system.

## 2.2.1 Role of the different UHV chambers

Fig. 2.1 to 2.3 show the sketch and photographs of the different chambers composing our UHV system.

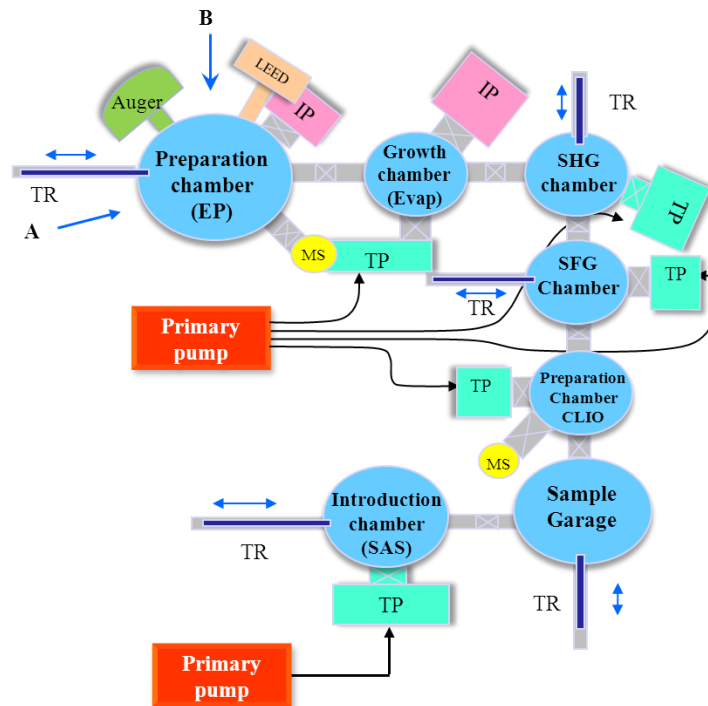


Fig. 2.1. Sketch of the UHV system. Ion pumps (IP), turbo pumps (TP), transfer rods (TR) and mass spectrometers (MS).

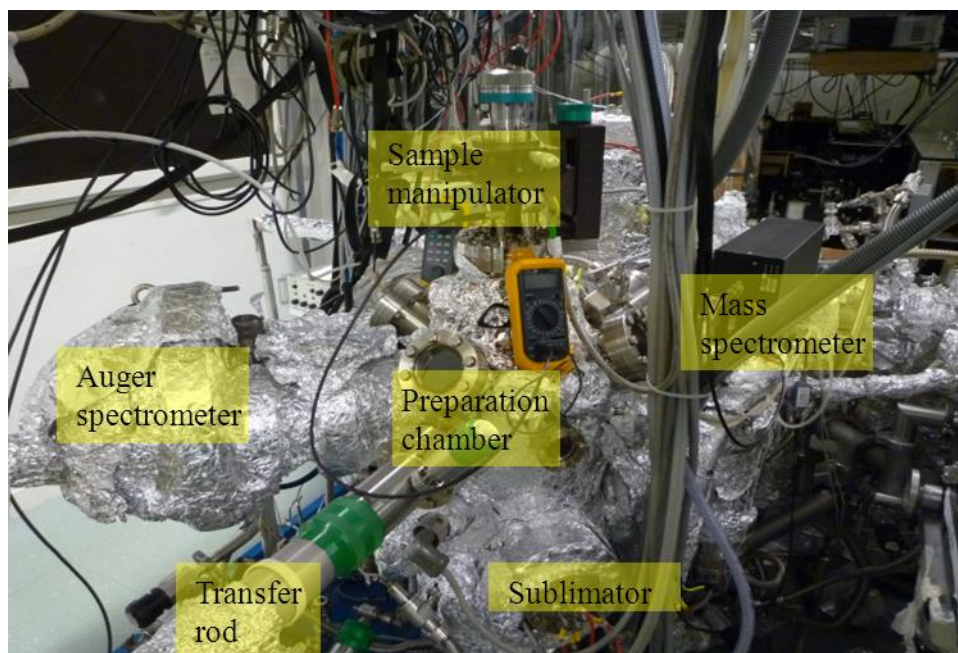
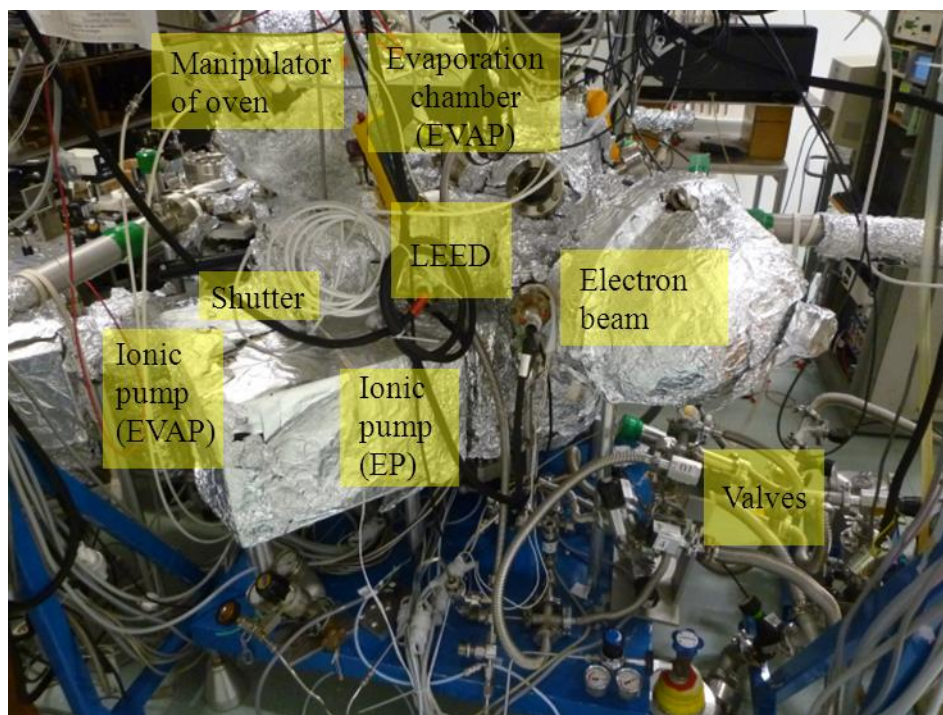


Fig. 2.2. Photograph made from the direction A in (a) showing the preparation chamber (EP) and the LEED and Auger analyzers installed on it.



*Fig. 2.3. Photograph made from the direction B in (a) showing the evaporation chamber (Evap) for the growth of oxide films and metallic nanoparticles.*

As shown in **Fig. 2.1**, the UHV system is composed of two preparation chambers (EP with characterization and CLIO without characterization), a growth chamber (EVAP) for preparing thin oxide layers and metallic nanoparticles, two optical analysis chambers (SFG and SHG), a “garage” chamber for sample storage and a portable chamber (SAS) to transport samples to other laboratories (SPCSI CEA Saclay (F. Charra), CINAM Marseille (C. Henry), or ISMO) for Atomic Force Microscopy (AFM) / Scanning Tunneling Microscopy (STM) characterization. In chambers EP and CLIO the samples can be prepared by argon sputtering and annealing up to 1200 °C. Annealing at lower temperature is also available in EVAP and SFG chambers. Low Energy Electron Diffraction (LEED) and Auger electron spectroscopy can be performed in the EP chamber to characterize the sample crystalline quality and cleanliness. After preparation in the EP / EVAP chambers, samples are transferred to the SFG or SHG chambers for optical experiments. In the SFG chamber, two CaF<sub>2</sub> windows allow input and output of visible and IR beams at an incidence angle of  $\approx 70^\circ$ . The SFG sample-holder can be cooled down to 95 K with liquid nitrogen. Two pyrometers are available to measure the temperature range from 50 °C to 300 °C and from 300 °C to 1100 °C. The introduction chamber (SAS) allows the insertion of samples into UHV. On the portable UHV “suit-case” a small ionic pump maintains the pressure below  $10^{-9}$  mbar for several days when disassembled from the (SAS). Four mechanical

(translation - rotation) transfer rods are used to transfer samples inside the UHV system. The EP transfer rod is also used to hold the sample during growth.

Bayer-Alpert UHV gauges working below  $10^{-3}$  mbar are used to control the pressure in all chambers. A mass spectrometer in CLIO and EP chambers controls the composition of the residual gas, and can be used as leak detectors. They could follow the gas composition as a function of time during catalysis experiments.

## 2.2.2 Evaporation chamber (EVAP)

Molecular or atomic beam epitaxy (MBE) is widely used in surface science [10]. It allows to deposit very small amounts of atoms, allowing growth of ultrathin films of high quality with a thickness accuracy much better than 1 ML. We use typically deposition rates of a few monolayers per minute. A quartz microbalance is used to calibrate the flux of the atomic beams, thanks to its good accuracy around 0.01 nm/sec. The ultra-high vacuum environment results in the highest achievable purity of the grown films and/or nanoparticles. Typically, with our system, the base pressure does not exceed  $10^{-9}$  mbar during epitaxy.

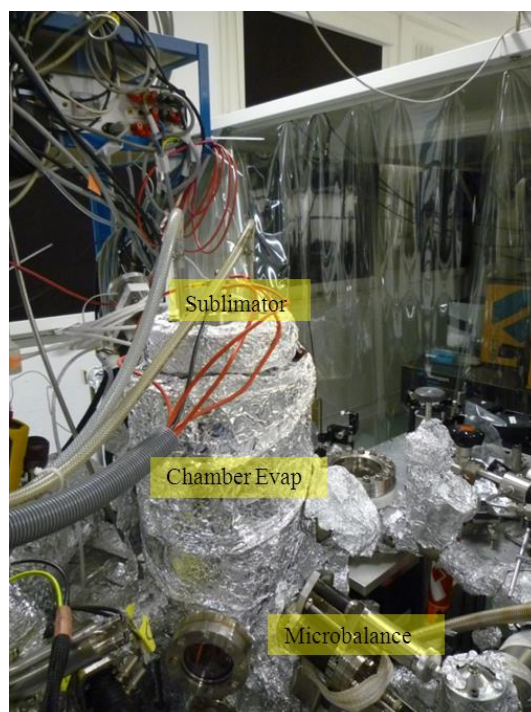
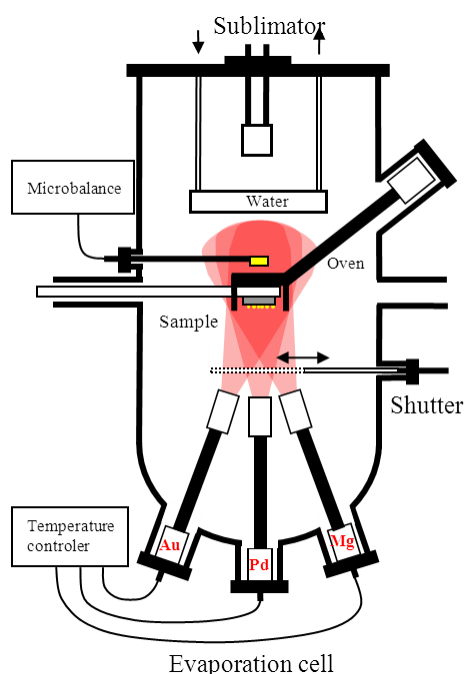


**Fig. 2.4.** (Left): Sketch of the evaporation chamber installed on our UHV system. (Right): Corresponding photograph.

The sketch of our evaporation chamber (EVAP) is shown in **Fig. 2.4** and **Fig. 2.5**. It is composed of evaporation cells with highly pure Au, Pd and Mg materials, a shutter, an oven, a microbalance, and a sublimator. The crucible which contains the high purity metals is heated to target evaporation temperatures chosen to produce effusive beams with the desired flux (Pd 1144 °C, Mg 282 °C and Au 1050 °C). When the crucible temperature is stable, the metal vapor flux is calibrated by the microbalance. After calibration of the flux and calculation of the growth time, the cleaned sample is inserted into the oven until it reaches the required deposition temperature with the shutter closed. The shutter is then opened for the time of growth. In the case of MgO, O<sub>2</sub> is introduced at 10<sup>-8</sup> mbar during metal evaporation on the sample. The oven, crucible and microbalance are cooled by a circulation of water to keep the pressure as low as possible.

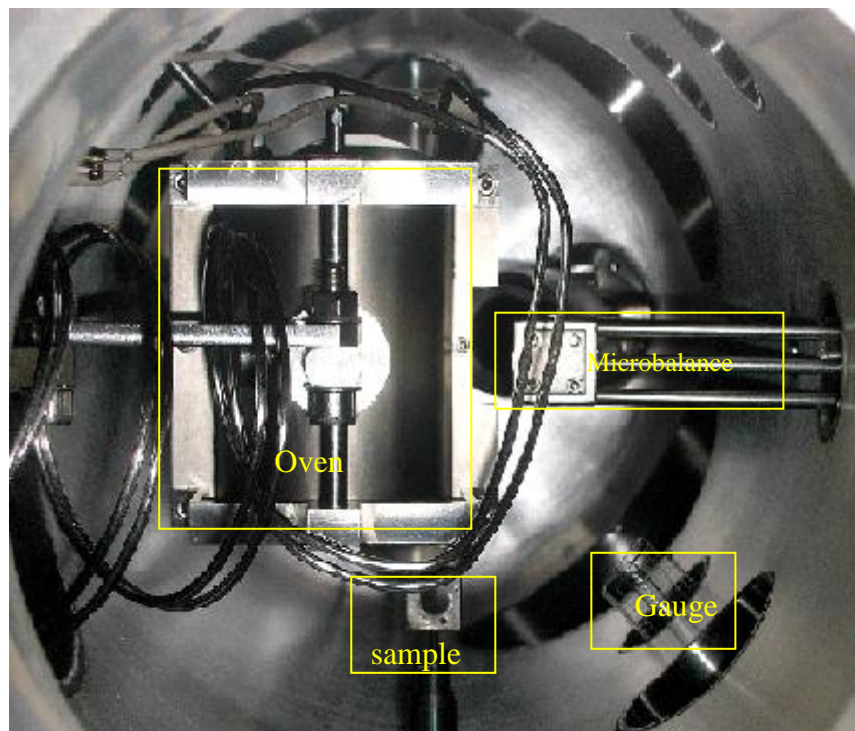


**Fig. 2.5.** Photograph of the inside of the EVAP chamber showing the oven, the microbalance on the right, the Bayard-Alpert gauge and the sample attached at the end of the transfer rod.

### 2.2.3 Pumping the UHV chambers and security systems

In standard UHV systems, several pumping devices are used to keep the base pressure as low as  $10^{-10}$  mbar. We used dry pumps to avoid the contamination by organic compounds. To keep a lasting ultra-high vacuum ( $\approx 10^{-10}$  mbar) we need to pump the chambers step by step (**Fig. 2.1**). The primary pump, which decreases the pressure from 1 bar to  $10^{-3}$  mbar is placed before turbo pumps. The turbo pumps can work in the pressure  $< 10^{-2}$  mbar and keeps a vacuum up to  $10^{-10}$  mbar providing that the chambers have been outgassed by heating. The ionic pump which works at pressures  $< 10^{-7}$  mbar can keep a vacuum of  $\approx 10^{-10}$  mbar even when the turbo pump of the chamber is not used. Two titanium sublimators in the EP and EVAP chambers allow to increase considerably the pumping speed, because Ti is deposited directed on the chamber walls, allowing fast pumping of  $H_2$ ,  $H_2O$ , CO,  $N_2$ ,  $CO_2$ ... which compose the residual gas. Since the Ti film gets saturated as molecules adsorb and react on it, the preparation and evaporation chamber (EP and EVAP) must be sublimated periodically especially before the preparation of the samples in order to get the best vacuum.

After exposure to air, the UHV chamber pressure cannot decrease below  $10^{-6}$  mbar after a few hours and  $10^{-8}$  mbar after one or two days, due to the continuous desorption of the many molecules that were adsorbed during exposure to the atmosphere, especially water. Thermal degassing between 100 and 150 °C during at least 12 h is required in order to increase the desorption rate of these gases. After thermal degassing, a pressure below  $10^{-10}$  mbar can be reached.

An automatically triggered security system is used to prevent accidental exposure to air and to manage power cuts without damage to the instruments and vacuum quality. When the pressure rises accidentally above a certain limit, or when turbo pump speed suddenly decreases, these securities are activated and instantly the compressed-air electro-valves between the chambers and the pumping stage are closed, and the power to all electron sources is shut down. The security system works by receiving an electric signal emitted by the gauge controller or by the controllers of the turbo pumps.

### 2.2.4 Sample characterization by LEED and Auger

**Low Energy Electron Diffraction (LEED)** allows us to obtain information on the crystal structure and quality of sample surface. A monochromatic electron beam, emitted from

an electron gun is impinging the sample surface at normal incidence. Electrons are back-scattered by the surface atomic lattice along the directions of the reciprocal lattice towards a phosphor screen through grids that allow for field free flight of the electrons from the sample to the first grid, rejection of inelastically scattered electrons, and then acceleration on the phosphor screen. Diffraction spots due to the diffracted electrons are directly observed at the back of the fluorescent screen, visualizing the surface reciprocal lattice (**Fig. 2.6**). Electron energy can be tuned between  $\approx 20$  eV and several hundreds eV. In practice, the 10-200 eV range is used. This energy range corresponds to the minimum penetration depth of electrons in matter (0.5-1.0 nm) [9] and is therefore most suitable for surface characterization. Thanks to this property, LEED is a surface sensitive tool. The LEED can see ordered structures on the surface, for example an ordered CO layer on the surface of Pd(100), which will be discussed in **Section § 3.4.1**. Care must be taken to reduce as much as possible the incident electron current in order to avoid electron induced desorption. The LEED power supply allows to measure directly this current.

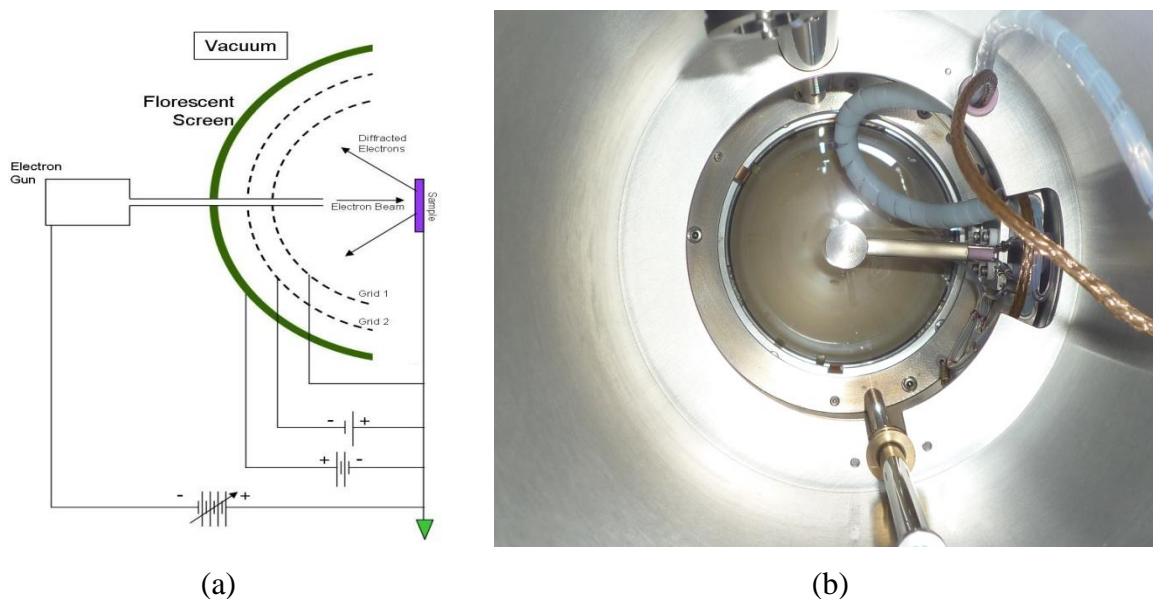


**Fig. 2.6.** (a) Sketch of the LEED. (b) View of the back of the screen. The cylinder in the center is the electron gun.

**Auger electron spectroscopy (AES)** is a technique that gives elemental surface composition of the surface of the sample. A high energy electron beam ( $\approx 2$  keV bias voltage and minimal current to avoid surface damage) is impinging the sample surface at  $\approx 20^\circ$  incidence from sample normal. Auger processes result from the relaxation that follows the excitation by the high energy electrons. Because Auger processes concern principally core

levels, electrons are emitted at characteristic, tabulated energies that allow elemental identification. The energy spectrum of electrons emitted by the sample is recorded via an hemispherical electron analyzer and a sensitive channeltron detector. Scanning and spectrum analysis is controlled by a computer program. The surface selectivity of Auger electron spectroscopy comes in part from the fact that the energy of the Auger electrons is smaller than that of the incident electrons, and from the fact that electrons emitted in the bulk are subject to multiple collisions before they are detected, giving rise to a continuous background. In addition, Auger spectra as a function of e. g. growth time allow to observe steps in the Auger intensity vs time as new layers are formed.

### 2.2.5 Modifications of the UHV system

During my thesis, I have modified the design of our sample holders in order to make our system compatible with Omicron holders. I used Solid Works to do this. Our samples can now be taken out of our UHV system using our UHV “suit case” where they are held by Omicron holders. When they are used inside our chamber, the Omicron holder is held on a second holder compatible with our previous holder. A 3D rendering view and a photograph of the fabricated new sample holder are presented in **Fig. 2.7** and **2.8** respectively. Molybdenum is used for the sample holders because very high temperatures may be required for sample annealing (up to 1200 °C).

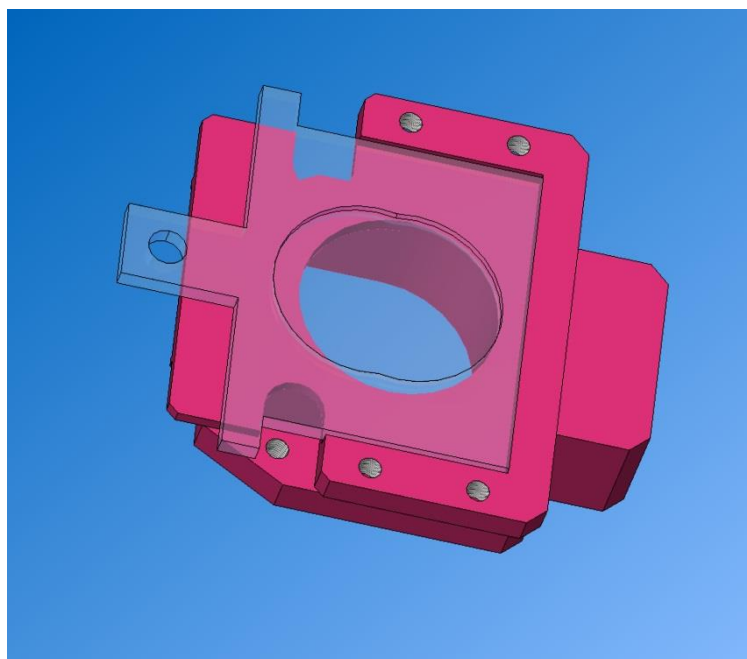


*Fig. 2.7. 3D rendering view of the modified sample holder designed using Solid Works.*



*Fig. 2.8. Photograph of the realized detachable sample holder.*

I also have participated at the development of the SAS chamber and the UHV “suit-case”. I have designed and made all electrical security required for this chamber. The garage has been modified in order to be able to store more samples. At the moment, 6 samples (or sample-holders) can be stored in it.

## **2.3 Preparation of Pd nanoparticles on MgO / Ag(100) samples**

### **2.3.1 Principles of the growth**

During deposition, a number of physical and chemical processes are operative. These mechanisms are presented in **Fig. 2.9**. Following adsorption on the surface, the atoms diffuse and chemisorb while some may desorb. These processes are strongly temperature dependent and have a direct influence on the quality of the growth of oxide films and metallic nanoparticles.

The layer growth starts at steps or on defects (adatom or missing atom) of the surface. In addition, when atoms meet each other, a growth nucleation may start. If the deposited layer has an atomic lattice matching with that of the surface, if interactions between adatoms are not larger than with surface atoms, and if temperature assisted surface diffusion is strong enough, layer by layer growth can be obtained. This is typically the case of the growth of metal on

metals. These growth conditions are required for good growth quality and are highly recommended in semiconductor industry, since defects decrease electronic device efficiency.

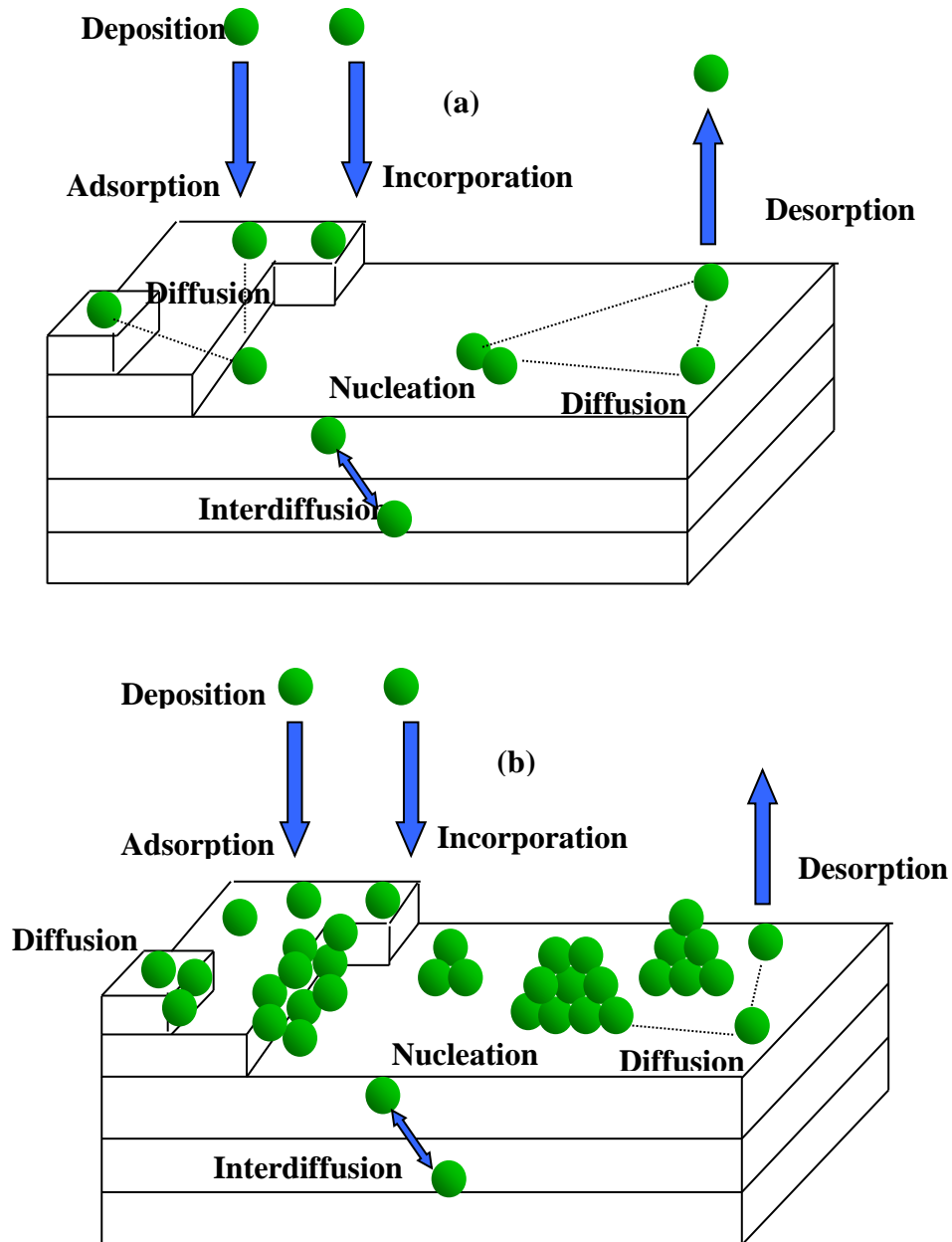


**Fig. 2.9.** Sketch of the different mechanisms occurring during the deposition of atoms on a surface. (a) atoms arrive at the surface, where they experience several dynamic processes: they can chemisorb, diffuse and find the preferential adsorption sites, or possibly are directly incorporated in the sub-surface (which is in general unwanted). (b) The atoms can diffuse towards the steps and grow layer by layer, or they can form random distributed clusters on the surface. Other processes like desorption or interdiffusion may influence the growth kinetics.

On contrary, for the growth of metallic nanoparticles or semiconductor quantum dots, growth conditions need to be completely different. Indeed three-dimensional growth is desired. These conditions are obtained when deposited atoms have a stronger binding energy between each other than with surface atoms. Thus clusters are formed on the surface. The distance between growing particles is governed by the diffusion length of adatoms on the surface, which is temperature dependent [11].

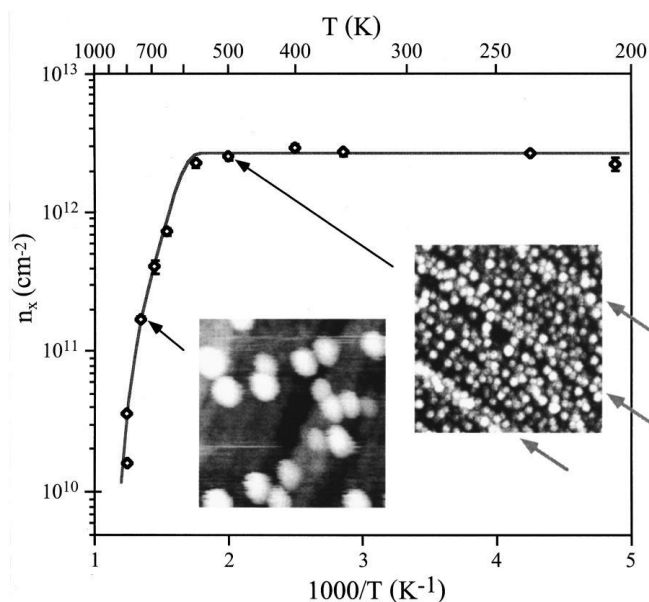


**Fig. 2.10.** Pd island density ( $\text{cm}^{-2}$ ) at 0.1 ML coverage as a function of the inverse of the temperature ( $\text{K}^{-1}$ ). Insets: non-contact AFM images of Pd deposits on MgO(100). The substrate temperature during deposition was 500 and 745 K for these two images. Three arrows point along steps in the 500 K micrograph. The size is  $100 \times 100 \text{ nm}^2$  for both images [11].

When the diffusion length is comparable to the distance between steps, we observe a preferential nucleation at the steps (**Fig. 2.10** right inset). It is the case for the growth of Pd or Au nanoparticles on MgO(100) at the appropriate temperature, as observed by G. Haas [11] or C. Henry [12]. The density of particles decreases and their size increase with increasing temperature. Below 500 K the diffusion length is less than the distance between steps, and the nucleation is distributed randomly on the terraces. At 500 K the diffusion length becomes comparable to the distance between steps. Above 600 K it is much higher than the distance between steps; in addition the available thermal energy is higher than the diffusion barrier on the steps. It results in different random distribution of the nucleation points and to even larger particles. The energy of diffusion and adsorption vary with the metal (**Table 2.1**). It results that the appropriate temperature for the growth is different for each system.

**Table 2.1:** Diffusion and adsorption energy of Au and Pd atoms on MgO(100).

Metal	Energy of diffusion (eV)	Energy of adsorption (eV)	Reference
Ag	0.083	0.33	[13]
Pd	0.22/0.16	0.95	[14, 15]

The formation of new growth nuclei continues until the distance between nuclei becomes shorter than the diffusion length at the growth temperature. Newly arrived atoms join either of the closest particles. The epitaxial growth of nanoparticles includes three steps. 1) Nucleation: the atom islands nucleated appear on the surface and their density increases; 2) Growth: the island density remains constant while their size increase; 3) Coalescence: the islands form a thin film [16, 17]. The quality of the epitaxial film depends not only on the temperature but also on the geometric (lattice parameters) and chemical (adsorption energy) compatibilities of the supported layer with respect to the surface. If the lattice mismatch is too large (more than a few percent) the layer cannot stand the induced strain and dislocations occur, whatever the growth temperature.

### 2.3.2 Structure of Pd nanoparticles / MgO / Ag(100)

Pd nanoparticles epitaxially grown on MgO(100) single crystal has been extensively studied in the literature [12]. Ultra-thin layers of Magnesium oxide (MgO) [12, 18] can be deposited on Ag(100) [19]. We have chosen to study Pd nanoparticles / MgO film / Ag(100) for several reasons: (i) the strong reflection of the Ag substrate is more appropriate for SFG measurements than the MgO one; (ii) the thin MgO film thickness (a few atomic layers) allows STM measurements [19]; (iii) MgO layer is an insulator, which reduces charge transfer between the metallic substrate and the NPs, allowing to study only the interaction between nanoparticles and adsorbed molecules using SFG pump-probe experiments; (iv) MgO is a good conductor of heat, which allows fast heat equilibrium; (v) the growth and the electronic and geometrical properties of Pd nanoparticles on MgO(100) and MgO film on Ag(100) is well documented in the literature [12,18-20]. (vi) Pd, MgO and Ag have similar lattice parameters, which permits relatively good crystal growth quality. The Ag lattice structure is face centered cubic (fcc) with a lattice parameter of 4.09 Å. In MgO, the Mg<sup>2+</sup> occupies a fcc network with a

lattice parameter of 4.21 Å. The ions  $O^{2-}$  are on the network shifted by half the lattice parameter in the direction shown in **Fig. 2.11**.

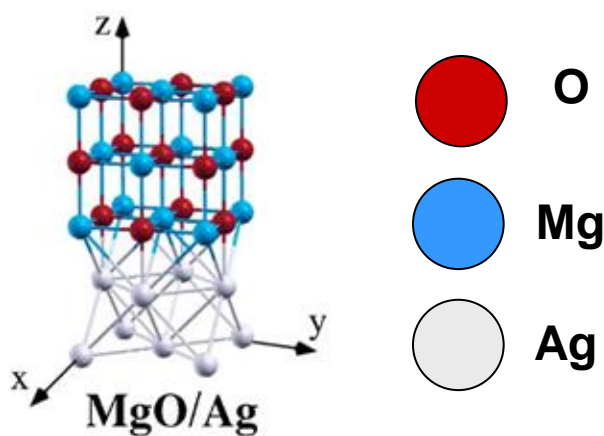


**Fig. 2.11:** Atomic structure of  $MgO/Ag(100)$ .

During MgO growth on  $Ag(100)$  three sites of Ag can be occupied by Mg or O atoms: linear, bridge and 4 fold hollow sites. As shown in **Fig. 2.12**, Kiguchi et al. [20] have studied the stability of MgO on the  $Ag(100)$  surface by DFT. They have shown that the oxygen is directly bonded to a Ag atom on a linear site (**Fig. 2.12b**). This site is respectively 0.12 and 0.41 eV more stable than the other ones (**Fig. 2.12a** and **c**).

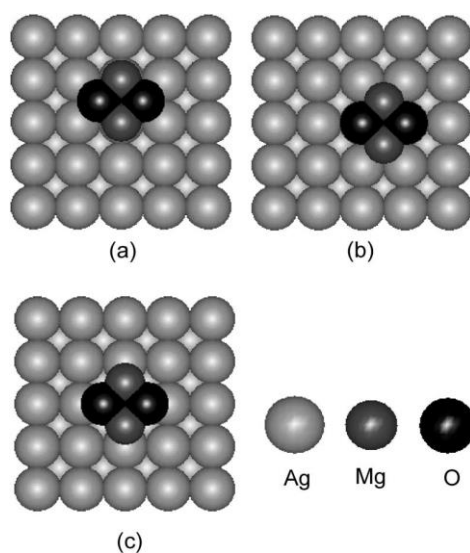


**Fig. 2.12.** Possible sites for MgO cluster on  $Ag(100)$  : (a) O is placed at the 4 fold hollow site and Mg site is at on-top linear position; (b) O is placed at the on-top linear site and Mg on the 4 fold hollow site; (c) O is placed at the bridge site and Mg on the bridge site. The most stable form is (b) [20].

### 2.3.3 Sample cleaning and characterizations

The metals studied, Ag(100) and Pd(100), are reactive and cannot be kept clean for more than one day even at the pressure to  $10^{-10}$  mbar. It is necessary to clean them before each experiment. The cleaning consists in two steps: argon sputtering and annealing. Argon sputtering allows to remove dozen of layers from the surface, including atoms from metallic nanoparticles, adsorbed molecules and impurities, atoms from the oxide layer and from the substrate. It is with an argon ion gun powered at several hundred Volts. A pressure of  $2.2 \times 10^{-6}$  mbar of pure argon is required to ignite the ionization of argon atoms. The current measured through the sample reaches between 10 and 30  $\mu\text{A}$ . The sputtering parameters for Ag(100) and Pd(100) are listed in **Table 2.2**.

*Table 2.2. Cleaning parameters used for the preparation of samples.*

Sample	Ar <sup>+</sup> sputtering			Thermal annealing		
	Duration	Voltage	Sample current	Temperature	Duration	Gas introduced
Ag(100)	30 min	800 eV	30 $\mu\text{A}$	500 °C	10 min	
Pd(100)	30 min	600 eV	20 $\mu\text{A}$	800 °C	5 min	
				400 °C	2 min	O <sub>2</sub> $5 \times 10^{-8}$ mbar
				450 °C	1 min	

After the bombardment, surface roughness is important and the crystal order is lost at the surface. Hence thermal annealing is needed to reconstruct the surface. The sample is heated to a high temperature which gives atoms enough mobility to find their places in a well ordered structure. The annealing for Ag(100) is done by heating the sample to 500 °C for 10 min in the oven of EVAP chamber. The annealing of Pd(100) is different, it is done by: 1) keeping the sample temperature 800 °C for 5 min. This annealing is done in EP chamber by electron bombardment from a filament located behind the sample. The filament is polarized to -600 V with respect to the sample; 2) let the sample temperature decrease to 400 °C, then expose the sample for 2 min to O<sub>2</sub> at  $5 \times 10^{-8}$  mbar in order to remove remaining C that may have come to the surface by segregation during high temperature annealing; 3) increase the sample temperature again to 450 °C for 1 min to desorb excess oxygen. The parameters for Ag(100) and Pd(100) is listed in **Table 2.2**. The cleaning process is repeated several times in order to

achieve a good crystal quality as judged by LEED (bright sharp spots with no background) and Auger (no traces of C and O) (**Fig. 2.13** and **Fig. 2.14**).

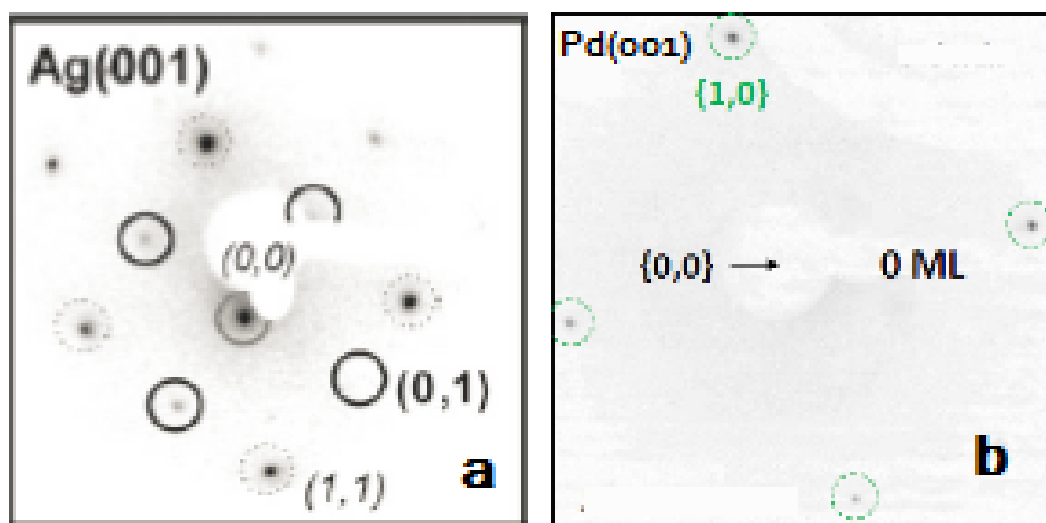


**Fig. 2.13.** LEED negative photographs of (a) cleaned Ag(100) at an electron energy of 120 eV and (b) cleaned Pd(100) at an incident electron energy of 43 eV.

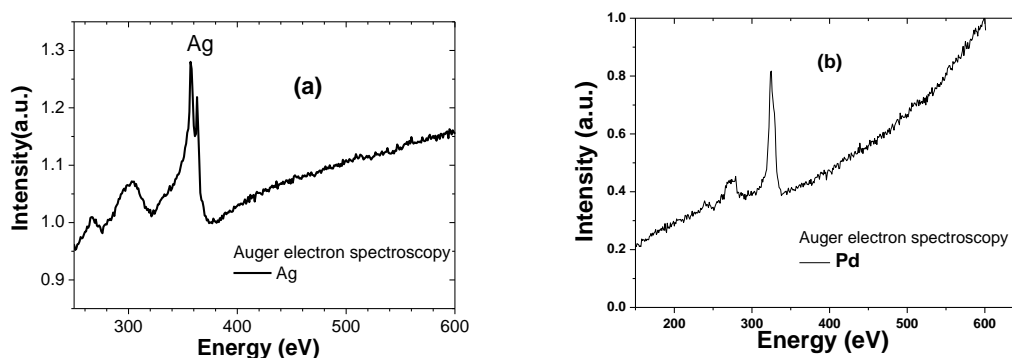


**Fig. 2.14:** Auger spectra of the clean (a) Ag(100); (b) Pd(100) surface.

### 2.3.4 Growth of MgO films on Ag(100)

After Ag(100) cleaning, the deposition of the magnesium oxide film can be done. First the Mg evaporation cell is heated to 282 °C to reach a flux on the sample of about 0.32 Å/s. When the temperature is stable, the flux of Mg is measured with the microbalance and the time growth for the MgO film of the desired thickness is calculated. Then Ag(100) is inserted into the oven for 20 min in order to heat it up to the optimal growth temperature of 300 °C with the shutter closed (no Mg flux) [19,21] which corresponds to the best compromise between the necessary Mg mobility and the unwanted Ag adatom mobility.  $5 \times 10^{-8}$  mbar O<sub>2</sub> is introduced

during the deposition of magnesium. O<sub>2</sub> molecules dissociate when they adsorb on Ag(100), then they diffuse and combine with Mg atoms to form (MgO)<sub>x</sub> clusters of height 1 atomic plane, which grow until coalescence. The growth parameters can be found in **Table 2.3**. The time required to obtain 1 ML of MgO is expressed as [21]:

$$\Delta t_{1ML}^{MgO} = \frac{2.63}{\tau_s^{Mg}} \quad (2.1)$$

where  $\tau_s^{Mg}$  (Å/s) is the deposition rate of Mg on the microbalance. The factor 2.63 includes several factors: the height of a MgO monolayer, the ratio of Mg fluxes on the microbalance and the sample.

**Table 2.3.** Growth parameters for the preparation and deposition of oxide films and nanoparticles.

Deposition type	Cell temperature (°C)	Oven temperature (°C)	Pressure (mbar)	Gas (O <sub>2</sub> ) introduced	Rate $\tau_\mu$ (Å/s)
MgO (on Ag)	282	300	$<2 \times 10^{-9}$	$5 \times 10^{-8}$	~0.316
Pd (on MgO)	1144	200	$<2 \times 10^{-9}$		~0.612

The MgO film can be characterized by LEED and Auger as shown in **Fig. 2.15** and **16**. In **Fig. 2.15** LEED patterns do not reveal new spots specific of MgO, which has the same unit cell as Ag(100). Only the relative intensities of the different spots change with MgO thickness as reported in [19]. Auger spectroscopy (red curve in **Fig. 2.16**) reveals the presence of oxygen at 510 eV. The peaks of Ag (300 and 358 eV) are still visible below a 3 ML MgO layer. The peaks of Mg lie at 60 eV and 1200 eV. They could not be observed with our Auger analyzer because it is not correctly shielded, which perturbs detection at these energies.

STM images of 2 ML MgO film on Ag(100) (**Fig. 2.17**) were recorded at CINaM [19], in order to determine the optimal deposition temperature of MgO on Ag(100). It turns out that a compromise at 300 °C must be done. A larger temperature would be better to give more mobility to MgO, but the deposition cannot be made at larger temperature because Ag atoms would diffuse into the MgO layer. The layer is therefore defective. It allows nevertheless to obtain atomically flat domains of < 20 nm which are separated by defective boundaries.

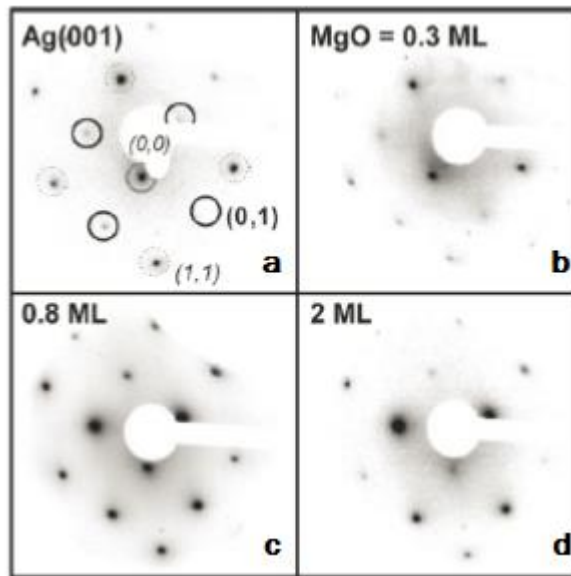


**Fig. 2.15.** LEED photograph of the (a) cleaned Ag(100), and Ag(100) deposited by (b) 0.3 ML; (c) 0.8 ML; (d) 2 ML MgO film with an incident electron energy of 120 eV

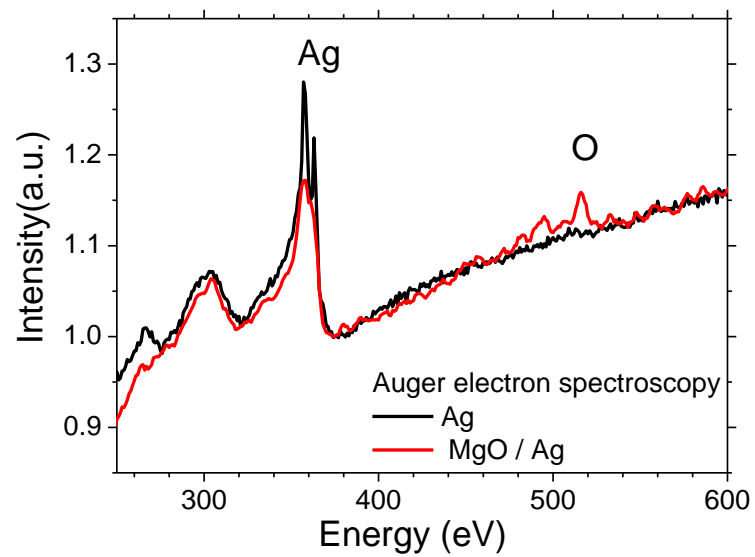


**Fig. 2.16.** Auger spectra of the clean Ag(100) surface (black curve) and the surface of Ag(100) covered by 3 ML of MgO (red curve).

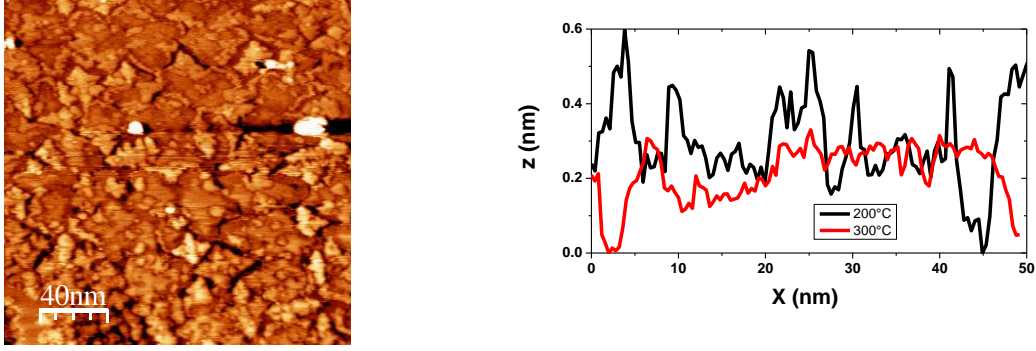


**Fig. 2.17.** 2 ML MgO film deposited on Ag(100) surface at 573 K. Left : STM image. Right : topographic profile along the grey line (red curve). The black curve shows a typical profile when MgO is grown at 473 K.

### 2.3.5 Growth of Pd nanoparticles on MgO films on Ag(100)

After the deposition of MgO, the Pd beam is measured with the microbalance and Pd is deposited on the MgO/Ag surface after stabilization of the sample temperature at 200 °C [15]. The calculation of the growth duration for Pd is easier than for MgO because there is only one type of atom that is deposited. The thickness of one monolayer of palladium is  $a_{Pd} / 2$ , with  $a_{Pd}$  the lattice parameter of bulk Pd. The time for depositing 1 ML of palladium equals to [21]:

$$\Delta t_{1ML}^{Pd} = \frac{a_{Pd}}{2} \times \frac{R}{\tau_s^{Pd}} \quad (2.2)$$

where  $\tau_s^{Pd}$  (Å/s) is the deposition rate of Pd on the microbalance and R is the ratio of the Pd atom deposition rates on the sample and the microbalance (R=2.1). The AFM image Pd nanoparticles of equivalent thickness 2.7 ML / MgO / Ag(100) is shown in **Fig. 2.18a**. The corresponding distribution of height and width of these Pd nanoparticles is given in **Fig. 2.18b**. The figure shows that in spite of the defects of the MgO layer the size distribution of the NPs is typical of this type of epitaxial system where nucleation occurs at random defects. Detailed examination of **Fig. 2.18a** indicates that sometimes NPs form a loop, presumably on a MgO domain boundary.

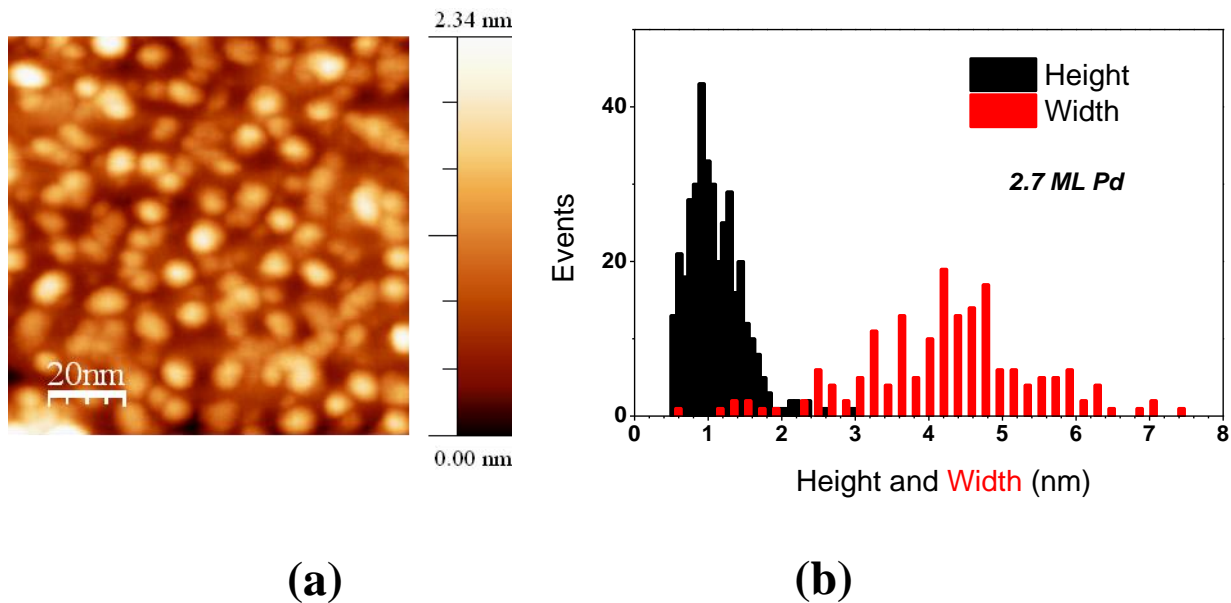


**Fig. 2.18.** (a) AFM image of Pd nanoparticles / MgO / Ag(100) obtained by a Pd deposit of equivalent thickness 2.7 ML. (b) distribution of the height (black) and width (red) of the nanoparticles presented in (a).

The shape of Pd NPs on MgO has been studied in details in the literature using STM and high resolution TEM. In AFM, the existence of a flat upper terrace can be observed in constant height mode. In this mode the height of the AFM tip is adjusted just above the NPs. There is only a signal at this height. The substrate surface is not seen. There is no convolution of NP and tip shapes. As a result NPs do not have a round shape any more. **Fig. 2.19** shows that all NPs have the same height and that they are atomically flat. The shape is approximately square, corresponding to the known truncated pyramid shape with shape ratio of  $\approx 4$  observed at high resolution (STM and TEM).

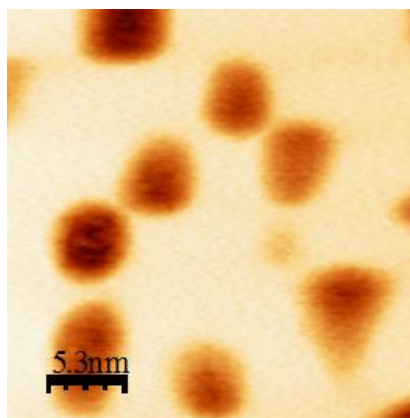


**Fig. 2.19.** AFM image in constant height mode.

**Table 2.4.** Geometric properties of Pd NPs in function of their size.

<b>Equivalent thickness (ML)</b>	<b>0.5</b>	<b>1</b>	<b>2</b>	<b>4</b>	<b>10</b>
<b>Height (nm)</b>	<i>0.70</i>	<i>0.88</i>	<i>1.11</i>	<i>1.40</i>	<i>1.95</i>
<b>Average Size of a NP (nm)</b>	<i>2.8</i>	<i>3,5</i>	<i>4,4</i>	<i>5.6</i>	<i>*</i>
<b>Number of atoms</b>	<i>330</i>	<i>660</i>	<i>1320</i>	<i>2640</i>	<i>*</i>
<b>Terrace / edge ratio</b>	<i>1.3</i>	<i>1.6</i>	<i>2</i>	<i>2.6</i>	<i>*</i>
<b>Surface coverage (%)</b>	<i>15</i>	<i>23</i>	<i>36</i>	<i>60</i>	<i>100</i>

*\* coalescence*

One can calculate the NP geometrical parameters as a function of size as shown in **Table 2.4** [21], for an equivalent thickness ranging from 0.5 to 10 ML. At 10 ML Pd NP have coalesced. As the nominal thickness of Pd increases, the ratio of sites at facets to edges decreases. The size of 0.25 ML (for which we have done SFG experiments) is not indicated in this table because the NP shape becomes different at smaller size.

## 2.4 Conclusion

Our UHV system allows us to prepare reproducible NPs grown on ultra-thin oxide layers and suitable as model catalysts as will be shown in the next chapters. STM and AFM characterization must be done outside our chamber. The method of preparation of the NPs was elaborated in collaboration with CINAM. Our portable UHV chamber allows to transport our samples into other vacuum systems for additional characterization (STM / AFM at CINAM and CEA Saclay). The Pd nanoparticles / MgO /Ag(100) is not in fact a very good system because the MgO layer cannot be annealed to a high enough temperature without interdiffusion of Ag atoms into the MgO layer. However it turns out to be manageable in the sense that Pd NPs of the expected shape can be obtained with a reasonable size distribution. In the future we will turn to a system that allows the growth of NPs on an ordered array, for which a much narrower size distribution can be obtained.

## References

- [1] D. Astruc, F. Lu, J. R. Aranzaes, *Angewandte Chemie International Edition*, 44, 48, (2005)
- [2] D. Briggs and M.P. Seal., *Practical surface analysis by Auger and x- ray photoelectron spectroscopy*, (1983)
- [3] M.A.Van Hove, *Advances in Solid State Physics*, 25, 517, (1985)
- [4] A. Benninghoven, F.G. Rudenauer, H.W. Werner, *Secondary ion mass spectrometry: basic concepts, instrumental aspects, applications and trends*, (1987)
- [5] L. Moro , R. S. Ruoff , C. H. Becker , D. C. Lorents , R. Malhotra, *J. Phys. Chem.*, 97, 6801, (1993)
- [6] C. Chin-An, R. Ludeke, L.L. Chang, L. Esaki, *Appl. Phys. Lett.*, 31, 11 (1977)
- [7] J. Kong, Alan M. Cassell, H. Dai, *Chem. Phys. Lett.* 292, 567 (1998)
- [8] E.M. Kaidashev et. al. *Appl. Phys. Lett.*, 82, 22, (2003)
- [9] J. Wollschläger, D. Erdös, R. Goldbach, H. Höpken, and K. M. Schröder. *Thin Solid films* 400, 1 (2001)
- [10] A. Y. Cho, J. R. Arthur, *J. Prog. Solid State Chem.* 10, 157. (1975)
- [11] G. Haas, A. Menck, H. Brune and J. V. Barth *Phys. Rev. B* 61, 11105 (2000)
- [12] K. Højrup-Hansen, S. Ferrero, C.R. Henry. *Appl. Surf. Sci.* 226, 167 (2004)
- [13] C. Li, R. Wu, A. J. Freeman, C. L. Fu. *Phys. Rev. B* 48, 8317 (1993)
- [14] C. Chapon, C.R. Henry, A. Chemam. *Surf. Sci.* 162, 747(1985)
- [15] C. R. Henry. *Surf. Sci. Rep.* 31 231 (1998)
- [16] J. L. Robins, T. N. Rhodin. *Surf. Sci.* 2, 346 (1964)
- [17] Y. Shigeta, K. Maki, Jpn. *J. Appl. Phys.* 18, 71 (1979)
- [18] H. Olli Pakarinen. *J. App. Phys.* 103, 054313 (2008)
- [19] A. Ouvrard et al. *J. Phys. Chem. C* 115, 8034 (2011)
- [20] M. Kiguchi, T. Goto, K. Saiki, T. Sasaki, Y. Iwasawa, A. Koma. *Surf. Sci.* 512, 97 (2002)
- [21] Thesis of Ahmed Ghalgaoui in University Paris-Sud (2012)

# Chapter 3

## CO adsorption on Pd(100) single crystal by SFG

<b>3.1. Introduction</b>	62
<b>3.2 CO adsorption on single Pd single crystals: State of the art</b>	63
3.2.1 Vibration modes of CO adsorbed on Pd surfaces	63
3.2.2 Adsorption sites and adsorption phases of CO on Pd(111) and Pd(100) surfaces	64
<b>3.3 Experimental procedure to expose the Pd surface to CO</b>	67
<b>3.4 SFG and LEED studies of CO adsorption as a function of CO coverage</b>	68
<b>3.5 SFG results in the time domain</b>	77
<b>3.6 Simulation of dipolar coupling</b>	79
<b>3.7 Discussion</b>	85
<b>3.8 Conclusion</b>	86
<b>References</b>	87

### 3.1. Introduction

For decades, surface science has focused attention on the study of CO adsorption on transition metals [1-7] especially on single crystal palladium surfaces [8-14] or on supported palladium nanoparticles [15-23]. The internal stretch frequency has often been used with great success to determine the coordination of the adsorption site [24, 25] by analogy with the IR spectra of metal carbonyl compounds, and the CO coverage [12, 25], since the Pd-C vibration far in the infrared is hard to access with conventional vibrational spectroscopies. Internal CO frequency measurements offer valuable information about molecule-metal (chemical bonding) and molecule-molecule (dipolar) interactions. For CO on Pd(100), the orbital hybridizations shift the frequency from 2143 cm<sup>-1</sup> in the gas phase down to 1890 cm<sup>-1</sup> (at the zero-coverage limit) for bridge-bonded sites [24]. Upon an increase in CO coverage, the frequency shifts up to 1990 cm<sup>-1</sup> for a coverage close to  $\theta = 0.8$  ML. G. Blyholder has first given a description of CO binding on metals, that involves both electron donation from the 5 $\sigma$  CO molecular orbital to the metal s-p bands and a back-donation from the metal d-band to the anti-bonding 2 $\pi^*$  orbital of CO [3, 8]. Dipolar interactions have been intensively studied in the past on single crystals [1, 12, 25-29]. They are not strong enough to explain the observed large blue-shift of CO frequency with coverage [1, 12], indicating that a change of the chemical bonding with CO coverage represents the strongest contribution to the coverage-dependent CO frequency shift [4, 12, 25]. From the experimental point of view, spectra of isotopic mixtures of CO have allowed to separate the two contributions [12], i.e chemical and dipolar interactions. CO adsorption on Pd(100) is known to take place only on bridge sites over the full range of coverage and a unique adsorption phase was identified using LEED:  $c(2\sqrt{2} \times \sqrt{2})R45^\circ$  for coverage between 0 and 0.5 ML [9, 10, 12, 24]. After saturation of this adsorption phase, compressions of the CO layer occur, by insertion of dense CO lines (“fault lines”) between  $c(2\sqrt{2} \times \sqrt{2})R45^\circ$  domains [30]. Compression gives rise to successive LEED patterns characterized by the splitting of  $\{\pm\frac{1}{2}, \pm\frac{1}{2}\}$  spots. The transition from saturation (0.5 ML) to compression is associated with a sudden 30% drop of the CO adsorption energy [9, 11, 31, 32], a saturation of the IRAS intensity, a decrease of the CO bandwidth and a 11 cm<sup>-1</sup> frequency hop [12, 24].

In this chapter is presented a new study of CO adsorption on Pd(100) using combined Sum Frequency Generation (SFG) spectroscopy and LEED. Revisiting this well-known system using SFG was done for comparison with a study of CO adsorption on Pd

nanoparticles supported on MgO thin films, that will be the purpose of the **Chapter 4**. The singleton frequency at zero coverage ( $1890\text{ cm}^{-1}$ ) and the CO frequency at half-coverage ( $1949\text{ cm}^{-1}$ ) are in good agreement with previous IRAS experiments in the 0-0.5 ML CO coverage range [12]. However SFG leads to novel observations in the compression regime. The SFG intensity drops quickly by a factor 4. By following carefully the early stages of compression, we were able to evidence the appearance of a second CO band blue-shifted by  $7.6\text{ cm}^{-1}$  and the red-shifting of the first band with coverage. This band is also visible in the time domain. Its dephasing time  $T_2$  is different from that of the main band. Spectral and temporal measurements agree. They correspond to a red-shift of the CO band from  $1949$  to  $1900\text{ cm}^{-1}$  from 0.5 to 0.65 ML and a reduction of  $T_2$  from 690 to 222 fs. Using a dipole-dipole interaction model, we show that the frequency hop can be explained by the different dipolar surrounding between compressed and uncompressed CO domains. But for higher coverage, close to 0.65 ML, when the first band has almost disappeared, the low value of its frequency can only be explained by means of an increased charge transfer from Pd to isolated uncompressed CO molecules.

After a brief description of the adsorption of CO on Pd single crystal surfaces and the experimental methods, we present SFG and LEED results as a function of CO coverage compared with IRAS results reported in the literature. Then, using decoherence time measurements by fs-fs SFG and dipolar coupling calculations, we focus on the novel observations done at the early stages of compression.

## **3.2 CO adsorption on Pd single crystals**

### **3.2.1 Vibrational modes of CO adsorbed on Pd surfaces**

When CO adsorbs on a metal surface, it preferentially chemisorbs through its carbon end to the metal with its axis along the surface normal because both the  $5\sigma$  HOMO (Highest Occupied Molecular Orbital) and the  $2\pi^*$  LUMO (Lowest Unoccupied MO) are centered on the C atom. Their overlap with the metal orbitals is then larger if the molecule is oriented with the carbon end towards the surface. The overlap of the  $2\pi^*$  orbital with the metal orbitals is more favorable in the linear geometry [3]. One exception is at high coverage on the Ni(100) surface where lateral interactions cause CO molecules to tilt alternately across the rows [33].

There are 4 vibrational modes of CO adsorbed on metal as shown in **Fig. 3.1**. The internal vibration of CO is perturbed by the creation of the bond between the C atom and the metal surface atoms. It is the only accessible vibrational frequency by our SFG experiment due to the limitation in IR frequency range of the OPA (1250 to 3200  $\text{cm}^{-1}$ ). The so-called low frequency vibrational modes correspond to the translational (frustrated translation and CO-metal vibration) and rotational (frustrated rotation) degrees of freedom which are no longer free when the molecule is adsorbed. These modes are not accessible by SFG, because there are found in the far and mid-IR spectral ranges (50-500  $\text{cm}^{-1}$ ).

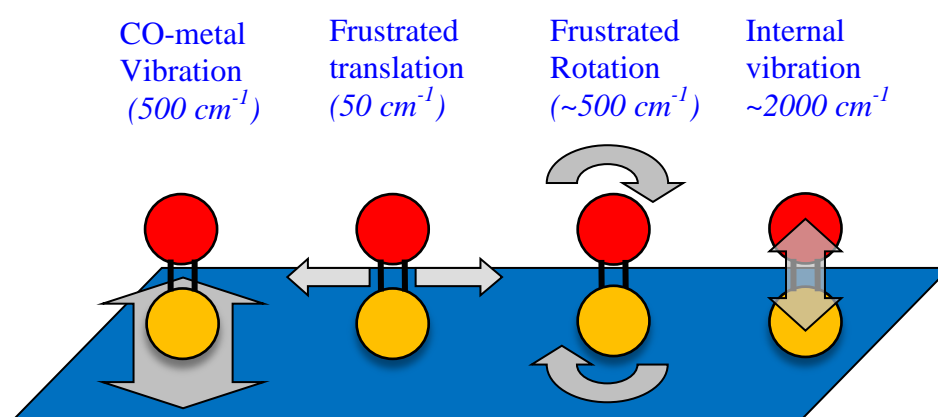


**Fig. 3.1.** Vibrational modes of CO molecules adsorbed on a metal surface. The red and yellow balls are oxygen and carbon atoms respectively.

### 3.2.2 Adsorption sites and structures of CO on Pd(111) and Pd(100) surfaces

The C–O stretching vibrational frequency is highly sensitive to the geometry of the binding site, where it can be bonded to one (on-top), two (bridge), three (threefold hollow) or four (fourfold hollow) metal atoms, and less dependent on the metal. The frequency of internal vibration of CO which is 2143  $\text{cm}^{-1}$  in the gas phase, varies from 1820  $\text{cm}^{-1}$  to 2110  $\text{cm}^{-1}$  when it is adsorbed on a Pd surface, depending on the adsorption site (**Fig. 3.2**).

According to the model of G. Blyholder [8], partial electron-transfers consisting of donation from CO  $5\sigma$  and back-donation from the d-orbitals of the metal to the CO  $2\pi^*$  orbital strengthens the metal-C bond and weakens the C-O bond, because  $5\sigma$  which is partially depleted is essentially non bonding for CO while  $2\pi^*$  which is partially filled is antibonding for CO. Since the CO bond strength correlates to the vibrational frequency [3], a

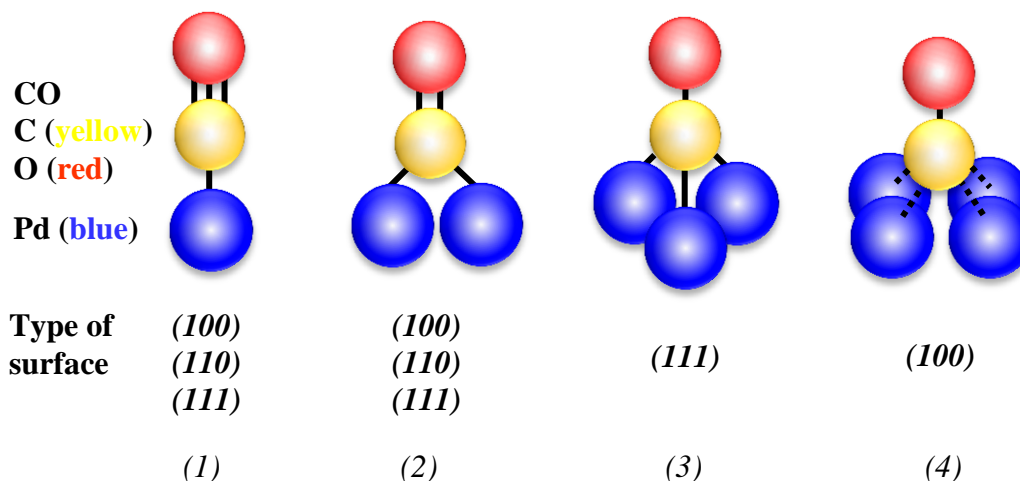


**Fig. 3.2.** Different CO adsorption sites of on the Pd surface. (1) On-top site (linear) around  $2100\text{ cm}^{-1}$ . (2) Bridge site (2f hollow), from  $1900\text{ cm}^{-1}$  to  $1990\text{ cm}^{-1}$  (depending on coverage). (3) Threefold hollow site (3f hollow), from  $1820\text{ cm}^{-1}$  to  $1890\text{ cm}^{-1}$ . (4) Four fold hollow site (4f hollow), from  $1720\text{ cm}^{-1}$  to  $1800\text{ cm}^{-1}$  (rare). The interpretation suggested by the sketch, that the CO internal bond evolves from triple to single from left to right, correlates with the observed trend of evolution of the CO frequency. However according to this sketch the CO-metal bond strength should be always stronger from left to right, whatever the metal, which is not observed : depending on metals, the site for which bonding is stronger may be any of cases (1) to (3), depending on subtle changes of geometric distances and orbital overlaps.

decrease of the vibrational frequency is observed from gas phase to adsorbed phase. As in coordination chemistry,  $2\pi^*$  overlap with the metal orbitals and back-donation to  $2\pi^*$  increase with increasing coordination number of the chemisorption site. Therefore we expect back-donation to increase in the order on-top < twofold bridge < threefold hollow. Correspondingly, the vibrational frequency should decrease in the order on-top > twofold bridge > threefold hollow. Of course such a description limited to the HOMO and LUMO orbitals does not allow for quantitative predictions. However the general trends are verified by ab initio DFT (Density Functional Theory) calculations [3, 25, 34, 35-39], with the noticeable exception of Pd(111), for which a structure with threefold hollow sites has been proposed while the CO frequency is in the range classically assigned to bridge sites [25] (Fig. 3.3b). We now discuss the Pd(111):CO structures since (111) facets are present on Pd NPs. A larger variety of structures than on Pd(100) can be found depending on coverage, as a result of CO-metal and CO-CO chemical interactions. The adsorption phases of CO/Pd(111) have been studied experimentally and theoretically by many groups [13, 24, 25, 40, 41-43]. The coordination of CO depends on coverage, as shown in Fig. 3.3.

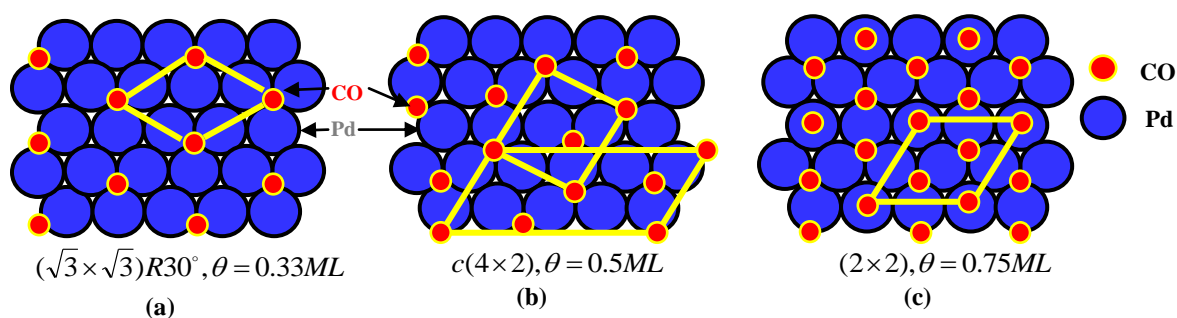


**Fig. 3.3.** Selected adsorption structures of CO on Pd(111) surface. (a)  $(\sqrt{3} \times \sqrt{3})R30^\circ$  at  $\theta = 0.33ML$  (threefold hollow sites only), (b)  $c(4 \times 2)$  at  $\theta = 0.5ML$  (threefold sites only\*), (c)  $(2 \times 2)$  at  $\theta = 0.75ML$  (threefold and atop sites). Other “compressed” structures (above 0.5 ML) combine bridge and atop sites with a rotated and decreasing unit cell. (\*from [25]. The experimental frequency is indeed that of bridge sites. Therefore the “classic” structure derived from LEED and IRAS involves only CO at equidistant bridge sites; the reasons why threefold hollow sites would appear at the frequency of bridge sites are discussed in [25]).

At small CO coverage, CO adsorbs at only threefold-hollow sites forming 2D islands with the  $(\sqrt{3} \times \sqrt{3})R30^\circ$  structure. Islands coalesce at 0.33 ML. The CO vibrational frequency varies from about  $1820 \text{ cm}^{-1}$  for zero coverage to about  $1890 \text{ cm}^{-1}$  at 0.33 ML. Above 0.33 ML the frequency shifts to  $1920 \text{ cm}^{-1}$  corresponding classically to a change of adsorption sites from threefold hollow to bridge [13]. As said above, this has been questioned by ref. [25]. The adsorption energy starts to decrease and the coverage saturates at room temperature before 0.5 ML, due to the repulsive interaction between molecules. Increase of the coverage can be obtained by “compression” in equilibrium with gas phase CO. At half-coverage, the CO arranges on the surface following a  $c(4 \times 2)$  structure as shown in **Fig. 3.3b**. Then in the range of  $\theta = 0.5$  to 0.65 ML, CO may occupy simultaneously linear and bridge sites ( $1920$ – $1970 \text{ cm}^{-1}$ ) [41, 43, 45]. At saturation ( $\theta = 0.75$ ), two strong bands at  $2110$  and  $1895 \text{ cm}^{-1}$  were observed and assigned to CO adsorbed on on-top and threefold-hollow sites [41, 43] (**Fig. 3.3c**). The primitive cell rotates so as to lower its size as coverage increases. The higher coverage of 0.75 ML can only be obtained at  $\approx 100 \text{ K}$ .

CO adsorption on Pd(100) is simpler than on Pd(111) by several aspects: only bridge sites are occupied; there is a single structure  $(2\sqrt{2} \times \sqrt{2})R45^\circ$  corresponding to 0.5 ML coverage as already mentioned in the introduction of this chapter [9, 10, 12, 24]. The structure is shown in **Fig. 3.4a**. The CO layer grows by 2D islands with local  $(2\sqrt{2} \times \sqrt{2})R45^\circ$  structure

until coalescence at 0.5 ML. Beyond this coverage, compression of the CO layer occurs by insertion of dense CO lines, instead of the more complex decrease - rotation of the unit cell and change from bridge to (linear + bridge) or to (linear + threefold) that occurs on the (111) surface. The corresponding compression structures are shown in **Fig. 3.4b**.

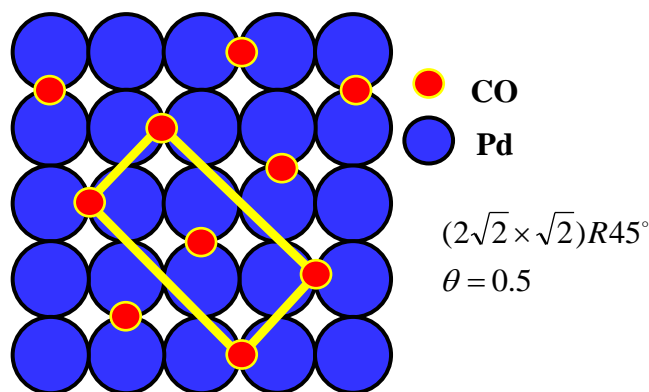


**Fig. 3.4 (a).** Adsorption phase of CO on Pd(100) surface:  $(2\sqrt{2} \times \sqrt{2})R45^\circ$  at  $\theta=0.5ML$ .

### 3.3 Experimental procedure to expose the Pd surface to CO

The Pd(100) sample is prepared by sputtering and annealing according to the preparation method given in **Chapter 2**. Then the sample is heated during 4 min under low CO pressure (below  $5 \times 10^{-11}$  mbar) in the SFG chamber in order to desorb all CO [11, 24]. The temperature required to obtain zero coverage is found around 500 K (measured by a IRcon InGaAs pyrometer), in good agreement with TPD experiments done by Bradshaw *et al.* [24]. Then we let the sample cool down for 32 min ( $\sim 60^\circ\text{C}$ ) without CO in the chamber. SFG spectra are recorded continuously after heating. After 32 min the coverage is close to 0.05 ML due to residual CO in the chamber. The CO pressure is then increased to  $2.6 \times 10^{-9}$  mbar. LEED experiments are conducted with the same timing than SFG measurements. A digital camera is used to record the LEED spot intensities every 3 min. After completion of the CO layer with the  $c(2\sqrt{2} \times \sqrt{2})R45^\circ$  structure at 0.5 ML, the CO layer is known to experience a compression that results in a smaller stability of CO. Adsorption can be continued up to 0.8 ML providing that the CO pressure is increased. Hence we have raised the pressure step by step up to  $2.2 \times 10^{-3}$  mbar. For LEED experiments the CO pressure is limited to  $1 \times 10^{-7}$  mbar.

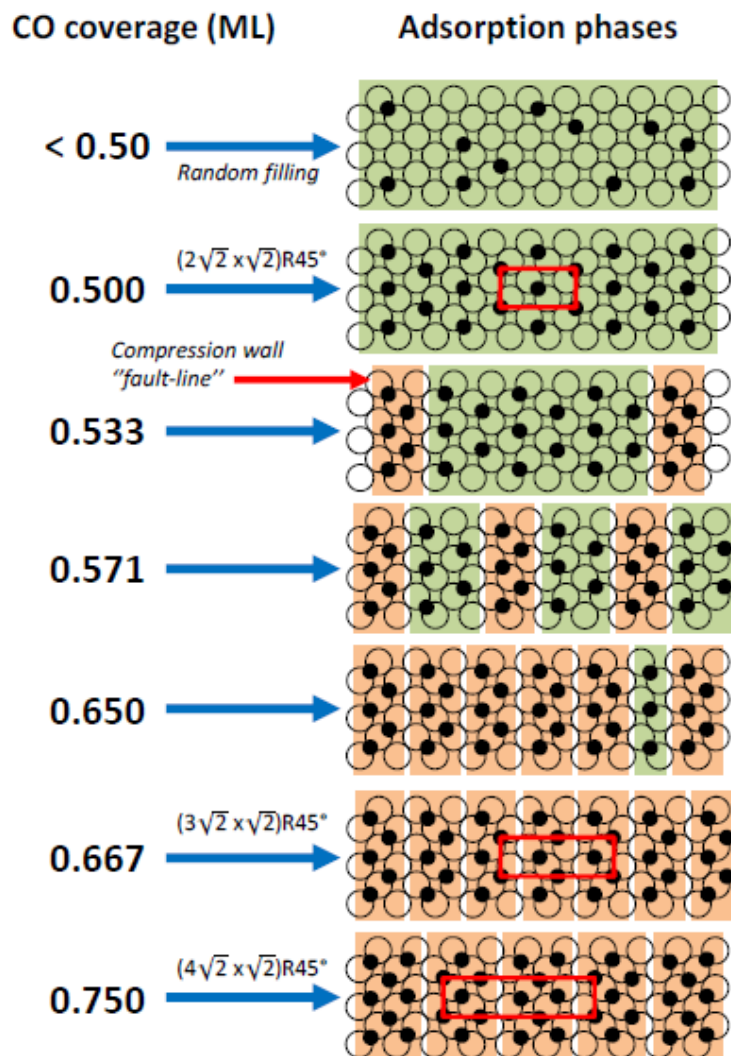


*Fig. 3.4(b): Some of the different adsorption phases and their corresponding CO coverage chosen for the fit of the SFG spectra using the dipolar interaction model. Green and orange frames correspond to uncompressed and compressed CO domains. At coverage lower than 0.5 ML, CO sites are randomly filled in the  $c(2\sqrt{2} \times \sqrt{2})R45^\circ$  adsorption phase.*

### 3.4 SFG and LEED studies of CO adsorption as a function of CO coverage

SFG spectra of CO on Pd(100) during adsorption are presented on **Fig. 3.5**. In agreement with literature [9, 10, 12, 30], we observe one band attributed to bridge bonded CO

at a frequency ranging from 1890 (singleton frequency) up to 1983  $\text{cm}^{-1}$  (compressed layer in

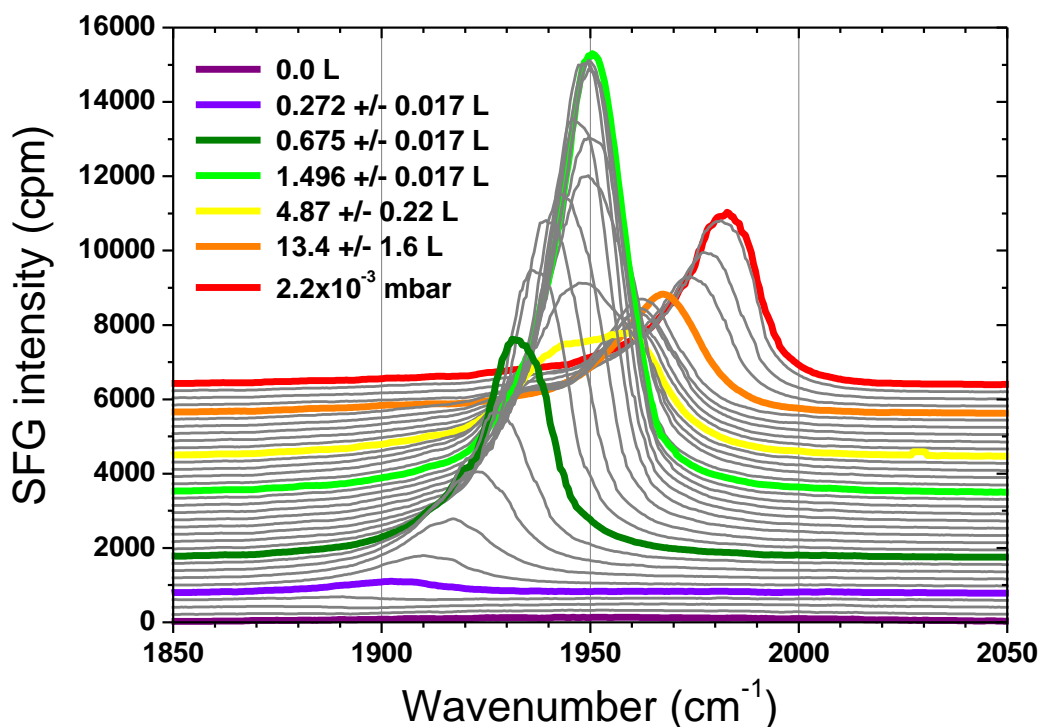


**Fig. 3.5.** SFG spectra (cpm = counts per minute) as a function of time for increasing CO coverage on Pd(100) between 0 and 13.4 L exposure. The largest coverage is obtained in equilibrium with CO gas at  $2.2 \cdot 10^{-3}$  mbar. Some spectra are enlightened with thick colored lines as guides to the eye. The green curve is closest to 0.5 ML (50 min at  $2.6 \cdot 10^{-9}$  mbar)

equilibrium with CO gas at  $2.2 \cdot 10^{-3}$  mbar) as coverage increases. The upper frequency is obtained at  $2.2 \cdot 10^{-3}$  mbar and 300 K. A close-up of the spectra between 0 and 0.272 Langmuir (L) is shown in **Fig. 3.5**. (1 Langmuir is defined as the dose that would allow to reach 1 ML with a sticking coefficient  $s = 1$ . It is obtained in 1 second under  $4.6 \cdot 10^{-6}$  mbar in the case of Pd(100)). During sample cooling from 500 K, the CO band can be detected after 10 min. **Fig. 3.6a** shows the presence of a small non resonant contribution that decreases upon CO adsorption. Clearly the interference between the NR signal arising from Pd and the resonant signal from CO requires spectrum deconvolution. The zero coverage limit of the CO singleton frequency is found at  $1890 \pm 3 \text{ cm}^{-1}$  in agreement with IRAS measurements [12]. After 50 min of exposure under  $2.6 \cdot 10^{-9}$  mbar, the CO frequency reaches  $1949 \text{ cm}^{-1}$  which is known to be the frequency of CO in  $c(2\sqrt{2} \times \sqrt{2})R45^\circ$  adsorption phase at saturation at

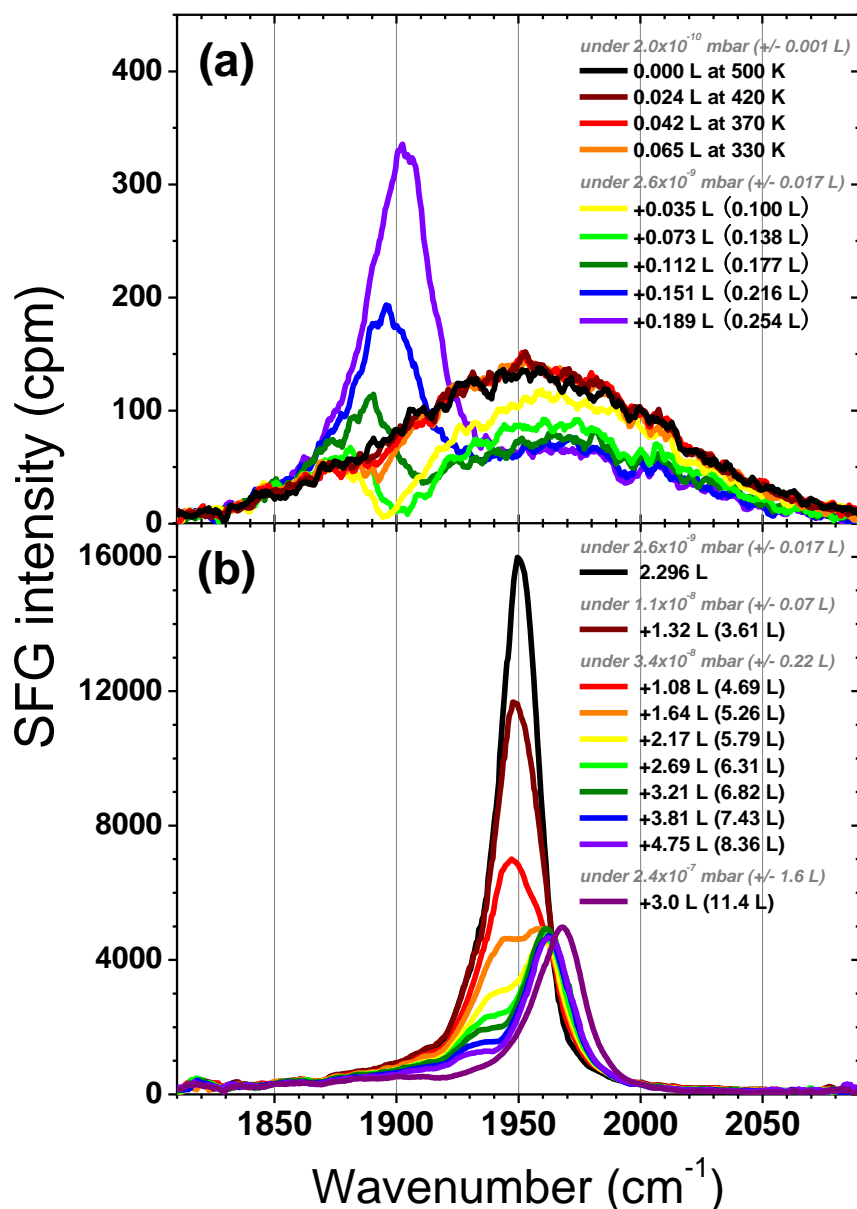


*Fig. 3.6. (a) SFG spectra at low CO exposure from 0 L, for which only the non-resonant response of the surface can be seen, to 0.272 L. In this short coverage range, the non-resonant response decreases down to a stable value. (b) SFG spectra recorded above 0.5 ML, enlightening the CO band splitting at the early stage of compression.*

room temperature corresponding to 0.5 ML [9, 12, 30]. The LEED diffraction pattern has maximal brightness and sharpness at this exposure as described below (Fig. 3.7c). The SFG intensity, which increased continuously until half-coverage, decreases abruptly after 0.5 ML, while the CO frequency keeps increasing as higher coverages are reached (Fig. 3.6b). At the early stages of compression (Fig. 3.5 and Fig. 3.6b), the CO band splits into two bands. The

higher frequency band continues to shift to the blue as the CO coverage increases. The lower frequency band which has a lower intensity continuously red-shifts from 1949 down to 1930  $\text{cm}^{-1}$  after 7.98 L of exposure. It ultimately disappears around  $\approx 1900 \text{ cm}^{-1}$  at slightly higher exposure (**Fig. 3.6b**). The experiment performed in the time domain described below confirms that the frequency decreases to such a low frequency.

**Fig. 3.7a-f** shows LEED diffraction patterns at 43 eV for different exposures (**a, b, c**: 0, 10, and 43 min under  $2.6 \times 10^{-9}$  mbar of CO). **e, f** and **g** show the LEED patterns obtained at higher pressures:  $5 \times 10^{-9}$ ,  $4 \times 10^{-8}$  and  $1 \times 10^{-7}$  mbar at equilibrium with CO gas. The contrast has been reversed in order to make spots more easily visible at low coverage. Similarly to Behm et al. [11], the electron beam has been found to desorb CO molecules from the surface; hence the sample was only facing the electron beam during the picture acquisition, i.e. 3 sec. The sample normal is nearly along the electron beam axis, which unfortunately prevents to see the  $\left\{ \pm \frac{1}{4}, \pm \frac{1}{4} \right\}$  spots of the CO overlayer [9]. **a** The diffraction pattern of Pd(100) shows the  $\{1, 0\}$  spots. Note that the electron energy of 43 eV is chosen to observe better the non-integer spots, but it has the disadvantage that the spots of Pd(100) are not bright. **b** 10 minutes after the beginning of CO adsorption, some blurry spots of the  $c(2\sqrt{2} \times \sqrt{2})R45^\circ$  diffraction pattern can be observed. **c** After an intensity rise at intermediate exposure times, the LEED maximal intensity and sharpness of the  $c(2\sqrt{2} \times \sqrt{2})R45^\circ$  diffraction pattern are reached after 43 min. This corresponds to the time at which the CO band is maximal and the CO frequency equals  $1949 \text{ cm}^{-1}$ . **d** At equilibrium under  $5 \times 10^{-9}$  mbar, the split of the  $\left\{ \pm \frac{1}{2}, \pm \frac{1}{2} \right\}$  spots indicates that the coverage is larger than 0.5 ML and that compression has started [9, 24, 30]. **e-f** By increasing further the CO pressure up to  $1 \times 10^{-7}$  mbar the splitting increases due to continuing compression.

According to the IRAS and TPD results of Bradshaw et al. [12], the CO internal stretch frequency and the IR absorbance are proportional to the coverage on the Pd(100) surface. Since SFG is a second-order non-linear optical process, its intensity is proportional to the square of the coverage, providing that the molecular hyperpolarizability is constant with coverage. Thus we expect the SFG intensity (band area) to rise quadratically with the CO band frequency. This is observed experimentally for frequencies below  $1949 \text{ cm}^{-1}$  ( $\theta < 0.5 \text{ ML}$ ). SFG and IRAS results are therefore consistent in intensity and frequency. From the linear

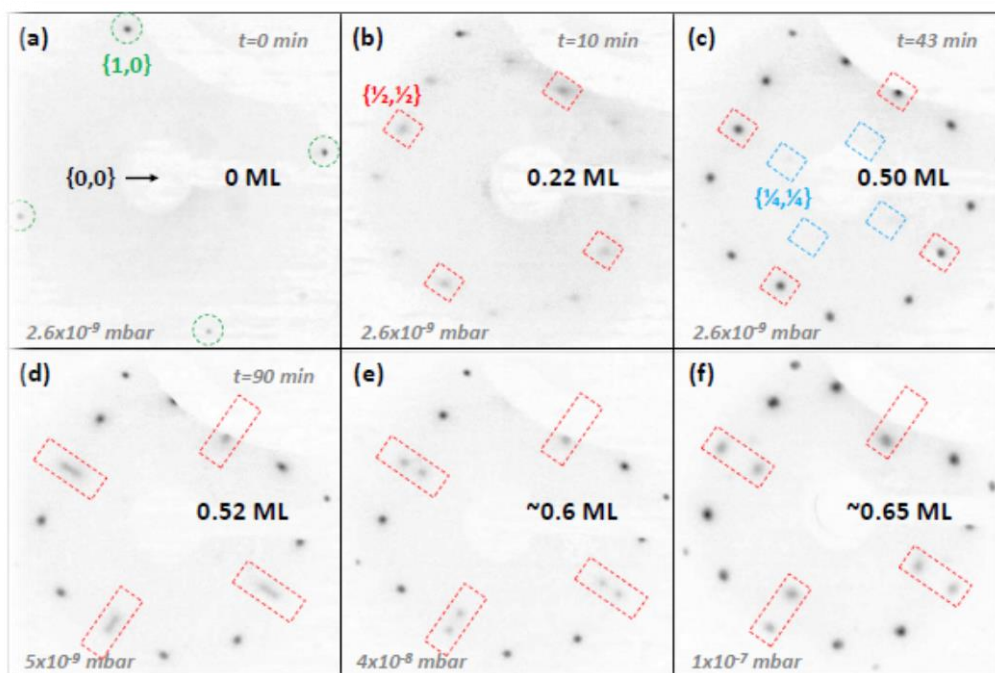


**Fig. 3.7.** LEED diffraction patterns of CO/Pd(100) at 43 eV as a function of time during CO adsorption at 300 K. (a) Pd(100) without CO. (b) and (c) under  $2.6 \times 10^{-9}$  mbar as coverage grows. (c) corresponds to the  $(2\sqrt{2} \times \sqrt{2})R45^\circ$  structure at 0.5 ML. (d-f) compressed layer in equilibrium with CO gas at the indicated pressure.  $\{1, 0\}$  and  $\{\pm \frac{1}{2}, \pm \frac{1}{2}\}$  spots are enlightened by green and red dashed frames respectively.  $\{\pm \frac{1}{4}, \pm \frac{1}{4}\}$  spots that should exist have in fact a null intensity at normal incidence. Their position is indicated by the blue dashed frames. For each LEED pattern, the estimated CO coverage is indicated.

dependence of the frequency with coverage and by using the particular point of the half-coverage at  $1949 \text{ cm}^{-1}$  where LEED provides an unambiguous signature of the coverage, we can deduce the CO coverage as a function of time (**Fig. 3.8a**) and derive the sticking coefficient  $s$  as a function of coverage as the derivative of  $\theta(t)$  [3, 11] (**Fig. 3.8b**). At the beginning, the adsorption rate is fast and the spectrum evolves during acquisition time (1 min), resulting in an uncertainty on the CO frequency (coverage) which is estimated to  $\sim 2.5 \text{ cm}^{-1}$  (0.02 ML). At higher frequency (coverage), the frequency drift is slower, hence the uncertainty is below  $1 \text{ cm}^{-1}$  (0.008 ML). The sticking coefficient at the limit of zero coverage is  $s_0 = 0.63 \pm 0.10$ . Then  $s(\theta)$  decreases from 0.5, at 0.35 ML of CO, to nearly zero at 0.5 ML. This value of  $s_0$  is in good agreement with a previous result on Pd(100) ( $s_0 \sim 0.6$ ) [11].

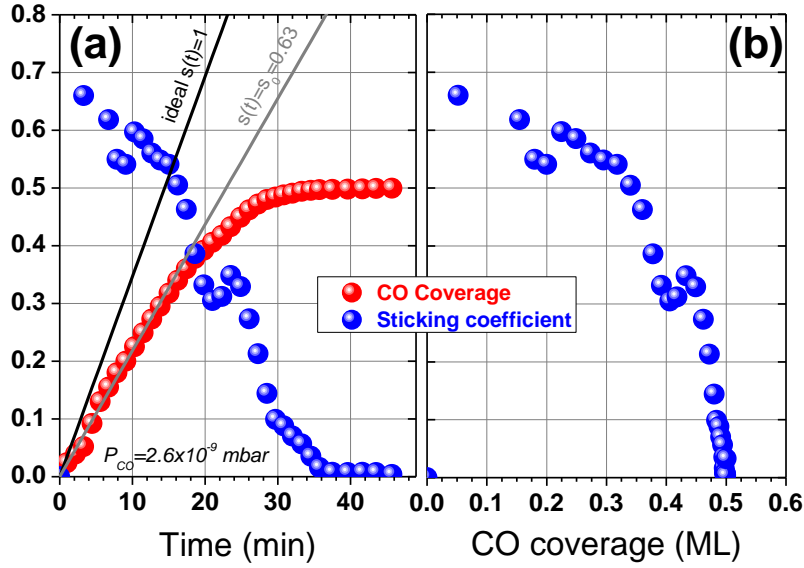


**Fig. 3.8.** (a) CO coverage  $\theta$  and sticking coefficient  $s$  as a function of the elapsed time after introduction of CO in the UHV chamber. The black and the gray thick lines correspond to  $\theta(t)$  assuming a constant sticking coefficient ( $s = 1$  and  $s = 0.63$ , respectively). (b) CO sticking coefficient deduced from (a) through the derivative of  $\theta(t)$  as a function of the CO coverage.

In **Fig. 3.9** are presented the results of SFG spectrum deconvolution by one single band below 0.5 ML and two bands above 0.5 ML, as derived from the fit to **Eq. 1.28**. We tentatively assign band “1” to uncompressed CO and band “2” to compressed CO. The central frequency, amplitude and width are plotted as a function of coverage. When the compression starts at 0.5 ML, a  $6.5 \text{ cm}^{-1}$  blue shift is observed. A frequency hop of  $\approx 11 \text{ cm}^{-1}$  has been reported previously [24]. The deconvolution confirms that the amplitude of the susceptibility is proportional to the coverage between 0 and 0.5 ML, showing that the molecular hyperpolarizability of CO is constant over this coverage range (**Fig. 3.9b**). By contrast, the susceptibility varies strongly during the compression: it decreases quickly down to zero for band 1, and it increases rapidly between 0.5 and 0.65 ML for band 2. CO half bandwidth decreases from  $\sim 14 \text{ cm}^{-1}$  at low coverage to  $9 \text{ cm}^{-1}$  at 0.5 ML. Then it increases again up to  $\sim 12 \text{ cm}^{-1}$  at 0.6 ML and finally decreases down to  $9 \text{ cm}^{-1}$  at the highest coverage (**Fig. 3.9c**): as may be expected the bandwidth is minimal for the most ordered structures. The non-resonant susceptibility  $\chi_{NR}$  and the phase difference between non-resonant and resonant signals  $\phi$  (not presented here) show a constant value across most of the coverage range, except a 20% decrease for  $\chi_{NR}$  and a 30% increase for  $\phi$  at low coverage between 0 and 0.15 ML. Both

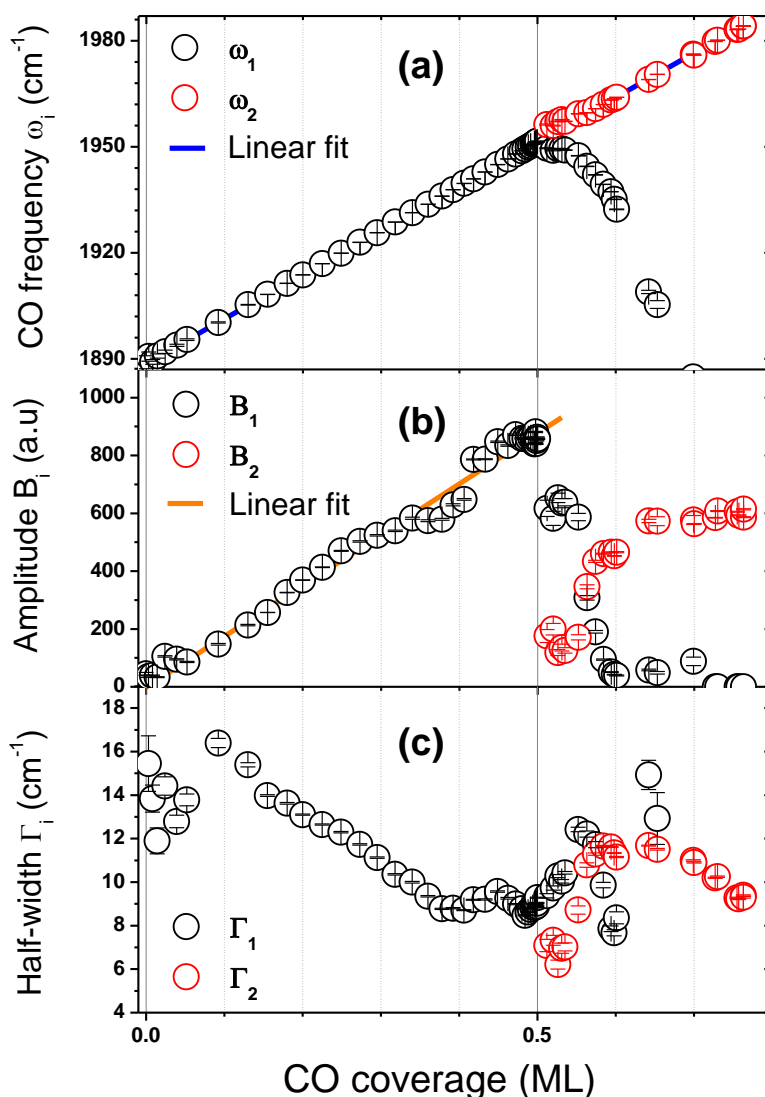


**Fig. 3.9.** Fitting parameters extracted from the SFG spectrum deconvolution using **Eq. 1.28** as a function of CO coverage. (a) CO frequencies  $\omega_i$ , (b) amplitudes  $B_i$  and (c) half-widths  $\Gamma_i$ . The black and red dots are assigned to uncompressed and compressed CO, respectively.

indicate a change of the DOS of Pd around Fermi level upon CO adsorption. The SFG intensity as a function of coverage is shown on **Fig. 3.10a**. As already pointed out the band intensity rises quadratically with CO coverage up to 0.5 ML. Some points around 0.35 ML are off the ideal  $\theta^2$  relationship. They correspond to small “accidents” of  $B_1$  and  $\Gamma_1$  (**Fig. 3.9b** and **c**) that might be related to inhomogeneous broadening. From the LEED diffraction patterns of (**Fig. 3.7**), we can plot the  $\left\{ \pm \frac{1}{2}, \pm \frac{1}{2} \right\}$  spot intensities as a function of coverage together with

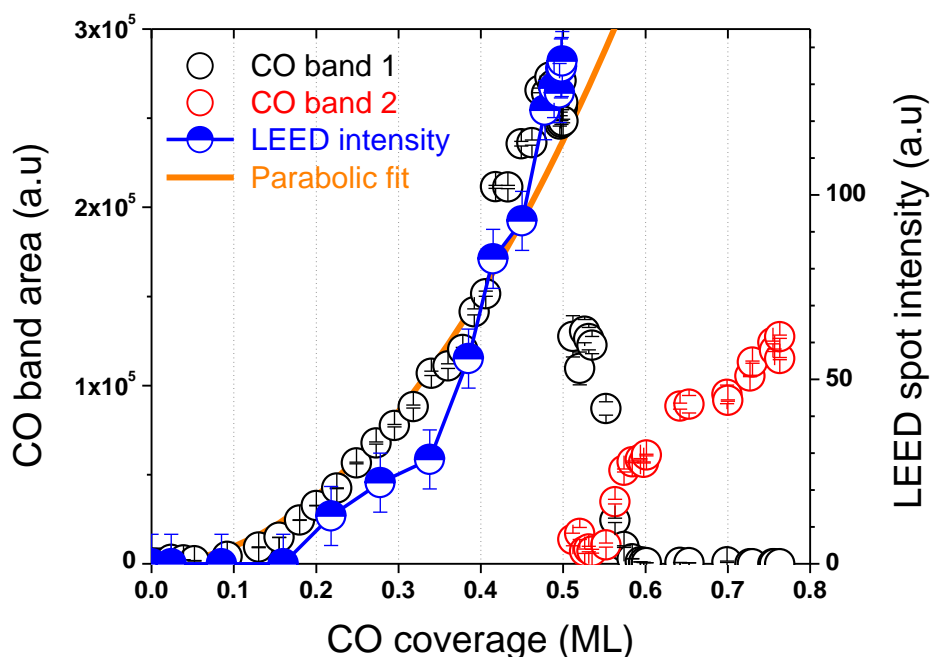


**Fig. 3.10(a).** Normalized SFG intensity for both CO bands (black and red dots) and corresponding  $\{\pm\frac{1}{2}, \pm\frac{1}{2}\}$  LEED spot intensities as a function of CO coverage (blue dots). The (orange) parabolic curve in the 0 - 0.5ML coverage range has been added to highlight the quadratical dependence of the SFG intensity of the first band.

that of SFG (**Fig. 3.10a**). Interestingly, the two curves present a similarity. A difference with SFG is that, in good agreement with the literature [11, 24], the LEED intensity starts to increase only above 0.22 ML. Below this coverage the average CO island size is too small to produce a coherent LEED pattern. After half-coverage, the SFG intensity drops very quickly by a factor 4, unlike the IRAS intensity [12] that saturates. Ortega *et al.* concluded that compression induces a linear reduction of the transition dipole moment that happens to compensate for coverage increase. Obviously, the molecular hyperpolarizability is even more affected by compression. We have tried to rationalize the evolution of the susceptibility with coverage by assuming that the molecular susceptibility depends on the compressed or uncompressed nature of the site, and that the susceptibility for each type of site is the product of the molecular susceptibility by the density of the molecules that occupy the sites. For uncompressed sites, we assume that the molecular susceptibility is not modified by compression. The coverage in the two types of sites can be derived from **Fig. 3.4b**. It is shown

in **Fig. 3.10b**. The fit of the SFG intensities to this simple model is shown in **Fig. 3.10c**. It shows a very good agreement. The molecular susceptibility for compressed sites is found to be half that of uncompressed sites. This result validates the assignment of the two bands to compressed and uncompressed sites.

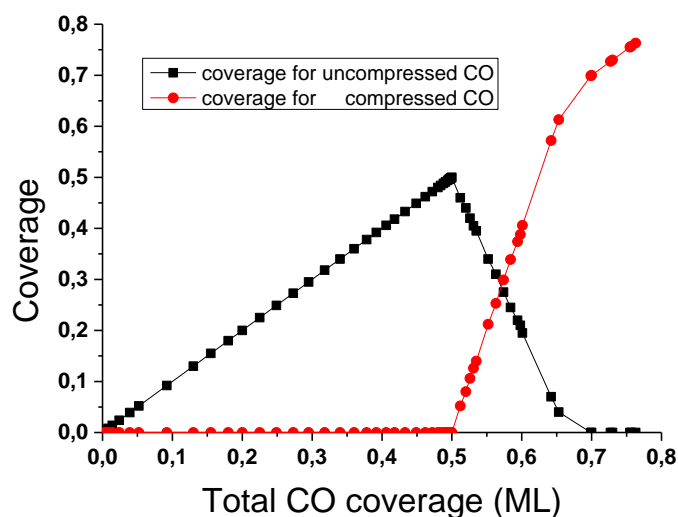


*Fig. 3.10(b). CO coverage in uncompressed and compressed adsorption sites on Pd(100).*

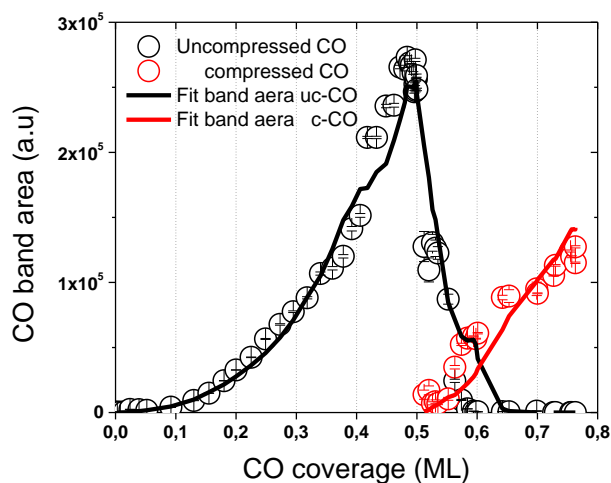


*Fig. 3.10(c). fit of the SFG band intensities of the compressed and uncompressed sites assuming that the molecular susceptibility at compressed sites is different from that at uncompressed sites.*

### 3.5 SFG results in the time domain

Measurements of the dephasing time ( $T_2$ ) have been done for coverages of 0.5 and 0.65 ML, which correspond to the saturation of the regular CO structure and to a compressed structure with few remaining uncompressed CO, respectively. A 140 fs visible pulse is time delayed with respect to the fs IR pulse. fs-fs SFG spectra are recorded for delays ranging from -600 to +1200 fs by steps of 50 fs. Spectral resolution is lost, but the experiment provides a means to measure directly the decay of the first order IR polarization (characterized by the  $T_2$  phase relaxation time) (**Fig. 1.4**). The CO coverage is controlled through the CO pressure ( $9.10^{-10}$  and  $5.10^{-8}$  mbar, respectively). The integrated SFG intensity as a function of time delay is shown in **Fig. 3.11a**. The corresponding SFG spectra recorded with a ps-VIS pulse are also shown together with their spectral fits in **Fig 3.11b**. The rise time of about 200 fs is due to the convolution of the rise times of VIS and IR pulses. At half-coverage, we observe a single exponential decay. The decay time (690 fs) and the experimental bandwidth ( $7.6 \text{ cm}^{-1}$ ) verify the relation  $T_2 \times \Gamma = 1/2\pi c$  (with  $c$  the speed of light) which is expected for a homogeneously broadened lorentzian band. By contrast a shorter dephasing time and oscillations are observed at 0.65 ML. From the SFG spectrum of **Fig. 3.11b**, the main frequency at 0.65 ML is  $\omega_2 = 1967 \pm 2 \text{ cm}^{-1}$ . The other band has a much smaller intensity, thus its actual frequency cannot be evaluated directly from the spectrum. However, the half-interference period allows a rough estimation of  $\omega_1 = \omega_2 - 1/(2c\Delta t)$ , with  $\Delta t = 220 \pm 50$  fs yielding  $\omega_1 = 1891 \pm 18 \text{ cm}^{-1}$  (**Table 3.1**). Therefore we assign these oscillations to the interference between two main frequencies (presumably that of compressed and uncompressed sites).

The above estimation is not very accurate because the pulse duration (140 fs) is not much shorter than the decay times ( $\approx 600$  and  $\approx 400$  fs). An accurate simulation has been done. It consists in four steps. (i) The induced IR polarizability of CO molecules by the IR fs-pulse is calculated in the time domain by solving the Bloch equations (**Eq. 1.14**). The two types of CO molecules are considered as independent two-state systems, each characterized by its own frequency and dephasing time. (ii) The IR polarizability is then multiplied in the time domain by the 140 fs VIS pulse for various time delays. (iii) The SFG spectra are calculated for selected delays by doing the Fourier transform of the time-dependent SFG polarization. (iv) The spectra are integrated and compared with experimental data as a

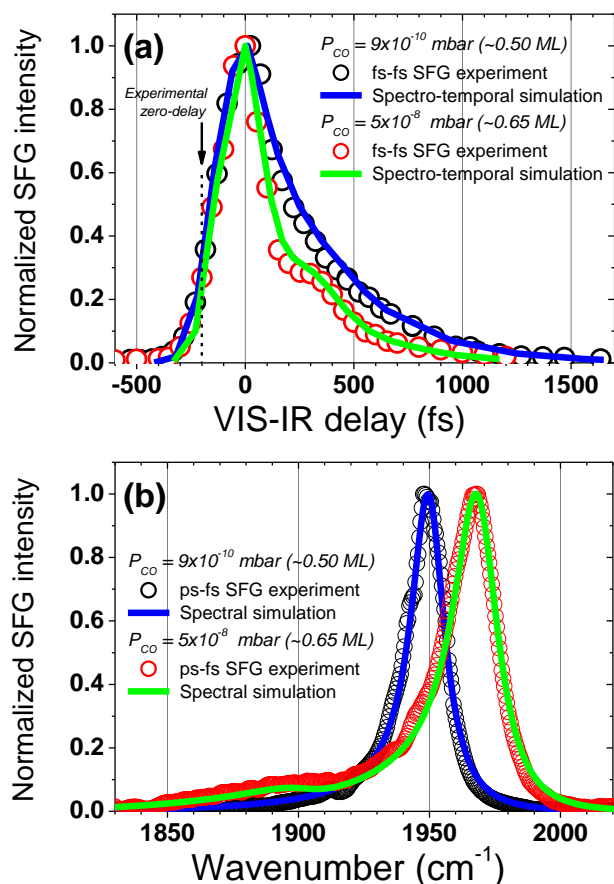


**Fig. 3.11.** (a) Normalized integrated SFG intensity as a function of the time delay between visible and IR pulses for two CO coverages of 0.5 ML and 0.65 ML, obtained in equilibrium with a CO gas at  $9 \times 10^{-10}$  (blue dots) and  $5 \times 10^{-8}$  mbar (red dots), respectively. Simulation of the fs-fs SFG intensity are represented by the thick lines. (b) Corresponding normalized experimental SFG spectra (dots) and their fits using **Eq. 1.28** (lines).

function of the VIS-IR time delay. The fit to experiment is done by trial and error. More details about this type of simulation are given later in **Chapter 6** and in [46]. The results are given in **Table 3.1**.

The striking feature concerning the weak band is that its frequency shifts quickly back to the red (down to  $1895 \text{ cm}^{-1}$ ), while the main band frequency continues to increase with coverage. These opposite trends can be rationalized easily considering dipolar coupling between molecules, which is well known to produce a frequency shift to the blue as the coverage increases. Dipolar coupling is only effective between resonant vibrations. Therefore the CO molecules in uncompressed sites decouple from the other molecules, which explains the shift to the red of the corresponding band. At 0.65 ML total coverage, the coverage in

uncompressed sites is very small ( $<0.1$  ML). Thus the shift induced by dipolar coupling is almost suppressed for uncompressed sites, while it is maximal for the compressed sites. However the large amplitude of the frequency shift is surprising. It was shown previously that dipolar coupling is not the only contribution to it [12]; in fact it accounts for less than half the shift, the rest being due to the evolution of the bonding as coverage increases (in particular the decrease of backdonation per CO molecule). However, we do observe that the frequency shifts back to the zero coverage limit, which is surprising. The explanation is probably that due to strong lateral interactions the CO molecules in the compressed structure are not located exactly on bridge sites. Preliminary VASP calculations by Sven Nave at ISMO indeed indicate that they are tilted and displaced. The observed large decrease of the phase relaxation time  $T_2$  at uncompressed sites from 690 fs to 222 fs from 0.5 ML to 0.65 ML indicates that the CO vibration is considerably more coupled to its environment in the uncompressed sites than in the compressed sites ( $T_2 = 540$  fs at 0.65 ML). This is a paradoxical result (the “regular”, uncompressed sites being more perturbed than the compressed sites).

*Table 3.1. parameters derived from the spectral fit and the spectro-temporal modeling for the two CO coverages of 0.5 and 0.65 ML : frequencies  $\omega_i$ , half widths  $\Gamma_i$ , and susceptibilities  $\beta_i$ .*

	Coverage (ML)	$\omega_1$ ( $cm^{-1}$ )	$\omega_2$ ( $cm^{-1}$ )	$\Gamma_1$ ( $cm^{-1}$ )	$\Gamma_2$ ( $cm^{-1}$ )	$\beta_1$ (a.u.)	$\beta_2$ (a.u.)
Spectral Fit	0.50	1949.5	-	7.9	-	0.96	-
	0.65	1902.0	1969.1	16.1	10.5	0.08	1
Spectro-Temporal Fit	0.50	1949.5	-	7.6 (690 fs)	-	1	-
	0.65	1895	1968	23.6 (222 fs)	9.7(540fs)	0.25	1

### 3.6 Simulation of dipolar coupling

The variation of CO frequency with coverage involves dipolar coupling, which can be simulated since it consists of electrostatic interactions between the molecular dipoles. The modeling of frequency dependence allows the determination of the relevant molecular parameters. However, as we will see below, the frequency changes also because the interaction of the molecules with the surface change with coverage. In particular back donation tends to decrease as coverage increases.

The low frequency value of the bridge band at uncompressed sites is found above to decrease down to  $1895 \text{ cm}^{-1}$ . This is very unexpected for the corresponding coverage, i.e. 0.67 ML. According to IRAS measurements made on a mixture of CO isotopes at the same coverage, the group of Bradshaw has shown that a chemical contribution of about  $55 \text{ cm}^{-1}$  to the CO internal stretch frequency shift is present in addition to the contribution of dipolar coupling [12]. Therefore if it is assumed that the dipolar coupling is negligible at 0.65 ML for uncompressed sites due to their low coverage and their large detuning from the frequency of compressed sites, the CO frequency is expected to be at least around  $1945 \text{ cm}^{-1}$ , only due to the CO - substrate interaction, i.e. much higher than the observed value. In order to understand how the CO frequency is affected by CO coverage, SFG spectra have been fitted using **Eq. 1.28** where dipole-dipole interactions between CO molecules and the chemical contribution from the Pd substrate have been included. For several decades, a classical electrostatic model has been developed for molecules on single crystal surfaces to describe dipolar interactions [26, 27, 29]. We have included the chemical contribution arising from bonding to the metallic substrate in this model by using the measurements done by Ortega *et al.* [12]. The other difference of our model is the fact that adsorption phases can be adjusted as a function of coverage. As a consequence the coverage is not anymore defined as a global constant and then dipolar coupling is no calculated for only one CO but for all molecules of the adsorption phase. We assume that we have an ordered layer of CO, thus because of vibrational interactions between adsorbates, vibrational modes cannot be described by localized vibrations and an interaction potential has to be introduced. For each CO molecules at position  $\{i, j\}$  on the surface, in the presence of an external electric field  $E$  (IR laser) and of electric fields  $-\sum_{m,n \neq i,j} u_{m,n} p_{m,n}$  radiated by neighbor CO molecules with polarization  $p_{m,n}$ , the induced polarization  $p_{i,j}$  is given by the following expression:

$$p_{i,j} = \alpha(\omega) \left( E - \sum_{m,n \neq i,j} u_{m,n} p_{m,n} \right) \quad (3.1)$$

where  $\alpha(\omega)$  is the molecular polarizability, proportional to the transition dipole moment, which is taken as [29]:

$$\alpha(\omega) = \alpha_e + \frac{\alpha_v}{1 - \left( \frac{\omega}{\omega_0 + \Delta\omega} \right)^2 \cdot (\omega + 2i\Gamma)} \quad (3.2)$$

Here  $\alpha_e$  ( $\text{\AA}^3$ ) and  $\alpha_v$  ( $\text{\AA}^3$ ) are the electronic and vibrational polarizabilities of the molecule respectively,  $\omega_0$  ( $\text{cm}^{-1}$ ) is the singleton frequency and  $2\Gamma$  ( $\text{cm}^{-1}$ ) the full-width at half-

maximum of the vibrational transition.  $\Delta\omega$  is the chemical contribution to the CO frequency shift from [12].  $u_{m,n}$  is the interaction potential or the perturbation of a surrounding molecule with  $u_{m,n}$  equals to [26, 28]:

$$u_{m,n} = \frac{1}{|r_{m,n}|^3} + \left( \frac{1}{|r_{m,n} + 2d|^3} - \frac{3|2d|^5}{|r_{m,n} + 2d|^5} \right) \quad (3.3)$$

The first term is arising from dipole-dipole interaction while the second term comes from dipole-image interaction.  $d = 0.4 \text{ \AA}$  is the distance between the CO dipole center of mass and the image plane of Pd bulk underneath [11, 28].  $r_{m,n}$  is the distance between molecules  $\{i, j\}$  and  $\{m, n\}$ . In the case of  $m = i$  and  $n = j$ , we obtain  $u_{m,n} = 0 \text{ \AA}^{-3}$ , because the perturbation coming from the image standing into the metal for a given molecule is null. This molecule-metal interaction is in fact already included in the singleton frequency, resulting from binding with Pd and dipole-image equilibrium. Typically  $u_{m,n}$  is varying between 0 and  $0.53 \text{ \AA}^{-3}$  at the maximum coverage.

All molecules are almost identical by translation, so that  $p_{i,j} \approx p_{m,n}$ . **Eq. 3.1** can be simplified as follows:

$$p_{i,j} = \frac{\alpha(\omega)}{1 + \alpha(\omega) \sum_{m,n \neq i,j} u_{m,n}} E \quad (3.4)$$

The denominator is called the local field correction term. Then we use the formalism of Cho et al. [29] to obtain from **Eq. 3.4** describing the first-order susceptibility, the perturbed second-order susceptibility  $\chi_{i,j}^{(2)}(\omega)$  for each CO molecule:

$$\chi_{i,j}^{(2)}(\omega) = \frac{B(\omega)}{\left(1 + \alpha(\omega) U_{i,j}\right) \cdot \left(1 + \alpha_e U_{i,j}\right)^2} \quad (3.5)$$

As a second order optical process,  $\chi_{i,j}^{(2)}(\omega)$  contains three local field correction terms, one at each IR, VIS and SFG frequency respectively.  $U_{i,j} = \sum_{m,n \neq i,j} u_{m,n}$  is the summed perturbation seen by each CO and  $B(\omega)$  is the molecular susceptibility.

Concerning the chemical contribution, DFT calculation would be required for a fully-consistent description of the coverage effect. Nevertheless, we introduced this contribution in a qualitative way using the experimental results of Bradshaw and coworkers [12]. The chemical contribution  $\Delta\omega$  shows a linear dependence as a function of CO coverage which can be expressed as  $\Delta\omega = 87.8x\theta$  above  $\theta = 0.575 \text{ ML}$  and  $\Delta\omega = 34.4 + 28.6x\theta$  below. In our model, this contribution has been added to the singleton frequency  $\omega_0$  in  $\alpha(\omega)$  and  $B(\omega)$ . The

chemical contribution can also be adjusted in order to be able to fit SFG spectra between 0.5 and 0.65 ML.

$U_{i,j}(\omega)$  is calculated for various coverages up to 0.77 ML over a domain of  $90 \times 90$  Pd atoms. The SFG spectrum is obtained by summing the  $\chi_{i,j}^{(2)}(\omega)$  using **Eq. 1.28** over  $30 \times 30$  sites in the center of the total domain in order to take into account the surrounding molecules at long range for a reduced calculation time. The size of this domain allows defining complex enough adsorption phase having a long-range periodicity for coverage higher than 0.5 ML. Based on the work of Berndt and coworkers [30], the width of compressed CO islands and the distance between each other are adjusted as a function of the coverage. The length of CO rows is set constant and limited by the width of the chosen domain of  $90 \times 90$  Pd atoms. In the coverage interval between two fixed adsorption phases, the adsorption phase remains identical but some of the possible sites are randomly filled with the required number of CO. For coverage below 0.5 ML, the adsorption phase remains  $c(2\sqrt{2} \times \sqrt{2})R45^\circ$ , but adsorption sites are randomly filled. We want to notice, that we have done the same calculation by using CO islands having local 0.5 ML coverage for coverages lower than 0.5 ML. The results are barely identical, random filling is preferred since, no clear indication of the island size can be deduced from the literature or from our LEED and SFG results. shows a summary of some of the possible adsorption phases for the CO coverage range explored by SFG. Finally the SFG spectrum is calculated using **Eq. 1.28** and the resonant contribution from CO molecules is replaced by **Eq. 3.5**.

In this model, the fitting parameters are the vibrational polarizability  $\alpha_v$ , the magnitude of the chemical contribution  $\Delta\omega$  and the adsorption phase corresponding to a particular coverage. The electronic polarizability  $\alpha_e$  is set to  $3 \text{ \AA}^3$ , because no strong change has been found between gas and adsorbed phase in the case of CO on various metal surface [12, 25-29]. For all coverages excepted those between 0.5 and 0.65 ML for which two CO bands are observed, the chemical contribution from the Pd surface is the value measured in the literature [12]. For this particular coverage range, according to the previous spectral and temporal observations, the value of the low CO frequency cannot be explained with the values of the chemical contribution found by Ortega *et al.* even by suppressing the dipolar coupling. As a consequence in our model, for the 0.5 - 0.65 ML coverage range, we have chosen to fix  $\alpha_v$  for both CO sites (compressed and uncompressed) at the same value than for CO at 0.5 ML and the chemical contribution was adjusted to fit the measured frequency.

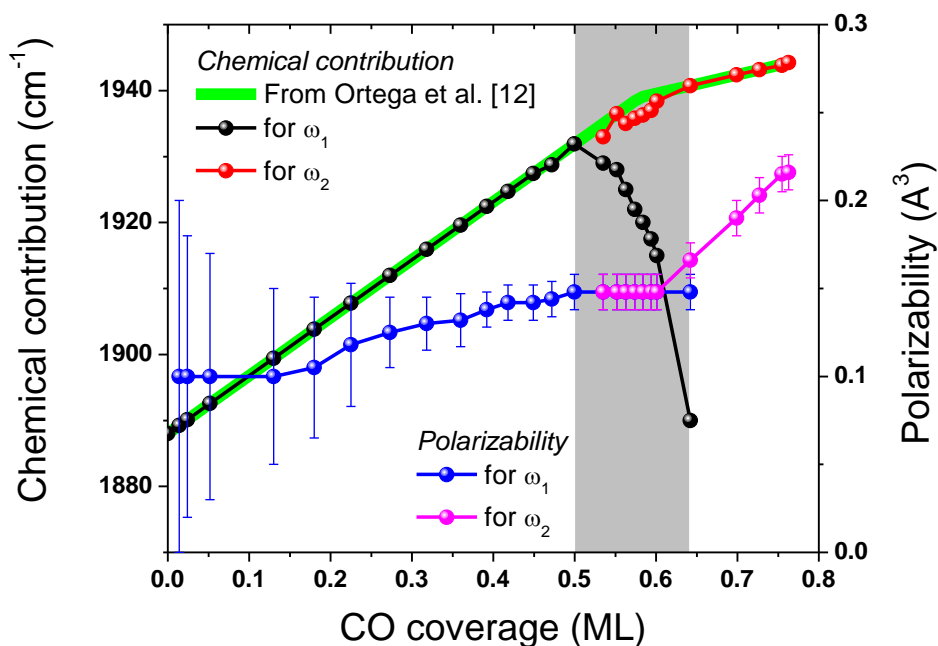


**Fig. 3.12.** CO frequency shift due to the chemical contribution (black and red) and vibrational polarizability (blue and magenta) extracted from the dipolar fit for both CO frequency  $\omega_1$  and  $\omega_2$  as a function of the CO coverage on Pd(100). The green line corresponds to the values reported by Ortega et al. [12] for the chemical contribution to the CO frequency as a function of the coverage.

**Fig. 3.12** presents the CO frequency shift from the singleton resulting from the chemical contribution alone and  $\alpha_v$  as a function of the CO coverage which was obtained after spectra fitting. The vibrational polarizability increases from  $0.1 \pm 0.05$  to  $0.22 \pm 0.01 \text{ \AA}^3$  over the total coverage range. In the 0 - 0.5 ML range, an increase by 50% is observed. As a consequence of our choice, in the 0.5 - 0.65 ML range, the vibrational polarizability is constant around  $0.15 \pm 0.01 \text{ \AA}^3$ , hence no conclusion on the effect of the compression on the molecular polarizability, i.e. the transition dipole moment, can be done. At higher coverages, the polarizability shows a linear increase by 50% presumably resulting from the compression. This result is at variance with previously reported IRAS experiments [12], that showed that above 0.5 ML, the compression induces a decrease of the transition dipole moment exactly compensated by the coverage increase, leading to a constant IRAS intensity above 0.5 ML.

Concerning the chemical contribution, in the 0.5 - 0.65 ML range, for the low frequency CO, a rapid decrease from 1930 to  $1890 \text{ cm}^{-1}$  is found, almost down to the chemical contribution for isolated CO. For the high CO frequency, the chemical contribution almost

follows the observations of Bradshaw group, but is slightly smaller. This suggests that the molecular polarizability is probably slowly increasing from  $0.15 \pm 0.01 \text{ \AA}^3$  to  $0.17 \pm 0.01 \text{ \AA}^3$  for compressed CO in this coverage range. The validity of these conclusions is based on the precision of the measurement of the chemical contribution done by Ortega *et al.* [12]. From the dipolar calculation, the increase of the polarizability above 0.5 ML is only due to the slowdown of the chemical contribution to the frequency shift. If a linear increase of the chemical contribution at the same rate than below the half-coverage would have been considered, we would have found the polarizability saturating around  $0.17 \pm 0.01 \text{ \AA}^3$  at 0.77 ML instead of  $0.22 \pm 0.01 \text{ \AA}^3$ .

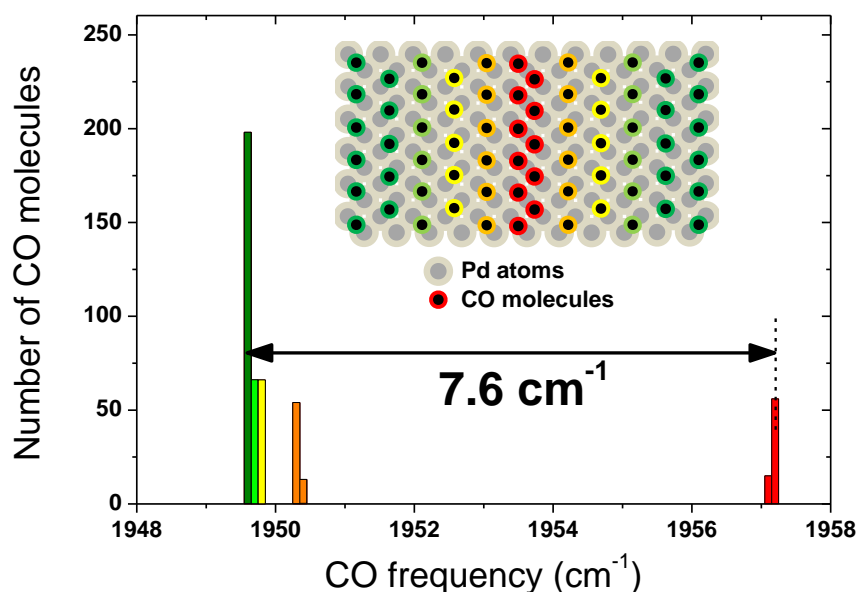


**Fig. 3.13.** Distribution of the CO internal stretch frequency around 0.52 ML on the Pd(100) surface obtained with the dipolar interaction model. The different colors from green to red correspond to increasing dipolar perturbation strength (surrounding) of the CO molecules as illustrated in insert.

From these dipolar calculations, we are able to confirm the existence of the frequency hop just above 0.5 ML that is here found to be around  $7.6 \text{ cm}^{-1}$  (**Fig. 3.13**), providing that the coverage is very close to 0.5 ML (0.52 ML). Indeed, at slightly higher coverages, CO layer compression leads to a red-shifting of the uncompressed CO while their concentration on the surface decreases. A similar value of  $6.5 \pm 1 \text{ cm}^{-1}$  was previously observed from the spectral fitting (**Fig. 3.9**). The dipolar calculation shows that this splitting is the consequence of the growth of compressed CO islands having a stronger dipolar surrounding.

### 3.7 Discussion

We have observed new features of CO adsorption when the compression occurs, which allow us to assign two bands to uncompressed and compressed CO, the two types of CO remaining on bridge sites, although most probably they are tilted and slightly displaced with respect to the actual bridge sites. Just above half-coverage, the higher CO frequency shifts by  $7.6 \text{ cm}^{-1}$ . Dipolar calculations show that this frequency hop results from the stronger dipolar interaction experienced by CO in the compressed domains. At higher coverage, a large red-shift of the lower CO frequency (down to  $1895 \text{ cm}^{-1}$ ) is clearly observed. Measurement of the polarization decay confirms that the two types of CO experience very different couplings to the surface as shown by  $T_2$  times that differ by nearly a factor of 3. From the dipolar interaction calculations, it is found that for the uncompressed CO the decrease of dipolar interaction is not sufficiently large to explain such a low frequency. There must be a strong chemical contribution of  $\approx 50 \text{ cm}^{-1}$ . It is unexpected that compressed and uncompressed CO frequencies experience opposite chemical shifts, since this shift is believed to be related to a decreasing back-donation to  $2\pi^*$  CO orbitals as the total coverage increases. Obviously it is not a simple matter of sharing the electron density between all CO molecules. Indeed, from Ortega *et al.* [12], the chemical contribution to the CO frequency blue-shift with coverage is attributed to the decrease of the amount of the charge transfer from the metal to the molecule due to a stronger competition between CO molecules. Although both types of CO molecules are thought to remain in bridge sites, the both of them experience different environments and strong interactions with neighboring molecules. It would be surprising if the molecules in the compressed domains would not be displaced and probably tilted with respect to the regular site due to repulsion from the neighboring compressed area, presumably contributing to a change of the local electronic density of states. If we can reasonably expect strong changes for compressed domains in comparison with uncompressed ones, the latter are in fact the most perturbed by the layer compression. In the light of our findings, we propose that in the early stages of compression, the charge transfer competition is more favorable for the uncompressed CO leading to the red-shift of the low frequency band. This is consistent with the slower increase of the frequency shift due to the chemical contribution for compressed CO.

### 3.8 Conclusion

CO adsorption on Pd(100) at room temperature has been revisited by SFG spectroscopy and LEED from very low coverages up to 0.77 ML. In the 0 - 0.5 ML coverage range IRAS results are confirmed. The CO frequency is shifted from the singleton frequency at  $1890\text{ cm}^{-1}$  up to  $1949\text{ cm}^{-1}$  at half-coverage as a result of dipolar coupling and chemisorption change with coverage. Above saturation of the unique  $c(2\sqrt{2} \times \sqrt{2})R45^\circ$  adsorption phase at 0.5 ML, compression of the layer leads to two new features when observed using the SFG technique: (i) the anomalous IRAS intensity variation with coverage (saturation) corresponds to a strong decrease of SFG intensity by a factor 4. It is most probably due to a decrease by a factor of 2 of the molecular polarizability at compressed CO sites. (ii) The CO band splits into two components in a narrow coverage range, that we assign to compressed and uncompressed CO molecules. The frequency of uncompressed CO shifts to the red from 1949 at 0.5 ML down to  $1895\text{ cm}^{-1}$  at 0.65 ML while that of compressed CO shifts normally to the blue. The large amplitude of these shifts cannot be explained by dipolar coupling alone. The two bands are also observed in the time domain, revealing that the two types of CO molecules experience very different coupling strength with their environment:  $T_2$  at uncompressed sites is nearly 3 times shorter than at compressed sites. This suggests that chemisorption, including charge transfer from the surface, differ strongly for uncompressed and compressed CO.

DFT calculations by Sven Nave from ISMO using VASP code are in progress for several CO coverages of 0.5 ML and above in order to study the effect of compression on the local geometry, the optical response of the molecules and the charge transfer between CO and Pd. Preliminary results confirm that CO in the compressed domains are indeed tilted and displaced with respect to the surface normal.

## References:

- [1] G. Mahan and A. Lucas, *J. Chem. Phys.* 68, 1344 (1978).
- [2] C. Olsen and R. Masel, *Surf. Sci.* 201, 444 (1988).
- [3] K. Kolansinski, *Introduction to Surface Science: Foundations of Catalysis and Nanoscience* (Wiley, 1994).
- [4] G. Pacchioni, S.-C. Chung, S. Krüger, and N. Rösch, *Surf. Sci.* 392, 173 (1997).
- [5] F. Gao, S. McClure, Y. Cai, K. Gath, Y. Wang, M. Chen, Q. Guo, and D.W. Goodman, *Surf. Sci.* 603, 65 (2009).
- [6] S. McClure and D. Goodman, *Chem. Phys. Lett.* 469, 1 (2009).
- [7] F. Vidal, A. Tadjeddine, C. Humbert, L. Dreesen, A. Peremans, P. A. Thiry, and B. Busson, *J. Elect. Chem.* 672, 1 (2012), ISSN 1572-6657.
- [8] G. Blyholder, *J. Phys. Chem.* 68, 2772 (1964).
- [9] J. C. Tracy and P. W. Palmberg, *J. Chem. Phys.* 51, 4852 (1969).
- [10] R. Behm, K. Christmann, G. Ertl, M. Van Hove, P. Thiel, and W. Weinberg, *Surf. Sci.* 88, L59 (1979).
- [11] R. J. Behm, K. Christmann, G. Ertl, and M.A. Van Hove, *J. Chem. Phys.* 73, 2984 (1980).
- [12] A. Ortega, F. Hoffman, and A. Bradshaw, *Surf. Sci.* 119, 79 (1982).
- [13] J. Szanyi, W. K. Kuhn, and D. W. Goodman, *J. Vac. Sci. Technol. A* 11, 1969 (1993).
- [14] X. Xu, P. Chen, and D. Goodman, *J. Phys. Chem.* 98, 9242 (1994).
- [15] C. Goyhenex, M. Croci, C. Claeys, and C.R. Henry, *Surf. Sci.* 352, 475 (1996).
- [16] D. Rainer, C. Xu, P. Holmblad, and D. Goodman, *J. Vac. Sci. Technol. A* 15, 1653 (1997).
- [17] T. Dellwig, J. Hartmann, J. Libuda, I. Meusel, G. Rupprechter, H. Unterhalt, and H.-J. Freund, *J. Mol. Cat. A* 162, 51 (2000).
- [18] G. Haas, A. Menck, H. Brune, J. V. Barth, J. A. Venables, and K. Kern, *Phys. Rev. B* 61, 11105 (2000).
- [19] S. Bertarione, D. Scarano, A. Zecchina, V. Johanek, J. Hoffmann, S. Schauer mann, M. M. Frank, J. Libuda, G. Rupprechter, and H.-J. Freund, *J. Phys Chem. B* 108, 3603 (2004).
- [20] H. Borchert, B. Jürgens, V. Zielasek, G. Rupprechter, S. Giorgio, C. Henry, and M. Bäumer, *J. Catal.* 247, 145 (2007).
- [21] A. Desikusumastuti, M. Happel, Z. Qin, T. Staudt, Y. Lykhach, M. Laurin, S. Shaikhutdinov, F. Rohr, and J. Libuda, *J. Phys. Chem. C* 113, 9755 (2009).

- [22] H. Abbott, A. Aumer, Y. Lei, C. Asokan, R. Meyer, M. Sterrer, S. Shaikhutdinov, and H.-J. Freund, *J. Phys. Chem. C* 114, 17099 (2010).
- [23] J. Flores-Camacho, J.-H. Fischer-Wolfarth, M. Peter, C. Campbell, S. Schauerermann, and H.-J. Freund, *Phys. Chem. Chem. Phys.* 13, 16800 (2011).
- [24] A. Bradshaw and F. Hoffman, *Surf. Sci.* 72, 513 (1978).
- [25] D. Loffreda, D. Simon, and P. Sautet, *Surf. Sci.* 425, 68 (1999).
- [26] B. Persson and R. Ryberg, *Phys. Rev. B* 24, 6954 (1981).
- [27] B. Persson and F. Hoffmann, *J. Chem. Phys.* 88, 3349 (1987).
- [28] H. Kato, H. Okuyama, S. Ichihara, M. Kawai, and J. Yoshinobu, *J. Chem. Phys.* 112, 1925 (2000).
- [29] M. Cho, C. Hess, and M. Bonn, *Phys. Rev. B* 65, 1 (2002).
- [30] W. Berndt and A. Bradshaw, *Surface Science Letters* 279, 165–169 (1992).
- [31] B. Shan, Y. Zhao, J. Hyun, N. Kapur, J. Nicholas, and K. Cho, *J. Phys. Chem. C* 113, 6088 (2009).
- [32] M. Peter, J. Flores-Camacho, J.-H. Fisher-Wolfarth, S. Adamovsky, S. Schauerermann, and H.-J. Freund, 28th European Conference On *Surface Science* (2011).
- [33] M.D. Alvey, M.J. Dresser and J.T. Yates Jr, *Surf.Sci.* 165, 147, (1986)
- [34] F. Abild-Pedersen and M.P. Andersson, *Surface Science* 601, 1747–1753, (2007)
- [35] K. Zorn, S. Giorgio, E. Halwax, C.R. Henry, H. Grönbeck, and G. Rupprechter, *J. Phys. Chem. C*, 115, 1103–1111 (2011)
- [36] I. Bakó, R. Schennach and G. Pálinkás, *Journal of Physics. Conference Series* 100, 052067, (2008)
- [37] C. J. Zhang and P. Hu, *J. Am. Chem. Soc.*, 123, 1166 (2001)
- [38] A. Föhlisch, M. Nyberg, P. Bennich, L. Triguero, J. Hasselström, O. Karis, L.G.M. Pettersson, and A. Nilsson, *J. Chem. Phys.* 112, 1946, (2000)
- [39] P. Hu, D.A. King, M.-H. Lee and M.C. Payne, *Chem. Phys. Lett.* 246, 73, (1995)
- [40] H. Unterhalt, P. Galletto, M. Morkel, G. Rupprechter, and H.-J. Freund, *phys stat sol* 188 No.4 1495 (2001)
- [41] M. Tüshaus, W. Berndt, H. Conrad, A.M. Bradshaw and B. Persson. *Appl. Phys. A* 51, 91 (1990)
- [42] H. Unterhalt, G. Rupprechter, and H.-J. Freund. *J. Phys. Chem. B.* 106, 356 (2002)
- [43] W. K. Kuhn, J. Szanyi, and D.W. Goodman. *Surf. Sci. Lett.* 274, L611 (1992)
- [44] T. Dellwig, G. Rupprechter, H. Unterhalt, and H.-J. Freund, *Phys. Rev. Lett* 85, 776 (2000)

[45] M. Tüshaus, Ph.D. thesis, Free University Berlin, (1990)

[46] F. Fournier, W. Zheng, S. Carrez, S. Dubost, and B. Bourguignon, *J. Chem. Phys.* 121, 4839 (2004).



# Chapter 4

## Study of CO adsorption on Pd nanoparticles

<b>4.1. Introduction</b>	92
<b>4.2. CO adsorption on Pd NP/MgO/Ag(100)</b>	92
<b>4.3. SFG experiments of CO adsorbed on Pd NP: Size effect of NP</b>	93
<b>4.4 Calculations of single CO adsorption on Pd NPs</b>	99
<b>4.5. Effect of CO adsorption on non-resonant contribution</b>	101
<b>4.6. SFG spectra of CO adsorption on Pd nanoparticles at high CO pressure</b>	103
<b>4.7. Conclusion</b>	104
<b>Reference</b>	105

## 4.1. Introduction

In this chapter we apply SFG vibrational spectroscopy to study the adsorption of CO on Pd NPs / MgO / Ag(100) as a function of size. Preparation and shape of NPs have been introduced in **Chapter 2**. Adsorption of CO on Pd(100) studied in **Chapter 3** will serve as a point of comparison. Preliminary DFT calculations done by Carine Michel at ENS Lyon are also presented and help understand the experimental results.

## 4.2. CO adsorption on Pd NP/MgO/Ag(100)

As mentioned in **Chapter 2**, the shape of Pd NPs on MgO is well documented. A sketch of a Pd NP / MgO / Ag(100) sample is shown in **Fig. 4.1**. The geometrical structure of NP includes: a top (100) terrace, (111) facets on the border, edges between facets, corners; in addition defects may be present. In the case of single crystals all the sites except for the “normal” ones located on the terraces are defects, e.g. the edges of steps, adatoms and missing atoms, are defects. In the case of NPs, the edges are not called defects. Defects are the sites induced by the imperfection of the shape, e.g. missing atoms, ad-atoms on terraces and edges. The density of defects on NPs is expected to come from the imperfect NP growth and be larger than on single crystals.

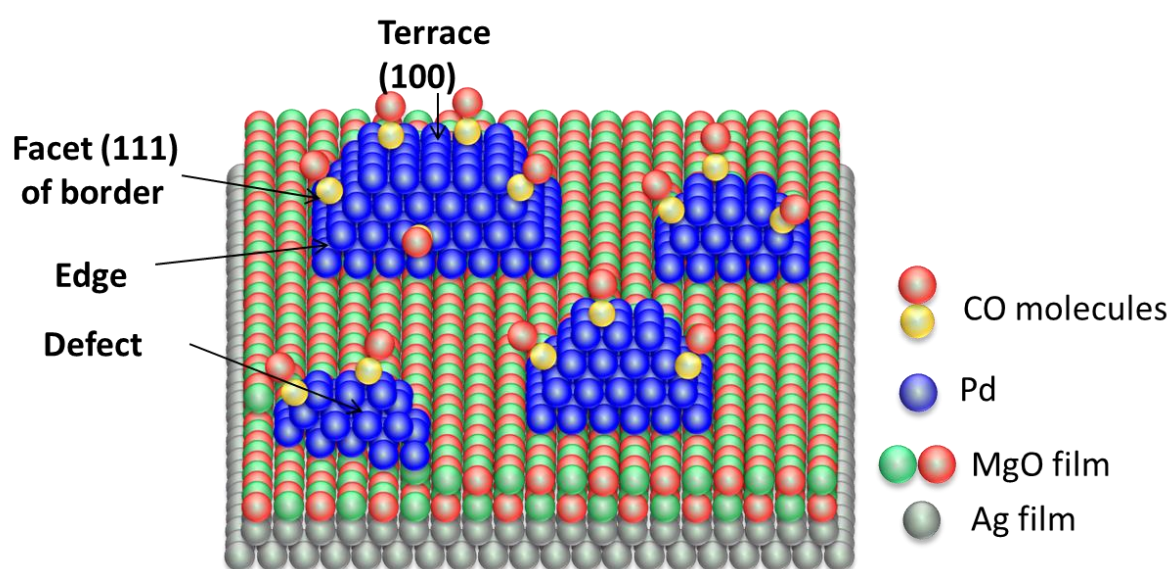


*Fig. 4.1. Sketch of the Pd NP / MgO / Ag(100) system.*

There are three types of CO adsorption sites on Pd surface: threefold hollow, bridge and on-top sites, (**Fig. 3.2 Chapter 3**), but on Pd NP the threefold hollow site is not observed. According to [1, 2], the CO adsorption on Pd NP / MgO(100) at low pressure ( $<10^{-3}$  mbar at 300 K) exhibits a band that shifts with CO coverage from 1890 to 1960  $\text{cm}^{-1}$  and a band at 2050  $\text{cm}^{-1}$ . The two bands correspond to CO adsorption on bridge and on-top sites, respectively. According to [3] at higher pressure ( $\geq 10^{-3}$  mbar at 300 K) CO adsorption on Pd NP/MgO(100) can exhibit another on-top band at 2090  $\text{cm}^{-1}$ . It is tempting to assign the bridge sites to the (100) facets and the linear sites to the other sites that do not exist on Pd(100), but this is too simplistic. Since on (100) terraces there is only CO adsorption on bridge sites, at least part of the bridge sites are located on the (100) facets, but there can also be bridge sites on (111) facets and/or edges or defects of the NP. By contrast, the on top adsorption can be only on (111) facets, edges and on defects.

Adsorption of CO on Pd NPs with (111) facets has also been investigated (for example on  $\text{Al}_2\text{O}_3$ ). The morphology of the Pd NP is dominated by (111) facets which are located both on the top and on the borders of the NPs, with a small contribution of (100) facets [4]. The spectra are different from on single crystal (111) surface: the bridge CO band is accompanied by a significant on-top CO band, and the threefold-hollow CO adsorption is not found [4, 5]. With a pressure varying from  $10^{-7}$  to 200 mbar, the CO adsorption on 6 nm Pd NP exhibits a bridge band whose frequency ranges from 1970  $\text{cm}^{-1}$  to 1990  $\text{cm}^{-1}$ . The on-top band appears at 1 mbar pressure, and does not change its frequency with the variation of CO pressure [4].

### **4.3. SFG experiments of CO adsorbed on Pd NP: NP size effect**

The experimental protocol of CO adsorption on Pd NPs is the following: 1) Heat the sample to about 500 K; 2) Increase the CO pressure to  $1.3 \times 10^{-9}$  mbar into the SFG UHV chamber while recording continuously SFG spectra. 3) When the surface is saturated by CO, higher pressure from  $1 \times 10^{-8}$  to  $1 \times 10^{-3}$  mbar of CO are introduced step by step in order to reach higher coverage. The SFG spectra of CO adsorbed on Pd NPs with different NP sizes are shown in **Fig. 4.2**.

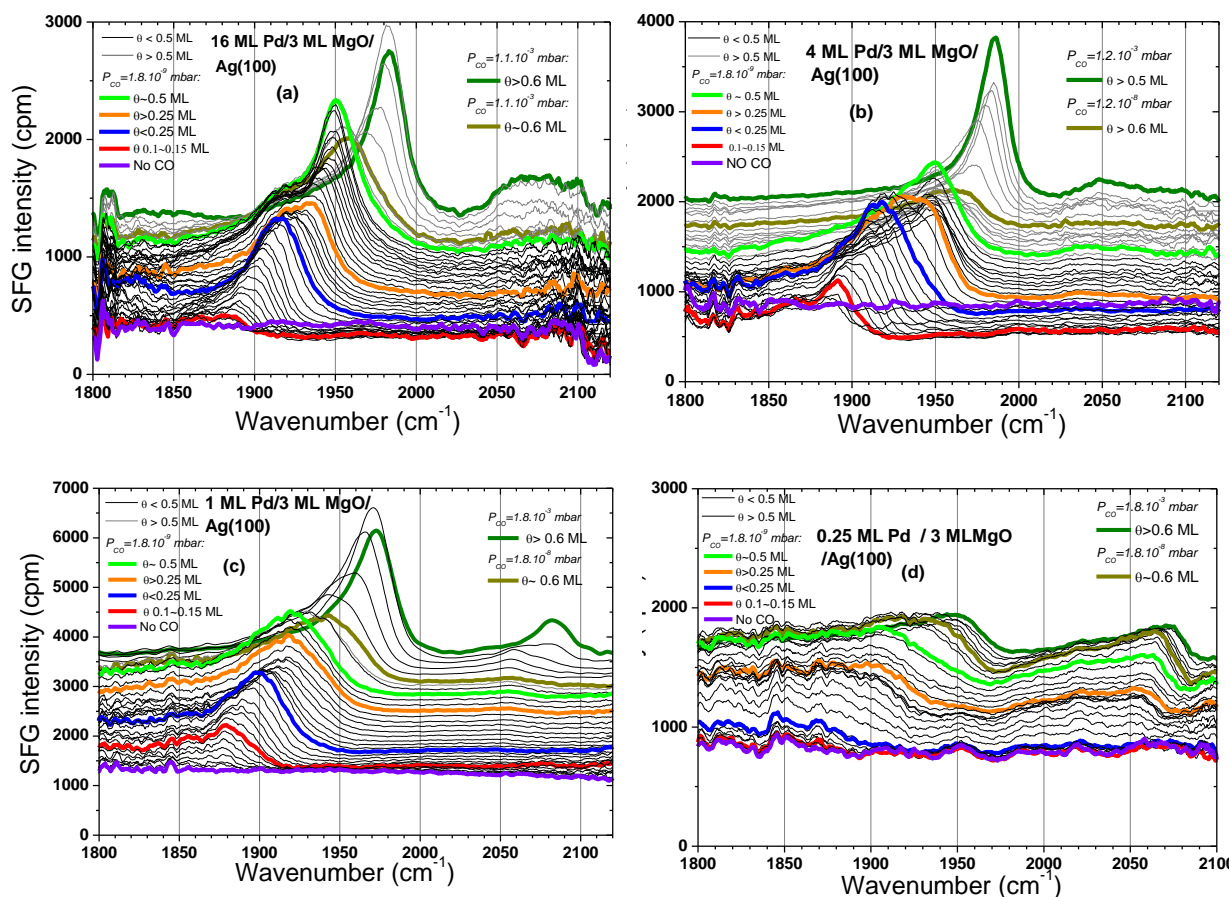


**Fig. 4.2.** SFG spectra recorded during CO adsorption on Pd nanoparticles with different equivalent thicknesses of Pd supported on 3 ML of MgO on Ag(100): (a) 16 ML of Pd; (b) 4 ML of Pd; (c) 1 ML of Pd; (d) 0.25 ML of Pd. All spectra are normalized using their reference spectrum.

In **Fig. 4.2a**, the series of CO adsorption SFG spectra on 16 ML of Pd is very similar to the CO adsorption on Pd(100) crystal shown in **Fig. 3.5** (See Chapter 3), as expected since the NPs coalesce for 16 ML equivalent thickness of Pd. The frequency of SFG intensity at 0.5 ML CO coverage (green) also agrees with CO adsorption on Pd(100). This indicates that the properties of adsorption sites of the (100) facets of the coalesced NP is similar to the ideal Pd(100) surface (as may be expected) [5]. A difference is that the peak intensity is smaller by 80% and the bandwidth is larger by 100%, reflecting an (expected) lower quality of (100) terraces of the coalesced layer with respect to the single crystal. The CO band maximum frequency under  $10^{-3}$  mbar of CO is  $1985\text{ cm}^{-1}$ , compatible within experimental uncertainty to that ( $1983\text{ cm}^{-1}$ ) found in the case of Pd(100). Besides the broadening of the bridge band, defects inherent to coalescence are responsible for the appearance of a small fraction of CO on on-top adsorption sites.

CO adsorption on a deposit of 4 ML of Pd shown in **Fig. 4.2b** looks very similar to the 16 ML case. Indeed the singleton frequency is at  $1884\text{ cm}^{-1}$ , the 0.5 ML peak frequency and maximum frequency under  $10^{-3}$  mbar of CO do not differ much as compared with the case of 16 ML. It shows that for 4 ML of Pd, CO adsorption properties remain little changed compared to the case of 16 ML of Pd or even to the single crystal, although the (100) terrace size has decreased to  $\approx 5.6\text{ nm}$  (See **Table 2.4, Section 2.3.5**). The only difference is observed at half-coverage for which the maximal bridge intensity is smaller than in the case of Pd(100).

In the case of CO adsorption on 1 ML of Pd presented in **Fig. 4.2c**, the singleton frequency has decreased by  $12\text{ cm}^{-1}$  ( $1878\text{ cm}^{-1}$ ) with respect to the singleton frequency on Pd(100). The CO maximal frequency at  $10^{-3}$  mbar ( $1972\text{ cm}^{-1}$ ) has decreased by  $13\text{ cm}^{-1}$  with respect to Pd(100). The intensity maximum at 0.5 ML has almost completely disappeared. The fraction of CO on atop sites is larger, because these sites are expected to be located at edges, and the ratio of edge atoms with respect to terrace atoms increases from 0.9 to 1.5 as the size decreases from 4 ML equivalent Pd height to 0.5 ML.

For CO adsorption at 0.25 ML Pd nanoparticles, the spectrum changes completely. Its overall intensity is significantly smaller. Two bands of similar intensity coexist. Their undeconvoluted frequencies redshift from  $\approx 1870$  to  $\approx 1850\text{ cm}^{-1}$  (bridge sites) and  $\approx 2050$  to  $\approx 2075\text{ cm}^{-1}$  (linear sites). The shape of the bands is much different from that at larger size, indicating that the phase of the non resonant contribution has changed. The size of these NPs is much smaller than that of the 1 ML Pd deposit. The number of atoms is about 170. That SFG has enough sensitivity to observe CO on such small objects is a good surprise. From the number of Pd atoms, the number of adsorbed molecules should be roughly 2.5 times smaller than for the 1 ML deposit, corresponding to a SFG signal 6.3 times smaller. If the aspect ratio was the same as for larger sizes, the height would be 1 single ML. For such small NPs, it has been reported that the shape changes. In fact it is believed that below 1 ML of Pd, the diameter/height aspect ratio of the nanoparticles decreases rapidly from 4 to 2. The singleton frequency is found at  $1868\text{ cm}^{-1}$ . Similarly to 1 ML of Pd, the on-top CO frequency increases with pressure. The widths of the CO bands are large ( $76\text{ cm}^{-1}$ ) differing from the narrow CO band on the Pd(100) surface ( $20\text{ cm}^{-1}$ ) and for Pd NPs of equivalent thickness larger than 1 ML. The broadening is probably inhomogeneous and may be due to a large NP size distribution. Indeed for such low Pd deposit, corresponding to short deposition duration ( $\sim 37$  sec), the growth regime is still the nucleation one [15], for which small aggregates of Pd can

still diffuse from low adsorption energy sites leading to a large NP size distribution with higher defect density.

The fact that the maximal intensity of bridge sites at 0.5 ML is less and less apparent as NP size decreases can be rationalized. In **Chapter 3** we have shown that it is related to a decrease by a factor of 2 of the molecular susceptibility of CO at compressed sites. Typically a number of the compressed structures described in **Fig. 3.12** correspond to large cells extending over a distance up to 3 nm. Therefore these structures cannot exist for small NPs. At 4 ML the size of the square of the truncated pyramid is already not large enough to support more than one or two cells (**Table 2.4**). For smaller NPs it decreases to  $\approx 3.5$  nm at 1 ML,  $\approx 2.8$  nm at 0.5 ML, and 1.2 nm at 0.25 ML (if the NP shape was the same at 0.25 ML).

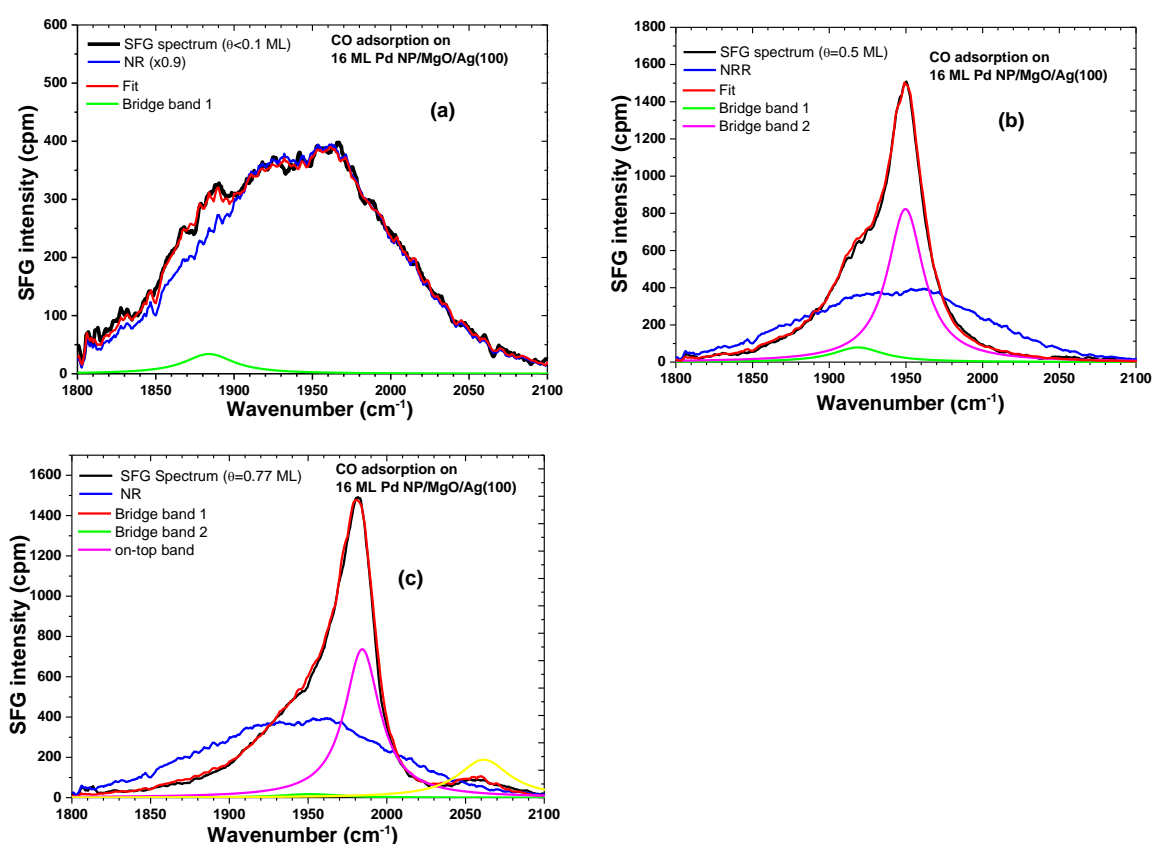


**Fig. 4.3** Deconvolution of SFG spectra of CO adsorbed on a 16 ML Pd layer (coalesced NPs) / 3 ML MgO / Ag(100) at: (a) limit of detection ( $\approx$  singleton frequency); (b) 0.5 ML (saturation of (100) terraces); (c) 0.77 ML (compression at  $10^{-3}$  ML). The black and red curves are the measured and fitted SFG spectra, the blue is the NR signal (shape of the IR spectrum), green, pink and yellow curves are the CO bands.

Therefore for our smaller NPs compression cannot correspond to the same structures as for Pd(100): the progressive disappearance of the intensity decrease above 0.5 ML

corresponds probably to the disappearing of any order above 0.5 ML, or to the change of the compressed CO layer structure. In all the cases, the facet (111) is too small to reflect the properties of a ideal (111) surface.

Although the spectra in **Fig. 4.2** are normalized to spectra of the ZnSe reference, the parameters should be extracted by a deconvolution of the spectra using **Eq. 1.28**. **Fig. 4.3** shows the deconvoluted CO SFG spectra on 16 ML Pd coalesced layer at near zero, 0.5 ML and 0.77 ML coverages.

As shown in **Fig. 4.3a** (near zero coverage), the deconvoluted parameters involve a single CO band at  $1884.8\text{ cm}^{-1}$ , with a band width of  $24.8\text{ cm}^{-1}$ . In **Fig. 4.3b** (0.5 ML coverage), the principal (pink) band at  $1949.7\text{ cm}^{-1}$  with a bandwidth of  $14.3\text{ cm}^{-1}$  is assigned to normal sites on (100) facets. This band is narrower than the CO singleton band because

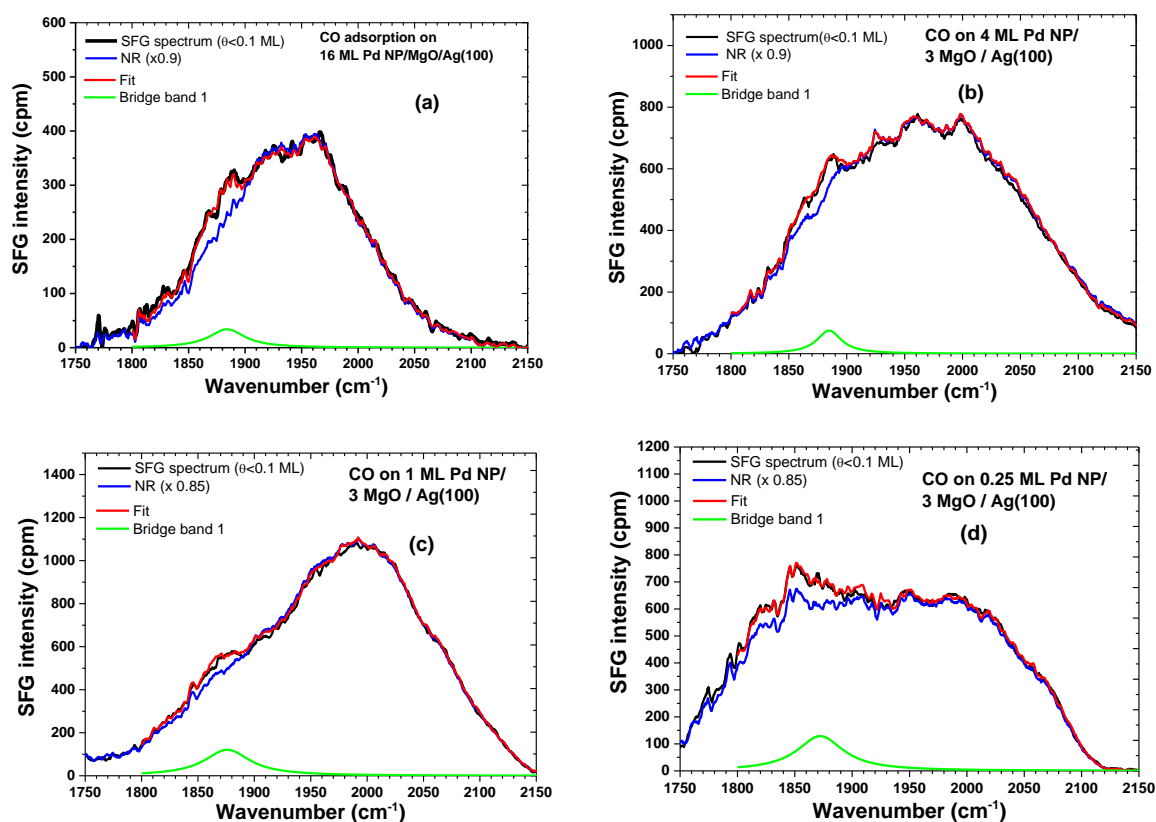


**Fig. 4.4.** Deconvolution of the SFG spectra at the detection limit (first spectrum after CO introduction at a pressure of  $1.3$  to  $1.9 \times 10^{-9}$  mbar) on supported Pd NPs / MgO / Ag(100) with different sizes: (a) coalesced NPs (16 ML); (b) 4 ML; (c) 1 ML; (d) 0.25 ML. The black and red curves are the measured and fitted SFG spectra, the blue is the NR intensity, and the green the singleton CO band.

terraces at this coverage are saturated by CO and well ordered. The presence of the small accompanying band at  $1918.8\text{ cm}^{-1}$  with a bandwidth of  $19.9\text{ cm}^{-1}$  shows that defects at domain boundaries involve bridge sites. In **Fig. 4.3c** (CO coverage of  $0.77\text{ ML}$  at  $10^{-3}\text{ mbar}$ ), the principal band is shifted to  $1984.8\text{ cm}^{-1}$  with a bandwidth of  $13.6\text{ cm}^{-1}$  due to the compression. The on-top CO band at  $2061.6\text{ cm}^{-1}$  with a bandwidth of  $20\text{ cm}^{-1}$  indicates that a second type of defect sites exists at domain boundaries. SFG spectra at the limit of detection are shown in **Fig. 4.4** for different NP sizes. The fits of **Fig. 4.4** have a larger uncertainty than at higher coverage due to the low signal. So it is better to take the singleton frequency as the limit at zero coverage of the frequency vs CO exposure (**Fig. 4.5**).

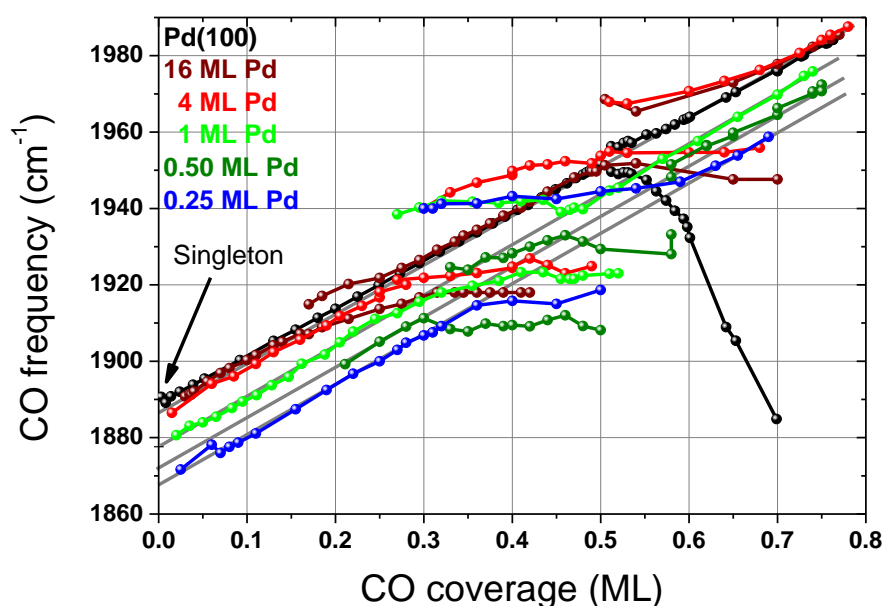


**Fig. 4.5** CO band frequency as a function of coverage. The singleton frequency is obtained by extrapolating to zero coverage. (In this deconvolution, the spectrum broadening around  $0.25\text{ ML}$  is tentatively interpreted in terms of two coexisting sites)

In addition to the fact that signals are low at nearly zero coverage, water absorption is also responsible for the noisy aspect of the spectra of **Fig. 4.4**. Since water is taken care of by our deconvolution program, one can see that a good fit can be obtained using a single band, as shown by comparison of experimental and simulated spectra. The CO singleton frequencies from  $1884.8\text{ cm}^{-1}$  for  $16\text{ ML Pd}$  coalesced layer to  $1872\text{ cm}^{-1}$  for  $0.25\text{ ML Pd}$  NPs agree within  $4\text{ cm}^{-1}$  with the values extrapolated from **Fig. 4.5** and reported in **Table 4.1**.

**Table 4.1.** CO adsorption for different equivalent thicknesses of Pd.

Equivalent thickness of Pd (ML)	0.25	0.5	1	4	16	Pd(100)
Singleton frequency (cm <sup>-1</sup> ) (spectrum deconvolution: Fig. 4.4)	1872 ±2	1898 ±2	1880 ±2	1887 ±2	1890 ±2	1890 ±2
Singleton frequency (cm <sup>-1</sup> ) (limit of zero coverage: Fig. 4.5)	1868 ±2	1874 ±2	1878 ±2	1886 ±2	1887 ±2	1888 ±2
Max. frequency at 10 <sup>-3</sup> mbar (cm <sup>-1</sup> )	1952 ±2	1972 ±2	1975 ±2	1987 ±2	1985 ±2	1983 ±2
Max. coverage at 10 <sup>-3</sup> mbar (ML)	0.68	0.74	0.73	0.78	0.78	0.77

**Table 4.1** shows that the singleton frequency of CO on particles varies by 22 cm<sup>-1</sup> from 1868 cm<sup>-1</sup> to 1890 cm<sup>-1</sup> from the smaller Pd NPs to Pd(100) single crystal. In order to understand how the NP size may affect the singleton frequency, DFT calculations as a function of the NP size have been carried out and will be discussed in **Section 4.4**.

## 4.4 DFT calculations of adsorption of a single CO molecule on Pd NPs

There are several calculations in the literature that can be used to explain the variation of singleton frequency with NP size. According to Ilya V. Yudanov et.al [5, 6], the CO binding energy on free Pd clusters [7, 8] increases with the average distance between surface Pd atoms which is known to increase with cluster size [5, 9-12]. On oxide films, the Pd-Pd distance is imposed by the oxide support to the first layer of Pd. In the case of MgO supported Pd NPs, the lattice parameter of MgO (4.21 Å) is larger than that of Pd (3.890 Å). But the most relevant parameter is that of the underlying Ag (4.09 Å) which is imposed by the epitaxial growth to the MgO layer. The Pd-Pd distance is therefore larger on MgO than for free clusters, and it decreases with NP height because the strain can be relaxed at each layer. Consequently smaller NPs have a larger Pd-Pd distance on their top facet, CO is expected to be more strongly bonded; if this happens at the expense of the internal CO bond, the CO frequency is expected to decrease. A DFT calculation (VASP 4.36 gamma vs. CP2K) was done by Carine Michel in the group of Philippe Sautet at ENS Lyon. She has calculated the CO singleton frequency as a function of the various parameters on which it may depend :

number of Pd layers, finite lateral size, lattice parameter, effective inclusion of the MgO layer and of the Ag substrate. Results are reported in **Table 4.2**:

**Table 4.2.** *Calculated CO singleton frequency on Pd in different cases : laterally infinite layers or cluster of 62 atoms, lattice constant, support.*

Case	Pd layers (ML)	Pd NP or layer	Support	Lattice constant	CO frequency (cm <sup>-1</sup> )
1	6	Layer	free	Pd	1870
2	3	Layer	free	Pd	1868
3	6 or 3	Layer	free	Ag	1857
4	3	NP	free	Pd	1862
5	3	Layer	2 ML MgO	Ag	1852
6	3	Layer	2 ML MgO / 6 ML Ag	Ag	1850
7	3	NP	2 ML MgO	Ag	1845

**Table 4.2** allows to evaluate the dominant parameter for the singleton frequency :

- number of Pd layers : cases 1 and 2, and 3, show that it is not important (< 2 cm<sup>-1</sup> between 1 and 2, no difference for cases 3).

- finite lateral size : comparison of cases 2 and 4 indicates a contribution of 6 cm<sup>-1</sup>, cases 5 and 7 of 7 cm<sup>-1</sup>.

- explicit inclusion of the MgO layer : cases 3 and 5 show a contribution of 5 cm<sup>-1</sup> (in both cases the lattice constant of Pd is that of Ag).

- explicit inclusion of the Ag substrate : cases 5 and 6 show that it has a negligible effect (2 cm<sup>-1</sup>) (in both cases the lattice constant of Pd is that of Ag).

- Pd lattice constant : cases 1 and 3 shows a reduction of the frequency by 13 cm<sup>-1</sup> when the lattice constant changes from that of Pd to that of Ag.

- cluster deposition : cases 4 and 7 show an effect of 17 cm<sup>-1</sup> that includes a change of lattice constant (from Pd to Ag) and the interaction with MgO.

If we compare the frequency shift from case 2 (close to Pd(100)) to case 7 (close to our NPs, but with a much smaller size), the total frequency decrease of 23 cm<sup>-1</sup> (to be compared to our experimental value of 22 cm<sup>-1</sup>) can be decomposed in a dominant effect of the lattice parameter (-10 cm<sup>-1</sup>, 43%) combined with an effect of NP lateral size (-6 cm<sup>-1</sup>, 26%), an effect of the MgO film (-5 cm<sup>-1</sup>, 22%) and Ag film (-2 cm<sup>-1</sup>, 9%). Inspection of the Pd d band shows that it is pushed up by the increase of the lattice constant (**Fig. 4.6**). This favors interaction of the Pd d band with the 2π\* CO orbital, increasing back donation, weakening the CO bond, redshifting the CO stretch. This agrees with the results of [5-8] recalled above.

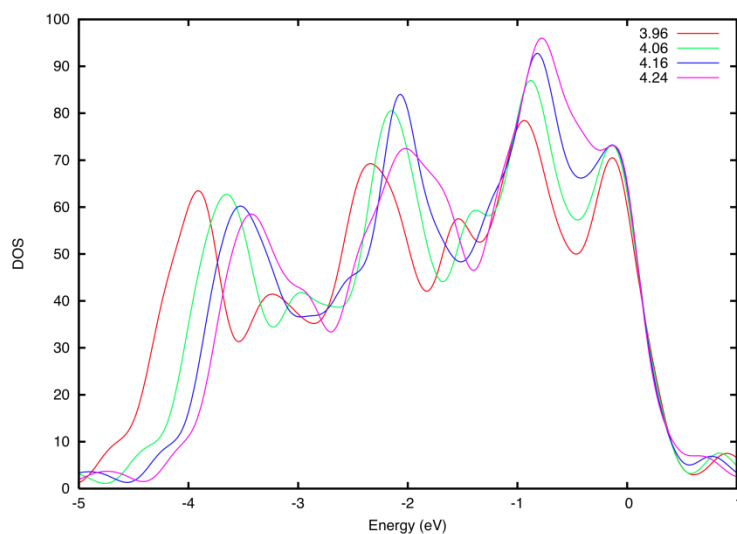


**Fig. 4.6.** *calculated d band density of states (DOS) as a function of the lattice parameter (shown in Å in the figure). The band shift is evident at the low energy edge of the DOS. The upper energy edge does not change because the d band occupancy is constant.*

## 4.5. Effect of CO adsorption on the non-resonant contribution

As discussed in **Chapters 1** and **3**, the non-resonant SFG signal (NR) comes from the excitation of electronic states near Fermi level [13]. At a given energy of the impinging lasers, different systems show different NR responses. For example, the presence of polystyrene film on Si makes the NR increase, but on Au it makes it decrease. These changes result from the interaction of the substrate with the adsorbates which can change the electronic density of states at the interface. In our measurements, the SFG spectra of CO on Pd NPs / MgO film / Ag(100) show an important variation of the intensity of the NR signal as a function of NP size. **Fig. 4.7** shows the NR SFG signals on Pd(100) and Pd NP with different sizes, compared with the SFG spectra of the CO band at the pressure of  $1 \times 10^{-3}$  mbar.

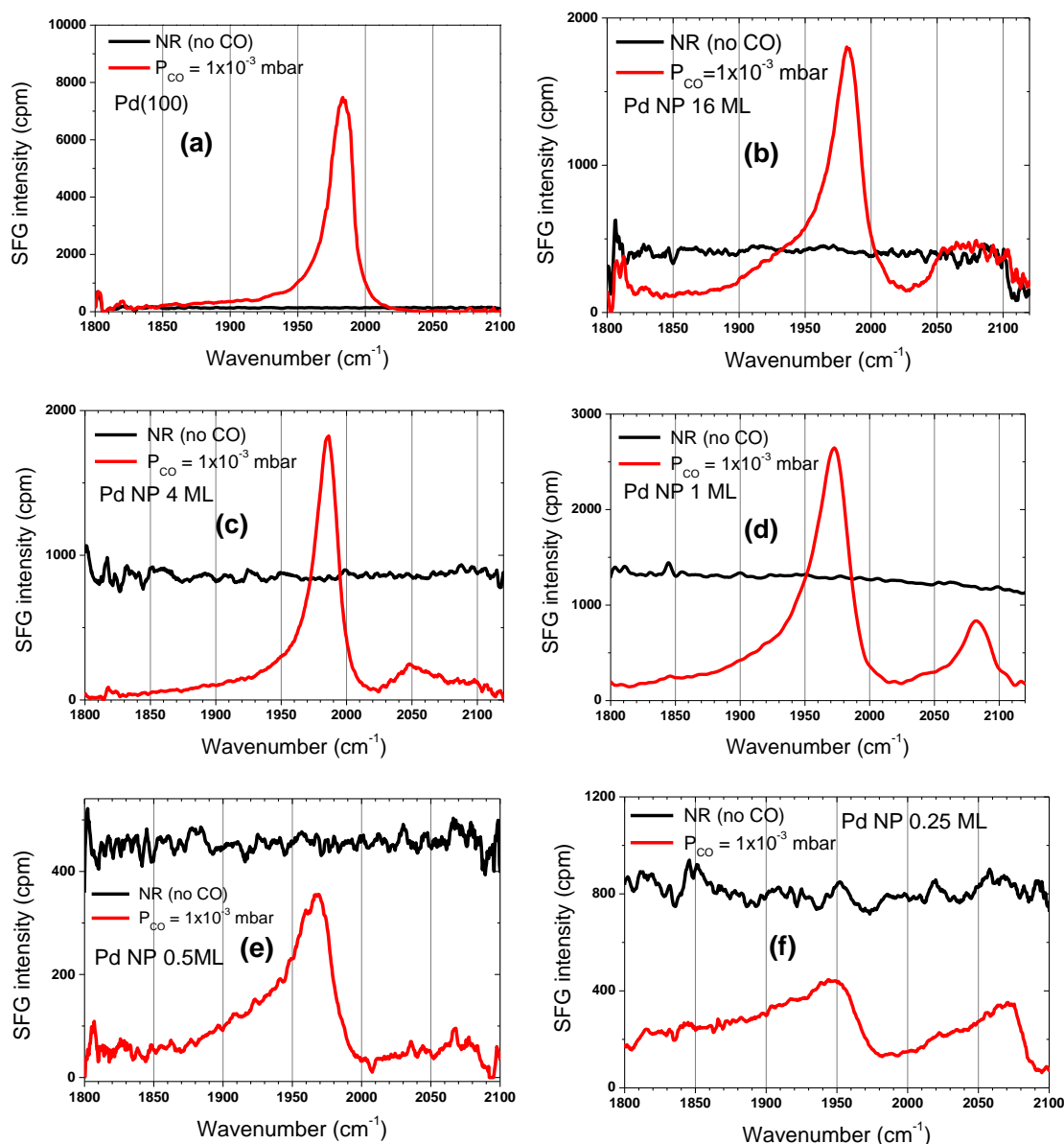


**Fig. 4.7.** Non-resonant SFG signal and CO adsorption spectrum at the pressure of  $10^{-3}$  mbar for different equivalent Pd thicknesses on MgO / Ag(100) samples and on Pd(100). (a) Pd(100) single crystal; (b) 16 ML (coalesced Pd layer); (c) 4 ML; (d) 1 ML; (e) 0.5 ML; (f) 0.25 ML Pd NPs. The spectra are normalized by the reference spectra.

As shown in **Fig. 4.7**, the NR SFG signal in the absence of CO is almost zero on the Pd(100) surface, then it appears on the 16 ML Pd layer and it increases for Pd NPs. The NR intensity reaches its maximum at 1 ML and then decrease. Upon CO adsorption, the NR signal decreases significantly, but not completely, especially for small NPs where it is not negligible with respect to the CO band. According to our previous measurements, the MgO / Ag(100) support hardly generates any NR signal. The NR might come from the Pd free interface or from the Pd/MgO interface. UV photoelectron spectroscopy has shown that

deposited Pd on clean MgO(100) shifts the O binding energy and change the electronic states of MgO [16]. This might have a NR signature. However, the quenching of the NR by CO shows that the NR arises primarily from Pd atoms where CO adsorbs. The NR signal could therefore be used as a means to control electronic aspects of CO bonding to the NPs. This would require a systematic study as a function of the frequency of the visible laser.

## 4.6. SFG spectra of CO adsorption on Pd nanoparticles at high CO pressure

In the previous experiments of CO adsorption on Pd NPs, the CO pressure was increased up to  $10^{-3}$  mbar. At this pressure the CO on-top band is smaller compared to the bridge band. But these sites can be populated with higher CO pressure [4, 14], as shown by Fig. 4.8.

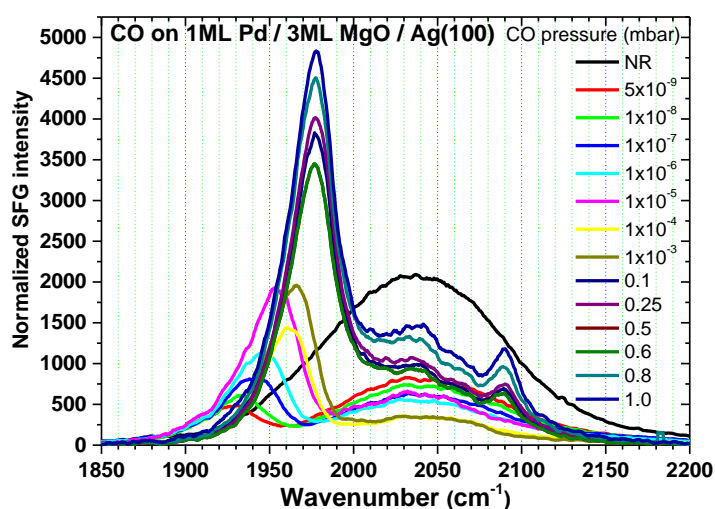


*Fig. 4.8. SFG spectra of CO on Pd NPs (1 ML equivalent Pd thickness) on 3 ML of MgO on Ag(100) as a function of CO pressure from  $5 \times 10^{-9}$  up to 1 mbar. The spectra are normalized by the area of the reference spectra recorded simultaneously.*

In this experiment, CO is quickly introduced from  $5 \times 10^{-9}$  mbar to 1.0 mbar at 300 K, so the CO adsorption is less ordered and the CO bridge frequency at  $10^{-3}$  mbar is lower than in the experiment of cooling down in Fig. 4.2c. For example the CO frequency at  $1 \times 10^{-3}$  mbar is found around  $1966 \text{ cm}^{-1}$  instead of  $1972 \text{ cm}^{-1}$ . The frequency of the CO bridge band increases to  $1977 \text{ cm}^{-1}$  when the pressure increases to 0.1 mbar. Then the frequency does not change up

to 1.0 mbar, because the Pd NPs are probably already saturated by CO under 0.1 mbar. A CO on-top band appears at  $2090\text{ cm}^{-1}$  under 0.1 mbar of CO and does not change from 0.1 mbar to 1.0 mbar. This band is much smaller than the bridge band, in agreement with the literature [4, 14].

## 4.7. Conclusion

In this chapter we are concerned with the impact of finite size of Pd NPs on CO adsorption, as probed by vibrational SFG spectroscopy of CO: spectroscopic sensitivity to the different sites, behavior of CO on the (100) facets, appearance of new sites related to edges and (111) facets or defects, stability of CO on NPs with respect to single crystals. Experiments of CO adsorption on 16 ML coalesced Pd film allow to observe the presence of defect linear sites and a broadening of bridge sites that shows that defect bridge sites do exist at (100) domain boundaries. CO behaves similarly on NP (100) facets, with differences in the actual dependence of frequency on coverage, which depends on NP size. In particular, the CO singleton frequency decreases at smaller size of NPs, indicating a change of bonding with size. The main reason is identified by DFT calculations done by Catherine Michel in the group of Philippe Sautet (ENS Lyon). It is the strain induced by the Ag substrate that imposes its lattice constant to the MgO layer and to the Pd NPs, increasing the Pd-Pd distance. This effect is largest for the smaller NP, because the strain is progressively released at each Pd layer. DFT shows that the strain increases the metal to CO backdonation, weakening the CO bond and accordingly decreasing the internal CO frequency. The lateral confinement plays a rather small role. The explicit inclusion of the MgO layer in the calculation contributes less than the strain. On our smallest NP size (0.25 ML equivalent Pd Thickness, or  $\approx 170$  atoms) the spectrum changes radically, most probably because the shape changes (smaller (100) facet). The non-resonant SFG signal depends on NP size and on CO coverage, suggesting that visible-frequency dependent SFG spectroscopy could help to understand the bonding of CO to NPs. Finally the maximal CO coverage is not reached at  $10^{-3}$  mbar: a strong on-top band appears at  $\approx 0.1$  mbar, showing that additional CO “reservoir sites” exist and can be occupied at high pressure.

## Reference

- [1] G. Sitja, C. R. Henry. *Surf. Sci.* 517, 115 (2002)
- [2] C. Goyhenex, M. Croci, C. Claeys, C. R. Henry. *Surf. Sci.* 352, 475 (1996)
- [3] S. Bertarione, D. Scarano, A. Zecchina, V. Johaneck, J. Hoffmann, S. Schaueremann, M. M. Frank, J. Libuda, G. Rupprechter, and H.-J. Freund, *J. Phys Chem. B* 108, 3603 (2004).
- [4] T. Dellwig, G. Rupprechter, H. Unterhalt, and H.-J. Freund, *Phys. Rev. Lett* 85, 776 (2000)
- [5] I. V. Yudanov, Riadh Sahnoun, Konstantin M. Neyman, and Notker Ro1sch, *J. Phys. Chem. B*, 107, 255 (2003)
- [6] I. V. Yudanov, A. Genest, S. Schaueremann, H.-J. Freund, and N. R ösch, *Nano Lett.*, 12, 2134,(2012)
- [7] F.-Wolfarth, J.-H. Farmer, J. A. Flores-Camacho, J. M. Genest, A., I.V. Yudanov, N. Rosch, C. T. Campbell, S. Schaueremann, H.-J. Freund, *Phys Rev B* 2010, 81, 241416.
- [8] I. V. Yudanov, M. Metzner, A. Genest, N. Rosch, *J. Phys. Chem. C*, 112, 20269 (2008)
- [9] G. Pacchioni, S.-C. Chung, S. Kr üger, N. R ösch, *Chem. Phys.*, 184, 125.(1994)
- [10] O. Häberlen, S.-C. Chung, M. Stener, N. R ösch, *J. Chem. Phys.*, 106, 5189 (1997)
- [11] S. Kr üger, S.Vent, N. R ösch, Ber. Bunsen-Ges. *Phys. Chem.* 101, 1640.(1997)
- [12] S. Kr üger, S.Vent, F. N örtemann, M. Staufer, N. R ösch, *J. Chem. Phys.*, 115, 2082. (2001)
- [13] A. D. Curtis, R. S. Burt, R. C. Angela, and J. E. Patterson. *J. Phys. Chem. C*, 115, 11550 (2011)
- [14] H. Unterhalt, P. Galletto1, M. Morkel, G. Rupprechter, and H.-J. Freund, *phys stat sol* 188 No.4 1495 (2001)
- [15] K. H ørup-Hansen, S. Ferrero, C.R. Henry. *Appl. Surf. Sci.* 226, 167 (2004)
- [16] Q. Guo, and P. J.M øller, *J. Phys. Chem. C* 114, 18167, (2010)



# Chapter 5

## Catalytic CO oxidation on Pd(100) and Pd nanoparticles

<b>5.1 Introduction</b>	108
5.1.1 O adsorption on Pd crystal and NP	110
5.1.2. CO oxidation pathway on Pd crystal surface	111
5.1.3 CO oxidation on nanoparticles	112
<b>5.2 SFG experimental results of CO catalytic oxidation on Pd crystal and nanoparticles</b>	113
5.2.1 Non resonant SFG on Pd NP / MgO / Ag interacted with O <sub>2</sub>	113
5.2.2 Self-poisoning by CO on Pd surface	115
5.2.3 Catalytic CO oxidation on Pd(100) crystal surface at 300 K and low pressure	118
5.2.4 Size effect of CO oxidation on Pd NPs	123
5.2.5 CO + O co-adsorption on Pd NPs with a high CO pressure at 300 K	130
<b>5.3 Pump-probe study of O<sub>2</sub>+CO co-adsorption on Pd NP</b>	131
5.3.1 Introduction	131
5.3.2 Pump-probe study of O <sub>2</sub> +CO co-adsorption on Pd NP	133
<b>5.4 Conclusion</b>	135
<b>Reference</b>	137

## 5.1 Introduction

The catalytic CO oxidation on metallic nanoparticles (NP) has raised a great interest in past decades because not only it is an important model to understand catalyzed reactions on metals in general, but also it has many industrial applications such as conversion of automobile exhaust or fuel cells [1]. Among catalysts of CO oxidation, the Pt-group metals especially Pd [2-7] are most commonly used for their high catalytic activity. On surfaces, catalytic CO oxidation may proceed through the Langmuir-Hinshelwood (LH) mechanism or exceptionally the Eley-Rideal (ER) mechanism. In the ER mechanism, the CO molecule in the gas phase reacts directly with activated O<sub>2</sub>. In the LH mechanism, adsorbed CO reacts with adsorbed O to form CO<sub>2</sub> [8]. Engel and Ertl [9] presented a strong evidence in favor of a Langmuir-Hinshelwood type mechanism on Pd. Alavi et al. [10] have reported that the reaction path of CO oxidation on Pt(111) follows the LH mechanism. On contrary, Stampfl and Scheffler have found that the ER mechanism is the most favored mechanism for the oxidation of CO on Ru(0001) [11]. T. Schalow et. al. have found facile oxidation and reduction reactions on small Pd NP supported by Al<sub>2</sub>O<sub>3</sub> [12]. NP size effects have been the object of many studies. The interest of NPs comes from three facts: (1) catalytic reactions occur at the surface of metals; the surface / volume ratio, and therefore the economical efficiency is considerably increased by using small NPs; this is important owing to the cost of metals such as Pt or Pd. (2) reactants may adsorb first on the NP support and diffuse to the NPs where they may react (spillover effect): this increases the reaction rate even if the reaction mechanism is independent of size. (3) NPs have specific adsorption sites, and even a different band structure for sizes below a few nm, opening the possibility that the reaction proceeds differently on NPs with respect to macroscopic surfaces (intrinsic effects). In many cases there are no intrinsic effects. For example Haruta has reported that the catalytic efficiency does not increase on smaller Pt NP. However there are definitively cases where intrinsic effects are definitively important. The most spectacular case is that of Au, which is the only non-reactive metal but for a very few number of reactants, but which becomes catalytic on very small Au NPs (<2-3 nm) because the properties of small Au NP change drastically with respect to the metal [13-15]. In addition to intrinsic effects, indications exist that reactants like oxygen may modify reversibly NPs in a way intermediate between O adsorption at the surface and bulk oxidation: “sub-surface” O, and oxidized sites near the oxide layer, are believed to play a role; this implies that the NPs are not necessarily in their

equilibrium state during the catalytic reaction. These possibilities stimulate the interest for probing catalytic reactions in situ and in “operando conditions”.

According to **Chapter 4**, the frequency of the CO vibration varies upon chemisorption of the molecule on the Pd surface, and it depends on the adsorption site and the size and morphology of NP. The catalytic reaction efficiency depends on various factors, including adsorption, diffusion and occupation of suitable adsorption sites. [16]. SFG spectroscopy gives access to the occupation of the different adsorption sites through the vibrational spectra, and it can be used at pressures where most of other surface science techniques are not usable. Therefore it is an attractive method to study the CO catalytic oxidation. The previous study of a CO catalytic reaction by SFG was made by Rupprechter and Pery T.. Rupprechter has studied the CO adsorption on Al<sub>2</sub>O<sub>3</sub> supported Pd NPs [17] and the CO+O<sub>2</sub> reaction on Pt(111) surface at high pressures (CO 40 torr and O<sub>2</sub> 100 torr) and temperature (>590 K) [18]: the CO<sub>2</sub> turnover rate (TOR) exhibits a strong increase at temperature higher than 540 K, and the CO band disappear at 640 K. The CO+O<sub>2</sub> reaction on Rh(111) at a total pressure of 20 mbar (CO:O<sub>2</sub>:Ar = 1:2:7 molar) has been studied by T. Pery *et. al.* using SFG [19, 20]. The CO<sub>2</sub> production increase quickly from 450 K and the CO band is suppressed at 600 K.

In this chapter we use our results on CO adsorption on Pd NP of **Chapter 4**, to study the size effect of Pd NP on the CO catalytic oxidation. SFG spectra of CO bands as a function of the sample temperature and the CO/O<sub>2</sub> partial pressures are recorded in order to follow the CO reaction. CO and oxygen pre-exposed surfaces are compared, because CO is a self-poison of the surface. The effect of adsorbed O on CO adsorption and NR SFG signal are discussed. Pd(100) crystal and thin MgO layers supported Pd NP on Ag(100) single crystal are compared. Pump-probe experiments on O<sub>2</sub>+CO co-adsorption on Pd NP are also discussed. The present study remains at a preliminary stage because there are experimental limitations that were not overcome. Our sample heating system (filament) does not allow to use O<sub>2</sub> pressures above  $\approx$  2 mbar. Therefore, we were not able to study the catalytic reaction in the optimal temperature range (where the CO desorption rate must not be zero). In addition, we have tried to detect CO<sub>2</sub> with a mass spectrometer through a low conductance valve : this arrangement could not be made sensitive enough. Therefore, this study provides direct information only on CO. The Pd-O bond lies too far in the IR to be detected by our SFG setup.

### 5.1.1 O adsorption on Pd crystal and NP

O<sub>2</sub> chemisorption on Pd is more complicated than CO because of the higher reactivity of O<sub>2</sub> with the Pd. CO does not dissociate at low temperature, however O<sub>2</sub> partially dissociates when the surface temperature is above 180 K [21]. The interaction of oxygen with the Pd crystal surface may be even more complex because it may involve surface and bulk oxide formation depending on temperature and O<sub>2</sub> pressure [4-6]. The details of the reaction mechanism can only be understood on the basis of the knowledge of the interaction of CO with the different possible oxygen species [22].

The adsorption of O on crystal Pd(111) and Pd(100) surface and CO oxidation has been calculated by C.J. Zhang et al. [26]. According to their results, as shown in **Fig. 5.1** the preferred sites for O(ads) on Pd(111) and Pd(100) surface at low coverage are the hcp hollow and 4-fold hollow sites respectively.

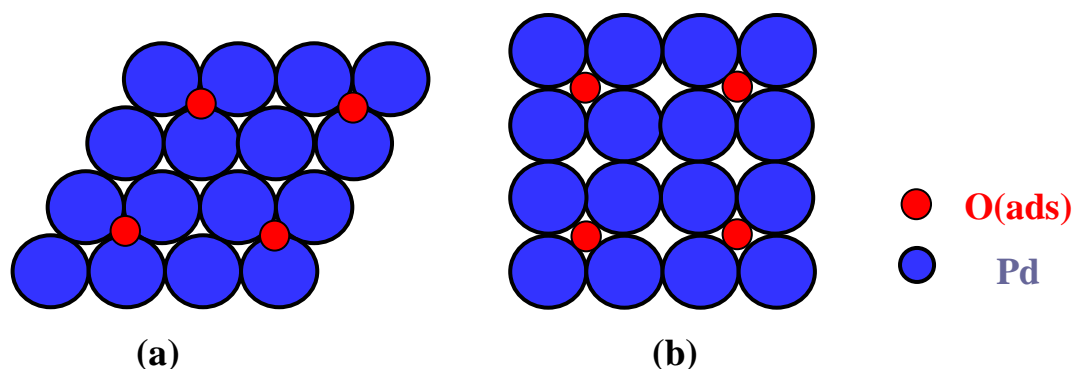


*Fig. 5.1. The dissociated O atoms adsorbed on (a) Pd(111) and (b) Pd(100) surface at coverage  $\theta=0.25\text{ML}$  on hcp hollow and 4-fold hollow sites respectively, the adsorption phase on both surfaces are  $p(2 \times 2)$ . [26,27]*

Harald Gabasch et al. [22] have reported that the oxygen reactivity with CO decrease with increasing oxidation state. O(ad) on Pd(111) exhibits the highest reactivity and could be reduced within a few minutes already at 223 K using low CO beam fluxes around 0.02 ML/s. The Pd<sub>5</sub>O<sub>4</sub> surface oxide on Pd(111) prepared by exposure to 6000 L O<sub>2</sub> at 603-673 K sample temperature, could react with CO at a comparable rate above 330 K using the same low CO beam flux [22]. Fully oxidized PdO nanoparticles require 10 mbar of CO for 15 min at 523 K in order to re-establish the metallic state. PdO does not react with CO below 493 K even around 10 mbar which is probably due to the lack of adsorption sites for CO on bulk PdO

compared to surface Pd<sub>5</sub>O<sub>4</sub>. In general, the surface oxide species are considerably less reactive than the chemisorbed p(2×2) O adsorbed layer. N. Kasper et. al. has reported that below 523 K, the formation of surface oxide and bulk oxide is observed to be kinetically hindered [29]. So in our experimental conditions (below 523 K), the formation of surface Pd oxide and its contribution to catalytic reactions can be neglected. On extended surfaces oxygen adsorbed on Pd desorbs around 800 K [28], meaning that during CO oxidation, in usual conditions (below 725 K), adsorbed oxygen will not desorb from Pd but be consumed by the catalytic reaction. It has recently been observed that oxygen migration into the subsurface region of a Pd(111) single crystal occurs at 523K [2] and 40 L oxygen exposure (1 langmuir =10<sup>-6</sup> Torr·s).

The dissociative adsorption of oxygen on supported Pd, Pt, and Rh clusters has already been studied by several groups [23-25]. It has been shown by molecular beam techniques that oxygen can be incorporated in the volume of the Pd clusters already at 250K-300 K [23, 25]. It has also been observed that the relative quantity of oxygen incorporated in the metal lattice increases when the particle size decreases [24]. But for 5.5 nm Pd NPs supported by Al<sub>2</sub>O<sub>3</sub> oxide film at a temperature T<500 K, only the surface oxygen, and not bulk and subsurface oxygen, can oxidize CO [25].

### 5.1.2. CO oxidation pathway on Pd crystal surface

The co-adsorption of O(ad) and CO(ad) on Pd(111) and Pd(100) crystal surface and the CO<sub>2</sub> product formation have been largely studied [7,9,31,32,33]. When O and CO are co-adsorbed on the Pd surface, CO may desorb or react with O. It might be possible that the reaction is more strongly activated than desorption, because the O atom is strongly bound to the surface, whereas the CO is only weakly bound, and its activation barrier for desorption closely corresponds to its rather weak binding energy [22]. The oxidation reaction of CO catalyzed by Pd proceeds already at 200 K [7], while CO desorption on Pd starts at 500 K [40]. The Langmuir-Hinshelwood mechanism [10, 22, 34] is described by following reactions [37]:



where \* represents an empty site. The first step is O<sub>2</sub> adsorption and dissociation and CO adsorption; the second is O(ads)+CO(ads) reaction to CO<sub>2</sub>; the third is CO<sub>2</sub> desorption. O<sub>2</sub>

dissociation may be a limiting step because the two \* empty sites must be next to each other : CO adsorption may block O<sub>2</sub> dissociation at low temperature and high CO coverage. The reverse reaction of recombinative desorption of O<sub>2</sub> is negligible in practice, which is not the case of the CO desorption. Step 3 proceeds quickly after step 2. **Fig. 5.2** shows the potential energy diagram of catalytic and non-catalytic CO oxidation. The difference between non-catalytic and catalytic CO oxidation is the considerable decrease of the activation barrier from 2.68 eV in the gas phase to globally exothermic; the local energy barrier of step 2 on the surface is 1.09 eV in the case of Pt(111) [16]. These results lead to the CO catalytic oxidation at a lower temperature.

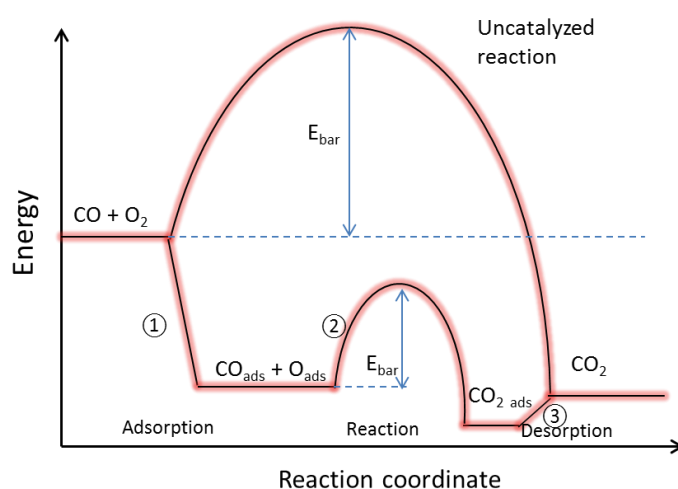


**Fig. 5.2.** The potential energy diagram of non-catalyzed and catalyzed CO oxidation.

The CO + O<sub>2</sub> adsorption and reaction depend on the surface temperature: at low T, when the metal surface is CO – covered, the surface is poisoned and the reaction is limited by O<sub>2</sub> adsorption [7]; at a high T when the surface is covered by O, and the reaction is limited by CO adsorption [18] because the CO desorption temperature is lower than O.

### 5.1.3 CO oxidation on nanoparticles

The CO oxidation efficiency depends on the size of NP. Several factors may contribute to this size effect, including the dependence of the adsorption energy of CO and O<sub>2</sub> on the size and morphology of the NP. The most spectacular case is that of Au NP. M. Haruta et al. [15] has shown the catalytic efficiency of CO oxidation on gold and Pt NP as a function of size.

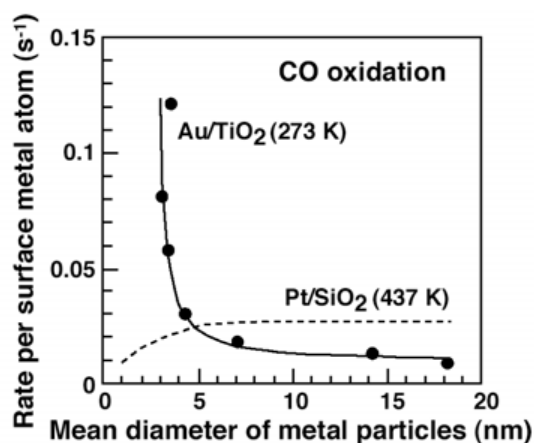


*Fig. 5.3. The CO oxidation rate by surface atom as a function of the diameter of gold and Pd nanoparticles [15].*

In **Fig. 5.3**, for the case of gold nanoparticles, the catalytic reactivity increases slowly with NP size decreasing to 5 nm, then increase quickly at smaller size. Because gold NP lose their metal properties at small size (< 2-3 nm) [41]. In the case of Pt NP the catalytic reactivity is very different, it keeps constant at larger NP and decreases when the NP size is smaller than 5 nm. In this section, the SFG spectrum is used to study the effect size of Pd NP on catalytic CO oxidation.

## 5.2 SFG experimental results of CO catalytic oxidation on Pd crystal and nanoparticles

### 5.2.1 Non resonant SFG on Pd NP / MgO / Ag interacted with O<sub>2</sub>

Because the frequency region of O-metal band (50~500 cm<sup>-1</sup>) cannot be reached by our experimental device to study O<sub>2</sub> adsorption on Pd surface by SFG experiment, the only way is to compare the variation of non-resonant (NR) signal on Pd surface during O<sub>2</sub> adsorption. Indeed at 300 K the adsorption and dissociation of O<sub>2</sub> dominates the interaction of O<sub>2</sub> with Pd [27] which can change the electronical density of states at the surface [38] and accordingly the generation of the NR signal.

The change of NR signal induced by the adsorbed O atom on Pd(100) crystal and Pd NP with different sizes were measured as shown in **Fig. 5.4**. The NR intensity is decreased by 20%

when  $1 \times 10^{-4}$  mbar  $O_2$  is introduced in the chamber for Pd(100) single crystal and has no effect on 16 ML Pd NP. On contrary for smaller NP size, the NR is decreased by 77% for 4 ML equivalent thickness of Pd NP, and by 83% for the case of 1 ML of Pd NP.

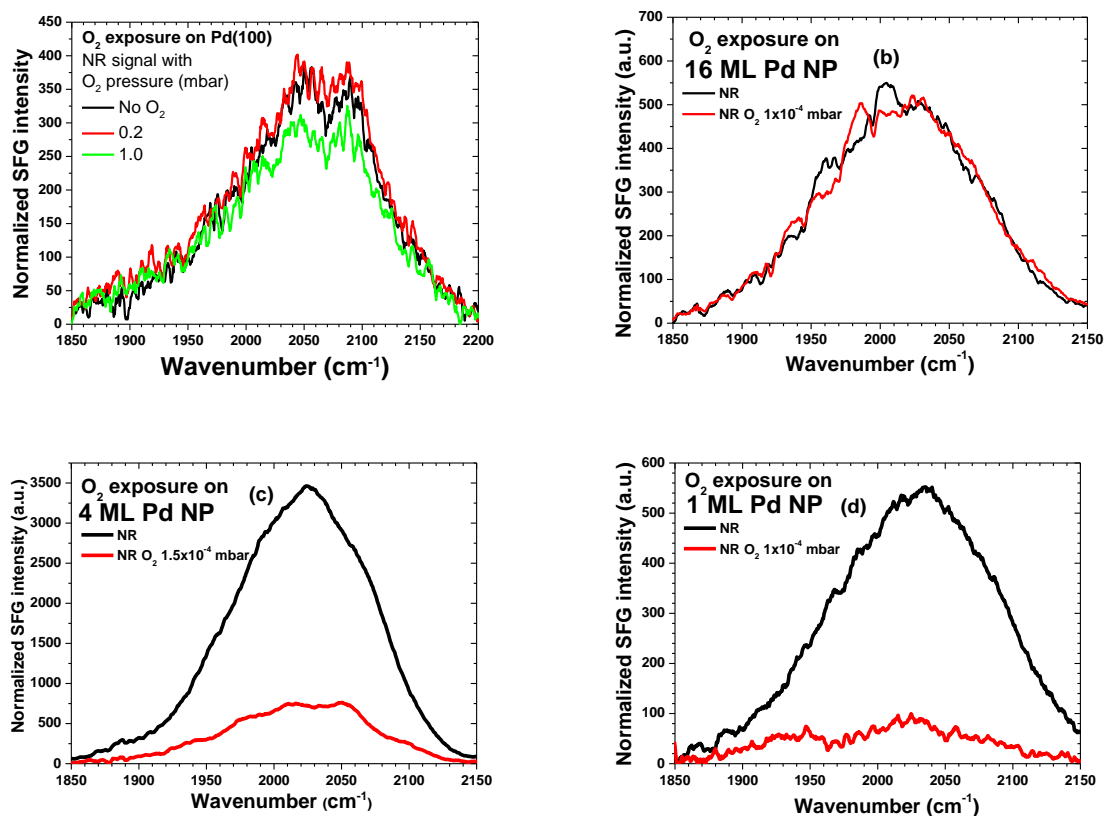


**Fig. 5.4.** NR SFG spectra under  $1 \times 10^{-4}$  mbar  $O_2$  for (a) Pd(100); (b) 16 ML; (c) 4 ML; (d) 1 ML of Pd NP at 300K.. All spectra are normalized by the reference intensity.

In **Fig. 5.4** it is difficult to compare the NR intensity level because it depends on the experimental conditions (laser intensities and alignments), but we have found in **Chapter 4** that the NR SFG signals increase at smaller NP size. In **Fig. 5.4a** the NR SFG signal is weak and is little reduced by  $O$  adsorption, indicating that the NR signals come rarely from the Pd free surface. In **Fig. 5.4b**, in the case of 16 ML NR is higher than Pd(100) meaning that the Pd/MgO interface generates more NR signals. It is proved by the effect of  $O$ : the  $O_2$  cannot interact with Pd/MgO interface, so the NR is not reduced in this case. In **Fig. 5.4c** and **d**, according to **Chapter 4** the NR signal is stronger at smaller NP size (4 ML and 1 ML), but the NR is much reduced by the presence of  $O_{ads}$ . Because in these cases the  $O_2$  can reach to the Pd/MgO interface and change their electrical states where the NR is generated.

The NR SFG spectra on 1 ML Pd NP as a function of  $O_2$  pressure are shown in **Fig. 5.5**.

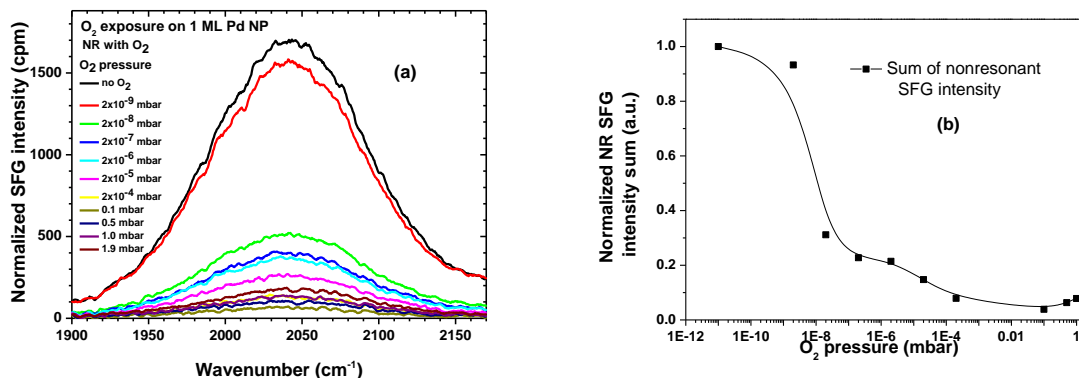


**Fig. 5.5.** The NR SFG spectra of O<sub>2</sub> in function of pressure adsorbed on 1 ML Pd NP/MgO/Ag(100) at 300K. (a) The SFG spectra; (b) The corresponding sum of SFG spectra intensity.

At 300K, upon an increasing of O<sub>2</sub> pressure from 10<sup>-9</sup> to 0.1 mbar, the NR SFG intensity of 1 ML Pd NP/MgO/Ag(100) greatly decreases to 5% of its initial value without oxygen in the chamber, then increases by a factor 2 when the O<sub>2</sub> pressure is varied from 0.1 mbar to 1.0 mbar. According to the previous discussion the decreasing of the signal intensity is due to the O<sub>2</sub> adsorption and dissociation. But what is surprising is the NR intensity increase at a higher O<sub>2</sub> pressure. It was shown in [23,25] by molecular beam techniques that oxygen can be incorporated in the volume of the Pd clusters already at 300 K. It has also been observed that the total quantity of oxygen incorporated in the metal lattice increases when the particle size decreases [24]. So the small increase of NR intensity with from 0.1 mbar to 1 mbar O<sub>2</sub> may probably be due to the incorporated O atom into the Pd NP which continuously modifies the electronic density of states of the Pd surface.

## 5.2.2 Self-poisoning by CO on Pd surface

CO poisoning on Pd is well known. H. Conrad *et.al.* [7] have reported that the adsorption of O<sub>2</sub> is blocked if the pre-adsorbed CO exceeds 0.33 ML coverage on the Pd(111) surface. The inverse is different: CO can adsorb on Pd(111) even if there is already O on the surface. This asymmetric effect is due to the fact that O<sub>2</sub> chemisorption is dissociative. It requires two open neighboring sites on the surface, which are not available when CO saturates the surface. By contrast, CO can adsorb on a Pd surface saturated with oxygen. In our SFG experiments, CO and O<sub>2</sub> are introduced in different orders: first CO, then O<sub>2</sub> (or the inverse) on a sample covered by NP (1ML of Pd). SFG spectra are measured as a function of sample

temperature. In **Fig. 5.6**, the NP have been pre-exposed to 1 mbar of CO at 300 K. Then 1 mbar O<sub>2</sub> is introduced in the UHV chamber. SFG spectra as a function of temperature are similar to the spectra shown in **Fig. 4.6** (1 mbar CO on the same kind of sample). A large bridge CO band accompanied by a small fraction of CO on top sites can be observed. Then the sample is heated step by step up to 2.5A. No significant change can be found. Under 1 mbar of CO around 400 K, no CO desorption is expected.

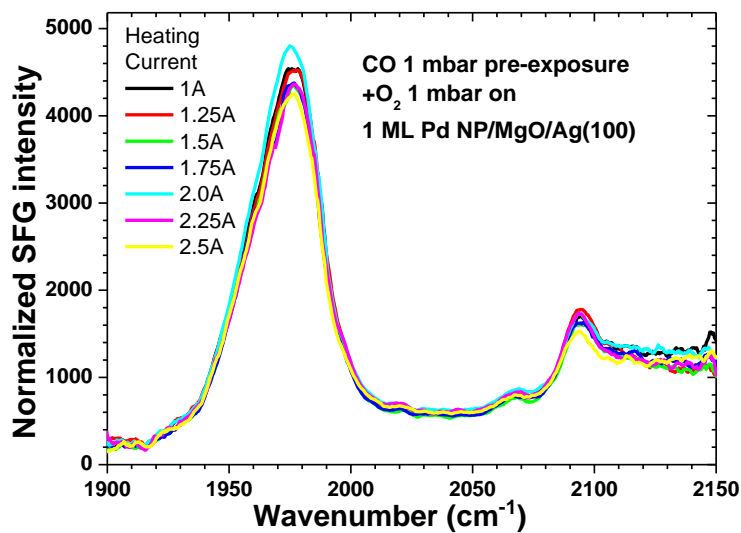


**Fig. 5.6.** SFG spectra of CO by introducing firstly 1 mbar of CO followed by 1 mbar O<sub>2</sub> on 1 ML of Pd NP on MgO/Ag(100) under heating from 300 K (0 A) to 390 K (2.5 A), all normalized by the spectra of their reference.

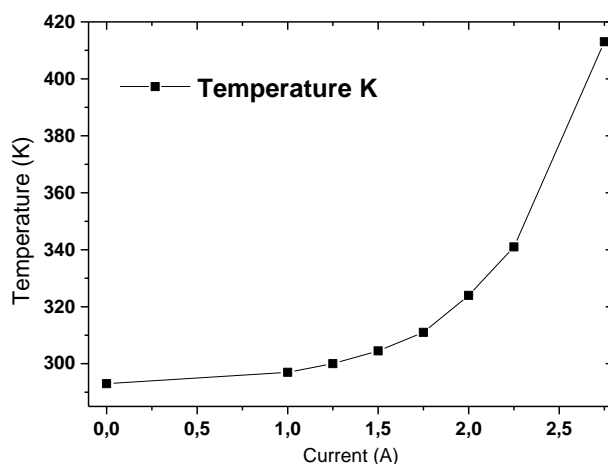


**Fig. 5.7** calibration of sample temperature as a function of heating current (15 mn after each step of 0.25 A) measured by a pyrometer.

If O<sub>2</sub> is introduced first, the spectra show that CO adsorbs. The SFG spectra of O<sub>2</sub> at 2 mbar then CO at 0.1 mbar are shown in **Fig. 5.8** for 1 ML of Pd NP on 3 ML MgO/Ag(100).

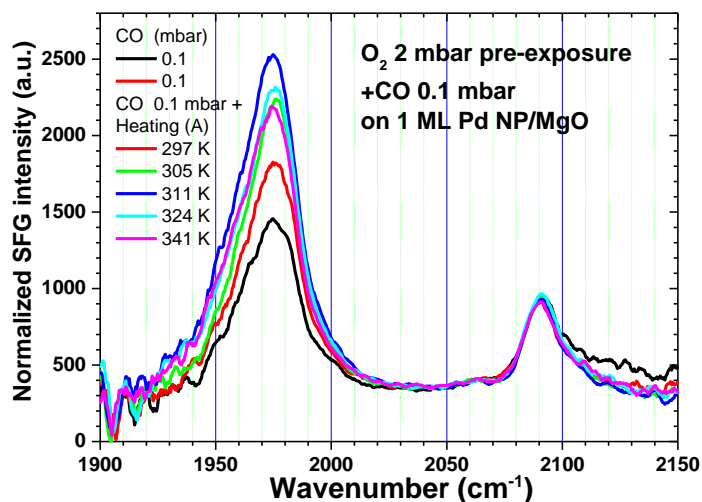


**Fig. 5.8.** SFG spectra of CO band by introducing 2 mbar O<sub>2</sub> followed by 0.1 mbar CO on 1 ML Pd NP/MgO/Ag(100) at 300 K. Then the sample is heated to 390 K (2.5 A). All spectra are normalized to the spectra of their reference.

In the experiment shown in **Fig. 5.8**, there are three differences with **Fig. 5.6**: 1) CO with a pressure of 0.1 mbar (20 times smaller than O<sub>2</sub>) can adsorb on the Pd NP, meaning that the adsorbed O(ads) does not inhibit the CO adsorption; 2) The intensity of the on top band with a smaller CO pressure (0.1 mbar) is comparable to that of **Fig. 5.6** for 1 mbar of CO; 3) heating the sample up to 390 K (2.5A) induces an increase of the CO bridge band intensity but not of the atop band. This is a sign of CO reaction: although the maximal coverage is not reached immediately, CO adsorbs very quickly. Heating at first improves the coverage, presumably by increasing the reaction rate of CO with O, which allows more CO to adsorb in competition with O<sub>2</sub>. As the temperature rises, CO desorption starts to occur and limits the coverage. From these differences between **Fig. 5.6** and **Fig. 5.8** we can deduce that in the former case the Pd NP is poisoned by CO adsorption, while in the latter case the surface is not poisoned by O atoms.

### 5.2.3 Catalytic CO oxidation on Pd(100) crystal surface at 300 K and low pressure

CO oxidation on Pd(100) crystal surface is important to understand the CO catalytic reaction on Pd NP [26,39]. The CO oxidation occurs already at 223 K [22] and even 200 K [7], but with a very low reaction rate. In this section the CO oxidation on Pd(100) will be discussed to compare with the CO reaction on Pd NP.

Referring to the previous discussion of CO poisoning on Pd surface, the cleaned sample Pd(100) crystal is pre-treated with  $10^{-5}$  mbar  $O_2$  during 20 min at 350 K, then the sample temperature is decreased to 300 K and the CO pressure is varied between  $10^{-9}$  and  $10^{-7}$  mbar in order to observe the oxidation process with different O/CO ratio.

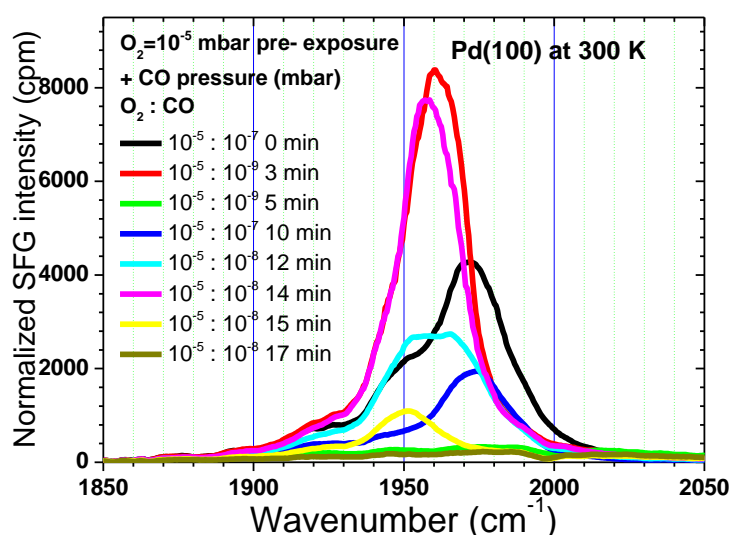


*Fig. 5.9. SFG spectra of CO oxidation on  $O_2$  pre-treated Pd(100) crystal surface.  $O_2$  pressure is kept at  $10^{-5}$  mbar and CO pressure is varied. All spectra are normalized by the area of their reference spectrum. (Note that the dip in the spectra at  $1995\text{ cm}^{-1}$  is an artifact due to data processing).*

In **Fig. 5.9**  $O_2$  pressure is fixed at  $10^{-5}$  mbar. First the CO pressure is increased to  $10^{-7}$  mbar, the CO band appears at  $1972\text{ cm}^{-1}$  indicating  $\sim 0.65$  ML coverage (black curve). Then the CO pressure is decreased to  $10^{-9}$  mbar, the CO band completely disappears in 2 minutes (red and green curves). Only the small NR signal can be observed. After that the CO pressure is returned to  $10^{-7}$  mbar in order to readsorb CO up to high coverage (blue curve). Then the

CO pressure is decreased to  $10^{-8}$  mbar (instead of  $10^{-9}$  mbar in the previous cycle of adsorption / desorption). The bridge CO band then disappears more slowly than previously (in 4.5 min), as may be expected since the readsorption rate is larger.

If we call the CO adsorption rate  $a_{CO}(\theta_{CO}, P_{CO}, T)$ , the CO desorption rate  $d_{CO}(\theta_{CO}, P_{CO}, T)$ , the CO oxidation rate  $\sigma_{O+CO}(\theta_O, \theta_{CO}, T)$ , the expression for the surface CO coverage variation rate  $d\theta_{CO} / dt$  is:

$$\frac{d\theta_{CO}}{dt} = a_{CO} - d_{CO} - \sigma_{O+CO} \quad (5.2)$$

Without oxygen in the chamber, the CO band frequency on Pd(100) would decrease from 1976 down to 1955  $\text{cm}^{-1}$  (from  $\approx 0.65$  ML to  $\approx 0.55$  ML) in 10 min under a CO pressure of  $10^{-9}$  mbar (See **Chapter 3**). When  $O_2$  is present, the reaction depletes completely the surface from CO in 2 mn at  $10^{-9}$  mbar or 4.5 mn at  $10^{-8}$  mbar, showing that the reaction rate is much larger than the desorption rate at 300 K.

**Table 1.** Comparison of  $d\theta_{CO}/dt$  with different CO pressures under  $10^{-5}$  mbar of  $O_2$  in the experiment of CO oxidation on Pd(100) single crystal.  $\Delta\theta_{CO}$  indicates the change direction after a change of the CO pressure.

$O_2$ pressure (mbar)	CO pressure (mbar)	$\Delta\theta_{CO}$	CO disappearing time
$10^{-5}$	$10^{-7}$ to $10^{-9}$	$\Delta\theta_{CO} < 0$	2 min
$10^{-5}$	$10^{-9}$ to $10^{-7}$	$\Delta\theta_{CO} > 0$	–
$10^{-5}$	$10^{-7}$ to $10^{-8}$	$\Delta\theta_{CO} < 0$	4.5 min

Because at  $10^{-9}$  mbar the CO adsorption rate is small, and the reaction rate is much larger than the desorption rate, we can estimate the oxidation rate of CO to be approximately  $0.65 \text{ ML} / 2 \text{ mn} = 0.0054 \text{ ML}\cdot\text{s}^{-1}$ . In the second experiment when the CO pressure is decreased from  $10^{-7}$  mbar to only  $10^{-8}$  mbar (instead of  $10^{-9}$  mbar), the CO coverage decreases from 0.65 ML to 0 ML in 4.5 min. This longer time of disappearance of the CO band is caused by the CO adsorption rate  $a_{CO}$ . If we compare with the first CO band disappearing experiment, the (reaction - adsorption) rate of CO is  $0.0024 \text{ ML}\cdot\text{s}^{-1}$ , showing that  $a_{CO}$  at  $10^{-8}$  mbar CO is approximately  $0.0030 \text{ ML}\cdot\text{s}^{-1}$ , corresponding to an average sticking coefficient of roughly 0.25 over the whole coverage range, which is a reasonable value.

We have also observed the evolution from a CO-poisoned surface to a reactive surface. Poisoning is obtained by increasing the CO pressure up to  $10^{-6}$  mbar for a couple a minutes. At this pressure the CO adsorption rate is much larger than the reaction rate and CO saturates the surface as shown by the fact that we observe a normal CO SFG spectrum with one band at  $1975\text{ cm}^{-1}$ . Then the CO pressure is decreased to  $10^{-9}$  mbar. The finite desorption rate at room temperature does not allow to maintain the coverage of 0.7 ML ; therefore it decreases down to it expected value of 0.55 ML at  $10^{-9}$  mbar (**Chapter 3**), like in **Fig. 5.9**, but more slowly. The low frequency band blue shifts when the coverage decreases and its intensity rises, while the high frequency band (compressed CO) red shifts and decreases in intensity. The evolution of the CO coverage is slower in this desorption experiment than in the experiment of **Fig. 5.9** and in the adsorption experiment of **Fig. 3.6**, allowing to observe a collection of  $\approx 7$  spectra between 0.55 and 0.7 ML, which show very clearly the shift of the band of uncompressed CO down to  $1920\text{ cm}^{-1}$ . Contrary to the experiment of **Fig. 5.9** for which under  $10^{-9}$  mbar of CO, we could only see the CO on the surface during 2 min before it was oxidized, here, CO can still be observed after 8 min (dark yellow curve) in the compressed phase (coverage above 0.5 ML).

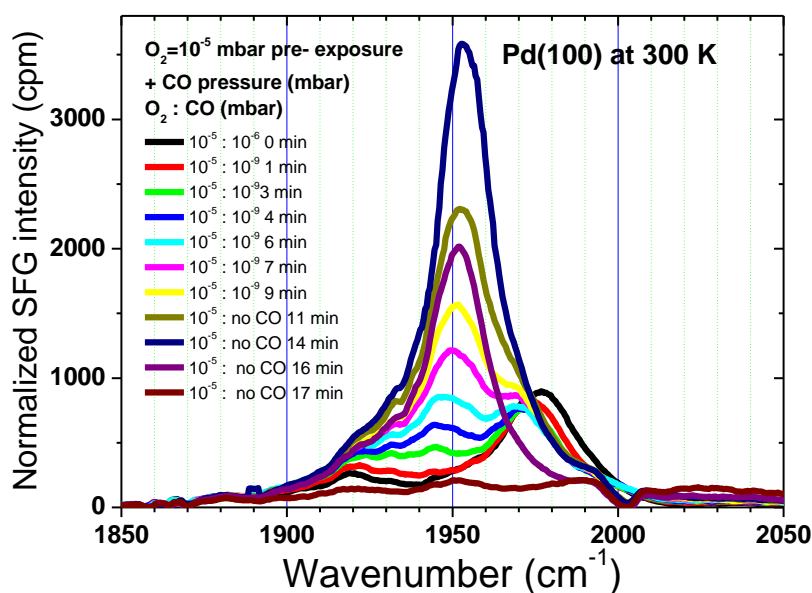


**Fig. 5.10.** SFG spectra of CO oxidation on CO poisoned Pd(100) crystal surface, the  $O_2$  pressure is kept at  $10^{-5}$  mbar and CO pressure is decreased from  $10^{-6}$  down to 0 mbar. All spectra are normalized by the area of their reference spectrum.

After 10 min, the CO valve has been closed in order to decrease further the adsorption rate. As a consequence, the coverage continues to decrease, reaches half coverage (which corresponds to the maximal SFG intensity (black curve on **Fig. 5.10**). After this point, 2-3 min are enough to completely remove the CO layer from the surface.

The comparison between the experiments of **Fig. 5.9** and **5.10** shows that the poisoning effect is to block completely the adsorption of O<sub>2</sub> only when the CO coverage is above 0.5 ML, in agreement with the literature. By contrast, below 0.5 ML O<sub>2</sub> adsorption occurs and CO is as quickly oxidized in **Fig. 5.10** (no pre-exposure to CO) as in **Fig. 5.9**. In **Fig. 5.9** and **5.10** the spectra above 0.5 ML correspond to CO with O present in **Fig. 5.9** and absent in **Fig. 5.10**. The spectra are shown in **Fig. 5.11** to visualize the influence of O on the CO spectra. The peak frequency of red curve is 9 cm<sup>-1</sup> higher than the black, compared to 4 cm<sup>-1</sup> shift from 10<sup>-7</sup> to 10<sup>-6</sup> mbar in the case of CO adsorption (**Fig. 3.5**). The effect of O is therefore essentially a frequency shift of ≈ 5 cm<sup>-1</sup> to the blue and a ≈ 25% increase of bandwidth at 0.5 ML CO coverage. What is remarkable is the fact that the presence of O atoms does not seem to prevent compression to occur. Well ordered structures of CO+O have been reported on different metals where the CO coverage is as large as in the absence of O [57]. However, the presence of O atoms in sufficient quantity and stability to insure the surface to remain reactive while the CO layer is compressed may seem surprising. We will see below that this is not observed at larger O<sub>2</sub> pressures.

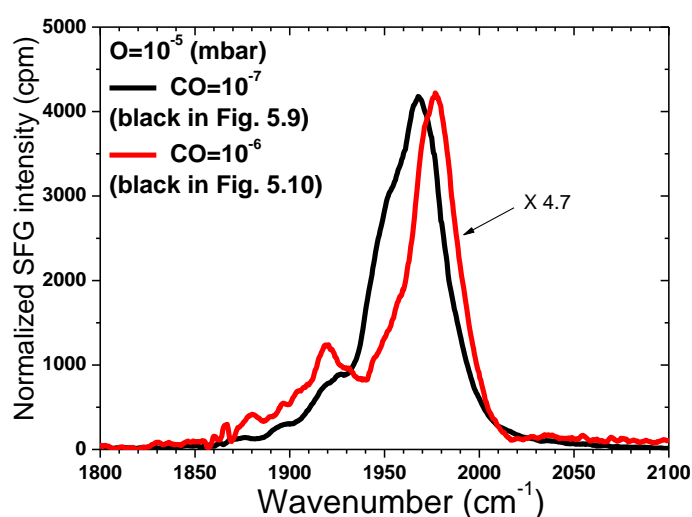


**Fig. 5.11.** Comparison of SFG spectra with 10<sup>-5</sup> mbar O<sub>2</sub> + 10<sup>-7</sup> mbar CO (black in **Fig. 5.9**) and 10<sup>-5</sup> mbar O<sub>2</sub> + 10<sup>-6</sup> mbar CO (black in **Fig. 5.10**) on Pd(100).

In summary, we observe that CO oxidation on bare Pd(100) is detectable at room temperature below 0.5 ML of CO. It is observable if the CO coverage is larger than 0.5 ML with a pressure ratio  $O_2/CO > 10^3$  only on an  $O_2$  pre-exposed Pd surface. For a smaller  $O_2/CO$  ratio, CO adsorption is faster than oxidation and the surface becomes saturated by CO and inactive. This limitation to the pressure ratio above  $10^3$  holds for the temperature domain to which we are restricted. It is known that at higher temperature, the onset of CO desorption allows to keep the CO coverage below saturation (i.e. below 0.5 ML), allowing to use a pressure ratio  $O_2 / CO$  close to unity.

In the industry, higher pressures are used. Therefore we have recorded spectra up to 1 mbar of  $O_2$ , and adapted the CO pressure as to avoid self-poisoning, that is, keeping the  $O_2 / CO$  pressure ratio above 1000 (we have tried to oxidize CO at high CO pressure : 1 mbar  $O_2$  + 1 mbar CO ; such high CO pressure leads to high CO adsorption rate overcoming the oxidation rate). A CO pressure of  $10^{-4}$  mbar is used while the  $O_2$  pressure is fixed around 1 mbar. The experimental method is the following: 1). Introduce  $1.0 \times 10^{-4}$  mbar  $O_2$  into the UHV chamber for 20 min. 2). Decrease  $O_2$  to  $2.0 \times 10^{-5}$  mbar and introduce  $1.0 \times 10^{-4}$  mbar CO; 3). Increase the  $O_2$  pressure until the CO band disappears. These two steps are for checking that the surface is reactive before we go to higher pressure. 4) If the CO band persists at 1 mbar  $O_2$  pressure, the sample is heated to make CO vanish. SFG spectra with 60 sec acquisition time are recorded at each step. The result for Pd(100) is shown in **Fig. 5.12**.

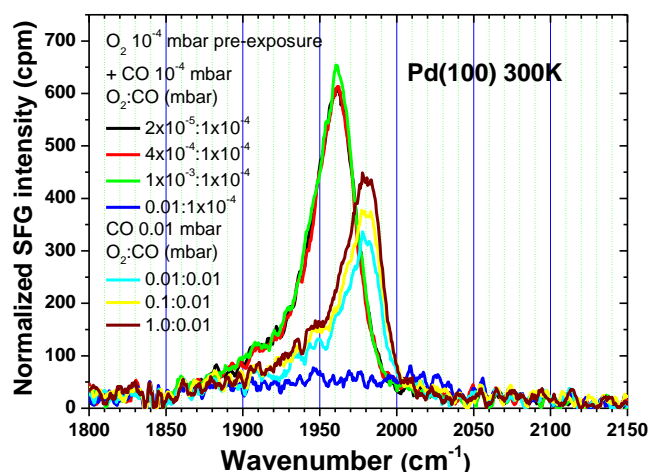


**Fig. 5.12.** SFG spectra of CO adsorbed on an  $O_2$  precovered Pd(100) at 300K. The  $O_2$  pressure is increased from  $1.0 \times 10^{-5}$  to 1 mbar under a fixed CO pressure, which is first of  $10^{-4}$  mbar (reaction observed) and then  $10^{-2}$  mbar (no reaction observed). Spectra are normalized by the area of the reference SFG spectrum.

In **Fig. 5.12**, after introducing  $1.0 \times 10^{-4}$  mbar CO to the  $O_2$  pre-treated Pd(100) sample, the SFG spectra of the adsorbed bridge CO band is at  $1962 \text{ cm}^{-1}$ , with no indication of CO layer compression. Upon increasing the  $O_2$  pressure from  $2 \times 10^{-5}$  to  $4 \times 10^{-4}$  and then to  $1 \times 10^{-3}$  mbar, the CO band (black, red and green curves) intensity and frequency do not change, indicating the same CO coverage. The CO coverage does not change in this case because  $a_{CO} > \sigma_{O+CO}$ . The adsorbed CO can quickly compensate the reacted CO. When the  $O_2$  pressure is increased from  $1 \times 10^{-3}$  to  $1 \times 10^{-2}$  mbar,  $a_{CO} < \sigma_{O+CO}$  and all the CO can be oxidized rapidly (blue). There is therefore a critical  $O_2$  pressure between  $10^{-3}$  and  $10^{-2}$  mbar for reacting all adsorbed CO. When the CO pressure is increased to  $10^{-2}$  mbar, the CO band appears again at higher frequency ( $1981 \text{ cm}^{-1}$ ) and smaller intensity, indicating that a compressed CO layer has now been formed. Accordingly, the surface is now poisoned as confirmed by the fact that increasing the  $O_2$  pressure again from  $10^{-2}$  mbar to 1.0 mbar has no effect on CO coverage. Thus in **Fig. 5.12** the blue ( $10^{-2}$  mbar  $O_2$  and  $10^{-4}$  mbar CO) and orange (1 mbar  $O_2$  and  $10^{-2}$  mbar CO) spectra, which are obtained for the same  $O_2/CO$  pressure ratio of  $10^2$ , correspond to reactive (O pre-exposed Pd) and poisoned surfaces.

### 5.2.4 Size effect of CO oxidation on Pd NPs

The same SFG experiments (shown in **Fig. 5.12**) have been realized on NP for different equivalent thicknesses of Pd (16 ML, 4 ML, 1 ML) to study the size effect of Pd NP on the catalytic CO + O reaction.

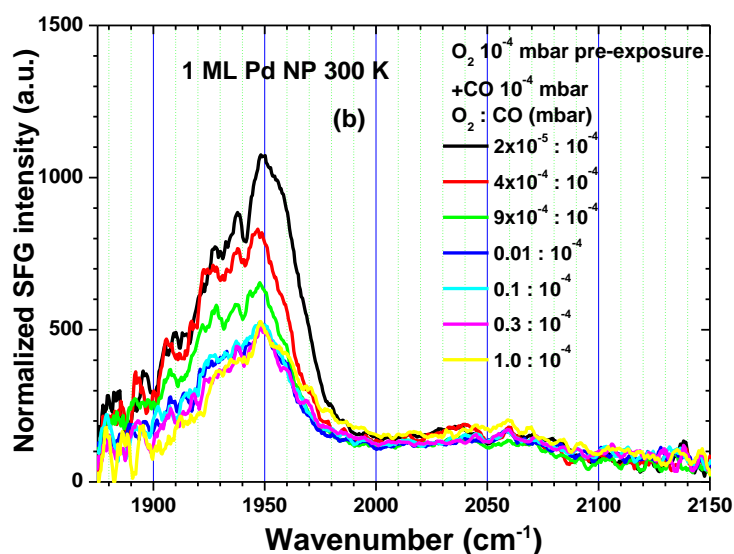
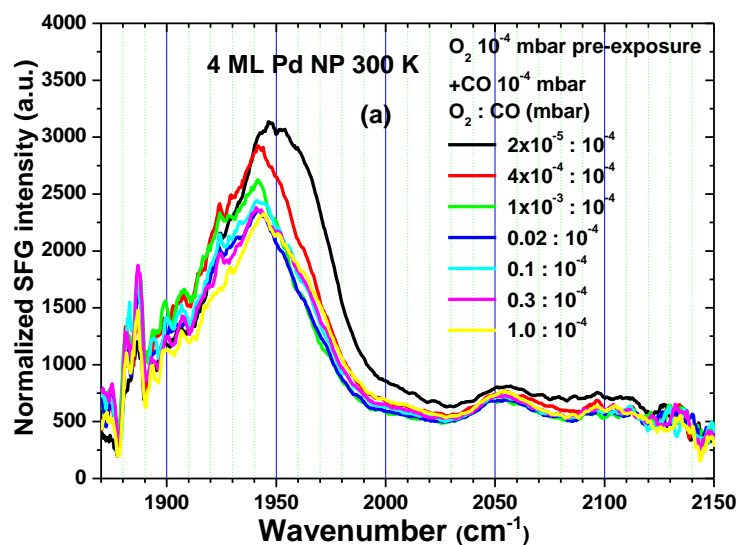


**Fig. 5.13.** SFG spectra of CO ( $10^{-4}$  mbar) adsorbed on  $O_2$  pre-treated ( $10^{-4}$  mbar  $O_2$  20 min) (a) 4 ML; (b) 1 ML Pd NP supported by 3ML MgO/ Ag(100) as function of  $O_2$  pressure at 300K. The spectra are normalized by the spectra of reference.

In the SFG results for 16 ML Pd NP, the bridge CO band decrease in frequency and intensity during the increase of  $O_2$  pressure then completely vanishes for an oxygen pressure of 0.03 mbar. This is a clear evidence for CO oxidation efficiency on large coalesced NP. The oxidation reaction on 16 ML Pd NP resembles to Pd(100) but the efficiency on NP seems to

be weaker than on the single crystal. In **Fig. 5.13a**, for 4 ML of Pd NP, with an increase of O<sub>2</sub>, a small decrease in intensity is observed, which is going along with a small red-shift of the CO frequency of 5 cm<sup>-1</sup>, but even an increase of O<sub>2</sub> to 1 mbar does not remove CO from the surface. It means that a small part of adsorbed CO are been oxidized. As a preliminary

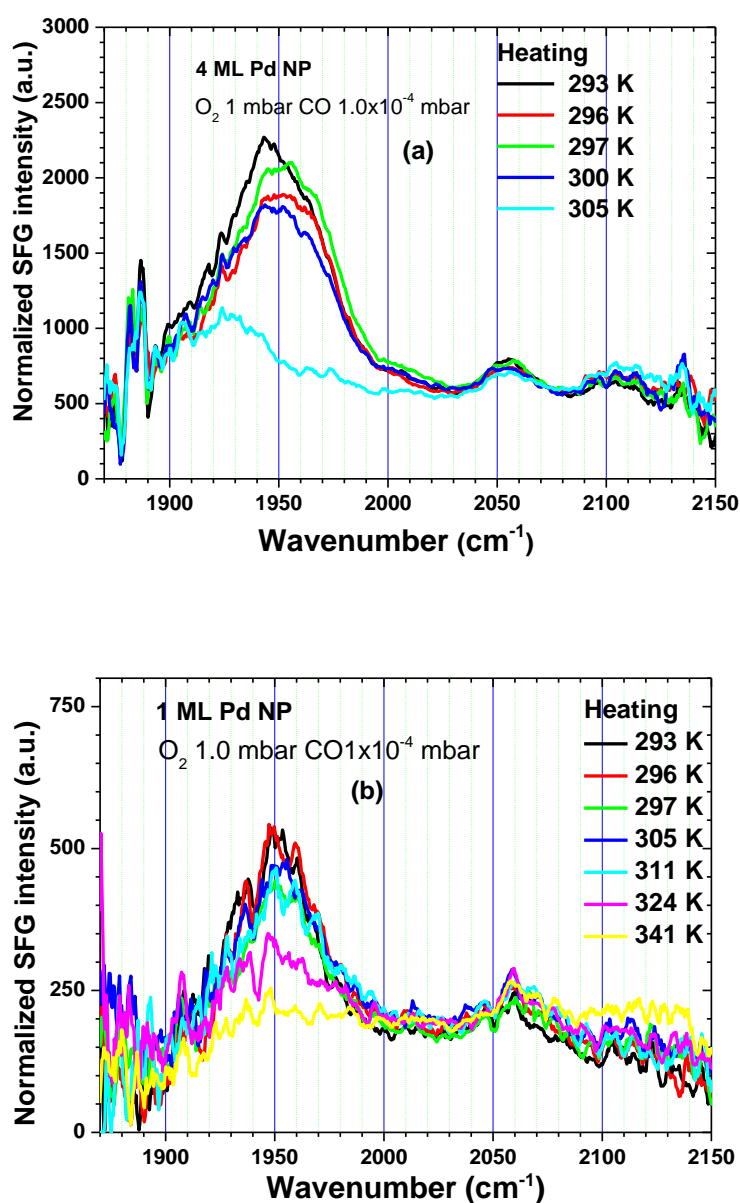


**Fig. 5.14.** SFG spectra of CO  $1.0 \times 10^{-4}$  mbar + O<sub>2</sub> 1.0 mbar adsorbed on (a) 4 ML; (b) 1 ML of Pd NP/ 3ML MgO/ Ag(100) samples upon heating. The spectra are normalized by the spectra of reference.

conclusion, we can argue that if some CO adsorption sites are equally reactive compared to coalesced films of Pd or Pd(100), the reactivity is lower for a large number of adsorption sites on the NP. In **Fig. 5.13b**, the CO bridge band intensity adsorbed on 1 ML of Pd NP decreases of ~60% upon an increase of O<sub>2</sub> pressure from 2.0×10<sup>-5</sup> to 9.0×10<sup>-4</sup> mbar, and then keeps constant until the O<sub>2</sub> pressure is increased up to 1 mbar. This result is similar to 4 ML Pd NP, i.e. there are two types of adsorbed CO, one can be oxidized at low O<sub>2</sub> pressure (< 10<sup>-3</sup> mbar), but the other one are more difficult to be reacted. Similarly to 4 ML of Pd NP case, the high-frequency part (~2060 cm<sup>-1</sup>) of the spectra is slightly modified. To oxidize the rest part of CO, both sample (4 ML and 1 ML of Pd NP) should be heated.

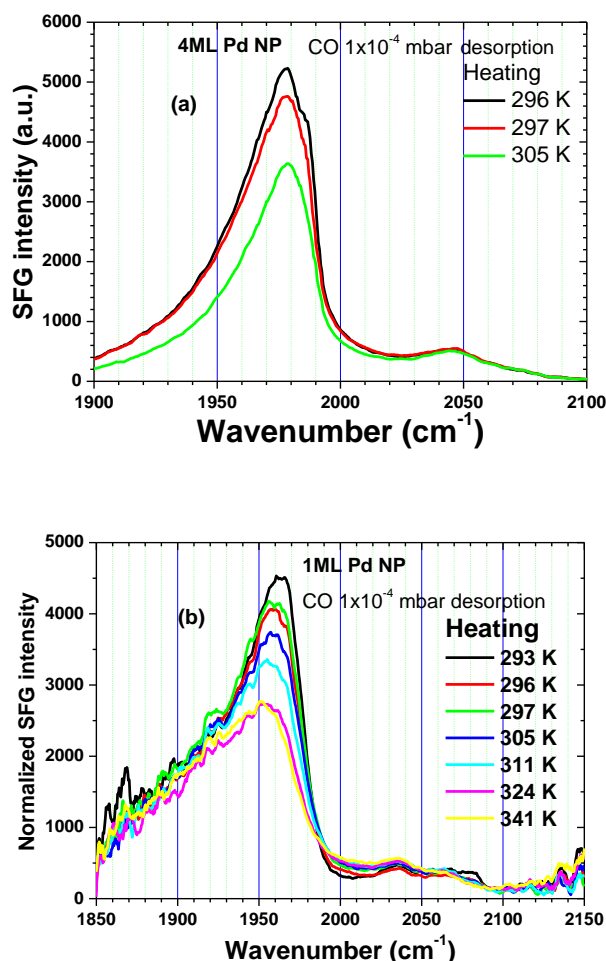


**Fig. 5.15.** SFG spectra of CO 10<sup>-4</sup> mbar during heating on (a) 4ML and (b) 1 ML of Pd NP. (a) All spectra are normalized by the reference areas and (b) all spectra are normalized by the reference spectra.

As shown in **Fig. 5.14a**, the CO band almost does not change from 293 K to 305 K. Then the temperature reaches 310 K, the CO band quickly decreases in intensity and stays at the same intensity even at 320 K. As soon as the temperature is high enough, the CO coverage decreases below 0.5 ML and CO oxidation becomes faster. But surprisingly, the stability of a small part of CO band above 320 K is still not well understood. Probably these CO are more strongly bind to the Pd NP. In **Fig. 5.14b**, a similar behavior is found for 1 ML of Pd, but the required temperature to oxidize CO is higher, i.e.  $\sim 370$  K. The effect of the CO desorption during heating without adsorbed  $O_2$  on 4 ML and 1 ML of Pd NP have been measured to compare with the CO oxidation during the heating as shown in **Fig. 5.15**. This allows us to remove its contribution.

As shown in **Fig. 5.15** the intensity of CO band decreases by 30-40%, which is induced by CO desorption during heating. These results clearly confirm that the disappearing of the CO band for both NP size in **Fig. 5.14** comes partially from the CO oxidation.

We have combined all the results of CO oxidation on Pd(100) and Pd NP with different sizes at 300 K (**Fig. 5.16a**) and upon heating (**Fig. 5.16b**).

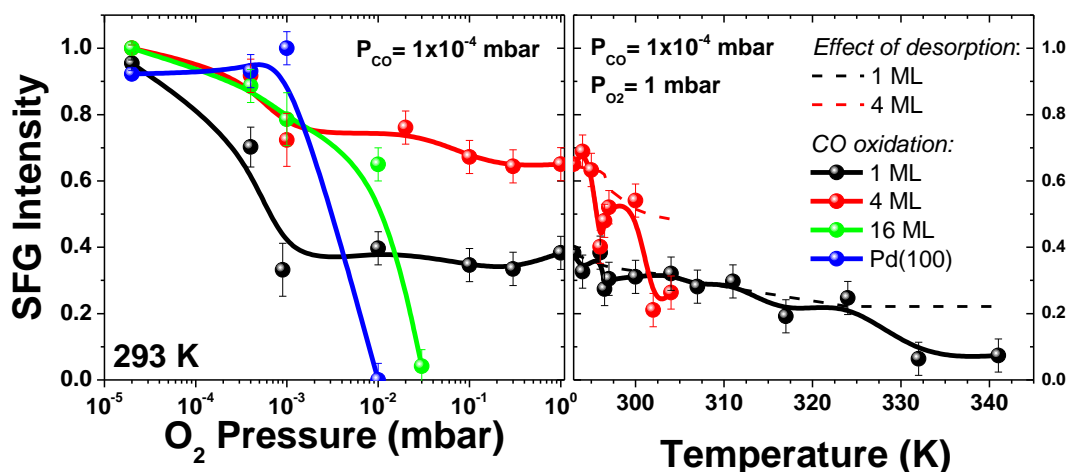


**Fig. 5.16.** The SFG spectra intensity of catalytic oxidation of bridge CO band on Pd(100) (blue) and Pd NP with different size 16 ML (green), 4 ML (red) and 1 ML (black), (a) At 300K,  $P_{CO} = 1 \times 10^{-4}$  mbar fixed,  $P_{O_2}$  varied from  $10^{-5}$  to 1 mbar; and (b) Heating (for only 4 ML and 1 ML),  $P_{CO} = 1 \times 10^{-4}$  mbar fixed,  $P_{O_2} = 1$  mbar fixed.

In **Fig. 5.16a**, we observe that on Pd(100) surface the CO band does not change with until to  $10^{-3}$  mbar  $O_2$ , then it disappears with 0.01 mbar  $O_2$ . 16 ML of Pd NP shows similar behavior as Pd(100).. For the case of 4 ML of Pd NP, except a small decrease of CO band intensity at the beginning of increasing the  $O_2$ , the CO band exists with up to 1.0 mbar  $O_2$ . Then during the heating, the CO band is almost removed at the temperature higher than 320 K. This disappearing of CO band should be CO on terrace (100) of NP because on 4 ML Pd NP, the main facet is terrace(100). By comparing the CO behavior on Pd(100), 16 and 4 ML Pd NP, we observe that the catalytic oxidation of CO adsorbed on terrace(100) becomes more difficult when the NP size is decreased. For 1 ML Pd NP, by such analogy, the disappearing of CO band with a heating to 340 K should be the CO on terrace(100) of Pd NP. But as discussed in the case of 4 ML Pd NP, there is another part of CO which have already been removed at 300 K with  $10^{-5}$  to  $10^{-2}$  mbar  $O_2$ . These CO are not on the terrace(100). According to [36] the  $O_2$  near the NP/support interface dissociate readily, resulting in self-limiting partial oxidation of the Pd NP, the NP/support interface with more dissociated O(ads) facilitate the CO oxidation. It is very possible that the part of CO which is oxidized with a low  $O_2$  pressure at 300K is the CO adsorbed near Pd/MgO interface. On the other hand, compared to CO oxidation process on Pd(100), on Pd NP there are different types of CO adsorption, and the CO diffusion on the Pd NP is less effective, especially from the edges facet to terrace or between the sites with different coordination numbers, which leads to the decreasing of the bridge CO on the Pd/MgO interface already at a lower  $O_2$  pressure such as  $4 \times 10^{-4}$  mbar, but the CO on terrace (100) keeping constant.

Why the CO catalytic oxidation happens easier on Pd NP at larger size? The CO which can be easily oxidized should be weakly bonded and have a lower adsorption energy. So the CO adsorbed on larger Pd NP has smaller adsorption energy. As shown in **Fig. 5.17** the potential diagram of CO+ $O_2$  catalytic reaction on Pd(100) and Pd NP with different size 16 ML, 4 ML and 1 ML. The CO adsorbed on Pd(100) has the lowest energy of adsorption and the smallest reaction barrier. Correspondingly the smaller Pd NP has the larger energy of adsorption and the larger reaction barrier. This is in good agreement with the result of the Chapter 4. Indeed the decrease of the singleton frequency at small NP size was attributed to an increase of the binding strength between CO and the NP, as confirmed by DFT calculations. On contrary, since the oxide support play an important role in the size effect of NP, the different oxide support can lead to an opposite trend in the change of the CO adsorption energy on smaller NP. For example T. Schalow et.al have reported that the oxidation of CO is easier at the smaller Pd NP supported by  $Fe_3O_4$  [12].

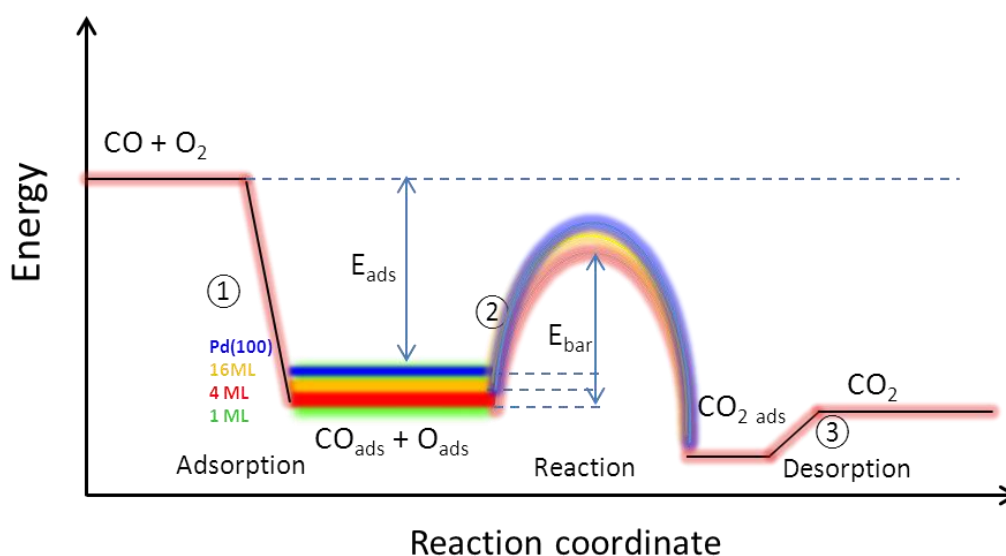


*Fig. 5.17. Potential energy diagram of catalyzed CO oxidation on Pd(100) and Pd NP with different size.*

### 5.2.5 CO + O co-adsorption on Pd NPs with a high CO pressure at 300 K

At high CO pressure, as discussed in **Chapter 4**, the bridge CO adsorbed on Pd NP is accompanied by a significant on top band. It is valuable to study the case of CO + O co-adsorption on Pd NP at a higher pressure.

In the SFG spectra of CO adsorption with until to 1 mbar on 1 ML Pd NP/ 3 ML MgO/ Ag(100) surface at 300 K shown in **Fig. 4.5** the on top CO adsorption band is small compared to the bridge band (about 10-15% in intensity). Even if shown in Ref [44] with a CO pressure up to 100 mbar on 1 ML Pd NP/Al<sub>2</sub>O<sub>3</sub>, the on top CO band fraction is 60% of the bridge band. But in the experiment of high pressure O<sub>2</sub>+ CO co-adsorption (O<sub>2</sub> first) at 300 K shown in **Fig. 5.18**, the SFG spectra show some different aspect of on top band.

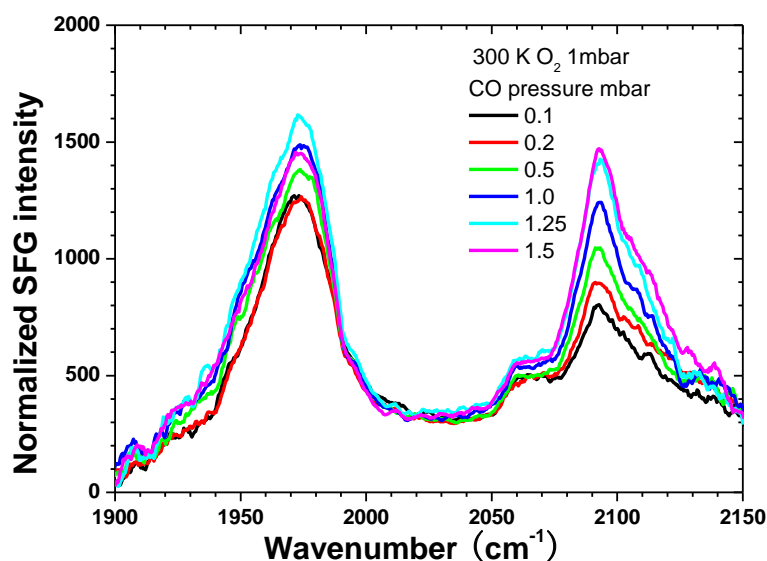


*Fig. 5.18. SFG spectra of O<sub>2</sub> 1.0 mbar + CO 0.1-1.5 mbar co-adsorption and catalysis on 1ML Pd NP/ 3ML MgO/ Ag(100) surface at 300K. The spectra are normalized by the area of reference.*

The experiment is done by: 1) introducing 1 mbar O<sub>2</sub> to the prepared 1ML Pd NP/ 3ML MgO/ Ag(100) surface at 300K in UHV, 2) increase the CO pressure and measure the SFG spectra.

As shown in **Fig. 5.18**, the on top band on O<sub>2</sub> pre-adsorbed (1.0 mbar) Pd NP increases quickly with the CO pressure from 0.1 to 1.5 mbar to almost the same intensity level of the bridge band. These results indicate that the O<sub>2</sub> pre-adsorption helps the on top CO adsorption on a 1 ML Pd NP sample. This suggests that at such high O<sub>2</sub> pressure, “incorporated” [24] O atoms exist and favor adsorption of CO in on top sites. This experiment is an indirect proof that NPs get more “oxidized” than single crystals.

## 5.3 Pump-probe study of O<sub>2</sub>+CO co-adsorption on Pd NP

### 5.3.1 Introduction

The knowledge of the dynamic of interaction between molecules and surfaces, such as the exchange of energy between electrons, phonons and vibrations of adsorbed molecules, the

diffusion of molecules, the photo-desorption, and the chemical reaction is of a basic importance in surface science [45-49]. The transfer of electron between metal and molecules is an essential characterization of molecular electronics. Especially the connection between the atomic structure of surface hybrid, the electronic structure of molecules and the photonic properties of the system are interdependent. The time scale of these processes arrange from picosecond to femtosecond. Therefore the ultra-short laser pulse (fs) allows us to observe directly the ultra-fast dynamic on the surface. As already discussed in Chapter 1 **Fig. 1.5**, The transient states of molecules excited by the laser pump pulse can be probed on time domain by a SFG probe [47, 48, 50]. The SFG is proved to be the tool most pertinent to study the dynamic of molecular interaction [51-53]. It can measure the characteristic time of energy exchange between electrons and molecule adsorbed, identify the mode of molecule-surface vibration, determinate if the photo-desorption process and the photo-induced oxidation reaction imply a direct electronic excitation [56].

On the metal, the direct excitation of molecules by the incident photons is not important because the excited electron of molecule rest only several femtoseconds on the molecules; the other side the molecules absorb only a small fraction of incident pump pulse. The rest photons are absorbed by less than ten nanometer of metal surface because the absorption of metal is strong at the wavelength of pump beam.

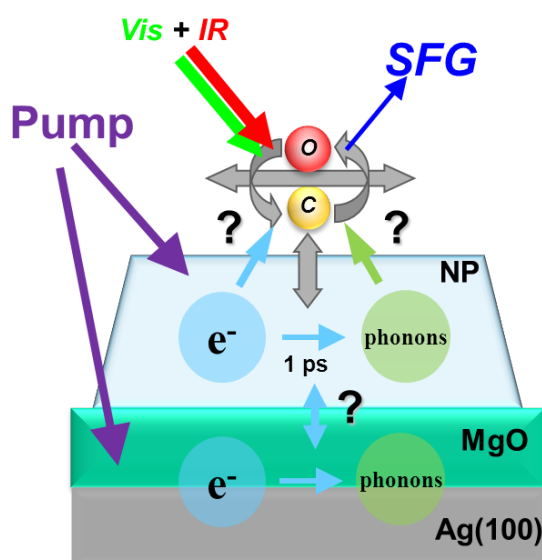


*Fig. 5.19. Sketch of CO pump – probe experiment on Pd NP/MgO/Ag(100) sample.*

The duration of impulsion is longer than the average collision time between electrons, but shorter than the characteristic time of energy exchange between electrons and phonons on

one hand, electron and molecules on the other hand (**Fig. 5.19**). The metal surface can be strongly excited by the incident pump pulse, with an energy distribution characterized by an electronic temperature  $T_e$  of several thousand Kelvin, out of the equilibrium with the phonons and the adsorbed molecules, which are still cold. The excited electrons evolve with three ways: they diffuse quickly to the metal volume, relax to the phonons and interact with the adsorbed molecules.

The interaction with the adsorbed molecules is effectuated by an important number of electrons transferred to molecules, which induces for every electron transfer an energy transfer  $E \rightarrow V$  in the molecule. This is considered as the principal mechanism of molecule excitation. (model of 'MGR' and of Antoniewicz) [54, 55]. If the transferred excitation at the molecule is enough, it can diffuse, react with a co-adsorbed molecule or desorb [56].

In the experiment of pump-probe leading to a significant excitation of electron and the energy transfer between electrons and molecules, we expect to observe a changing of the width and frequency of CO vibrational band. The change of width is accompanied necessarily a change peak intensity of band (In SFG, in the case of Lorentzienne, the intensity is  $B^2/\Gamma^2$ , where  $B$  is the non-linear susceptibility and the width). We also expect that the intensity of the band of vibration decreases if the electronic excitation induces the diffusion or the desorption of the molecule. In [56] the desorption of CO induced by the pump pulse has been discussed: at a CO pressure  $10^{-4}$  mbar, the pump pulse (with a repeat frequency 1 kHz, energy 50  $\mu$ J) induced CO desorption can not be compensated by the rate of adsorption, so the probe pulse (SFG) at a long delay time (limit 200 ps), where the equilibrium of the surface (relaxation of electron-phonon and diffusion of heat) is almost terminated, gets the information of CO desorption induced by one pump pulse [56].

The pump pulse can excite the electrons of solid to a temperature of several thousands Kelvin. Then they start to relax to a temperature of several hundreds of Kelvin in about 1 ps on a poor metal conductor such as platine, 10 ps on a better conductor such as copper [48]. During this interval, the electrons can excite the adsorbed molecules, and we want to know if this excitation is efficient, i.e. if it occurs in hundreds of femtoseconds. This excitation has an effect of heating the modes of substrate-adsorbate vibration. This mode is manifested by the ultra-rapid, measurable changing of frequency and the vibration width. Therefore by measuring the frequency and vibration width changing of the CO band, we can evaluate the phenomenon of excitation of the metal surface electrons by the pump pulse and the exchange of energy between the electrons and the adsorbed molecules. In fact these dynamic depends

on the property of the sample surface, in our sample model the size of Pd NP, the thickness of MgO etc. The related work has been done in [56].

In this section, the pump-probe experiment is extended to the case of O<sub>2</sub>+CO co-adsorption on Pd NP.

### 5.3.2 Pump-probe study of O<sub>2</sub>+CO co-adsorption on Pd NP

As discussed in **Section 5.3.4**, the O<sub>2</sub>+CO co-adsorption on 1ML Pd NPs exhibits a large CO on top band at 1 mbar CO and O<sub>2</sub>. It is interesting to observe simultaneously the effect of a strong electronic excitation (by a pump pulse) on the two types of sites, bridge and on top, which to our knowledge has never been studied.

The experiment is done by 1) Pre-treatment of the sample (1 ML Pd NPs / 3 ML MgO / Ag(100)) with 10<sup>-4</sup> mbar O<sub>2</sub> 20 min; 2) Introduction of 1 mbar O<sub>2</sub> then 1.5 mbar CO; 3) adjust the 0 delay time of the pump pulse with respect to the SFG probe pulses (maximum of the VIS femto - IR femto SFG signal); 4) measurement of the pump-probe spectra for different pump energies of 5 μJ to 45 μJ.

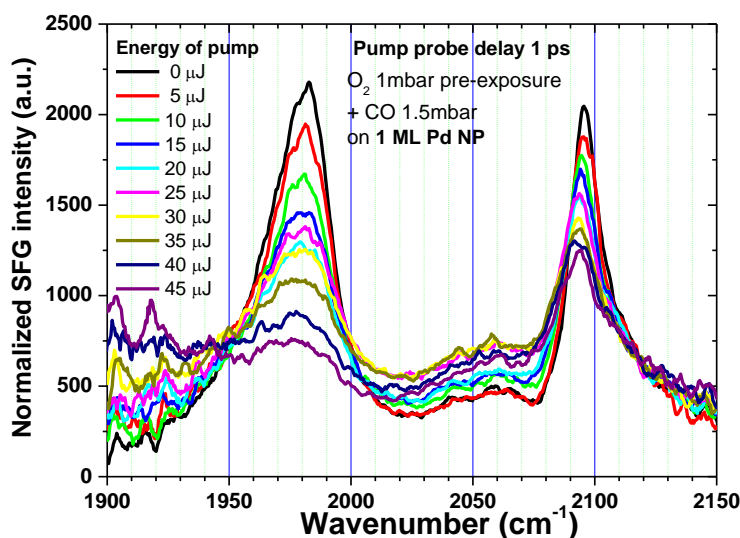


*Fig. 5.20* Pump-probe SFG spectra of O<sub>2</sub>+CO co-adsorption on 1 ML Pd NPs. The probe IR pulse arrives at the delay of 1 ps after the pump pulse. The pulse energy is varied from 5 μJ to 45 μJ.

In **Fig. 5.20** the “no-pump” (0 μJ) spectrum exhibits the bridge CO band at 1980 cm<sup>-1</sup> and the on top CO band at 2095 cm<sup>-1</sup> with a comparable intensity. By increasing the pump

energy from 0  $\mu\text{J}$  to 45  $\mu\text{J}$ , we observe that the effect of the pump pulse on the bridge CO band is significantly larger than on on top CO. The CO bridge band intensity decreases down to 17% of its original value with a pump energy 45  $\mu\text{J}$ , compared to 50% for the CO on top band. The frequency of both bands decreases by  $\approx 5 \text{ cm}^{-1}$ .

The preliminary conclusion of this experiment is that the on top sites populated at high pressure are little sensitive to the presence of electrons above Fermi level. **Fig. 5.21** is made to explain how the pump pulse excites electrons which then interact with empty bands above Fermi level. In **Fig. 5.21** the red distribution indicates the hot electrons excited by the pump pulse. Hot electrons are subject to multiple excitations and to collisions between them that result in a “Boltzmann-like” distribution. The blue part is the filled part of the metal conduction band. The green and orange lines represent bands that may involve molecular orbitals of bridge and on top CO, respectively. This preliminary experiment shows that pump-probe may reveal differences in the electronic structure of CO at the different sites. DFT calculations are required to interpret them in details.

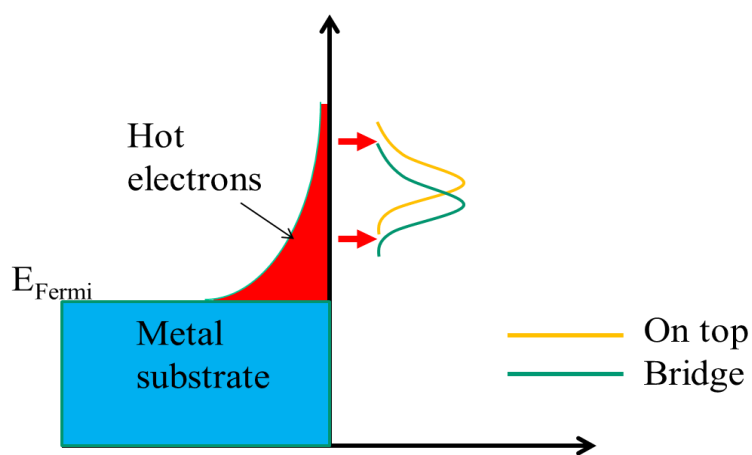


*Fig. 5.21 Possible energy diagram of CO bridge and on top density of states disturbed by electrons excited by the pump pulse.*

## 5.4 Conclusion

This preliminary study of catalysis by SFG is limited to pressures of 2 mbar, and to a sample temperature that does not allow to probe the optimal catalytic conditions because the CO desorption rate cannot be raised high enough. As a result, we must work with a large

excess of O<sub>2</sub> over CO (3 orders of magnitude on the single crystal and 1-2 orders of magnitude on NPs). In addition, our tentative measurement of CO<sub>2</sub> production rate did not work, so our only observable is adsorbed CO. This allows nonetheless to obtain relevant information on the pressure and material gaps, that is if adsorption sites of reactants change from UHV conditions to mbar range pressure.

On Pd(100) single crystal, we observe in details the self-poisoning effect of CO. From a spectroscopic point of view, the bridge band shifts to the blue by  $\approx 5 \text{ cm}^{-1}$  when O<sub>2</sub> is pre-adsorbed and its bandwidth increases by  $\approx 25\%$ . The reaction seems to proceed like in UHV up to  $10^{-3}$  mbar CO / 1 mbar O<sub>2</sub>. The main special effect of O<sub>2</sub> pressure is that the compression of the CO layer is observed at pressures below  $10^{-4}$  mbar and not above. This suggests that more oxygen adsorbs above  $10^{-4}$  mbar, and/or in a different state than at low pressure.

On Pd NPs, several observations are made : (1) O<sub>2</sub> adsorption quenches most of the NR contribution to SFG (which is stronger on NP than on the single crystal). This occurs below  $10^{-4}$  mbar. It shows that states around Fermi level exist on the NPs and not on the single crystal, and they are involved in O<sub>2</sub> chemisorption. A candidate for these states is the Pd atoms near the oxide, whose chemical environment is most different from Pd metal. (2) bridge sites are by far the sites where CO is most affected by the conditions at the surface (partial pressures and temperature). The observations suggest that several types of bridge bonded CO coexist : Pd(100)-type, more reactive CO, and less reactive CO. The less reactive CO only reacts as the temperature is raised. By contrast, CO in the atop sites is unreactive in our temperature range. Reactive sites may be expected to be little populated (because they are reactive) : filled from other sites and emptied by the catalytic reaction. The reactive site could be any of the regular (100) facet sites, the (100) facet edges or the small lateral facets near the oxide. (3) above  $10^{-1}$  CO pressure, linear sites are significantly more populated, but we could not check their impact on reactivity.

In summary, CO occupies a variety of adsorption sites on NPs that depend on the pressure and temperature. For CO pressures below  $10^{-4}$  mbar, bridge sites are the key sites for reactivity, but there are several types of them. Our results are not in contradiction with the suggestion made in the literature that the NP are more reactive near the oxide. More detailed information could be obtained : (1) from experiments in a broader, more relevant temperature

range, and with a measurement of the CO<sub>2</sub> production rate. (2) from quantum chemistry calculations that might help to learn about the location and stability of the bridge bonded sites.

## Reference

- [1] T. Engel, and G. Ertl, et.al. *The chemical physics of solid surfaces and heterogeneous catalysis*. Elsevier. Amsterdam, Oxford, and New York, (1982)
- [2] F.P. Leisenberger, G. Koller, M. Sock, S. Surnev, M.G. Ramsey, F.P. Netzer, B. Klötzer, K. Hayek, *Surf. Sci.* 445, 380, (2000)
- [3] W. Andrzej, R. Elena Savinova, G. V. Constantinos, *Catalysis and Electrocatalysis at Nanoparticle Surfaces*, (2003)
- [4] D. Zemlyanov, B. Aszalos-Kiss, E. Kleimenov, D. Teschner, S.Zafeiratos, M. Haevecker, A. Knop-Gericke, R. Schlögl, H. Gabasch, W. Unterberger, K. Hayek and B. Klötzer, *Surf. Sci.*, 600, 983. (2006)
- [5] E. H. Voogt, A. J. M. Mens, O. L. J. Gijzeman and J. W. Geus, *Surf. Sci.*, 373, 210. (1997)
- [6] G. Ketteler, D. F. Ogletree, H. Bluhm, H. Liu, E. L. D. Hebenstreit and M. Salmeron, *J. Am. Chem. Soc.*, 127, 18269. (2005)
- [7] H. Conrad, G. Ertl and J. Küppers, *Surf. Sci.*, 76, 323. (1978)
- [8] H. W. Meng and P. J. Shin, *J. Phys. Chem. C*, 116, 18803 (2012)
- [9] T. Engel, and G. Ertl, *J. Chem. Phys.* 69, 1267, (1978)
- [10] A. Alavi, P. Hu, T. Deutschl, P. L. Silvestrelli and J. Hutter, *Phys. Rev. Lett.* 80, 3650 (1998)
- [11] C. Stampfl and M. Scheffler, *Phys. Rev. Lett.* 78, 1500 (1997)
- [12] T. Schalow, B. Brandt, D. E. Starr, M. Laurin, S. K. Shaikhutdinov, S. Schauer mann, J. Libuda and H.-J. Freund, *PCCP*, 9, 1347, (2007)
- [13] M. Haruta, *Catal. Today* 36 153. (1997)
- [14] N.F. Zheng and G. D. Stucky, *J. Am. Chem. Soc.* 128, 14278. (2006)
- [15] M. Haruta. *Gold Bull.* 37, 27 (2004)
- [16] J. R. Anderson, M. Boudart *Catalysis: Science and Technology, Volume 4*, (1983)
- [17] T. Dellwig, G. Rupprechter, H. Unterhalt, and H.-J. Freund, *Phys. Rev. Lett.* 85, 776 (2000)
- [18] G. A.Somorjai and G. Rupprechter, *J. Phys. Chem. B* 103 1623, (1999)
- [19] T. Pery, M.G. Schweitzer, H.-R. Volpp, J. Wolfrum, L. Ciossu, O. Deutschmann and Warnatz, *J. Proceedings of the Combustion Institute, The Combustion Institute*, 973. (2002)
- [20] G.Rupprechter, *Adv. Catal.* 51, 133, (2007)
- [21] K. W. Kolasinski *Surface Science-Foundations of Catalysis and Nanoscience*. (2002)

- [22] H. Gabasch et al. *Phys. Chem. Chem. Phys.*, 9, 533, (2007)
- [23] I. Stara. V. Nehasil, V. Matolin, *Surf. Sci.* 365, 69, (1996)
- [24] E.S. Putna, J.M. Vohs, R.J. Gorte, *Surf. Sci.* 391, L1178, (1997)
- [25] I. Meusel, J. Hoffman, J. Hartmann, M. Heemeir, M. Baumer, J. Libuda, H.J. Freund, *Catal. Lett.* 71, 5, (2001)
- [26] C. J. Zhang and P. Hu, *J. Am. Chem. Soc.* 123, 1166 (2001)
- [27] U. Burghaus, I. Z. Jones and M. Bowker, *Surf. Sci.*, 456, 326, (2000)
- [28] K. Yagi. D. Sekiba, H. Fukutani, *Surf. Sci.* 442, 307, (1999)
- [29] N. Kasper, P. Nolte and A. Stierle, *J. Phys. Chem. C*, 116, 21464, (2012)
- [30] S. Ladas, R. Imbihl, G. Ertl, *Surf. Sci.* 280, 14 (1993)
- [31] T. Engel and G. Ertl, *Adv. Catal.*, 28, 1–78. (1979)
- [32] T. Engel and G. Ertl, *Chem. Phys. Lett.*, 54, 95. (1978)
- [33] T. Engel and G. Ertl, *Proc. 7th Int. Vac. Congr.*, 2, 1365. (1977)
- [34] P. Salo, K. Honkala, M. Alatalo and K. Laasonen, *Surf. Sci.*, 516, 247.(2002)
- [35] K. Bleakley, P. Hu, *J. Am. Chem. Soc.* 121, 7644. (1999)
- [36] Bokwon Yoon and Uzi Landman, *J. Phys. Chem. C*, 116, 9594, (2012)
- [37] C. N. Hinshelwood, *The Kinetics of Chemical change* (Clarendon press, Oxford, 1940).
- [38] W. Liu, Y. F. Zhu, J. S. Lian, and Q. Jiang, *J. Phys. Chem. C*, 111, 1005, (2007)
- [39] Feng Gao, Mathew Lundwall, and D.Wayne Goodman, *J. Phys. Chem. C*, 112, 6057, (2008)
- [40] W. K. Kuhn, J. Szanyi, et D.W. Goodman. *Surf. Sci. Lett.* 274, L611 (1992).
- [41] C. Louis. *La catalyse hétérogène à base d'or. L'actualité chimique - janvier 2005 - n 282*
- [42] A. Politano and G. Chiarello, *J. Phys. Chem. C*, 115, 13541 (2011)
- [43] H. Unterhalt, P. Galletto<sup>1</sup>, M. Morkel, G. Rupprechter, and H.-J. Freund, *phys stat sol* 188 No.4 1495 (2001)
- [44] I. V. Yudanov, R. Sahnoun, K. M. Neyman and N. Roisch, *J. Phys. Chem. B*, 107, 255 (2003)
- [45] H. L. Dai. *Laser Spectroscopy and Photochemistry on Metal Surfaces, Singapore* (1995)
- [46] H. Arnolds, M. Bonn. *Surf. Sci. Rep.* 65, 4566 (2010)
- [47] F. Fournier, W. Zheng, S. Carrez, H. Dubost, B. Bourguignon. *Phys. Rev. Lett.* 92, 216102 (2004)
- [48] F. Fournier, W.Q. Zheng, S. Carrez, H. Dubost, B. Bourguignon. *J. Chem. Phys* 121, 4839 (2004)
- [49] I.M. Lane, Z.P. Liu, D.A. King, H. Arnolds, *J. Phys. Chem. C* 111, 14198 (2007).

- [50] H. Nigouchi, E. Yoda, N. Ishizawa, J. N. Kondo, A. Wada, H. Kobayashi, K. Domen, *J. Phys Chem B*, 109, 17217 (2005)
- [51] S. Nihonyanagi, D. Miyamoto, S. Idojiri, K. Uosaki, *J. Am. Chem. Soc.*, 126, 7034 (2004)
- [52] K. Uosaki, T. Yano, S. Nihonyanagi. *J. Phys. Chem. B*. 108, 19086 (2004)
- [53] M. Bonn, Ch. Hess, S. Funk, J. H. Miners, B. N. J. Persson, M. Wolf, G. Ertl. *Phys. Rev. Lett.* 84, 4653(2000)
- [54] P. R. Antoniewicz. *Phys Rev B*. 21, 3811 (1980)
- [55] D. Menzel. *Nucl. Instrum. Methods Phys. Res. B* 101, 1 (1995)
- [56] Thesis of Ahmed Ghalgaoui in University Paris Sud, (2012)
- [57] S. Schwegmann, H. Over, V. De Renzi, G. Ertl, *Surf. Sci.* 375, 91, (1997)



## Chapter 6

### Simulation and experiment SFG spectra on ODT with a visible pulse formed by a pulse shaper and a Fabry-Perot

<b>6.1 Introduction</b>	142
<b>6.2 Theory of SFG with a delayed visible pulse</b>	144
<b>6.3 Model of calculation</b>	146
6.3.1 Octadecanethiol (ODT)	147
6.3.2 Calculation of first-order polarization	148
6.3.3 Visible pulse formed by a Fabry-Perot etalon	149
6.3.4 Calculation of SFG with a delayed visible pulse in time domain	152
6.3.5 Effect of delay between IR and visible pulse in frequency domain: spectral phase	154
<b>6.4 Experiment set-up</b>	160
<b>6.5 Results and discussion</b>	161
6.5.1 SFG spectra of ODT	161
6.5.2 Experimental spectra	162
6.5.2.1. Spectra obtained with the FPetalon	162
6.5.2.2 Spectra obtained with the 4f pulse shaper	166
6.5.3. Spectro-temporal fit	167
6.5.3.1 Spectra obtained with the FP etalon	167
6.5.3.2 Spectra obtained with the 4f pulse shaper	169
6.5.4 Accuracy of purely spectral deconvolution into Lorentzian bands	169
6.5.4.1 FP etalon	169
6.5.4.2 4f pulse shaper	171
<b>6.6 Conclusion</b>	172
<b>References</b>	174

## 6.1 Introduction

An important drawback encountered in BroadBand Sum Frequency Generation (BBSFG) spectroscopy of molecules at surfaces arises from the existence of a so-called nonresonant (NR) contribution of the substrate to the SFG polarization. Numerous materials including metals, semi-conductors and insulators give rise to a background through the excitation of their electronic states. In particular the gold substrate is well known to give a strong nonresonant response [1]. The problem with NR background arises from the interference between resonant (R) and NR contributions. The NR phase and amplitude depend on the nature of the surface, on the presence of adsorbates and also on the wavelength of the visible light [2]. The phase difference between R and NR contributions is not known and is usually treated as an adjustable parameter in the fitting procedure. The parameters relative to molecular resonances, i.e. peak frequency, width and relative amplitude, can still be in principle obtained from SFG spectra. However Busson and Tadjeddine [3] have shown recently that the set of parameters extracted from the deconvolution of resonant spectra from the NR background was not necessarily unique when all parameters are allowed to vary. In addition to this background problem, BBSFG spectra suffer from distortion caused by truncation or apodization resulting from the imperfect upconversion of the first order polarization by the visible pulse.

In the recent years Dlott and his co-workers [4-8] have shown that it was possible to make a temporal discrimination between the shorter NR and longer R contributions. As a matter of fact the dephasing time of the electronic transitions of the metallic substrates is very short, e.g.  $T_2 = 8$  fs for polycrystalline gold [9], so that the nonresonant response can be considered as instantaneous and follows the excitation pulse ( $\sim 10$ - $100$  fs). In contrast the dephasing time of molecular vibrations at metal surfaces is typically in the ps range, so that both contributions can be separated in time. Temporal discrimination can in principle be achieved by delaying the visible with respect to the IR pulse by  $\sim 300$  fs. However time windowing with a symmetric picosecond pulse does not achieve a sufficiently high level of discrimination (**Fig. 6.7a**). A key innovation originally proposed by Lagutchev *et al.* [4] consists in using a Fabry-Perot (FP) etalon to produce an asymmetric picosecond pulse (**Fig. 6.7b**).

Other drawbacks of BBSFG have been reported by several authors. Even with a symmetric pulse shape the timing of the IR and visible pulses may significantly affect the

BBSFG spectra, as observed by Ishibashi and Onishi [10] and Stiopkin *et al.* [11], because the typical duration of the visible pulse is still too short with respect to typical  $T_2$  lifetimes to avoid distortion of the first order IR polarization. With asymmetric pulses, Curtis *et al.* [12-15] have pointed out the fact that any degree of background suppression modifies the sampling of the initial portion of the resonant spectrum. In the case of vibrational modes with different  $T_2$  times, relative intensities vary with the IR-visible time delay. A simultaneous fit of multiple spectra recorded at several time delays was found to dramatically improve the quality of the fit [14] and the determination of the resonant parameters, including the number of bands present in the spectrum. Weeraman *et al.* [16] have proposed a different method of NR suppression involving asymmetric pulses characterized by an exponential rise followed by an abrupt decay. However they did not address the problems related to the temporal profile of the visible pulse. Laaser *et al.* [17] have recently pointed out the drawbacks of frequency-domain SFG spectroscopy resulting from the frequency dependent phase shift induced by the time delay between IR and visible pulses. Simulations of the SFG spectra using visible pulses with different temporal profiles have shown that distortion is more pronounced with a FP etalon than with a pulse shaper while it is almost suppressed by time-domain SFG spectroscopy with a scanned femtosecond visible pulse.

It is important to evaluate the consequences of these drawbacks on the accuracy of BB SFG spectroscopy in order to use a suitable method of spectrum analysis. The purpose of this Chapter is to compare experimental and simulated BBSFG spectra of an OctaDecaneThiol Self Assembled Monolayer (ODT SAM) on gold obtained using a delayed picosecond visible pulse produced by either a 4f pulse shaper (PS) or a FP etalon. ODT is chosen because its main three SFG bands are close enough to each other ( $26$  and  $58\text{ cm}^{-1}$ ) to be sensitive to interferences between them. Two deconvolution methods are used : the first one is the standard deconvolution into Lorentzians. The second one uses the resolution of the Bloch equations to model the SFG pulse in the time domain, followed by Fourier transform into the frequency domain. In section 3 we recall the basis of the two methods of deconvolution and we examine the spectral intensity and spectral phase as a function of the delay for each pulse shaping method for two model systems consisting of either one single band or three bands, without NR background. In section 4 we first report the ODT spectra obtained with the two methods of pulse shaping and then we examine the degree of accuracy of the relative intensities obtained from the two deconvolution methods and the two pulse shaping methods.

## 6.2 Theory of SFG with a delayed visible pulse

In **Chapter 1** we have discussed the theory of SFG, the polarization of SFG in the frequency domain has been given by **Eq. 1.25. Chapter 1**:

$$\tilde{P}_{\text{SFG}}^{(2)}(\omega = \omega' + \omega'', \tau) \propto \left[ \left( \chi_{\text{NR}} e^{i\varphi_{\text{NR}}} + \sum_i A_i e^{i\varphi_i} \right) \tilde{E}_{\text{IR}}(\omega) \right] \otimes \tilde{E}_{\text{vis}}^{\text{str}}(\omega, \tau) \quad (6.1)$$

where  $\omega'$  or  $\omega''$  are the central frequency of IR and visible pulses. This integration can be performed over either  $\omega'$  or  $\omega''$ . Using  $\omega''$  we get

$$\tilde{P}_{\text{SFG}}^{(2)}(\omega, \tau) \propto \int_{-\infty}^{+\infty} d\omega'' \left( \chi_{\text{NR}} e^{i\varphi_{\text{NR}}} + \sum_i A_i e^{i\varphi_i} \right) \tilde{E}_{\text{IR}}(\omega - \omega'') \tilde{E}_{\text{vis}}^{\text{str}}(\omega'', \tau = 0) e^{-i\omega''\tau} \quad (6.2)$$

As it is well known in spectral interferometry [28], the time delay  $\tau$  results in a linear phase retardation  $\omega''\tau$ . It should be pointed out that the validity of **Eq. 6.2** is restricted to positive delay values due to the causality. For negative time delays (the visible pulse arriving before the IR pulse) the portion of the visible electric field before the IR pulse does not generate any SFG signal and therefore is not seen by the sample.

In fact the effective visible pulse generating SFG does not occur earlier than the IR pulse but is rather truncated, i.e.

$$\mathcal{E}_{\text{vis}}^{\text{eff}}(t \geq 0) = \mathcal{E}_{\text{vis}}^{\text{str}}(t) \quad \text{and} \quad \mathcal{E}_{\text{vis}}^{\text{eff}}(t < 0) = 0. \quad (6.3)$$

Consequently the phase factor  $e^{-i\omega''\tau}$  arising from the Fourier transform of the visible field for positive  $\tau$  values disappears for negative delays.

The SFG spectral phase is defined by:

$$\varphi_{\text{SFG}}(\omega) = \tan^{-1}(\text{Im}[\tilde{P}_{\text{SFG}}^{(2)}(\omega, \tau)] / \text{Re}[\tilde{P}_{\text{SFG}}^{(2)}(\omega, \tau)]) \quad (6.4)$$

where  $\text{Im}[\tilde{P}_{\text{SFG}}^{(2)}(\omega, \tau)]$  and  $\text{Re}[\tilde{P}_{\text{SFG}}^{(2)}(\omega, \tau)]$  are the imaginary and real parts of the SFG polarization.

The spectral phase  $\varphi_{\text{SFG}}(\omega, \omega'')$  of a particular  $\omega''$  component of the resonant SFG signal at frequency  $\omega$  can be formally expressed as:

$$\varphi_{\text{SFG}}(\omega, \omega'') = \varphi_{\text{vib}}(\omega - \omega'') - \omega''\tau + \varphi_{\text{str}}(\omega'') \quad (6.5a)$$

where  $\varphi_{\text{vib}}(\omega - \omega'')$  is the phase due to the vibrational bands. In the case of a single vibrational band (**Eq. 6.5**) can be expressed

$$\varphi_{SFG}(\omega, \omega'') = \varphi_R + \tan^{-1}\left(\frac{\Gamma}{\omega_{10} - \omega + \omega''}\right) - \omega'' \tau + \varphi_{str}(\omega'') \quad (6.5b)$$

The last term in this equation represents the additional frequency dependent phase factor possibly brought by the stretcher.

In fact as shown by **Eq. 6.2** many  $\omega''$  components contribute to the SFG signal at a given frequency  $\omega$ . The spectral phase of the resonant contribution needs to be numerically calculated. However  $\varphi_{SFG}(\omega)$  can be directly extracted in two ideal situations for which a simple expression of  $\tilde{P}_{SFG}^{(2)}(\omega, \tau)$  is obtained. The first one occurs when the visible pulse is spectrally very narrow, i.e.  $\tilde{E}_{vis}^{str} \cong E_{vis}^0 \delta(\omega'' - \omega_{vis})$ . In this case **Eq. 6.2** reduces to

$$\tilde{P}_{SFG}^{(2)}(\omega, \tau) \propto \left( \chi_{NR} e^{i\varphi_{NR}} + \sum_i A_i (\omega - \omega_{vis}) e^{i\varphi_i} \right) \tilde{E}_{IR}(\omega - \omega_{vis}) E_{vis}^0(\omega_{vis}, \tau = 0) e^{-i\omega_{vis}\tau} \quad (6.6)$$

Except for the phase change  $\Delta\varphi_i = \pi$  across the resonances the SFG spectral phase is independent of the frequency  $\omega$ . The SFG spectrum is independent of the IR-visible delay. Only the contributions from overlapping vibrational modes arising from the same visible frequency  $\omega''$  interfere.

The second ideal situation is that of very narrow band vibrational modes, i.e.

$$A_i \cong \frac{B_i}{\Gamma_i} \delta[(\omega - \omega'') - (\omega_{10})_i]. \text{ In this case } \mathbf{Eq. 6.2} \text{ becomes}$$

$$\tilde{P}_R^{(2)}(\omega, \tau) \propto \sum_i \frac{B_i}{\Gamma_i} \tilde{E}_{IR}(\omega_{10})_i \tilde{E}_{vis}^{str}[\omega - (\omega_{10})_i, \tau = 0] e^{-i[\omega - (\omega_{10})_i]\tau} \quad (6.7)$$

The SFG spectral line shape is entirely controlled by the visible pulse. The resonant spectral phase shows a linear dependence as a function of frequency  $\omega$ : as far as the vibrational resonances broadened by the visible pulse do not overlap, i.e. the spectral width of  $\tilde{E}_{vis}^{str}$  is sufficiently narrow, the SFG spectrum is independent of the delay. If they overlap, **Eq. 6.7** shows that the  $\omega$  components corresponding to different modes and arising from different visible frequencies  $\omega''$ , i.e. with different phase factors  $\varphi_{str}(\omega'') - \omega''\tau$ , interfere constructively or destructively depending on their phase difference. In this case the SFG spectrum is expected to change as a function of the IR-visible delay. In spite of the fact that the situation depicted by **Eq. 6.7** is usually not experimentally encountered, its interest resides in highlighting the delay dependence of interferences between the vibrational bands.

### 6.3 Model of calculation

In order to deconvolute the vibrational bands from the nonresonant background, experimental spectra are usually fitted to the standard SFG intensity expression given by **Eq. 1.28**. The IR laser profile is obtained from a reference sample (e.g. GaAs) providing a flat nonresonant response. However two problems arise in the deconvolution procedure. First of all, the purely spectral analysis would be perfectly adequate only if the visible pulse was infinitely long. The use of a pulse of finite duration introduces an error because it distorts the temporal profile of the second-order polarization  $P_{SFG}^{(2)}(t)$  with respect to that of  $P_{IR}^{(1)}(t)$ . Secondly too many parameters are necessary to describe the spectrum and fitting of a single spectrum does not allow to determine them accurately. As a matter of fact it is generally difficult to obtain a unique set of fitting parameters, a drawback inherent to numerical fitting routines including a large number of parameters [18]. It is essential to minimize the number of fitting parameters. For example in the fit of ODT/Au spectra the phase difference  $\varphi$  between NR and R is assumed to be constant throughout the SFG spectrum, the vibrational frequencies  $(\omega_{10})_i$  taken from the literature are not allowed to change and the half-width  $\Gamma_i$  are assumed to be the same for all vibrational bands. The relative phase  $\varphi$  is determined by fitting simultaneously the spectra recorded on many different samples (e.g. a dozen). The set of adjustable parameters are then the amplitudes of the resonant bands  $B_i$ , their common half-width  $\Gamma$  and the nonresonant amplitude  $\chi_{NR}$  [19]. Under such assumptions the determination of the relative intensities has proven to be reproducible at the cost of a larger uncertainty on the fixed parameters although it remains affected by the fact that **Eq. 1.28** is strictly valid only for an infinitely narrow-band visible laser. The recent approach proposed by Curtis et al [14] uses multiple delays of visible pulse with full suppression of the nonresonant signal and then numerical fit to determine a single set of spectral parameters, which has been shown to result in an improved accuracy on the determination of the resonant parameters. In this section we shown the model of calculation of an IR induced 1 order polarization which is upconverted by a visible pulse formed by a Fabry-Perot (FP) to generate an impulsion which has in time domain a sharp increase in intensity and an exponential decay to remove the short nonresonant signal and distinguish temporally the resonant vibrational polarization. The introduced delay suppresses the NR contribution but induces another problem: the deformation of relative intensities of molecular vibrational bands. The reason is discussed in time domain by the SFG polarization and in frequency domain by the spectral phase.

### 6.3.1 Octadecanethiol (ODT)

In this chapter the SFG studies are based on octadecanethiol (ODT) self assembled molecules (SAM).

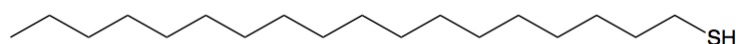


*Fig. 6.1. Sketch of an ODT molecule.*

An ODT is an alkyl chain, in which there are several vibrational modes: the modes S-C (the frequency is far away the IR for the SFG measurement), the mode of C-C and C-H elongation and folding. The terminal methyl group has 3 modes of vibration in the band range of 2850 - 3000  $\text{cm}^{-1}$ : a mode of symmetric elongation normally observed at about 2876  $\text{cm}^{-1}$ , a mode corresponding to the Fermi resonance between symmetric elongation and the level with two quanta in the folding mode around 2935  $\text{cm}^{-1}$ , and the mode of anti-symmetric elongation at about 2961  $\text{cm}^{-1}$ . A methylene group of an alkyl chain have a mode of symmetric elongation at about 2850  $\text{cm}^{-1}$  and an anti-symmetric mode in which the frequency varies between 2918  $\text{cm}^{-1}$  and 2927  $\text{cm}^{-1}$ , following the conformation of the chain. The coupling between the different  $\text{CH}_2$  group is weak, (compared with the coupling in the mode of folding), but sufficient for a measurable frequency shift. From a consensus of IR studies, 2918  $\text{cm}^{-1}$  indicates an all-trans chain and 2927  $\text{cm}^{-1}$  indicates a chain of aleatory conformation. The information of different bands are placed in table 1.

*Table 6.1: Frequency of of the C-H modes of ODT SAM observed by SFG.*

Num.	Frequency ( $\text{cm}^{-1}$ )	Intensity	Assignment
1	2851	Weak	$\text{CH}_2$ symmetric elongation
2	2877	Strong	$\text{CH}_3$ symmetric elongation
3	2905	Weak	S- $\text{CH}_2$ symmetric elongation
4	2918	Weak	$\text{CH}_2$ asymmetric elongation
5	2936	Strong	$\text{CH}_3$ resonance of Fermi
6	2962	Strong	$\text{CH}_3$ asymmetric elongation
7	$\approx 2972$	Weak	S- $\text{CH}_2$ asymmetric elongation

### 6.3.2 Calculation of first-order polarization

As discussed in Chapter 1, the IR induced NR and R polarization can be calculated using **Eqs 1.12-1.14**. The off diagonal matrix element  $\rho_{10}(t)$  has been calculated by numerical integration of **Eq. 1.14** for each vibrational mode. There are three independent resonant bands including the three strong vibration modes Num. 2, 5 and 6 in **Table 6.1**. The NRs are calculated as a resonant band described by a broad Lorentzian with a damping constant  $\Gamma=5000 \text{ cm}^{-1}$  (corresponding to the dephasing time of Au) to avoid the singularity introduced by the  $\delta$  function in **Eq. 1.17**. A numerical application is illustrated in the **Fig. 6.2**.

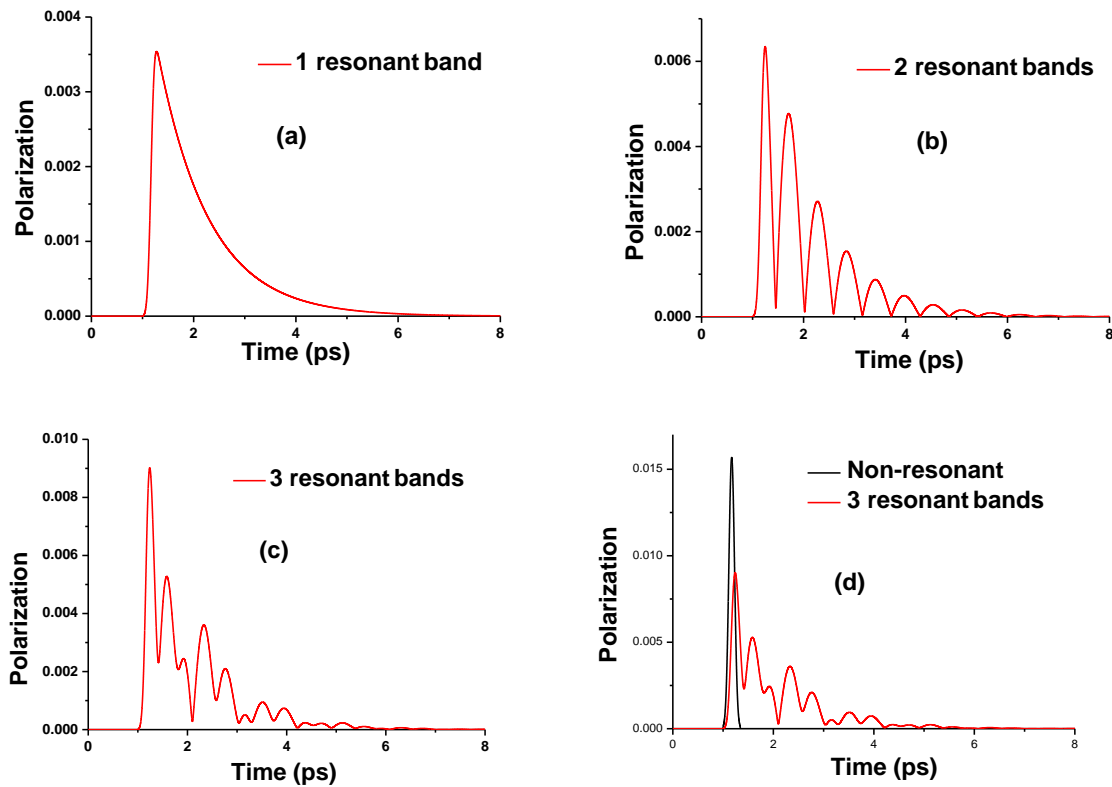


**Fig. 6.2.**  $P_{\text{IR}}^{(1)}(t)$  calculated of (a) 1 resonant band, (b) 2 resonant bands, (c) 3 resonant bands, (d) 3 resonant band (red) with a non-resonant band (black).

In **Fig. 6.2** A polarization with a single mode has a form of exponential decay. The three resonant bands interfere and their sum presents the beats. The polarization of NR is very short compared to the R. Then the first-order polarization  $P_{\text{IR}}^{(1)}(t)$  is converted into a second-order polarization  $P_{\text{SFG}}^{(2)}(t, \tau)$  by the visible pulse using **Eq. 1.24**.

### 6.3.3 Visible pulse formed by a Fabry-Perot etalon

The visible pulse should be formed by a stretcher to obtain the needed form. By a 4f pulse shaper as discussed in Chapter 1, the obtained visible pulse with a large temporal duration and narrow width allows a good spectral resolution. In this section another stretcher Fabry-Perot etalon (FP) will be introduced. The FP is an optical interferometer consisted of two parallel surfaces with a high reflection coefficient (often 95%). The light which emerges from FP results in a multiple interference.

The visible pulse with a form of Gaussian transmitted by the FP etalon has been calculated in two ways to confirm the accuracy of results. In the first way the time envelope of the output pulse has been computed directly in the time domain. Within the FP interferometer the visible laser pulse undergoes many reflections, in each reflection, a part of the incident pulse traverses the FP, finally a train of fs pulses with an interval time  $\tau_{RT}$  are generated (**Fig. 6.3**).

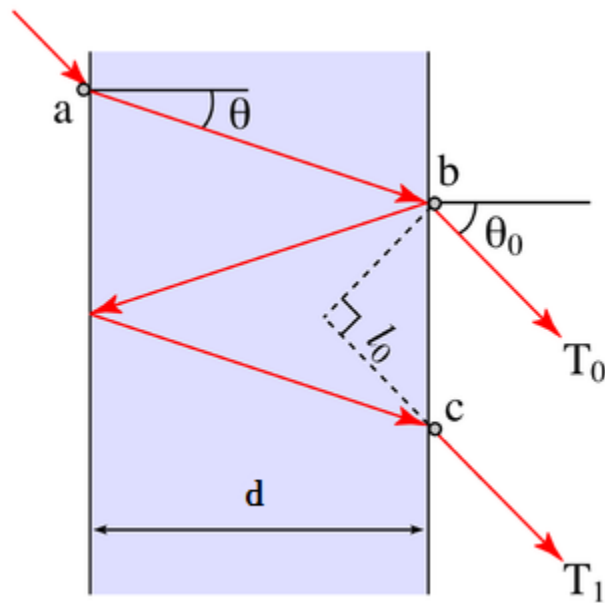


**Fig. 6.3.** Sketch diagram of the reflection and transmission of light pulse in the Fabry-Perot.  $\theta_0$  is the incident angle of pluse,  $\theta$  is the refraction angle.  $d$  is the thickness of FP,  $T_i$  is the transmitted light pulses.

The corresponding time dependent electric field is given by:

$$E_{vis}^{FP}(t, \tau) = \mathcal{E}_{vis}^{FP}(t, \tau) e^{-i\omega_{vis}(t-\tau)} \quad (6.8a)$$

with

$$\mathcal{E}_{\text{vis}}^{\text{FP}}(t, \tau) = E_{\text{vis}}^0 (1-R) \sum_{m=0}^{\infty} R^m e^{-\left(\frac{t-\tau-m\tau_{\text{RT}}}{\Delta t_{\text{vis}}}\right)^2} e^{i\omega_{\text{vis}} m \tau_{\text{RT}}} \quad (6.8b)$$

where  $R$  is the reflectivity at the two surfaces of the FP separated by an air space of thickness  $d$  and  $\tau_{\text{RT}} = \frac{2d \cos \theta}{c}$  the round trip travel time at an incident angle  $\theta$ .

Provided that the round trip time  $\tau_{\text{RT}}$  is short compared to the input pulse duration  $\Delta t_{\text{vis}}$  the successively transmitted pulses overlap in time and the FP output is a smooth asymmetric pulse with an amplitude exponentially decaying with the cavity lifetime [20]

$$\tau_c = \frac{d \cos \theta}{c \ln \frac{1}{R}} \approx (2\pi \delta \nu)^{-1} \quad (6.9)$$

where the FP bandwidth  $\delta \nu = \text{FSR}/F$  is equal to the ratio of the Free Spectral Range (FSR) to the finesse of the etalon (which is slightly lower than the reflective finesse  $F_R = \frac{\pi \sqrt{R}}{1-R}$ ) [29].

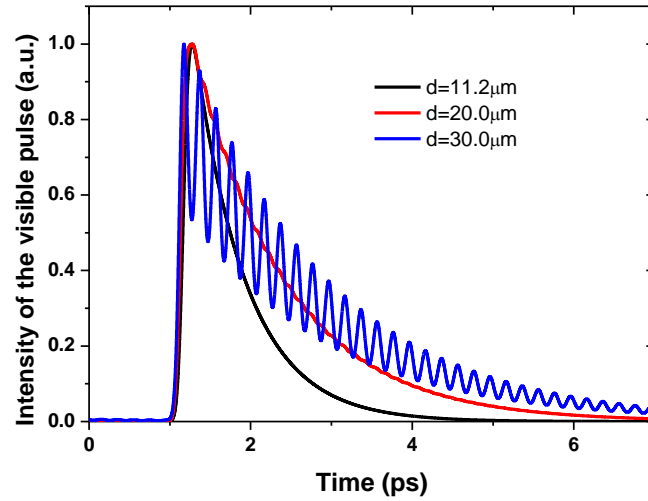


**Fig. 6.4.** The temporal form of the visible pulse transmitted by a Fabry-Perot with the parameters :  $d=11.2 \mu\text{m}$  (black),  $20 \mu\text{m}$  (red) ,  $30 \mu\text{m}$ (blue), indice  $n=1.0$ ; finesse=55.

As shown in **Fig. 6.4**, the black, red, and blue curves are the temporal form of visible pulse formed by a FP with different width  $d$ . The cavity lifetime  $\tau_c$  of the curves increases with the width of the  $d$  (black<red<blue), which can be explained by **Eq. 6.9**. When the interval time between two neighboring pulses is larger than the half width of visible pulse, the train of pulses reflected can be distinguished, as shown the blue curve.

The second way to calculate a Gaussian visible pulse transmitted from a FP is in the frequency domain.

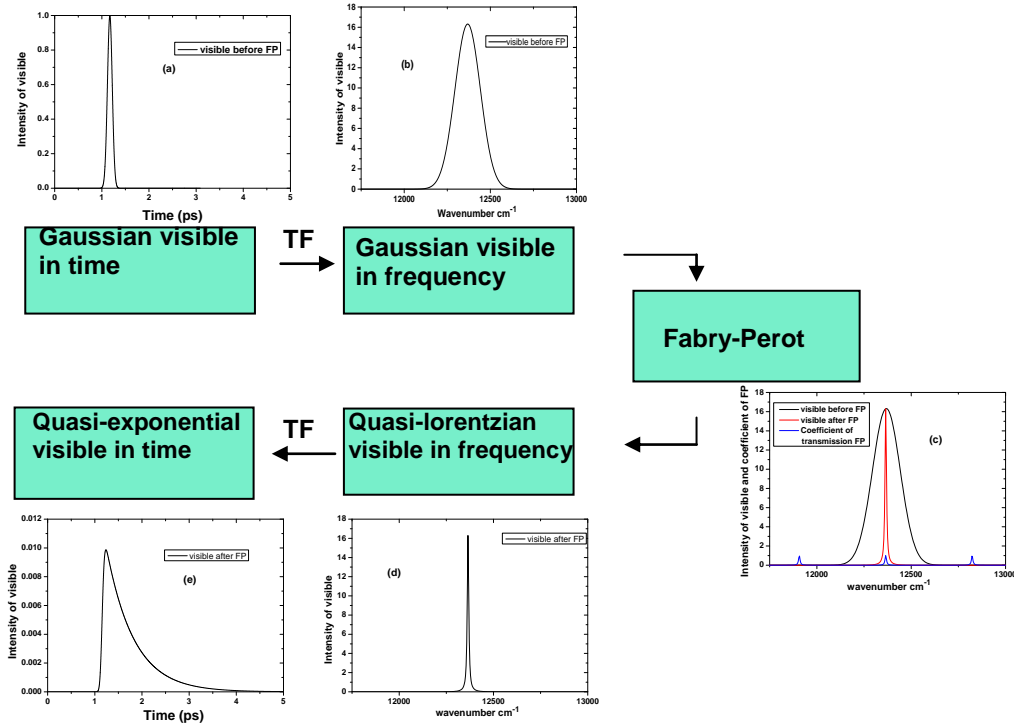


**Fig. 6.5.** Steps of the calculations of a Gaussian visible pulse formed by a FP in frequency domain.

The Gaussian spectrum of the input pulse was first obtained by Fourier transform of the electric field time envelope (**Fig. 6.5a, b**):

$$\tilde{E}_{vis}^{in}(\omega'', \tau) = \tilde{E}_{vis}^{in}(\omega'', \tau = 0) e^{-i\omega''\tau} \quad (6.10 \text{ a})$$

with

$$\tilde{E}_{vis}^{in}(\omega'', \tau = 0) = E_{vis}^0 e^{-\left[ \frac{(\omega'' - \omega_{vis}) \Delta t_{vis}}{2} \right]^2} \quad (6.10 \text{ b})$$

The spectrum of the visible pulse at the output of FP etalon was then obtained by multiplying the input electric field (**Eq. 6.13a**) and the transmission function of FP etalon (**Fig. 6.5c, d**), i.e.

$$\tilde{E}_{vis}^{FP}(\omega'', \tau) = \tilde{E}_{vis}^{in}(\omega'', \tau) T_{FP}(\omega'' \tau_{RT}) \quad (6.11)$$

where

$$T_{FP}(\omega'' \tau_{RT}) = A_{FP}(\omega'' \tau_{RT}) e^{i\phi_{FP}(\omega'' \tau_{RT})} \quad (6.12)$$

is the transmission function of the FP etalon with the amplitude and phase respectively given by:

$$A_{\text{FP}}(\omega''\tau_{\text{RT}}) = \frac{1-R}{\left[ (1-R \cos \omega''\tau_{\text{RT}})^2 + R^2 \sin^2 \omega''\tau_{\text{RT}} \right]^{1/2}} \quad (6.13)$$

and

$$\varphi_{\text{FP}}(\omega''\tau_{\text{RT}}) = \tan^{-1} \left( \frac{R \sin \omega''\tau_{\text{RT}}}{1 - R \cos \omega''\tau_{\text{RT}}} \right) \quad (6.14)$$

The obtained visible pulse in frequency domain has a form of quasi - lorentzian **Fig. 6.5d**. The time dependent transmitted pulse was then obtained by subsequent Fourier transform. The corresponding time envelope of visible consists of a sharp rise followed by a slower quasi-exponential decay **Fig. 6.5e**.

The two ways have been proved to be identical in the simulation (**Fig. 6.6**),

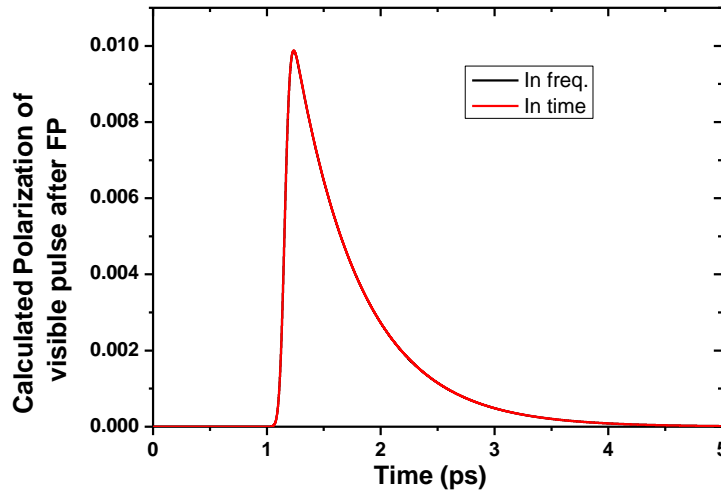


*Fig. 6.6. The temporally obtained impulsions calculated in frequency (black) and in time (red)*

### 6.3.4 Calculation of SFG with a delayed visible pulse in time domain

Since the SFG polarization is proportional to the visible electric field, it is interesting to compare the temporal amplitude of the pulses produced by both types of stretcher. The time envelope of the visible pulse intensity calculated for a 120 fs input pulse is shown in **Fig. 6.7** for both the pulse shaper and the FP etalon together with the R and NR first-order polarizations induced by the 145 fs IR pulse in the ODT SAM on gold (calculated using the

parameters of the three main bands). In the case of the pulse shaper the time envelope of the output pulse intensity is nearly Gaussian according to **Eq. 1.28**, with a 5 ps FWHM (**Fig. 6.7a**). The ps pulse produced by the FP etalon consists of a  $\cong 200$  fs sharp rise followed by a slower exponential decay with a 0.8 ps time constant (**Fig. 6.7b**).

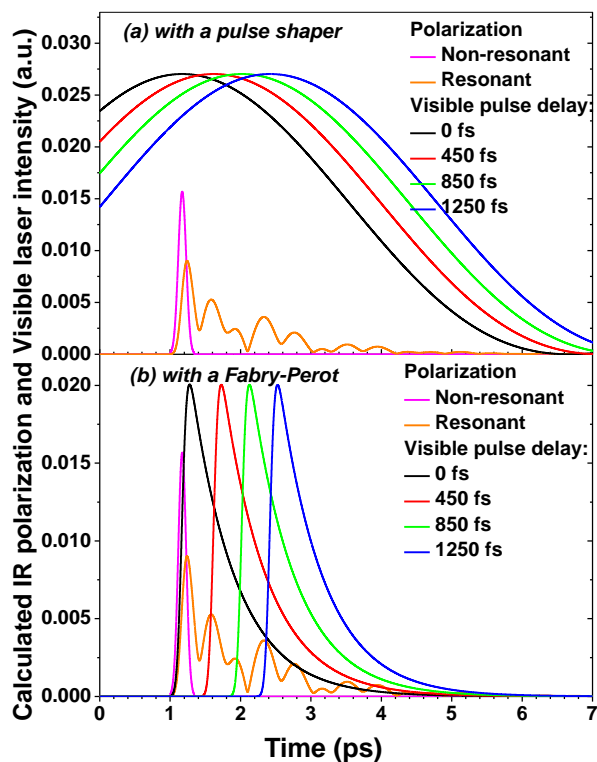


**Fig. 6.7.** Computed time envelope of the ps visible pulse intensity together with the resonant and nonresonant components of the first-order polarization of ODT SAM on Au induced by the IR laser for several values of the IR-visible delay. (a) In the case of the pulse shaper ( $10\text{ cm}^{-1}$  bandwidth); (b) In the case of the FP etalon ( $R = 95\%$ ,  $\text{FSR} = 448.2\text{ cm}^{-1}$ )

We firstly show the SFG polarization in time domain. **Fig. 6.8.** includes the intensities of SFG polarizations with a visible pulse formed by a PS and a FP. The IR polarization of the 3 vibrational bands beat each other in time domain giving rise to the deformed sum of IR polarization. In the case of a PS with 3 vibrational bands (**Fig. 6.8. a1, a2**), the profile of the temporal pulse of visible is very large, and symmetric, as shown in **Fig. 6.7a**. So the shift of visible pulse in time by 1.0 ps does not change the SFG polarization. In the case of FP with 3 band (**Fig. 6.8. b1, b2**), the beating of 3 vibrational bands deforms the IR polarization and has

no longer exponential form, so the delay of the asymmetric visible pulse by 1.0 ps in time change absolutely the product temporal form of SFG polarization, which leads to the different SFG spectra. This results show us that the deformation of SFG spectra with a delayed visible pulse formed by a FP is due to 1) the beating of adjacent vibrational bands giving a deformed IR polarization and 2) the temporally asymmetric visible pulse.

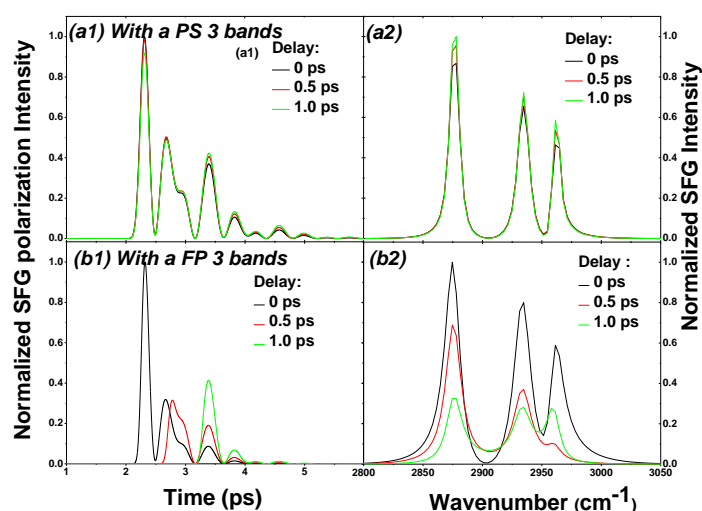


**Fig. 6.8.** The SFG polarizations of 3 bands of ODT  $2878\text{ cm}^{-1}$   $2936\text{ cm}^{-1}$  and  $2963\text{ cm}^{-1}$  and SFG spectra calculated with a delayed visible pulse formed by a PS and a FP. (a1) The resonant SFG polarization of 3 bands with a PS with delays 0 ps 0.5 ps and 1.0 ps. (a2) The corresponding SFG spectra of (a1). (b1) Resonant SFG polarization of 3 bands of ODT with a visible pulse formed by a FP at delays 0 ps 0.5 ps and 1.0ps. (b2) The corresponding spectra of (c1).

### 6.3.5 Effect of delay between IR and visible pulse in frequency domain: The spectral phase

To find the effect of a delay on the spectrum of visible pulse, we do a Fourier transform of a temporally delayed visible pulse.

$$TF(E_{vis}(t-\tau)) = \tilde{E}_{vis}(\omega)e^{-i\omega\tau} \quad (6.15)$$

This transform can be visualized by **Fig. 6.9:**

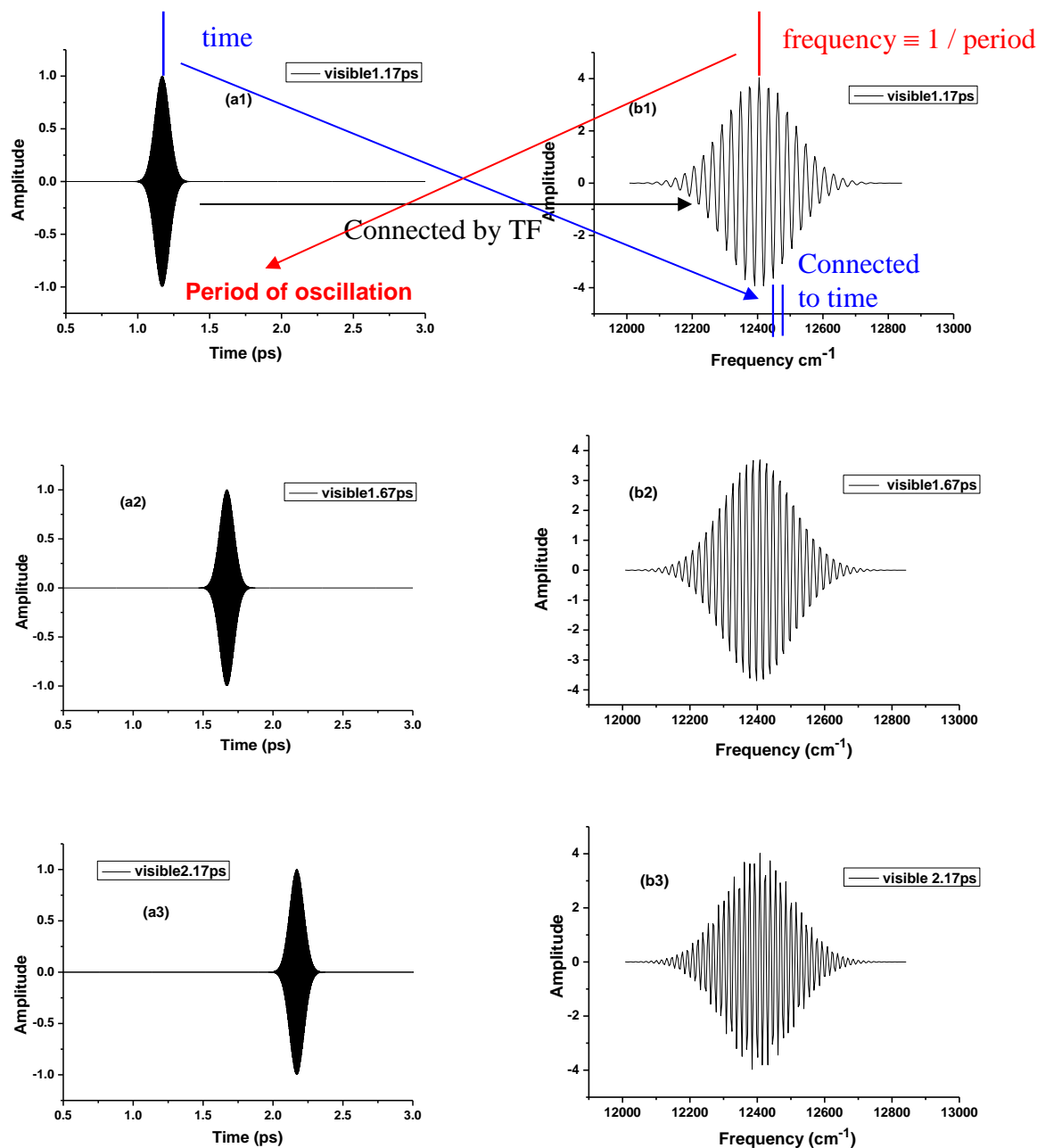


**Fig. 6.9.** Real part of amplitude of visible pulse in time (a) and in frequency (b) with a delay of (1) 1.17 ps, (2) 1.67 ps and (3) 2.17 ps.

In **Fig. 6.9a** and **b** is connected by TF. The temporal oscillation speed of visible pulse in (a1) corresponds to the frequency position in (b1), ( $\text{frequency} \equiv 1 / \text{period}$ ), accordingly the spectral oscillation speed of visible pulse in (b1) should correspond to time position (delay) (a1). This spectral oscillation changed by a delay corresponds to the spectral phase of visible pulse, i.e. the term  $e^{-i\omega\tau}$  in **Eq. 6.15**. But this delay does not change the profile of impulsions.

Accordingly, as shown in **Eqs. 6.2** and **6.5**, the time delay  $\tau$  between IR and visible pulses produces a frequency dependent phase shift  $\omega\tau$  for each frequency component of the

SFG polarization. To clearly observe the effect of phase shift  $\omega''\tau$ , we calculate the oscillated and accumulated phase of SFG spectrum by **Eq. 6.4** and **6.5**. The **Eq. 6.4** give only the phase oscillated between  $\pi/2$  and  $-\pi/2$  (black curve in **Fig. 6.10**). To get the sum phase, we add  $\pi$  to sum phase when the value of oscillated phase passes  $\pi/2$ . The accumulated phase is therefore obtained shown as the red curve in **Fig. 6.10**, corresponding to the SFG spectrum (green curve). At the zone of SFG spectrum, the oscillated phase and accumulated phase increase quicker than the other zone because of the jump of  $\pi/2$  caused by the spectral phase of vibrational band, i.e. the item  $\varphi_{\text{vis}}(\omega-\omega'')$  shown in **Eq. 6.5**.

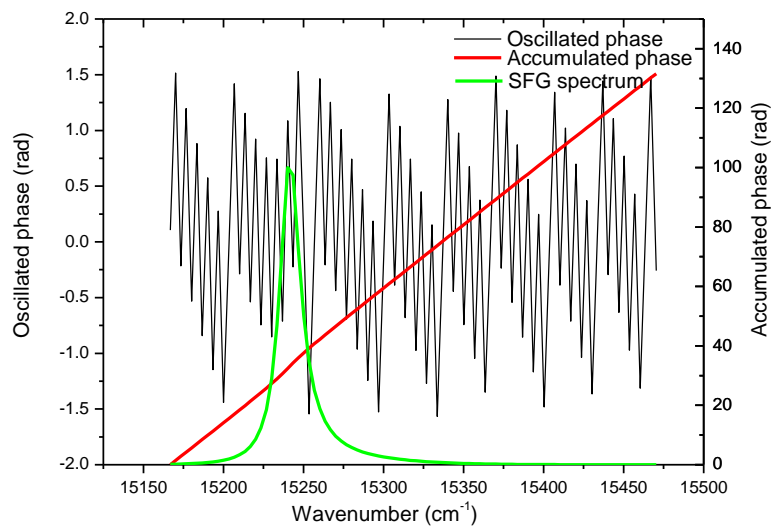


**Fig. 6.10.** The calculated oscillated (black), accumulated (red) phases and the corresponding SFG spectrum (green) corresponding to the single band at  $2878 \text{ cm}^{-1}$ .

We first show the result of model calculations to illustrate the way pulse shaping affects SFG spectra. Since the SFG intensity spectrum does not contain all the information, the spectral phase is also shown. We have computed the amplitude and spectral phase of the SFG polarization for two model systems without any nonresonant contribution. The first one consists of a single vibrational band of width  $\Delta\nu = 15.7 \text{ cm}^{-1}$  centered at  $\nu_{10} = 2878 \text{ cm}^{-1}$ . **Fig. 6.12** shows the spectral phase of the SFG polarisation and the intensity spectrum computed for three different visible pulses at different delay values. When the 120 fs pulse generated by the laser is used as the visible pulse (**Fig. 6.12a**), the spectral phase shows a linear frequency dependence with a slope increasing with the delay in the proportion of 0 : 0.5 : 1 for delay values of 0, 0.5 and 1 ps, respectively. The phase change  $\Delta\varphi = \pi$  which is

expected to occur across the resonance does not appear in **Fig. 6.12a** because it is very small compared to the  $\sim 120$  rad change of the linear contribution. In contrast when the visible pulse is generated by the pulse shaper the spectral phase is nearly independent of the SFG frequency  $\omega$  and of the delay  $\tau$  (**Fig. 6.12b**) except for the phase change  $\Delta\phi = \pi$  : such a different behaviour is related to the spectral width of the visible pulse which is reduced from  $122\text{ cm}^{-1}$  to  $<10\text{ cm}^{-1}$  (with no wings) at the output of the pulse shaper. The SFG spectrum is much narrower with the ps pulse produced by the pulse shaper (**Fig. 6.12b**) than with the 120 fs laser pulse (**Fig. 6.12a**) because the spectral resolution in BBSFG is controlled by the spectral width of the visible light. The SFG intensity is found to be nearly independent of the delay (**Fig. 6.12b**) as expected from the long duration and the symmetric shape of the visible pulse (**Fig. 6.7a**). **Fig. 6.12c** shows the results obtained with the ps pulse generated by the FP etalon. The SFG spectrum is narrowed like in the case of the pulse shaper but the spectral phase behaviour is very similar to that observed with the 120 fs visible pulse. This is due to the fact that the wings of the amplitude spectrum transmitted by the FP etalon extend over a frequency range much broader than the spectral band selected by the slit of the pulse shaper (**Fig. 6.11**). Also note that the computed spectral phase is independent of the delay for negative  $\tau$  values as discussed in **Eqs. 6.6- 6.7**. The spectral width is independent of the delay for each type of visible pulse, except for a broadening at zero delay in the case of a femtosecond pulse (**Fig. 6.12a**): at zero delay the IR polarization is severely distorted and shortened.

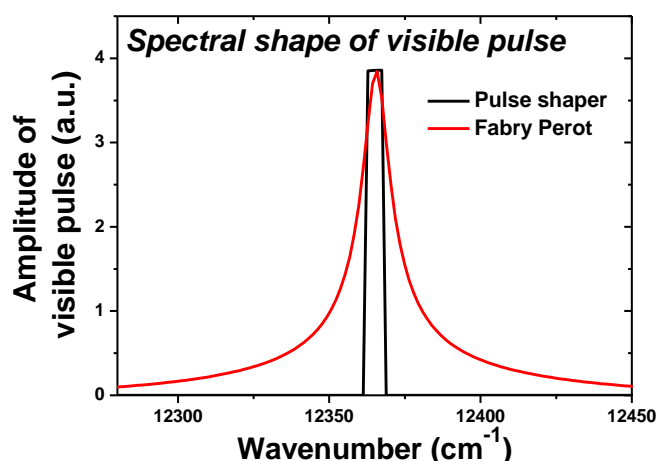


*Fig. 6.11. Computed amplitude spectra of the PS- and FP-produced visible pulses.*

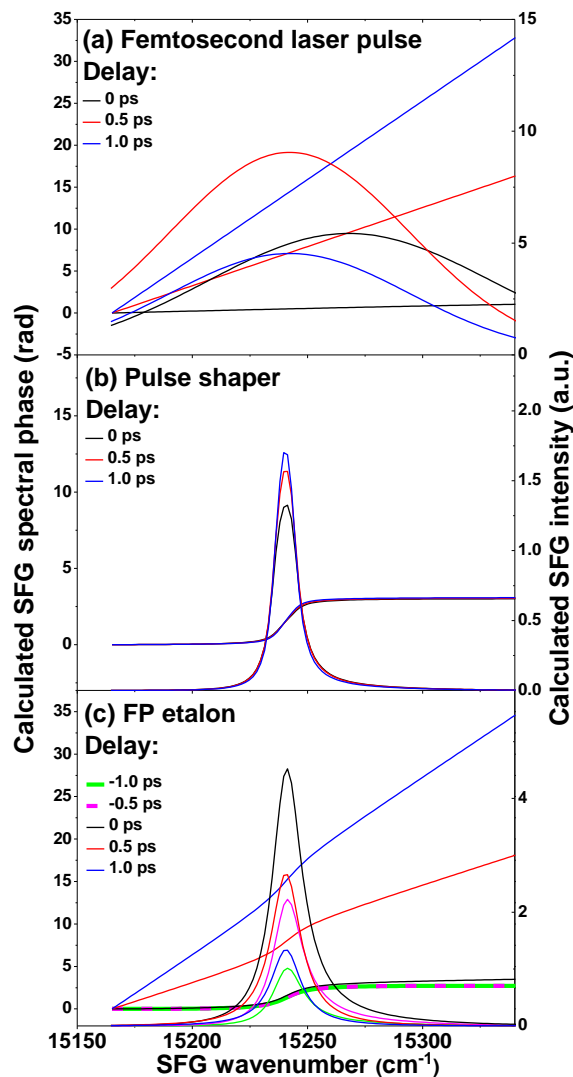


**Fig. 6.12.** Calculated SFG spectral phase and intensity spectrum in the case of a single vibrational band (peak frequency  $2878\text{ cm}^{-1}$  and FWHM  $14.8\text{ cm}^{-1}$  ( $T_2 = 0.72\text{ ps}$ ) and no NR background for three different temporal shapes of the visible pulse with a peak frequency of  $12365\text{ cm}^{-1}$  and different values of the IR-visible time delay. a) Gaussian pulse of  $120\text{ fs}$  duration at the output of the laser system; b) quasi-Gaussian ps pulse at the pulse shaper output (spectral width  $10\text{ cm}^{-1}$ ). Note that the scale of the spectral phase is magnified, c) quasi-exponential ps pulse at the output of a FP etalon of thickness  $d = 11.2\text{ }\mu\text{m}$  and finesse  $F = 55$  (spectral width  $9\text{ cm}^{-1}$ ).

The second model system consists of three closely spaced bands corresponding to those of  $\text{CH}_3$  in the ODT SAM without NR background. In the case of the pulse shaper the

SFG spectrum and the spectral phase are nearly independent of the delay (**Figs. 13a1** and **a2**) like in the case of the 1-band model. The spectral phase is very close to that of a sum of three pure Lorentzian bands. In particular the phase jump of  $\pi$  across each additional resonance is clearly visible.

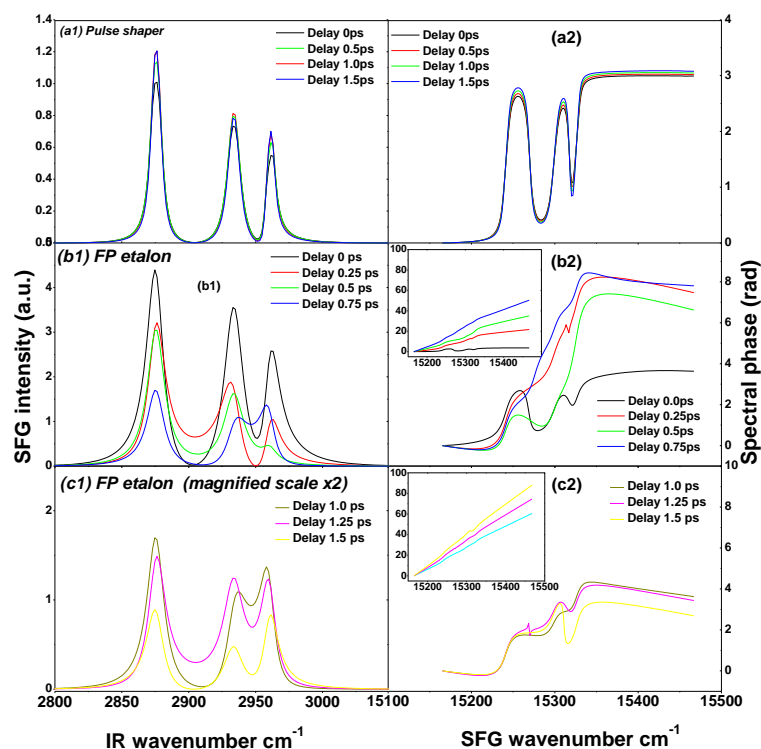


**Fig. 6.13.** Computed delay dependence of the SFG intensity spectrum and spectral phase for a model system including three vibrational bands (peak frequencies 2878, 2936 and 2963  $\text{cm}^{-1}$ ) with FWHM 14.8, 20 and 10  $\text{cm}^{-1}$  and the peak intensity ratio 1: 0.47:0.31, with no NR background contribution. The central frequency of visible pulse is at 12365  $\text{cm}^{-1}$ . The phase origin is arbitrarily chosen at the frequency 15165  $\text{cm}^{-1}$ . (a) Quasi-Gaussian ps pulse at the output of the pulse shaper (spectral width 9  $\text{cm}^{-1}$ ) and IR-visible delay values  $\tau = 0, 0.5, 1.0$  and 1.5 ps, (b) Quasi-exponential pulse at the output of a FP etalon (spectral width 9  $\text{cm}^{-1}$ ) and delay values  $\tau = 0, 0.25, 0.5, 0.75$  ps. In order to magnify the phase changes in the frequency region of the resonant bands the quantity  $(\omega_{\text{SFG}} - 15165)\tau$  has been subtracted from the total spectral phase (which is shown in the inset), (c) Same as (b) at longer delays  $\tau = 1, 1.25$  and 1.5 ps.

With the FP etalon, in contrast to what is observed with the pulse shaper, the relative intensities of the three bands show a strong dependence as a function of the delay (**Figs. 13b1**

and **c1**). The overall intensity decrease can be explained by the temporal shift of the visible pulse with respect to the IR polarization (**Fig. 6.7b**). By contrast to the case of a single band, the calculated SFG spectral phase shows only approximately a linear dependence on the delay (insert of **Figs. 13b2** and **c2**). The  $\varphi(\omega)$  curves plotted in **Figs. 13b2** and **c2** have been obtained by subtracting the quantity  $(\omega_{\text{SFG}} - 15165) \cdot \tau$  in order to highlight the phase changes around the vibrational resonances. The behaviour is no longer that of a sum of three pure Lorentzian bands, as anticipated from **Eq. 6.2**, because the phase factor and the visible pulse spectrum are now intricately intertwined into the Lorentzians. The comparison between **Figs. 13a** and **b, c** shows that although the difference between PS and FP may seem small in the frequency domain (rectangular vs Lorentzian shape of the visible pulse spectrum (**Fig. 6.11**)), it has indeed a strong impact on the SFG spectrum and on the spectral phase.

## 6.4 Experimental set up

SFG spectra of an ODT SAM onto a gold substrate have been measured as a function of the time delay (-2 to 2 ps) between fs IR and ps visible pulses, (**Fig. 6.14**). Tunable IR (4  $\mu\text{J}$ , 145 fs and 120  $\text{cm}^{-1}$  bandwidth) and visible (809 nm, 2  $\mu\text{J}$ , adjustable duration 0.12-6 ps and bandwidth 120-2.5  $\text{cm}^{-1}$ ) pulses were overlapped spatially and temporally in a collinear co-propagating configuration. The ps visible pulse was obtained by passing the 120 fs laser pulse through either a folded 4f pulse shaper or a Fabry-Perot etalon. The home-made pulse shaper includes a grating, a  $f = 10$  cm lens, a plane mirror and in front of it a slit which selects a small portion (ca. 5-10  $\text{cm}^{-1}$ ) of the visible pulse spectrum. The FP etalon supplied by SLS Optics ( $R = 95\%$ , effective finesse  $F \cong 50$ , spacer thickness  $d_s = 11.2$   $\mu\text{m}$ , FSR = 448.2  $\text{cm}^{-1}$ ) was tilted by  $\theta = 11.9^\circ$  with respect to the input beam in order to ensure that the peak laser wavelength  $\lambda_{\text{vis}} = 809$  nm coincides with a transmission peak of the etalon. When a FP is used, the slit of PS is removed. The visible pulse is injected to a delay line to overlap temporally with the IR pulse, and the spatial overlap is reached by a ZnSe dichroic plate which is reflective in visible but transparent in IR. The P polarized (Electric field in the plane of incidence) IR + visible pulses are focused on an ODT SAM or on a GaAs reference. Because the measurement of ODT requires a horizontal sample surface, the pulses are lifted and descended by the elevators to form the vertical incident plane to the sample surface. The SFG signals were collected in 30 to 120 seconds to obtain an acceptable signal to noise ratio and

analyzed with a detection system including high rejection filters and a polychromator with a resolution of  $0.4 \text{ cm}^{-1}$  at  $650 \text{ nm}$  equipped with a cooled CCD camera (Roper Scientific).

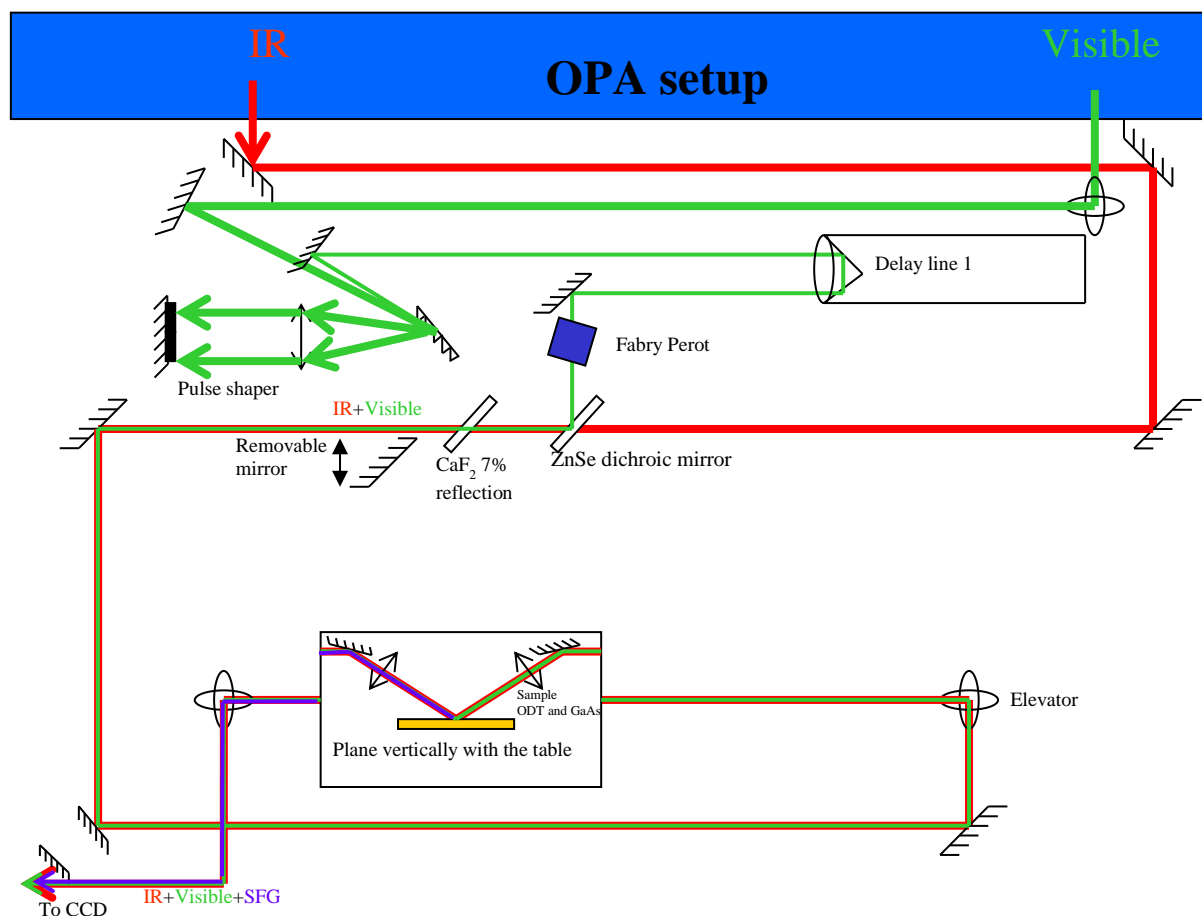


**Fig. 6.14.** Sketch of the experimental set up for the measurement of SFG spectra on ODT sample.

## 6.5 Results and Discussion

### 6.5.1 SFG spectra of ODT

Simulated and experimental SFG spectra of ODT SAM on gold obtained with either the pulse shaper or the FP etalon for several values of the time delay between IR and visible pulses are shown in **Figs. 6.15-6.18**. The spectra mainly consist of three strong vibrational bands arising from the terminal methyl group of ODT chains superimposed on the Au NR response. Two of them are belonging to the symmetric and asymmetric stretching vibrations at  $2878$  and  $2963 \text{ cm}^{-1}$ , respectively, while the third one at  $2936 \text{ cm}^{-1}$  corresponds to the Fermi

resonance of the symmetric stretch with two quanta of the bending mode [1]. In addition to the strong CH<sub>3</sub> bands, three very weak bands originating from the methylene groups are also present in the ODT spectra. Two bands are originating from the symmetric and asymmetric stretching CH<sub>2</sub> vibrations at 2851 and 2918 cm<sup>-1</sup>. The third one at 2905 cm<sup>-1</sup> is assigned to the symmetric vibration of the CH<sub>2</sub> group close to the sulphur atom of the alkyl thiolate chain. While the CH<sub>2</sub> symmetric stretch may be visible providing the signal to noise ratio is high [1], the presence of the S-CH<sub>2</sub> symmetric and CH<sub>2</sub> asymmetric stretch is revealed by the impossibility to fit satisfactorily the spectra around 2905 cm<sup>-1</sup> [19]. The fact that the CH<sub>2</sub> band intensities are not negligible is also supported by a previous calculation using a realistic model of molecular conformation and hyperpolarizability [1]. When these weak bands are not included, it is impossible to obtain a good quality of the fit as judged by eye ; quantitatively, the deviation of the coefficient of determination R<sup>2</sup> from unity is twice as large. Although the relative intensities of the weak bands is typically at least ten times smaller than that of the main bands, inclusion of the former has a significant effect on the relative intensities of the latter.

## 6.5.2 Experimental spectra

### 6.5.2.1. Spectra obtained with the FP

The normalized SFG spectra obtained with the FP for several negative values of the delay are shown in **Fig. 6.15**. Except for an overall intensity increase by a factor of 4 as the delay is changed from  $\tau = -1250$  to  $-250$  fs, the spectra are delay independent. Accordingly the calculated spectral phase is independent of the delay at negative  $\tau$  values (**Fig. 6.12c**) as discussed in **Eq. 6.3** and illustrated by the inset of **Fig. 6.15**: the fraction of the visible pulse that overlaps the first order polarization has the same shape at any negative delay.

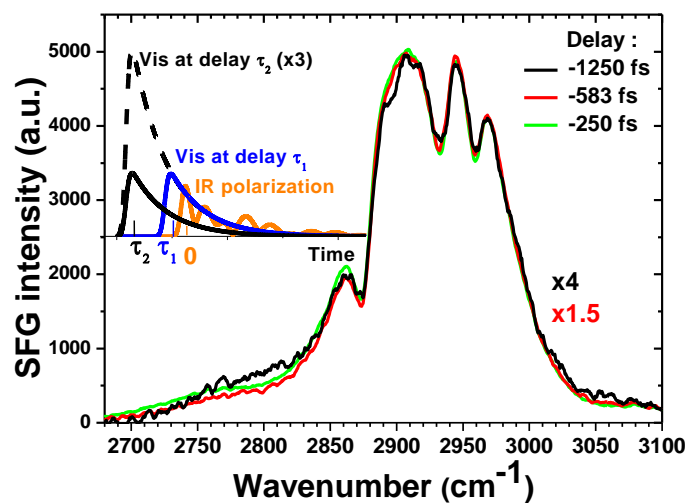


**Fig. 6.15.** Normalized experimental SFG spectra obtained using the FP etalon for different negative values of the IR-visible time delay. Inset shows that the first order polarization  $P_{\text{IR}}^{(1)}(t)$  “sees” the same (exponential) temporal shape of the visible pulse for two delay values  $\tau_1 < 0$  and  $\tau_2 < \tau_1$ . It follows that the spectral shape does not depend on the delay when it is negative.

In contrast the SFG spectra shown in **Fig. 6.16** for positive  $\tau$  values are strongly delay dependent. As the delay is increased the NR background shows a strong intensity decrease and is fully suppressed at delay values around 300 fs (**Fig. 6.16a**). Above 300 fs, the relative intensities of the ODT vibrational bands change significantly (**Fig. 6.16b**), as expected from the model calculations (**Fig. 13b, c**).

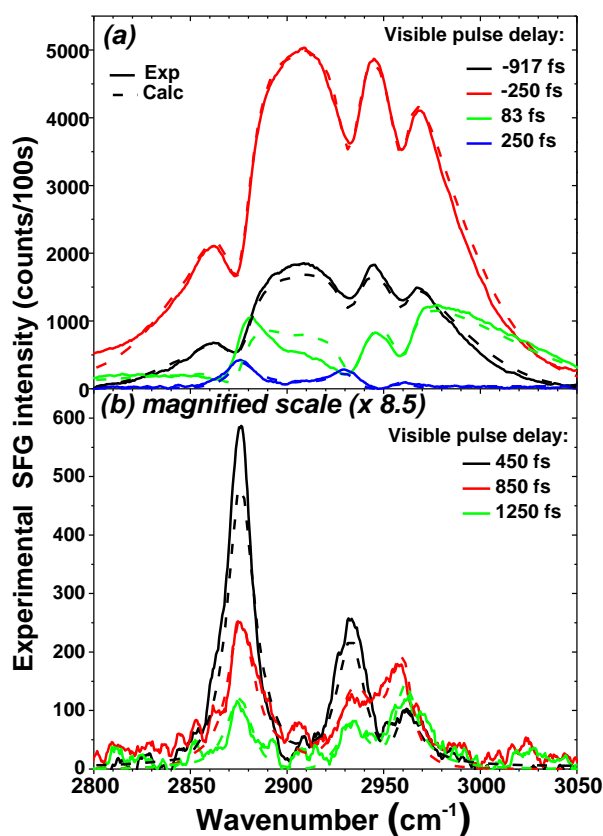


**Fig. 6.16.** Comparison between experimental SFG spectra (solid lines) of ODT SAM obtained using FP- produced visible pulses for different values of the IR-visible time delay and simulated spectra (broken lines) calculated with the spectro-temporal model. (a) at delay values between  $-917$  and  $250$  fs, (b) at longer delay times ranging from  $450$  to  $1250$  fs. Note that the scale is magnified by  $8.5$  with respect to a).

**Fig. 6.17** shows the SFG intensities at the peak frequencies of the three methyl bands as a function of the IR-visible time delay. For negative delay values the intensity ratio at these three frequencies does not change (**Fig. 6.17a**), in agreement with **Fig. 6.16a**. The SFG intensity increases as the delay decreases and reaches its maximum value at  $-200$  fs (more precisely estimated than on **Fig. 6.16a**). This corresponds to the increasing overlap between the IR first order polarization and the visible pulse (inset of **Fig. 6.17a**). Then the SFG intensity decays abruptly in  $\sim 300$  fs at a rate controlled by the rise time of the visible pulse and by the IR pulse duration which governs the fast decay of the NR first order polarization. At positive delays longer than  $300$  fs the SFG intensity originates only from the ODT vibrational bands (**Fig. 6.17b**). Obviously the relative intensities of the 3 bands do not decay exponentially as a function of the IR-visible time delay but interfere with each other and

oscillate, as could be anticipated from **Eq. 6.2** and from the model calculations of **Section 6.3**. This should be related to the fact that at positive  $\tau$  values the SFG spectral phase is delay dependent (**Fig. 13b2** and **c2**).

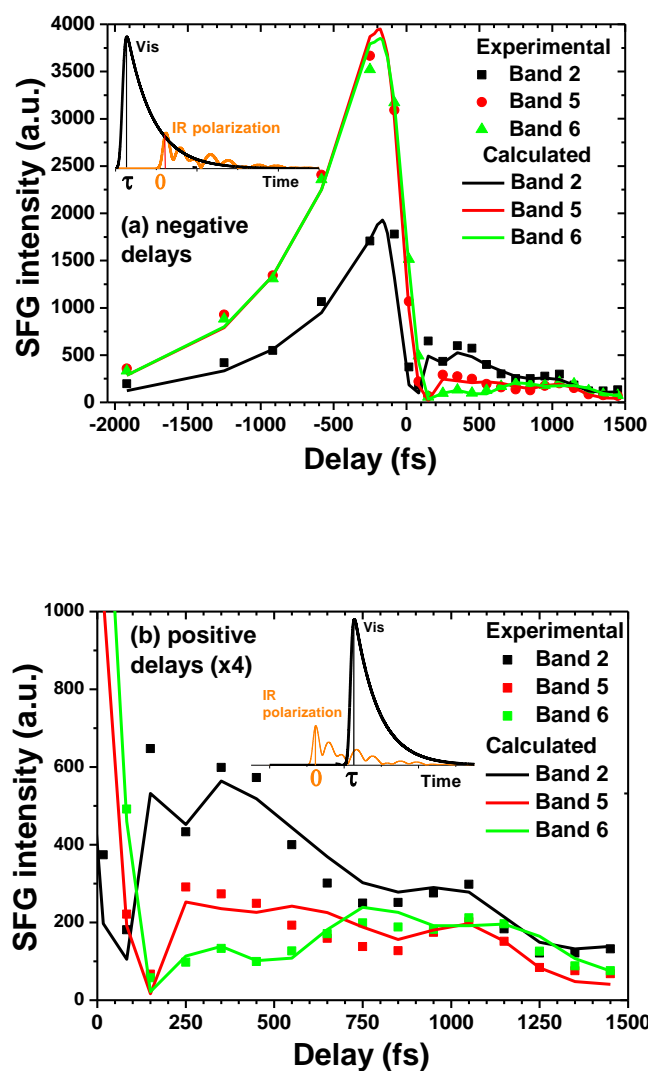


**Fig. 6.17.** Comparison between experimental and simulated SFG intensities generated by FP-produced ps visible pulses at the peak frequencies of the three methyl bands of ODT SAM at  $2878\text{ cm}^{-1}$  (band 2),  $2936\text{ cm}^{-1}$  (band 5) and  $2963\text{ cm}^{-1}$  (band 6) as a function of the IR-visible time delay: (a) at negative and positive delay values between  $-1800$  and  $1450$  fs, (b) at positive delays with a magnified scale ( $\times 4$ ).

### 6.5.2.2 Spectra obtained with the 4f pulse shaper

In the case of the 4f pulse shaper equipped with a slit, the SFG spectra are practically independent of the IR-visible delay for both negative and positive values (**Fig. 19a**). Therefore acquiring multiple spectra at variable delays has no practical interest with this pulse shaping method. Spectra are similar to those obtained with the FP etalon at negative delay values (**Fig. 6.15**), except for a larger intensity ratio between R and NR contributions due to a better sampling of the resonant signal and a slightly better spectral resolution. The NR background is present at any IR-visible delay, as expected from the time envelope of the PS-produced visible pulse which does not allow for discrimination of R and NR contributions. **Fig. 19b** shows the simulated SFG spectra normalized to unity at the maximum NR signal for three different positive delay values. The weak delay dependence observed for the R/NR intensity ratio is well reproduced in the calculation. It results from the longer dephasing times of the resonant IR polarizations with respect to the nonresonant one, leading to a slight increase of the ODT vibrational bands intensity relatively to the NR background as the IR-visible delay is increased.

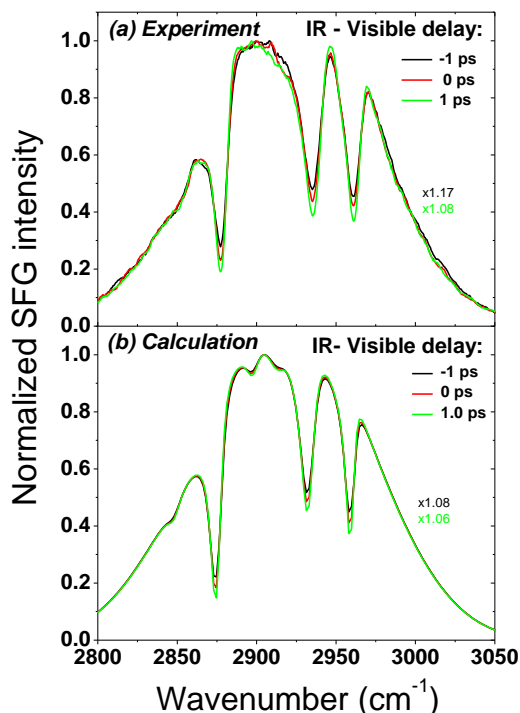


**Fig. 6.18.** Normalized experimental (a) and simulated (b) SFG spectra obtained using PS-produced visible pulses at different IR-visible delay values  $\tau = -1, 0$  and  $1$  ps.

### 6.5.3. Spectro-temporal fit

#### 6.5.3.1 Spectra obtained with the FP etalon

**Fig. 6.16** and **6.17** show that the spectro-temporal modeling is able to reproduce very satisfactorily the whole set of spectra. The 6 vibrational bands of ODT /Au have been fitted to the set of FP spectra recorded at different IR-visible delay values for which full NR background suppression is obtained (**Fig. 6.16b** and **6.17b**). The fitting parameters are the amplitudes  $B_i$  and the halfwidths  $\Gamma_i = 1 / (2\pi c T_{2i})$ . The vibrational frequencies are known and not allowed to vary. The values of the resonant parameters extracted from this spectro-temporal analysis are collected in Table 1a and the corresponding experimental, fitted and deconvoluted spectra are shown in **Fig. 6.19a**. The fit is done by trial and error. The quality of the fit is judged good when the delay dependent intensity oscillations is well reproduced for each of the three main bands (**Fig. 6.17b**). A good fit of the entire set of spectra can only be obtained with different  $\Gamma_i$  values for the three methyl bands, leading to  $\Gamma_2 = 7.35$ ,  $\Gamma_5 = 10$  and  $\Gamma_6 = 5 \text{ cm}^{-1}$  (**Table 6.2b**). These numbers are consistent with the values  $\Gamma_2 = 5.3$ ,  $\Gamma_5 = 9.5$  and  $\Gamma_6 = 6.5 \text{ cm}^{-1}$  determined by Suzuki and coll. [24] for an ODT SAM on gold by frequency-resolved picosecond SFG. These authors have also performed time-resolved SFG free induction decay (SFG-FID) experiments on the same system [25]. However the 2 ps time resolution was not sufficient to separate R and NR contributions. Bordenyuk *et al.* [26] have measured the  $\text{CH}_3$  vibrational coherences of Langmuir-Blodgett monolayers of heptadecanoic acid in various phases by combining time and frequency resolved femtosecond SFG. The reported half-widths  $\Gamma_2 = 7.5$ ,  $\Gamma_5 = 4.0$  and  $\Gamma_6 = 5.0 \text{ cm}^{-1}$  for the  $\text{O}_v$  phase and  $\Gamma_2 = 5$ ,  $\Gamma_5 = 8$  and  $\Gamma_6 = 4.5 \text{ cm}^{-1}$  for the  $\text{L}_{2d}$  phase, as well as the values  $\Gamma_2 = 8$  and  $\Gamma_5 = 7 \text{ cm}^{-1}$  recently found for the methyl vibrations of octadecylsilane (ODS) SAM on fused silica by Nihonyanagi *et al.* [27] are in the same range as our values for ODT SAM. The relative peak intensities  $(B_i/\Gamma_i)^2$  of the three methyl bands are in the ratio 1:0.47:0.31. It should be noted that a reasonably good fit of the simulated to the experimental FP spectra with NR background at negative delay is readily obtained by simply adjusting the NR amplitude  $\chi_{\text{NR}}$  and setting the relative phase  $\varphi$  to 5.07 rad (a value previously determined from the simultaneous fit of spectra recorded on a collection of samples [19]), while keeping the same resonant parameters. This fact indicates that contrary to the case of polystyrene on silicon [13] or OTS on fused silica

[14] the NR model consisting of a constant amplitude  $\chi_{NR}$  and phase  $\varphi$  is adequate for ODT on gold.

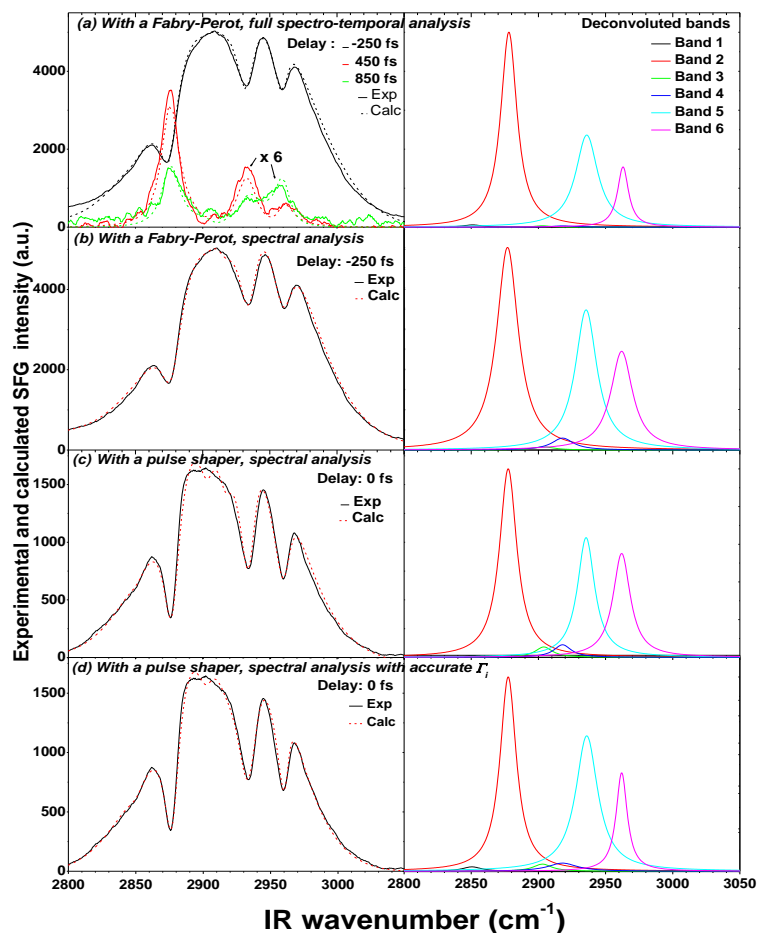


**Fig. 6.19.** Deconvoluted vibrational bands of ODT SAM on gold (right column) obtained from the comparison between experimental (full lines) and fitted (dashed lines) SFG spectra (left column) in four different manners). The fitting parameters are the peak intensities  $(B_i/\Gamma_i)^2$ , the halfwidths  $\Gamma_i$  and the NR amplitude. The phase difference between R and NR contributions is taken as  $\varphi = 5.07$  rad and is not allowed to vary. (a) Spectro-temporal analysis of the entire set of spectra obtained using the visible pulse generated by the FP etalon at positive delay values ranging from 300 to 1450 fs. The spectra at delays of 450 and 850 fs are magnified ( $\times 6$ ). Note that the spectrum at the delay  $\tau = -250$  fs is also reasonably well fitted, (b) Purely spectral analysis of the spectrum obtained using the FP-produced visible pulse at the delay  $\tau = -250$  fs, (c) Purely spectral analysis of the spectrum obtained using the PS-produced visible pulse at zero delay, (d) Same as c) but using the  $\Gamma_i$  values found in a).

### 6.5.3.2 Spectra obtained with the 4f PS

The spectra are almost insensitive to the IR-visible time delay (**Fig. 19a**). The simulated spectra shown in **Fig. 19b** have been obtained by using the values of the resonant parameters determined from the spectro-temporal analysis of a series of delay dependent spectra generated by the FP- produced visible pulse. A good agreement between experimental and simulated PS spectra is obtained by simply adjusting the value of the NR amplitude.

## 6.5.4 Accuracy of purely spectral deconvolution into Lorentzian bands

### 6.5.4.1 FP etalon

Having successfully fitted the entire set of spectra recorded at different delays, we now examine the validity of the standard deconvolution procedure of a single spectrum generated by a FP-produced visible pulse in the presence of NR background. In this case a reduced number of fitting parameters should be used. The vibrational linewidths are assumed to be identical for all bands and described by a single parameter  $\Gamma$ . Fits are first judged by eye using the Manipulate function of Mathematica. Then the coefficient of determination is determined numerically. The comparison shows that the eye is very sensitive to the fit quality. Typically  $R^2$  coefficients of determination of 0.993 are obtained. They can be improved up to 0.9995 when all the parameters are allowed to vary, but in such a case the frequencies or widths are not physically acceptable : this is a consequence of the fact that the number of parameters is too large. When the number of parameters is limited, the standard error is typically less than 2% on Lorentzian amplitudes and 1% on the widths. However the standard error characterizes the deviation of the data with respect to the model and it is not a true evaluation of the absolute error. **Fig. 6.19b** shows the deconvoluted vibrational bands resulting from the fit to the experimental spectrum obtained at the IR-visible delay  $\tau = -250$  fs. The values of the fitting parameters are listed in Table 1b. The relative peak intensities of the methyl bands extracted from the fit are in the ratio 1:0.69:0.48. These values differ significantly from those determined by fitting a series of spectra obtained at different delay values (**Table 6.2a** and **Fig. 6.19a**). This is rather expected in this case considering that the sampling of  $P_R^{(1)}(t)$  by the FP-produced visible pulse is obviously not ideal as illustrated by **Fig. 6.7b** : the decay of the

visible pulse is too fast with respect to that of the resonant polarization which is the less efficiently sampled as the dephasing time is longer, resulting in an incorrect ratio between the intensities of bands with different  $T_2$  values.

**Table 6.2.** Peak intensities  $(B_i/\Gamma_i)^2$  in relative units normalized to unity for band 2 and halfwidths  $\Gamma_i$  of the ODT vibrational bands extracted from fitting of the SFG spectra in four different manners.

ODT vibrations			a FP-produced SFG spectro-temporal analysis		b FP-produced SFG spectral analysis		c PS-produced SFG spectral analysis		d PS-produced SFG spectral analysis	
# band	mode	$\nu_i$ (cm <sup>-1</sup> )	$(B_i/\Gamma_i)^2$	$\Gamma_i$ (cm <sup>-1</sup> )	$(B_i/\Gamma_i)^2$	$\Gamma_i$ (cm <sup>-1</sup> )	$(B_i/\Gamma_i)^2$	$\Gamma_i$ (cm <sup>-1</sup> )	$(B_i/\Gamma_i)^2$	$\Gamma_i$ (cm <sup>-1</sup> )
1	CH <sub>2</sub> s	2851	0.01	8.7	0.00	9.8	0.01	7.8	0.02	8.7
2	CH <sub>3</sub> s	2878	1	7.4	1	9.8	1	7.8	1	7.4
3	CH <sub>2</sub> -S	2905	0.01	8.4	0.02	9.8	0.05	7.8	0.04	8.4
4	CH <sub>2</sub> as	2918	0.01	13.1	0.06	9.8	0.07	7.8	0.04	13.1
5	CH <sub>3</sub>	2936	0.47	10.0	0.69	9.8	0.64	7.8	0.70	10.0
6	CH <sub>3</sub> as	2963	0.31	5.0	0.48	9.8	0.55	7.8	0.51	5.0

One may wonder whether it is possible to extract the relative intensities of the vibrational bands from a single spectrum obtained with a FP-produced visible pulse at a delay for which full NR suppression is achieved. We have deconvoluted two particular spectra recorded at delays of 250 and 450 fs. Fitting to **Eq. 1.28** using the  $B_i$  amplitudes and a single halfwidth  $\Gamma$  common to all bands as fitting parameters failed : it was necessary to include either the frequencies  $\nu_i$  or the phase factors  $\varphi_i$  in the fitting parameters. The results are shown in **Fig. 6.20**. Treating the frequencies as adjustable parameters leads to a fit of poor quality with extracted  $\nu_i$  shifted by several cm<sup>-1</sup> from their true values (**Fig. 6.20a**). Using adjustable phase factors  $\varphi_i$  instead of frequencies results in a better fit (**Fig. 6.20b**). The reason is probably that since spectra are distorted by interferences with a delay dependent spectral phase, the introduction of a phase  $\varphi_i$  for each band mimics to some extent the effect of the phase. However it does not allow to correctly determine the relative band intensities.

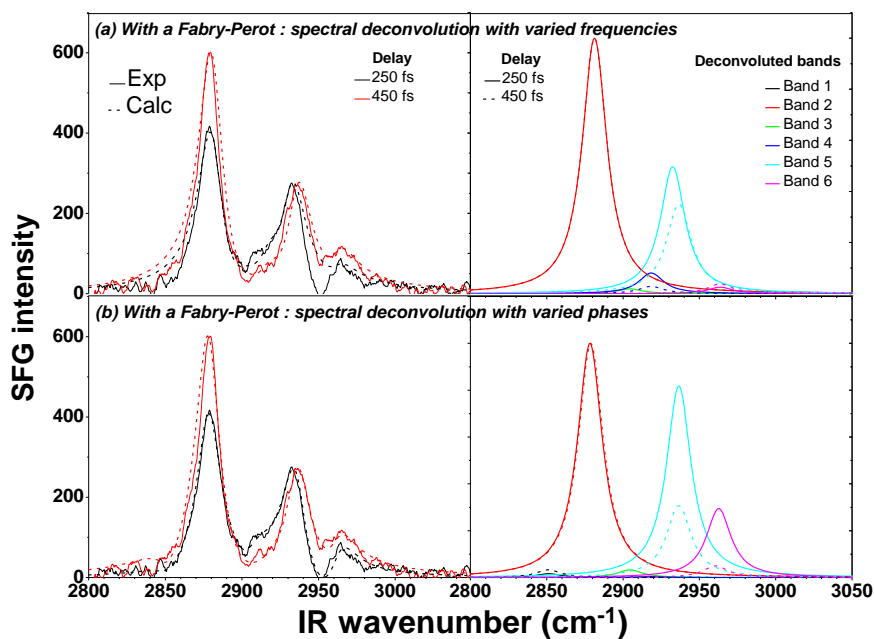


**Fig. 6.20.** Deconvolution of SFG spectra generated by FP-produced visible pulse at the two particular delay values  $\tau = 250$  and  $450$  fs using two different sets of fitting parameters. (a) Frequencies  $\nu_i$  and amplitudes  $B_i$ , (b) Phase factors  $\varphi_i$  and amplitudes  $B_i$ .

#### 6.5.4.2 4f pulse shaper

The amount of available information from PS spectra alone turns out to be insufficient to allow for an accurate determination of both intensities and widths of the vibrational bands. In order to evaluate the extent of this problem of accuracy, we have done fits of a single spectrum obtained with the PS-produced visible pulse using the purely spectral analysis and either a single  $\Gamma$  parameter (**Fig. 6.19c**) or fixed  $\Gamma_i$  values derived from the spectro-temporal analysis of the entire set of delay dependent spectra generated by the FP-produced visible pulse (**Fig. 6.19d**). The R-NR phase difference is not allowed to vary and is kept to the value  $\varphi = 5.07$  rad. The relative peak intensities are in the ratio 1:0.64:0.55 for the fit with a single  $\Gamma$  parameter (**Table 6.2c**) and 1:0.70:0.51 for the fit with the fixed  $\Gamma_i$  values (**Table 6.2d**). Note that the fit quality as judged by the coefficient of determination is similar in both cases. A striking result is that the relative peak intensities of the  $\text{CH}_3$  bands extracted from the purely spectral analysis of a single spectrum obtained using either the PS or the FP are equal within  $\pm 5\%$  for band 5 and  $\pm 7\%$  for band 6 and are not significantly modified by using the  $\Gamma_i$  values

derived from the more accurate spectro-temporal analysis. In contrast their values differ by 44% and 66% for bands 5 and 6, respectively, from the accurate ones (**Table 6.2a** and **Fig. 6.19a**). The difference between the spectro temporal, variable time-delay approach and the traditional deconvolution of a single SFG spectrum at delay zero is therefore significant. It is more surprising in the case of the PS which produces an envelope of the visible pulse more slowly varying than in the case of the FP etalon and no delay dependence of the spectral phase. This is probably due to the fact that the distortion of the time dependent resonant polarization by the PS-produced pulse is not taken into account in the purely spectral fit.

## 6.6 Conclusion

Spectra of ODT SAM on Au have been recorded using ps visible pulses generated by a Fabry-Perot etalon as a function of the IR-visible time delay in the range  $-2$  ps to 1.5 ps, and compared to spectra obtained with a 4f zero-chirp pulse shaper. The FP has the advantage to allow full suppression of the NR background by temporal discrimination, thus avoiding the difficulties brought by the interference between R and NR contributions. However the SFG spectra are distorted because of apodization effects related to the temporal profile of the FP-produced visible pulse. Moreover further distortion is caused by interference effects between the closely spaced vibrational bands of ODT resulting from the broad wings of the visible pulse that extend over a frequency range larger than the ODT vibrational spacings. These problems can be overcome by recording a series of SFG spectra at different delays. The combination of information in time and frequency domains allows for an accurate determination of the resonant parameters, namely relative intensities and linewidths. The full set of experimental SFG spectra recorded at different delay values is satisfactorily reproduced by a simulation model based on exact numerical computation of SFG polarization in the time domain and subsequent Fourier transform. In addition to providing accurate relative intensities the spectro-temporal analysis of the FP spectra has also the advantage to allow for a much more precise measurement of vibrational bandwidths compared to a purely spectral deconvolution. The  $T_2$  dephasing times extracted from spectral widths measurements are in the same range as the values found in other time resolved studies of similar systems [26,27].

In the case of the PS, the SFG spectra are practically independent of the delay because the amplitude spectrum of the PS-produced visible pulse has no wings and thus interferences between SFG components belonging to different vibrational bands are avoided. However interference effects between the resonant bands and the NR background which is present at

any delay, and apodization effects related to the temporal profile of the visible pulse prevent intensities and widths to be accurately determined. In addition, because the PS spectra are independent of the IR-visible delay, there is no way to overcome the problem that the number of unknown parameters is too large. The relative band intensities found using the standard, purely spectral deconvolution procedure of a single spectrum obtained with either a PS at any IR-visible delay or a FP at negative or zero delay differ by up to 66 % from those extracted from the spectro-temporal analysis of a set of spectra obtained with a FP at variable delay. Note that the purely spectral analysis works even worse in the case of the FP at positive delays.

Reported studies of the methyl group orientation in alkanethiol SAMs rely on measurements of the relative intensities of the CH<sub>3</sub> bands [11,19]. The present results suggest that the accuracy of these measurements performed on PS-produced spectra at zero IR-visible delay could be significantly improved by revisiting the data using the spectro-temporal analysis of FP-produced spectra at various delay times. However, the intensity of the asymmetric stretch (band 6 in this work) relative to the symmetric stretch (band 2) is extremely sensitive to the methyl orientation [1] so that large relative intensity changes happen to correspond to small methyl tilt angle variations. Therefore previous determinations of the methyl orientation based on the purely spectral analysis of the PS spectra are not as inaccurate as the relative intensities of the vibrational bands. Qualitative results or conclusions about the dependence of molecular orientation on experimental conditions, where only trends are really important [19] are probably not to be questioned. A similar conclusion may hold for single FP spectra recorded at a fixed delay around the minimum value allowing for background suppression.

## References

- [1] B. Bourguignon, W. Zheng, S. Carrez, D. Ouvrard, F. Fournier, H. Dubost, *Phys. Rev. B* 79, 125433. (2009)
- [2] L. Dreesen, C. Humbert, M. Celebi, J.J. Lemaire, A.A. Mani, P.A. Thiry, A. Peremans, *Appl. Phys. B* 74, 621. (2002)
- [3] B. Busson A. Tadjeddine, *J. Phys. Chem. C* 113, 21895. (2009)
- [4] A. Lagutchev, S.A. Hambir, D.D. Dlott, *J. Phys. Chem. C* 111, 13645. (2007)
- [5] J.A. Carter, Z. Wang, D.D. Dlott, *J. Phys. Chem. A* 112, 3523. (2008)
- [6] J.A. Carter, Z. Wang, D.D. Dlott, *Acc. Chem. Res.* 42, 1343. (2009)
- [7] S.K. Shaw, A. Lagutchev, D.D. Dlott, A.A. Gewirth, *Anal. Chem.* 81, 1154. (2009)
- [8] A. Lagutchev, A. Lozano, P. Mukherjee, S.A. Hambir, D.D. Dlott, *Spectrochim. Acta, Part A* 75, 1289. (2010)
- [9] N.E. Karatzas, A.T. Georges, *J. Opt. Soc. Am. B* 26, 2218. (2009)
- [10] T. Ishibashi, H. Onishi, *Chem. Phys. Lett.* 346, 413. (2001)
- [11] I.V. Stiopkin, H.D. Jayathilake, C. Veeraman, A.V. Benderskii, *J. Chem. Phys.* 132, 234503. (2010)
- [12] A.D. Curtis, S.B. Reynolds, A.R. Calchera, J.E. Patterson, *J. Phys. Chem. Lett.* 1, 2435. (2010)
- [13] A.D. Curtis, S.R. Burt, A.R. Calchera, J.E. Patterson, *J. Phys. Chem. C* 115, 11550. (2011)
- [14] A.D. Curtis, M.C. Asplund, J.E. Patterson, *J. Phys. Chem. C* 115, 19303. (2011)
- [15] A.D. Quast, A.D. Curtis, B.A. Horn, S.R. Goates, J.E. Patterson, *Anal. Chem.* 84, 1862. (2012)
- [16] C. Weeraman, S.A. Mitchell, R. Lausten, L.J. Johnston, A. Stolow, *Opt. Express*, 18, 11483. (2010)
- [17] J.E. Laaser, W. Xiong, M.T. Zanni, *J. Phys. Chem. B* 115, 2536. (2011)
- [18] A.M. Weiner, J.P. Heritage, E.M. Kirschner, *J. Opt. Soc. Am. B* 5, 1563. (1988)
- [19] E. Bulard, Z. Guo, W. Zheng, H. Dubost, M.-P. Fontaine-Aupart, M.-N. Bellon-Fontaine, J.-M. Herry, R. Briandet, B. Bourguignon, *Langmuir*, 27, 4928. (2011)
- [20] R.J. Meier, *Vib. Spectrosc.* 39, 266. (2005)
- [21] F. Fournier, W. Zheng, S. Carrez, H. Dubost, B. Bourguignon, *J. Chem. Phys.* 121, 4839. (2004)

- [22] A.L. Harris, L. Rothberg, *J. Chem. Phys.* 94, 2449. (1991)
- [23] R.W. Boyd, in *Nonlinear Optics*, *Academic Press*, (1992)
- [24] Y. Tanaka, S. Lin, M. Aono, T. Suzuki, *Appl. Phys. B* 68, 713. (1999)
- [25] S. Ma, M. Aono, T. Suzuki, *Colloids Surf. A : Physicochem. Eng. Aspects*, 257-258, 357. (2005)
- [26] A.N. Bordenyuk, H. Jayathilake, A.V. Benderskii, *J. Phys. Chem. B* 109, 15941. (2005)
- [27] S. Nihonyanagi, A. Eftekhari-Bafrooei, E. Borguet, *J. Chem. Phys.* 134, 084701. (2011)
- [28] L. Lepetit, G. Chériaux, M. Joffre, *J. Opt. Soc. Am. B* 12, 2467. (1995)
- [29] A. Kastler, *Nouv. Rev. Optique*, 5, 133., (1974)
- [30] E. Hecht, in *Optics* 4<sup>th</sup> ed.; Addison Wesley, San Francisco, (2002)



## Conclusion

In this thesis SFG is used to study the interaction of CO and CO+O<sub>2</sub> on a model catalyst. The aim is to bring new types of information on the mechanisms of catalysis by exploiting the fact that SFG can be used at much higher pressure and temperature than most surface science techniques. In this work Pd nanoparticles (NPs) grown on an ultrathin MgO layer on Ag(100) are exposed up to 2 mbar of CO+O<sub>2</sub> and up to 390 K. The existence of adsorption sites distinct from the regular sites of the main (100) facets is searched at domain boundaries of coalesced NPs and as a function of NP size and CO pressure. CO removal by oxidation is followed as a function of O<sub>2</sub> pressure, surface temperature and NP size. The work has been organized in three steps : (1) the SFG and LEED study of the (100) surface as compared to previous IRAS and LEED studies; (2) the comparison of CO adsorption on Pd(100), coalesced NPs, and NPs of decreasing size (down to  $\approx 170$  atoms) to bring out the adsorption sites related to defects and finite size; (3) the effect of size on the CO oxidation.

(1) Because NPs involve (100) facets, we have studied CO adsorption on Pd(100). Below 0.5 ML SFG results confirm previous IRAS studies. Above 0.5 ML, we have obtained new results that concern the compression of the CO layer in equilibrium with gas phase. Compression of the CO layer, or increase of the CO coverage in equilibrium with gas phase, is important since it takes place already below  $10^{-8}$  mbar at room temperature and may therefore be present in catalytic conditions. We have observed in much more details than previously two vibrational bands that we have assigned to CO at compressed and uncompressed bridge sites. Their frequencies vary in opposite directions with coverage. Their properties are unexpectedly strongly different: the second order susceptibility is two times smaller at compressed sites and the relaxation time is three times shorter for uncompressed CO. This shows that a large CO pressure leads to high coverages for which surface bonding may be strongly modified with respect to “static” conditions.

(2) At pressures below  $\approx 10^{-3}$  mbar the CO spectra on a coalesced layer and on large NPs are dominated by the same bridge band as on Pd(100), which is related to the dominant (100) facet located on top of the truncated pyramid formed by the NPs. However, bridge and atop defect sites are also present both on the domain boundaries of coalesced NPs and on NPs. The CO singleton frequency decreases with coverage, revealing the evolution of chemisorption with size. DFT calculations done at ENS Lyon reveal that the main mechanism is the strain induced by the substrate which increases the Pd-Pd bondlength, favoring electron back

donation to CO and weakening the CO bond. Compressed structures are still present on large NPs. But while compression continues to occur as evidenced by the variation of frequency with CO pressure, the SFG intensity signature of compression disappears as facets become smaller than the cell size of ordered compressed structures, showing that the compressed CO layer has a different structure on small NPs. Finally, as the CO pressure reaches  $\approx 0.1$  mbar, a new type of less-bonded atop sites is populated. All these results show that all properties : available sites, surface structures, surface bonding, stability, are all size dependent and that the behavior of CO in catalytic conditions will necessarily depend on temperature and CO pressure.

(3) When oxygen is preadsorbed up to  $10^{-4}$  mbar, CO adsorption does not seem to be significantly modified. The only spectroscopic signature of the presence of oxygen is a frequency red-shift of a dozen of  $\text{cm}^{-1}$ . Above  $10^{-3}$  mbar of oxygen, compression seems to be hindered, revealing that the state of oxygen on the NPs depends on the pressure, perhaps due to “sub surface” oxygen or to other structural changes. Above 1 mbar of  $\text{O}_2$ , adsorption of CO on atop sites is strongly favored, suggesting that some oxygen species (again, perhaps “subsurface”) favors CO adsorption on linear sites. Our maximal temperature does not allow us to increase the CO desorption above the limit that allows to avoid self-poisoning by CO. This forces us to study the reaction in an excess of oxygen. We can nevertheless monitor the evolution of CO coverage in the different sites due to oxidation as the  $\text{O}_2$  pressure is increased, and as the temperature is increased. The results strongly suggest that atop sites play no role in the oxidation, and that bridge sites are the key sites. However, while a fraction of bridge sites are more reactive on NPs, a large fraction of them seem less reactive with respect to Pd(100). This supports a picture of catalysis where reactions are favored by the existence of sites where the reaction is facilitated with respect to regular sites at facets, while the adsorption of reactants may be facilitated by more strongly bound sites. In this picture diffusion of reactants on the NP is essential (which is known to occur in typical catalytic conditions).

In summary this work confirms two main ideas: 1) that besides the regular sites present on the NP facets, other more reactive and less reactive sites exist. 2) that oxygen modifies the adsorption of co-reactants. In the case of  $\text{CO} + \text{O} / \text{Pd NPs} / \text{MgO}$ , there are at least three different oxygen pressure ranges that presumably correspond to increased oxidation “states”. These states could be surface oxygen and “subsurface” oxygen, whatever it may be, perhaps at different locations depending on oxygen pressure. Below  $10^{-4}$  mbar oxygen does not seem to influence significantly CO adsorption; between  $10^{-3}$  and  $10^{-1}$  mbar the spectroscopic signature of CO compression disappears, and above 1 mbar a new class of atop sites appears.

All this confirms the interest of SFG vibrational spectroscopy for catalysis. Several improvements of our apparatus need to be implemented, like the combination with mass spectrometry to measure the CO<sub>2</sub> production rate and the increase of the maximal surface temperature at high pressure.

An additional contribution of this thesis to SFG is the study of the spectro- temporal aspects of SFG emission which need to be taken into account not only to understand the time dependent measurements (pump probe or decay), but also spectra in static conditions. SFG spectra containing several bands are modeled in details and compared to experimental spectra, showing that in BB SFG spectra are affected by the spectro-temporal shape of the visible laser. The standard deconvolution method used in the literature is only approximate. Accurate spectro-temporal spectrum modeling is required to evaluate precisely the relative intensities when several bands are present.

## Abbreviation

**SFG** (Sum Frequency Generation),  
**SHG** (Second Harmonic Generation)  
**DFG** (Difference Frequency Generation)  
**NP** (Nanoparticles)  
**BBSFG** (BroadBand SFG)  
**R** (Resonant)  
**NR** (Non Resonant)  
**IR** (Infrared)  
**ML** (Mono Layers)  
**FSR** (Free Spectral Range)  
**PS** (Pulse Shaper)  
**FP** (Fabry-Perot)  
**UHV** (Ultra High Vacuum)  
**MBE** (Molecular Beam Epitaxy)  
**LEED** (Low Energy Electron Diffraction)  
**AES** (Auger Electron Spectroscopy)  
**XPS** (X-ray Photoelectron Spectroscopy)  
**AFM** (Atomic Force Microscopy)  
**STM** (Scanning Tunneling Microscopy)  
**BBO** (Beta Barium Borate)  
**OPA** (Optical Parametric Amplification)  
**CCD** (Charge Coupled Device)  
**MGR** (Menzel Gomer Redhead)  
**ODT** (Octa-Decane-Thiol)  
**SAM** (Self Assembled Monolayer)  
**IRAS** (InfraRed Absorption Spectroscopy)  
**TEM** (Transmission Electron Microscopy)  
**TPD** (Temperature Programmed Desorption)  
**TOR** (Turnover rate)